THE UNIVERSITY OF
WARWICK

University of Warwick institutional repository: http://go.warwick.ac.uk/wrap

A Thesis Submitted for the Degree of PhD at the University of Warwick

http://go.warwick.ac.uk/wrap/47656

This thesis is made available online and is protected by original copyright.

Please scroll down to view the document itself.

Please refer to the repository record for this item for information to help you to cite it. Our policy information is available from the repository home page.

Investigation on the Dynamics of Gravity-Driven Coastal Currents

Sandy GREGORIO

This report is submitted as partial fulfilment
of the requirements for the PhD Programme of the
School of Engineering
University of Warwick
September 2011

THE UNIVERSITY OF
WARWICK

LIBRARY DECLARATION

Candidate's name: SANDY GRÉGORIO

Date of birth: 24/01/1979 ID Number: 0461497

I agree that this thesis shall be made available by the University Library in accordance with the regulations governing University of Warwick theses.

I agree that the summary of this thesis may be submitted for publication.

I agree that the thesis may be photocopied (single copies for study purposes only) **YES** / ~~**NO**~~
(please delete as appropriate)

Theses with no restriction on photocopying will also be made available to the British Library for microfilming. The British Library may supply copies to individuals or libraries, subject to a statement from them that the copy is supplied for non-publishing purposes. All copies supplied by the British Library will carry the following statement: "Attention is drawn to the fact that the copyright of this thesis rests with its author. This copy of the thesis has been supplied on condition that anyone who consults it is understood to recognise that its copyright rests with its author and that no quotation from the thesis and no information derived from it may be published without the author's written consent."

Author's Signature: [redacted] Date: 30/09/2011

USER'S DECLARATION

1. I undertake not to quote or make use of any information from this thesis without making acknowledgement to the author.

2. I further undertake to allow no-one else to use this thesis while it is in my care.

DATE	SIGNATURE	ADDRESS

WRAP Deposit form

Name of student: SANDY GRÉGORIO
Department: ENGINEERING
University ID number: 0261497
Title of Thesis: INVESTIGATION ON THE DYNAMICS OF GRAVITY-DRIVEN COASTAL CURRENTS

E-mail address: [redacted]
Telephone number:

Please tick **one** of the options below

- ✓ This thesis can be made publicly available online.
- ○ This thesis **should not** be made publicly available online.
- ○ This thesis can be made publicly available online only after the following date……………………………..(please tell us the date)
- ○ I am submitting an additional, abridged version which can be made publicly available online, whilst the whole version cannot be.

Candidate's declaration:

I confirm that I have submitted an electronic copy of my thesis to the University of Warwick repository that is the same version as my final, hard bound copies submitted in completion of my degree.

I understand that the University of Warwick reserves the right to restrict or withdraw access to this electronic version of my work, should there be any cause for the University of Warwick to do so.

I understand that the University of Warwick reserves the right to preserve my thesis and to migrate its file format, as required for preservation purposes.

I have read the library's guidelines on third party copyright and understand the importance of obtaining rights holders' permissions before agreeing that my thesis can be made publicly available online through WRAP.

Signed: [redacted]
Date: 30/09/2011

Date of hand in of bound copies: *(To be completed by Graduate School at hand in.)*

To my Daddy Pierre and my Brother Fabrice,
With Love.

Abstract

Numerical simulations of buoyant, gravity-driven coastal plumes are summarized and compared to the inviscid geostrophic theory of Thomas & Linden (2007) and to laboratory studies for plumes flowing along a vertical-wall coastline (those of Thomas & Linden (2007) and additional experiments performed at Warwick University). In addition, results of two new laboratory studies with different scales for plumes flowing along a more realistic inclined-wall coastline are presented and compared to an extended theoretical model from the geostrophic theory of Thomas & Linden (2007). The theoretical and experimental results for plumes flowing along inclined-wall coastlines are compared to the inclined-wall experimental studies of Avicola & Huq (2002), Whitehead & Chapman (1986) and Lentz & Helfrich (2002), to the inclined-wall scaling theory of Lentz & Helfrich (2002), and to oceanic observations. The lengths, widths and velocities of the buoyant gravity currents are studied. Agreement between the laboratory and numerical experiments, and the geostrophic theories for both vertical-wall and inclined-wall studies is found to depend mainly on one non-dimensional parameter which characterizes the strength of horizontal viscous forces (the horizontal Ekman number). The best agreement between the experiments and the geostrophic theories is found for plumes with low viscous forces. At large values of the horizontal Ekman number, laboratory and numerical experiments depart more significantly from theory (e.g., in the plume propagation velocity). At very low values of the horizontal Ekman number (obtained in the large-scale inclined-wall experimental study only), departures between experiments and theory are observed as well. Agreement between experiments and theory is also found to depend on the steepness of the plumes isopycnal interface for the vertical-wall study, and on the ratio between the isopycnal and coastline slopes for the inclined-wall study.

Keywords: Rotating Flows, Buoyancy-Driven Plumes, Topography Effects.

List of Publications

Conference Presentations

Grégorio, S. O., Thomas, P. J., Haidvogel, D. B., Skeen, A. J., Taskinoglu, E. S., Linden, P. F. "Laboratory Experiments and Numerical Simulations of Gravity-Driven Coastal Currents". The 8th Euromech Fluid Mechanics Conference, Bad Reichenhall, Germany, 13-16 September 2010.

Grégorio, S. O., Thomas, P. J., Brend, M. A., Ellingsen, I. H., Linden, P. F. "Oceanographic Coastal Currents over Bottom Slope". The 7th Euromech Fluid Mechanics Conference, Manchester, United Kingdom, 14-18 September 2008.

Grégorio, S. O., Thomas, P. J., Brend, M. A., Linden, P. F. "Topographic Effects on Oceanographic Coastal Currents". Euromech Colloquium 501, Ancona, Italy, 8-11 June 2008.

Grégorio, S. O., Thomas, P. J., Brend, M. A., Linden, P. F. "Large-Scale and Small-Scale Laboratory Simulations of Gravity-Driven Coastal Currents". The 2008 Ocean Sciences Meeting, Orlando, Florida, USA, 2-7 March 2008.

Grégorio, S. O., Thomas, P. J., Linden, P. F., Levin, J. C., Haidvogel, D. B., Taskinoglu, E. S. "Investigation of Gravity-Driven Coastal Currents". 18ème Congrès Français de Mécanique, Grenoble, France, 27-31 August 2007.

Conference Publications

Thomas, P. J., Grégorio, S. O., Brend M. A. "Laboratory Simulations Investigating Effects of the Bottom Topography on the Dynamics of Oceanographic Coastal Currents". In Proceedings of the HYDRALAB III Joint Transnational Access User Meeting (editors Joachim Gruene and Mark Klein Breteler), pp. 127-130, ISBN-987-3-00-030141-4, Hannover, Germany, 2-4 Fvrier 2010.

Thomas, P. J., Linden, P. F., Grégorio, S. O., Levin, J. C., Haidvogel, D. B. “Oceanographic Coastal Currents: Small-Scale and Large-Scale Laboratory Simulations and a Geostrophic Model”. Geophysical Research Abstracts, Vol. 9, ISSN 1029-7007, published by the European Geosciences Union. EGU General Assembly, Vienna, Austria, 15-20 April 2007.

Journal Papers in Preparation

Grégorio, S. O., Thomas, P. J., Brend, M. A., Linden, P. F. “Rotating Gravity Currents over Inclined Bottom Topographies”. Under consideration for publication in J. Fluid Mech.

Journal Papers Submitted

Grégorio, S. O., Haidvogel, D. B., Thomas, P. J., Taskinoglu, E. S., Skeen, A. J. “Laboratory and Numerical Simulations of Gravity-Driven Coastal Currents: Departures from Geostrophic Theory”. Dynam. Atmos. Oceans, in press, 2011.

Acknowledgements

I would like to begin by thanking my supervisor Prof. Peter Thomas for his continuing support, assistance and insight into coastal current dynamics, and for giving me the opportunity to perform experiments on the large-scale facility at Trondheim. I would further like to thank Prof. Dale Haidvogel and the Ocean Modeling Group from Rutgers University (in particular Dr Ezgi Taskinoglu and Dr Julia Levin) to have set up the Regional Ocean Modeling System and run the numerical simulations described in this study. I really enjoyed collaborating with Prof. Dale Haidvogel, and appreciate the time Prof. Dale Haidvogel has spent on my research project and all the interesting, motivating and stimulating discussions we have had on coastal current dynamics. I would like to thank Dr Andrew Skeen for assisting in performing, processing and analyzing the *PIV* experiments presented in this thesis and Dr Mark Brend for helping with experimental, numerical and software issues, and with performing the large-scale experiments at Trondheim. This PhD research would not have been realizable without Prof. Peter Thomas, Prof. Dale Haidvogel, Dr Andrew Skeen and Dr Mark Brend.

I would like to thank Dr Gregory King who introduced me to the ”world” of Geophysical Fluid Dynamics and to my supervisor Prof. Peter Thomas. I would also like to thank Prof. Thomas McClimans and Dr Ingrid Ellingsen who welcomed Prof. Peter Thomas, Dr Mark Brend and myself at Trondheim, and who assisted us in the realization of the large-scale experiments presented in this study. In addition, thanks must go to the technical staff at Warwick University, in particular Paul Hackett, Steve Wallace and Edwards Robert, for assisting with experimental material issues, and to Kerrie Hatton for dealing with all the administrative issues. I am thankful to my two examiners Prof. Joel Sommeria and Dr Petr Denissenko for providing comments that have improved and clarified the content of this thesis.

I am grateful to my parents, Pierre Grégorio and Annie Stein, for giving me the opportunity to pursue such long studies. I would like to thank my PhD colleagues and friends, Dr Mark Brend, Dr Andrew Skeen, Dr Amit Kiran, Dr Joe Naswara, Dr David Hunter and Dr Paul Dunkley for helping and supporting me during difficult times. I have to thank as well my friends Sonia Dedic, Linda Homann, Cedric Tisseyre and Julien Palmeira for their support. Finally thanks must go to Yannick Manet for his strong support (especially during this last year).

Contents

Abstract **v**

List of Publications **vi**

Acknowledgements **viii**

I Introduction & Problem Definition 1

1 Introduction **2**

2 General background **4**
- 2.1 Coriolis effects on gravity currents 6
- 2.2 Potential vorticity 8
- 2.3 Governing non-dimensional parameters 9

3 Overview of prior studies **11**
- 3.1 Prior studies on coastal current dynamics 12
- 3.2 Prior studies on the bulge region 14
- 3.3 Prior studies on the stability of a coastal current 16

II Methods 18

4 Geostrophic Theory **19**
- 4.1 Summary of the results for coastal currents flowing along a vertical coastline 19
- 4.2 Generalization of the analysis to coastal currents flowing along inclined boundaries 22
- 4.3 Predictions of the inclined-wall model 30
  - 4.3.1 Variations of the non-dimensional theoretical inclined-wall velocity U_i 30
  - 4.3.2 Comparison between the inclined-wall velocity, u_i, and the vertical-wall velocity, u_0 35

5 Experimental methods **40**
5.1 Small-scale experiments 40
5.1.1 Dye visualization of coastal currents 44
5.1.2 Particle Image Velocimetry Measurements 45
5.2 Large-scale experiments 51

6 Numerical methods **57**
6.1 Numerical configuration 57
6.2 Flow rate extraction 60
6.3 Data extraction methods 61
6.4 Comparison between the numerical, experimental and theoretical approaches 63

III Numerical Study **64**

7 *ROMS* simulations **65**
7.1 Introductory Remarks 67
7.2 Qualitative aspects of the coastal currents 67
7.3 Coastal current length 69
7.4 Coastal current width 72
7.5 Coastal current velocity 78
7.6 Plume-edge instabilities 86

8 Departures from the theory: Internal structure and dynamics **89**
8.1 Internal velocity structure and momentum balances 89
8.2 Mixing in the plumes 97
8.3 Theoretical considerations 102

IV Experimental Study **105**

9 The effect of sloping bottom on coastal current evolution **106**
9.1 Introductory remarks 106
9.2 Coastal current length and propagation velocity 109
9.2.1 Comparison between inclined-wall and vertical-wall experiments 109
9.2.2 Comparison of inclined-wall experiments with inclined-wall theory 112
9.3 Coastal current height 123
9.4 Coastal current width 127

10 Comparison of the present theoretical and experimental results with other studies 135
10.1 Summary of the experimental set-up of Whitehead & Chapman (1986), Avicola & Huq (2002) and Lentz & Helfrich (2002) 135
10.1.1 Experiments of Whitehead & Chapman (1986) 135
10.1.2 Experiments of Avicola & Huq (2002) 136
10.1.3 Experiments of Lentz & Helfrich (2002) 138
10.2 Comparison with other experimental study 138
10.2.1 Coastal current propagation velocity 138
10.2.2 Coastal current width 147
10.3 Comparison with the scaling of Lentz & Helfrich (2002) 149
10.3.1 Coastal current propagation velocity 151
10.3.2 Coastal current width 152
10.4 Comparison with oceanic observations 152

11 The effect of the ambient ocean depth on vertical-wall coastal current evolution 162
11.1 Current length 162
11.2 Current surface velocity 164

V Conclusion 168

12 Conclusion 169

References 177

A Appendix A 182

B Appendix B 187

C Appendix C 192

D Appendix D 197

E Appendix E 202

List of Tables

5.1 Summary of the ranges of the independent parameters in the small-scale experiments. 43

5.2 Summary of the ranges of the independent parameters in the large-scale experiments. 56

6.1 Summary of the characterizations for the theory, the laboratory experiments and the $ROMS$ simulations. 63

7.1 Experimental parameters of the $ROMS$ simulations: plumes 118 to 136 have no lateral viscosity while plumes 148 to 155 have the lateral viscosity set to the molecular value of 10^{-2} cm^2 s^{-1}. 66

10.1 Parameters used in describing some oceanic coastal currents. . . . 158

A.1 Parameters of the small-scale experiments of Thomas & Linden (2007). 183

A.2 Parameters of the small-scale experiments of Thomas & Linden (2007). 184

A.3 Parameters of the small-scale experiments of Thomas & Linden (2007). 185

A.4 Parameters of the small-scale experiments of Thomas & Linden (2007). 186

B.1 Parameters of the small-scale experiments conducted at Warwick. 188

B.2 Parameters of the small-scale experiments conducted at Warwick. 189

B.3 Parameters of the small-scale experiments conducted at Warwick. 190

B.4 Parameters of the small-scale experiments conducted at Warwick. 191

C.1 Parameters of the large-scale experiments conducted at Trondheim. 193

C.2 Parameters of the large-scale experiments conducted at Trondheim. 194

C.3 Parameters of the large-scale experiments conducted at Trondheim. 195

C.4 Parameters of the large-scale experiments conducted at Trondheim. 196

D.1 Parameters of the PIV experiments conducted at Warwick. . . . 198
D.2 Parameters of the PIV experiments conducted at Warwick. . . . 199
D.3 Parameters of the PIV experiments conducted at Warwick. . . . 200
D.4 Parameters of the PIV experiments conducted at Warwick. . . . 201
E.1 Parameters of the experiments of Avicola & Huq (2002). 203
E.2 Parameters of the experiments of Whitehead & Chapman (1986). 204
E.3 Parameters of the experiments of Lentz & Helfrich (2002). 205
E.4 Parameters of the experiments of Lentz & Helfrich (2002). 206

List of Figures

2.1 Foam fronts observed in the Flakk Fjord at Trondheim in Norway (from Ellingsen (2004)). 5

2.2 Shadowgraph of a gravity current in lock-exchange flow (from Simpson & Britter (1979)). 5

2.3 Definition of a local Cartesian framework of reference on a spherical Earth. The coordinate x is directed eastward, y northward, and z upward (from Cushman-Roisin (1994)). 7

2.4 Conservation of volume and circulation of a fluid parcel undergoing squeezing or stretching, implying conservation of potential vorticity (from Cushman-Roisin (1994). 9

3.1 Hudson river outflow. The image was obtained from $MODIS$ at $17:13$ GMT. Blue arrows show $CODAR$ field, black arrows result from shelf moorings and white arrows from $NOAA$ mooring at the Narrows. The color bar (right side) is for surface salinity from the shiptrack shown in the figure (from Chant *et al.* (2008)). 12

3.2 Sketches depicting (a) a surface-advected plume and (b) a bottom-trapped plume. The large arrows indicate the direction of the coastal plumes and the small arrow represents offshore transport in the bottom Ekman layer (from Chapman & Lentz (1994)). . . . 15

3.3 Advanced very high resolution radiometer ($AVHRR$) IR image on 22 July 1980, showing a series of well-developed cyclonic and anticyclonic eddies ~ 50 km in diameter. In both figures, A stands for Algiers. The eddies are underlined and labelled in the bottom view to show that, going eastward, the cyclones (C) decrease while the anticyclones (A) increase (From Millot (1985)). 17

4.1 Sketch illustrating the nomenclature employed to develop the theoretical model for coastal currents flowing along a vertical wall (from Thomas & Linden (2007)). 20

4.2 Schematic of the view, along the across-shore direction, of a coastal current flowing over an inclined wall in the laboratory. 23

4.3 Variations of the non-dimensional theoretical inclined-wall coastal current velocity, U_i, as a function of the bottom slope, α, and, the non-dimensional height, H. 31

4.4 Variations of U_i, as a function of (a) Ω, for different values of α, with $q_0 = 20\ cm^3\ s^{-1}$ and $g\prime = 5\ cm\ s^{-2}$,(b) q_0, for different values of α, with $\Omega = 1.5\ rad\ s^{-1}$ and $g\prime = 5\ cm\ s^{-2}$, (c) $g\prime$, for different values of α, with $\Omega = 0.5\ rad\ s^{-1}$ and $q_0 = 20\ cm^3\ s^{-1}$. Crosses indicate the maxima of U_i, found at (a) $\Omega = (\tan(\alpha))^{4/5} g\prime^{3/5}/4q_0^{1/5}$, (b) $q_0 = (\tan(\alpha))^4 g\prime^3/2^{10}\Omega^5$, (c) $g\prime = 2^{10/3}\Omega^{5/3}q_0^{1/3}/(\tan(\alpha))^{4/3}$. . . 34

4.5 Variations of the ratio, u_i/u_0, of the predicted inclined-wall coastal current speed to the predicted vertical-wall coastal current speed as a function of the bottom slope, α, and, the non-dimensional height, H. 37

4.6 Variations of u_i/u_0 as a function of (a) Ω, for different values of α, with $q_0 = 20\ cm^3\ s^{-1}$ and $g\prime = 5\ cm\ s^{-2}$,(b) q_0, for different values of α, with $\Omega = 1.5\ rad\ s^{-1}$ and $g\prime = 5\ cm\ s^{-2}$, (c) $g\prime$, for different values of α, with $\Omega = 0.5\ rad\ s^{-1}$ and $q_0 = 20\ cm^3\ s^{-1}$. Crosses indicate the maxima of u_i/u_0, found at (a) $\Omega = (\tan(\alpha))^{4/5} g\prime^{3/5}/4q_0^{1/5}$, (b) $q_0 = (\tan(\alpha))^4 g\prime^3/2^{10}\Omega^5$, (c) $g\prime = 2^{10/3}\Omega^{5/3}q_0^{1/3}/(\tan(\alpha))^{4/3}$. 38

5.1 Small-scale turntable at the *Fluid Dynamics Research Center* (University of Warwick). 41

5.2 The two inclined walls for the small-scale experimental study . . . 42

5.3 Side-view video camera for capturing the coastal current height profile. 44

5.4 *PIV* setup. 46

5.5 Results of the spatial and time averages on a single along-shore velocity profile extracted from the *PIV* experiment $J07$ at the fixed distance, d_S, downstream from the source with $d_S = 77.5cm$. The colour bar on the figures is for velocity ($cm\ s^{-1}$). 49

5.6 PIV width extraction method (the colour bar on the top image represents velocity ($cm\ s^{-1}$)). 50

5.7 Picture of the Coriolis basin. 51

5.8 A cross-section of the 5 m diameter rotating turntable at the $NTNU$ in Trondheim (from Vinger & McClimans (1980)). 52

5.9 Turntable drive mechanism. 52

5.10 Rotameter for measuring the flow rate, q_0, at the source. 53

5.11 Freshwater Source. 54

5.12 Illustration of the method to measure the coastal current depth. . 55

5.13 Camera recording the coastal current depth. 55

6.1 $ROMS$ configuration. 59

6.2 The different steps to find the flow rate in the $ROMS$ simulations; the figures display results for one specific run (plume 153, Table 7.1). 62

7.1 Top view of a coastal current simulated, (a) in the laboratory, (b) numerically. The images are taken at T=30. $I = 0.301 \pm 0.026$, $Ek_V = (1.4 \pm 0.3) \times 10^{-3}$, $ROMS$: $Ek_H = 0$, Laboratory experiment: $Ek_H = 2.68 \times 10^{-4}$. In (b), the color bar is for density(in $kg\ m^{-3}$). 68

7.2 Nose propagation of the inviscid plumes. 70

7.3 Nose propagation of the viscous plumes. 71

7.4 Comparison of the non-dimensional plume length, L, as a function of the non-dimensional time, T, for inviscid and viscous numerical simulations, and laboratory experiments of Thomas & Linden (2007). The solid line represents the theoretical prediction, $L = (3/4)T$. 73

7.5 Summary of the non-dimensional plume width, W, as a function of the dimensionless time, T, for (a) all the inviscid numerical simulations and (b) all the viscous numerical simulations. The width was measured at the non-dimensional distance, D_S, downstream from the source, with $D_S = 12$. The black curve on the figures of equation $0.2(T)^{\frac{1}{2}}$ is just to show that plume widths grow as $T^{\frac{1}{2}}$. . 75

7.6 Summary of the non-dimensional plume width, W, as a function of the dimensionless time, T, for the PIV vertical-wall experiments. The width was measured at the distance, d_S, downstream from the source, with $d_S = 57.8\ cm$. The black curve on the figure of equation $0.2(T)^{\frac{1}{2}}$ is just to show that plume widths grow as $T^{\frac{1}{2}}$. . 76

7.7 Comparison of the non-dimensional plume width, W, as a function of the dimensionless time, T, between one inviscid numerical simulation, one viscous numerical simulation and one laboratory experiments. The width was measured at the non-dimensional distance, D_S, downstream from the source, with (a) $D_S = 28.8$ and (b) $D_S = 10$. 77

7.8 Summary of the (averaged) non-dimensional plume width, W, as a function of (a) the dimensionless parameter, I, and (b) the horizontal Ekman number, Ek_H, respectively, for the viscous and inviscid numerical simulations, and for the PIV laboratory experiments. The black line on the figures identifies $W = 1$, that is agreement between experiments and theory. The error bars are standard deviation errors of the averaged non-dimensional plume width. . . . 79

7.9 Summary of the maximum non-dimensional plume speed, U_{max}, as a function of the dimensionless time, T, for (a) all the inviscid numerical simulations and (b) all the viscous numerical simulations. U_{max} was measured at the non-dimensional distance, D_S, downstream from the source, with $D_S = 12$. The black line on the Figure 7.9b identifies $U_{max} = 1$, that is agreement between experiments and theory. 81

7.10 Summary of the maximum non-dimensional plume speed, U_{max}, as a function of the dimensionless time, T, for the PIV vertical-wall experiments. U_{max} was measured at the distance, d_S, downstream from the source, with $d_S = 57.8$ cm. The black line on the figures identifies $U_{max} = 1$, that is agreement between experiments and theory. 82

7.11 Maximum non-dimensional plume speed, U_{max}, as a function of the dimensionless time, T, measured at the non-dimensional distance, D_S, downstream from the source, with $D_S = 10$, for one inviscid simulation, one viscous simulation and one laboratory experiment. U_{max} was measured at the surface for the laboratory experiment and the viscous simulation, and, at the surface ($N = 60$) and around 9 mm below the surface ($N = 56$) for the inviscid simulation. $I = 0.126 \pm 0.03$, $Ek_V = (5.73 \pm 1.79) \times 10^{-3}$, Inviscid simulation: $Ek_H = 0$, Viscous simulation and laboratory experiment: $Ek_H = (1.26 \pm 0.29) \times 10^{-4}$. 83

7.12 Summary of the (averaged) maximum non-dimensional plume speed, U_{max}, as a function of (a) the dimensionless parameter, I, and (b) the horizontal Ekman number, Ek_H, respectively, for the viscous and inviscid numerical simulations, and for the PIV laboratory experiments. The black line on the figures identifies $U_{max} = 1$, that is agreement between experiments and theory. The error bars are standard deviation errors of the averaged maximum non-dimensional plume speed. 85

7.13 Surface density field showing the unstable plumes (a) 148 and (b) 151 from the viscous numerical simulations. Color bar is for density (in $kg\ m^{-3}$). 87

7.14 I-Ek_H diagram displaying the parametric locations where the plumes are found to be stable/unstable. The dashed line is suggestive of the stability boundary. 88

8.1 Cross-section in the y-z plane of (a)-(c) the non-dimensional Coriolis term in the v-momentum equation, and (b)-(d) the non-dimensional pressure gradient term in the v-momentum equation, taken at the alongshore distance upstream from the nose, $d_N = 5\ cm$, and at the times (a)-(b) $t = 4.25\ s$ and (c)-(d) $t = 36.25\ s$ for the viscous plume 150. 91

8.2 Cross-section in the y-z plane of (a)-(c) the non-dimensional alongshore velocity, U, for the inviscid plume 134 and the viscous plume 150, respectively, and (c)-(d) the density field for the inviscid plume 134 and the viscous plume 150, respectively, taken at the alongshore distance upstream from the nose, $d_N = 5\ cm$, and at the time, $t = 4.25\ s$. The color bar in the right images is for density (in $kg\ m^{-3}$). 92

8.3 Cross-section in the y-z plane of (a)-(c) the non-dimensional alongshore velocity, U, for the inviscid plume 125 and the viscous plume 151, respectively, and (c)-(d) the density field for the inviscid plume 125 and the viscous plume 151, respectively, taken at the alongshore distance upstream from the nose, $d_N = 5\ cm$, and at the time, $t = 4\ s$. The color bar in the right images is for density (in $kg\ m^{-3}$). 93

8.4 Cross-section in the y-z plane of (a)-(c) the non-dimensional alongshore velocity, U, for the inviscid plume 134 and the viscous plume 150, respectively, and (c)-(d) the density field for the inviscid plume 134 and the viscous plume 150, respectively, taken at the alongshore distance upstream from the nose, $d_N = 5\ cm$, and at the time, $t = 36.25\ s$. The color bar in the right images is for density (in $kg\ m^{-3}$). 95

8.5 Cross-section in the y-z plane of (a)-(c) the non-dimensional alongshore velocity, U, for the viscous plumes 150 and 151, respectively, and (c)-(d) the density field for the viscous plumes 150 and 151, respectively, taken at the alongshore distance upstream from the nose, $d_N = 50\ cm$, and at the time, $t = 36\ s$. The color bar in the right images is for density (in $kg\ m^{-3}$). 96

8.6 Variations along the radial position of (a) the alongshore velocity, u, (b) the across-shore velocity, v, and (c) the vertical velocity, w, taken at the free surface, at different alongshore distances upstream from the plume nose, d_N, and at the time, $t = 40\ s$, for the inviscid plume 134. 98

8.7 Variations along the radial position of (a) the alongshore velocity, u, (b) the across-shore velocity, v, and (c) the vertical velocity, w, taken at the free surface, at different alongshore distances upstream from the plume nose, d_N, and at the time, $t = 40\ s$, for the viscous plume 150. 99

8.8 Cross-section in the x-z plane of the density field taken at 4.8 mm from the wall and at the time $t = 50\ s$ for the inviscid plume 134 and the viscous plume 150, respectively. 100

8.9 Non-dimensional volume, V_i, of intermediate water in the coastal plume and bulge system, as a function of (a) the dimensionless time, T, and (b) the non-dimensional plume length, L, for the inviscid and viscous numerical simulations. 101

8.10 Difference between the non-dimensional plume length, L, for the viscous simulations, and the theory of Thomas & Linden (2007), $L = (3/4)T$. 103

8.11 Velocity deficit as a function of the horizontal Ekman number, Ek_H. The curve is the best fit for the data of equation $8.4 \times (Ek_H)^{0.46}$. The velocity deficits are simply the slope of the best linear fits for the curves of Figure 8.10 computed from $T \geq 50$. . . 104

9.1 A typical coastal current (experiment $T35$) flowing along an inclined plate mounted across the diameter of the Coriolis tank at Trondheim. $\alpha = 50°$, $I = 0.292$, $Ek_V = 6.6 \times 10^{-4}$, $Ek_H = 1.21 \times 10^{-4}$, $h_0/H_D = 0.49$. 107

9.2 An unstable coastal current (experiment $T32$) flowing along an inclined wall in the large-scale Coriolis tank at Trondheim. $\alpha = 50°$, $I = 0.481$, $Ek_V = 2.43 \times 10^{-4}$, $Ek_H = 1.56 \times 10^{-4}$, $h_0/H_D = 0.92$. 108

9.3 Comparison of the non-dimensional plume length, L_i, as a function of the dimensionless time, T, for small-scale experiments with different sloping angles, α. 110

9.4 Comparison of the non-dimensional plume length, L_i, as a function of the dimensionless time, T, for large-scale experiments with different sloping angles, α. 111

9.5 Comparison of the non-dimensional plume length, L_i, as a function of the non-dimensional time, T, for small-scale experiments with different sloping angles, α. The solid lines represent the theoretical predictions for the different sloping angles according to (4.43). . . 113

9.6 Comparison of the non-dimensional plume length, L_i, as a function of the non-dimensional time, T, for large-scale experiments with different sloping angles, α. The solid lines represent the theoretical predictions for the different sloping angles according to (4.43). . . 114

9.7 Non-dimensional measured mean inclined-wall velocity, U_i^{exp}, as a function of the non-dimensional theoretical inclined-wall velocity, U_i^{th}, for the small-scale and large-scale inclined-wall experiments. The solid line identifies $U_i^{exp} = U_i^{th}$, while the dashed line identifies the best linear fit given by $0.62\, U_i^{th} + 0.51$ with a correlation of 0.21.116

9.8 Difference between the non-dimensional measured mean inclined-wall speed, U_i^{exp}, and the non-dimensional predicted inclined-wall speed, U_i^{th}, as a function of (a) the dimensionless parameter, I, (b) the non-dimensional ambient depth parameter, h_0/H_D, for the small-scale and large-scale inclined-wall experiments. The solid line on each figure identifies $U_i^{exp} = U_i^{th}$. 118

9.9 Difference between the non-dimensional measured mean inclined-wall speed, U_i^{exp}, and the non-dimensional predicted inclined-wall speed, U_i^{th}, as a function of (a) the horizontal Ekman number, Ek_H, (b) the vertical Ekman number, Ek_V, for the small-scale and large-scale inclined-wall experiments. The solid line on each figure identifies $U_i^{exp} = U_i^{th}$. 119

9.10 Velocity deficit for the small-scale and large-scale inclined-wall experiments as a function of the horizontal Ekman number, Ek_H. . 120

9.11 Non-dimensional measured mean inclined-wall speed, U_i^{exp}, as a function of the horizontal Ekman number, Ek_H, for the small-scale and large-scale inclined-wall experiments 122

9.12 Non-dimensional measured mean inclined-wall velocity, $(U_i^{exp})_{w_i}$, as a function of the non-dimensional theoretical inclined-wall velocity, $(U_i^{th})_{w_i}$, for the small-scale and large-scale inclined-wall experiments. The solid line identifies $(U_i^{exp})_{w_i} = (U_i^{th})_{w_i}$, while the dashed line identifies the best linear fit given by 1.19 $(U_i^{th})_{w_i} + 0.08$ with a correlation of 0.64. 122

9.13 Non-dimensional measured mean inclined-wall speed, $(U_i^{exp})_{wi}$, as a function of (a) the dimensionless parameter, I, (b) the non-dimensional ambient depth parameter, h_0/H_D, for the small-scale and large-scale inclined-wall experiments. 124

9.14 Sketch from Thomas & Linden (2007) illustrating a side-view of a plume. 125

9.15 Maximum measured plume height, h_{i_m}, near the source, as a function of the theoretical heights, h_0 and h_i, for vertical-wall and inclined-wall plumes, respectively. The solid line identifies agreement between the experiments and the theories, while the blue and red dashed lines identify the best linear fits given by 0.91 $h_0 + 2.52$ with a correlation of 0.88, and 1.51 $h_i + 0.7$ with a correlation of 0.8, respectively. 126

9.16 Non-dimensional maximum plume height, H_i^{exp}, near the source, as a function of the dimensionless parameter, I, for the large-scale inclined-wall experiments. The solid line represents the theoretical prediction, $H = 2I^{5/4}$, while the dashed line is the best fit line given by $2.22(I)^{1.15}$. 127

9.17 Summary of the non-dimensional plume width, W_i, as a function of the dimensionless time, T, for the PIV small-scale vertical-wall and inclined-wall experiments. The width was measured at the distance, d_S, downstream from the source, with $d_S = 57.8\ cm$. The black curve on the figure of equation $0.2(T)^{\frac{1}{2}}$ is just to show that the majority of the plume widths grows as $T^{\frac{1}{2}}$. 128

9.18 Comparison of the non-dimensional plume width, W_i, as a function of the non-dimensional time, T, for PIV experiments with different sloping angles, α. 130

9.19 Summary of the (averaged) non-dimensional plume width, W_i, as a function of $H/\tan(\alpha)$ for the PIV small-scale inclined-wall experiments. The solid line represents the theoretical prediction, $W_i = \sqrt{(H/\tan(\alpha))^2 + 1}$. The error bars are standard deviation errors of the averaged non-dimensional plume width. 131

9.20 Summary of the (averaged) non-dimensional plume width, W_i, as a function of the non-dimensional ambient depth parameter, h_0/H_D, for the PIV small-scale vertical-wall and inclined-wall experiments. The error bars are standard deviation errors of the averaged non-dimensional plume width. 131

9.21 Summary of the non-dimensional plume width, $(W_i)_{w_i}$, as a function of the dimensionless time, T, for the PIV small-scale vertical-wall and inclined-wall experiments. The width was measured at the distance, d_S, downstream from the source, with $d_S = 57.8\ cm$. The black curve on the figure of equation $0.2(T)^{\frac{1}{2}}$ is just to show that the majority of the plume widths grows as $T^{\frac{1}{2}}$. 132

9.22 Summary of the (averaged) non-dimensional plume width, $(W_i)_{w_i}$, as a function of (a) the non-dimensional ambient depth parameter, h_0/H_D, and (b) the horizontal Ekman number, Ek_H, respectively, for the PIV small-scale vertical-wall and inclined-wall experiments. The solid line on the figures identifies $(W_i)_{w_i} = 1$, that is agreement between experiments and theory. The error bars are standard deviation errors of the averaged non-dimensional plume width. 134

10.1 Schematic depicting the experimental configuration of Avicola & Huq (2002) using the sloping bottom tank (from Avicola & Huq (2002)). 137

10.2 Non-dimensional measured mean inclined-wall velocity, U_i^{exp}, as a function of the non-dimensional theoretical inclined-wall velocity, U_i^{th}, for the experiments of Avicola & Huq (2002), Lentz & Helfrich (2002) and Whitehead & Chapman (1986). The solid line identifies $U_i^{exp} = U_i^{th}$, while the dashed line identifies the best linear fit given by 0.95 $U_i^{th} + 0.04$ with a correlation of 0.86. 139

10.3 Ratio, U_i^{exp}/U_0, of the non-dimensional measured mean inclined-wall velocity to the non-dimensional theoretical vertical-wall velocity, as a function of $H/\tan(\alpha)$, for the experiments of Avicola & Huq (2002), Lentz & Helfrich (2002) and Whitehead & Chapman (1986). The solid line represents the theoretical prediction according to (4.65). 140

10.4 Non-dimensional measured mean inclined-wall velocity, $(U_i^{exp})_{w_i}$, as a function of the non-dimensional theoretical inclined-wall velocity, $(U_i^{th})_{w_i}$, for the experiments of Avicola & Huq (2002), Lentz & Helfrich (2002) and Whitehead & Chapman (1986). The solid line identifies $(U_i^{exp})_{w_i} = (U_i^{th})_{w_i}$, while the dashed line identifies the best linear fit given by 1.04 $(U_i^{th})_{w_i} - 0.005$ with a correlation of 0.98. 141

10.5 Non-dimensional measured mean inclined-wall speed, U_i^{exp}, as a function of (a) the dimensionless parameter, I, (b) the non-dimensional ambient depth parameter, h_0/H_D, for the experiments of Avicola & Huq (2002), Lentz & Helfrich (2002) and Whitehead & Chapman (1986). 142

10.6 Difference between the non-dimensional measured mean inclined-wall speed, U_i^{exp}, and the non-dimensional predicted inclined-wall speed, U_i^{th}, as a function of (a) the dimensionless parameter, I, (b) the non-dimensional ambient depth parameter, h_0/H_D, for the large-scale and small-scale experiments of this study, and for the experiments of Avicola & Huq (2002), Lentz & Helfrich (2002) and Whitehead & Chapman (1986). The solid line on each figure identifies $U_i^{exp} = U_i^{th}$. 144

10.7 Difference between the non-dimensional measured mean inclined-wall speed, U_i^{exp}, and the non-dimensional predicted inclined-wall speed, U_i^{th}, as a function of (a) the horizontal Ekman number, Ek_H, (b) the vertical Ekman number, Ek_V, for the large-scale and small-scale experiments of this study, and for the experiments of Avicola & Huq (2002), Lentz & Helfrich (2002) and Whitehead & Chapman (1986). The solid line on each figure identifies $U_i^{exp} = U_i^{th}$. 145

10.8 (h_0/H_D)-Ek_H diagram displaying the parametric locations where the plumes are found to be faster/slower than the theory, or to have same speed than the theory. 146

10.9 Non-dimensional measured mean inclined-wall speed, U_i^{exp}, as a function of the horizontal Ekman number, Ek_H, for the large-scale and small-scale experiments of this study and for the experiments of Avicola & Huq (2002), Lentz & Helfrich (2002) and Whitehead & Chapman (1986). 147

10.10 Measured inclined-wall width, w_i^{exp}, as a function of the theoretical inclined-wall width, w_i^{th}, for the PIV small-scale inclined-wall experiments and for the experiments of Avicola & Huq (2002) and Lentz & Helfrich (2002). The solid line identifies $w_i^{exp} = w_i^{th}$, while the dashed line identifies the best linear fit given by $0.95\ w_i^{th} + 3.16$ with a correlation of 0.9. 148

10.11 Summary of the non-dimensional plume width, W_i, as a function of the non-dimensional ambient depth parameter, h_0/H_D, for the PIV small-scale inclined-wall experiments and for the experiments of Avicola & Huq (2002) and Lentz & Helfrich (2002). 149

10.12 Summary of the non-dimensional plume width, $(W_i)_{w_i}$, as a function of (a) the non-dimensional ambient depth parameter, h_0/H_D, and (b) the horizontal Ekman number, Ek_H, respectively, for the PIV small-scale vertical-wall and inclined-wall experiments and for the experiments of Avicola & Huq (2002) and Lentz & Helfrich (2002). The solid line on the figures identifies $(W_i)_{w_i} = 1$, that is agreement between experiments and theory. 150

10.13 Measured mean inclined-wall speed, u_i^{exp}, as a function of (a) the theoretical inclined-wall speed, u_i^{th}, defined in (4.42), and (b) the theoretical inclined-wall speed, c_p, of Lentz & Helfrich (2002), for the small-scale experiments of this study and for the experiments of Avicola & Huq (2002), Lentz & Helfrich (2002) and Whitehead & Chapman (1986). The solid line in the figures identifies (a) $u_i^{exp} = u_i^{th}$ and (b) $u_i^{exp} = c_p$, while the dashed line identifies the best linear fit given by (a) $0.89\ u_i^{th} + 0.08$ with a correlation of 0.75 and (b)$0.65\ c_p + 0.52$ with a correlation of 0.66. 153

10.14 Measured mean inclined-wall speed, u_i^{exp}, as a function of (a) the theoretical inclined-wall speed, u_i^{th}, defined in (4.42), and (b) the theoretical inclined-wall speed, c_p, of Lentz & Helfrich (2002), for the large-scale experiments of this study. The solid line in the figures identifies (a) $u_i^{exp} = u_i^{th}$ and (b) $u_i^{exp} = c_p$, while the dashed line identifies the best linear fit given by (a) $1.65\ u_i^{th} + 0.35$ with a correlation of 0.73 and (b)$1.17\ c_p + 2.13$ with a correlation of 0.63. 154

10.15 Measured inclined-wall width, w_i^{exp}, as a function of the theoretical inclined-wall width, w_p, of Lentz & Helfrich (2002), for the PIV small-scale inclined-wall experiments and for the experiments of Avicola & Huq (2002) and Lentz & Helfrich (2002). The solid line identifies $w_i^{exp} = w_p$, while the dashed line identifies the best linear fit given by $0.94\ w_p + 1.93$ with a correlation of 0.9. 155

10.16 Summary of the non-dimensional plume width, $(W_i)_{w_p}$, as a function of (a) the non-dimensional ambient depth parameter, h_0/H_D, and (b) the horizontal Ekman number, Ek_H, for the PIV small-scale vertical-wall and inclined-wall experiments and for the experiments of Avicola & Huq (2002) and Lentz & Helfrich (2002). The solid line on the figures identifies $(W_i)_{w_p} = 1$, that is agreement between experiments and theory. 156

10.17 Observed alongshore speed, u_i^{field}, as a function of (a) the theoretical inclined-wall speed, u_i^{th}, defined in (4.42), and (b) the theoretical inclined-wall speed, c_p, of Lentz & Helfrich (2002), for the plumes tabulated in Table 10.1. The solid line in the figures identifies (a) $u_i^{field} = u_i^{th}$ and (b) $u_i^{field} = c_p$, while the dashed line identifies the best linear fit given by (a) 1.04 $u_i^{th} + 0.06$ with a correlation of 0.79 and (b)0.48 $c_p + 0.25$ with a correlation of 0.55. 159

10.18 Ratio, U_i^{field}/U_0, of the non-dimensional observed alongshore velocity to the non-dimensional theoretical vertical-wall velocity, as a function of $H/\tan(\alpha)$, for the plumes tabulated in Table 10.1. The solid line represents the theoretical prediction according to (4.65). 160

10.19 Observed width, w_i^{field}, as a function of (a) the theoretical inclined-wall width, w_i^{th}, defined in (4.36), and (b) the theoretical inclined-wall width, w_p, of Lentz & Helfrich (2002), for the plumes tabulated in Table 10.1. The solid line in the figures identifies (a) $w_i^{field} = w_i^{th}$ and (b) $w_i^{field} = w_p$, while the dashed line identifies the best linear fit given by (a) 0.85 $w_i^{th} + 6009$ with a correlation of 0.67 and (b)0.54 $w_p + 11690$ with a correlation of 0.55. 161

11.1 Non-dimensional current length, L, as a function of the dimensionless time, T,for three small-scale vertical-wall experiments with different ambient ocean depth, H_D. 163

11.2 Non-dimensional current length, L, as a function of the dimensionless time, T, for the surface-advected plumes from the small-scale experiments of Thomas & Linden (2007). 164

11.3 Non-dimensional current length, L, as a function of the dimensionless time, T, for the surface-advected plumes from the small-scale inclined-wall experiments presented in this study and for the bottom-trapped experiment, F, of Avicola & Huq (2002). 165

11.4 Alongshore velocity, u ($cm\ s^{-1}$), as a function of the time, t (s), measured at the alongshore distance downstream from the source, $d_s = 112.4\ cm$, for two PIV vertical-wall experiments with different ambient ocean depth, H_D. The color bar in each figure is for velocity (in $cm\ s^{-1}$). 166

11.5 Alongshore velocity, u, as a function of the radial position for three PIV vertical-wall experiments with different ambient ocean depth, H_D, measured at the alongshore distance downstream from the source, $d_s = 112.4\ cm$, and at the time $t = 124.48\ s$. 167

Part I

Introduction & Problem Definition

CHAPTER 1

Introduction

An important objective in physical oceanography is to understand the dynamics of buoyant discharge and mixing in the coastal ocean. The oceans and coastal areas of the Earth are indeed complex and dynamic natural systems. Pollution and human effects can impact these delicate ecosystems drastically.

Buoyant fluid entering the coastal ocean from, for example, an estuary will typically form a gravity-driven surface flow. The flow develops as a consequence of the density difference between the discharged, buoyant freshwater and the denser, more saline ocean water. Such flows are a major source of nutrients, sediments and contaminants to coastal waters, and may help to support diverse and productive ecosystems. These flows often play an important role in enabling the exchange of water between coastal channels and the open sea. When the buoyant outflow exceeds length scales larger than the Rossby deformation scale, its dynamics is affected by the Coriolis force arising from the rotation of the Earth. As a result, the discharged fresh water is confined to the coastal zone where it forms a current flowing along the coast in the direction of Kelvin wave propagation. This study concentrates on examining the dynamics and evolution of gravity-driven coastal currents flowing along a simple vertical-wall coastline, and along a more realistic coastline topography as represented by inclined coastlines.

Firstly, laboratory studies for gravity-driven coastal currents flowing along a vertical-wall coastline (those of Thomas & Linden (2007) and additional experiments performed at Warwick University) are combined with numerical simulations employing the Regional Ocean Modeling System (*ROMS*) to further investigate departures from the geostrophic theory of Thomas & Linden (2007). A particular attention is paid to the internal dynamics of the plumes, the occurrence of instabilities within them, and the role of viscous forces in their evolution.

Secondly, the geostrophic model of Thomas & Linden (2007) for gravity-driven coastal currents flowing along vertical-wall coastlines is extended to the more realistic case of inclined coastlines. The prediction of the extended model is compared to two new laboratory studies for coastal currents flowing along inclined coastlines and to the experimental studies of Avicola & Huq (2002), Whitehead & Chapman (1986) and Lentz & Helfrich (2002) who also carried out experiments for coastal currents flowing along sloping walls. The extended model and the five experimental studies are as well compared to the scaling theory of Lentz & Helfrich (2002) for inclined-wall coastal currents. Both, the extended geostrophic model and the scaling theory of Lentz & Helfrich (2002), are finally compared to oceanic observations. Lastly, a small set of laboratory experiments for coastal currents flowing along vertical-wall coastlines when decreasing the ambient ocean depth is examined.

The plan of this thesis is as follows. In the first part of this thesis, the general background on gravity-driven coastal currents, some previous numerical and experimental studies, and the methods (theoretical, experimental, numerical) employed here are reviewed. The second part uses the vertical-wall laboratory and numerical studies together to explore the kinematic properties of the buoyancy-driven plumes, and to identify their non-dimensional dependencies. The internal dynamics of the plumes are also investigated. The third part presents the results of the two new inclined-wall laboratory studies and compared them to the extended geostrophic model, the experimental studies of Avicola & Huq (2002), Whitehead & Chapman (1986) and Lentz & Helfrich (2002), and the scaling theory of Lentz & Helfrich (2002). The extended geostrophic model and the scaling theory of Lentz & Helfrich (2002) are compared as well to oceanic observations. The results of the study for vertical-wall coastal currents when decreasing the ambient ocean depth are lastly explored. A final part offers a summary and concluding remarks.

CHAPTER 2

General background

A gravity current, also called density current or buoyancy current, is the flow of one fluid within another caused by the density difference between the fluids. The density difference between two fluids, or between different parts of the same fluid, can exist because of a difference in temperature, salinity, or concentration of suspended sediment. It is characterised by the reduced gravity[*], g', defined by

$$g' = \frac{\rho_2 - \rho_1}{\rho_1} g, \tag{2.1}$$

where ρ_1 and ρ_2 are the densities of the two fluids and $g = 981$ cm s^{-2} is the acceleration due to gravity. Gravity currents are primarily horizontal, occurring as either top or bottom boundary currents, or as intrusions at some intermediate level, and are associated with strong density fronts. On the ocean surface, the front of a gravity current sometimes forms a colour change in the water, but more often can be seen from foam and floating debris which collect along the line of converging flow. These fronts may have multiple lines, as shown in Figure 2.1 taken at Trondheim in Norway.

Much of the dynamics of gravity currents has been discovered from laboratory experiments in which salt water was released from behind a lock gate into a large tank of freshwater. Figure 2.2 is a photograph of this type of laboratory experiment from Simpson & Britter (1979), using shadowgraphy, which displays the side view of a gravity current moving from left to right in lock-exchange flow.

The structure of the leading front in Figure 2.2 is typical of the structure of a gravity current. There is a raised part, which is called the head, and a following shallower part, called the tail. In the tail and in the ambient fluid ahead, the

---

[*] The reduced gravity represents the effective change in the acceleration of gravity acting on one fluid in contact with a fluid of different density due to buoyancy forces.

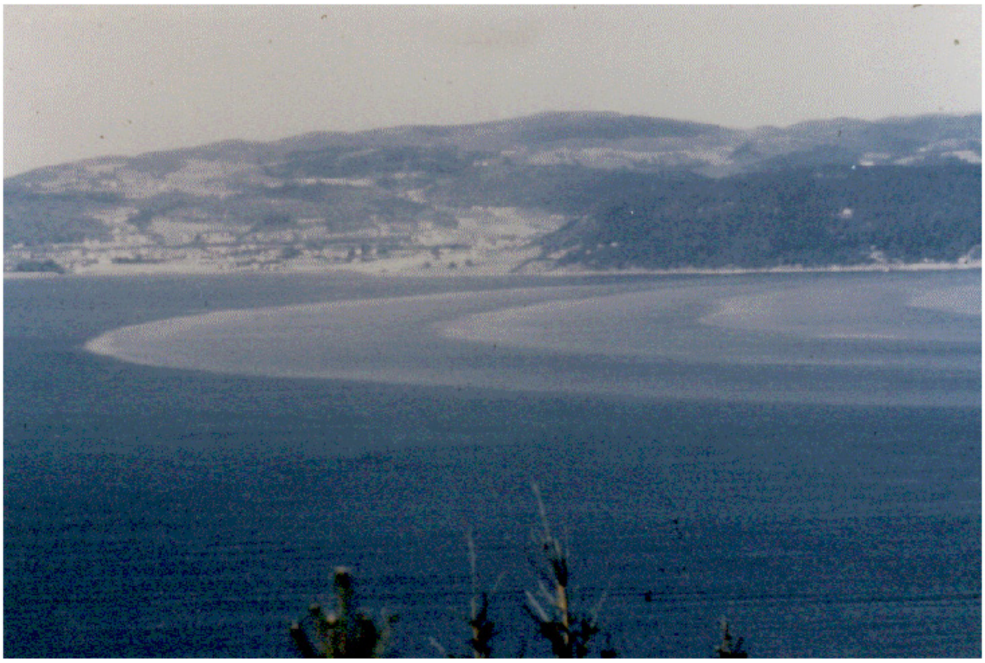

Figure 2.1: Foam fronts observed in the Flakk Fjord at Trondheim in Norway (from Ellingsen (2004)).

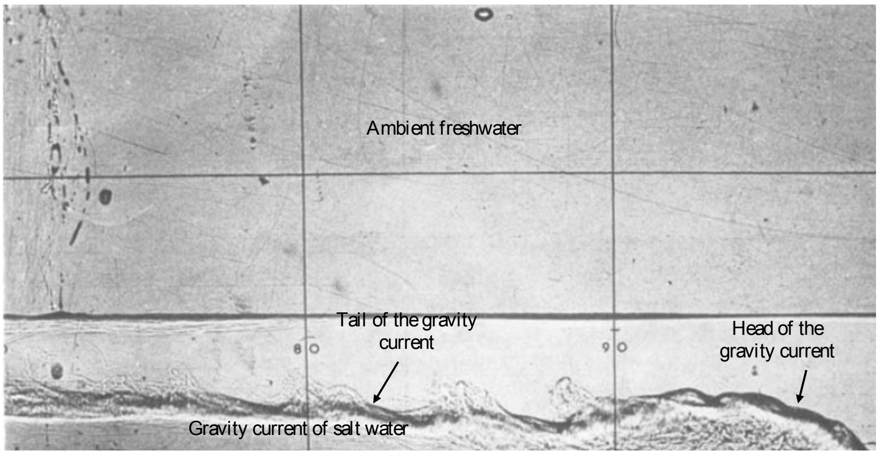
Ambient freshwater
Tail of the gravity current
Head of the gravity current
80
90
Gravity current of salt water

Figure 2.2: Shadowgraph of a gravity current in lock-exchange flow (from Simpson & Britter (1979)).

pressure is hydrostatic. At the head the ambient fluid is displaced upwards over the gravity current; consequently, the pressure there is not hydrostatic. The main transfer of momentum (between the gravity current and the ambient fluid) occurs at the head, and so this is the most dynamically significant part of the flow. Indeed, the formation of the "head" may be considered to be the fluid's response to the imposed difference in hydrostatic pressure (Hacker (1996)).

There are many examples of gravity currents occurring in the environment, which are discussed in Simpson (1987). One particular example of gravity currents produced by direct inputs of buoyancy, and of particular interest for this thesis, is in the estuarine environment, where the freshwater from a river meets the saltier sea water.

2.1 Coriolis effects on gravity currents

When gravity currents occur on length and time scales which are sufficiently large, their dynamics are influenced by the rotation of the Earth and they undergo a Coriolis force, $\boldsymbol{F_C} = -2\boldsymbol{\Omega} \times \boldsymbol{u}$, where $\boldsymbol{u}$ represents the velocity vector of a gravity current fluid particle, and $\boldsymbol{\Omega}$ is the angular velocity vector of the Earth, pointing out of the ground in the northern hemisphere. The Earth is taken as a perfect sphere. This sphere rotates about its North Pole-South Pole axis. At any given latitude φ, the north-south direction departs from the local vertical. Figure 2.3 depicts the traditional choice for a local Cartesian framework of reference: the x-axis is oriented eastward, the y-axis, northward, and the z-axis, upward. The corresponding unit vectors are denoted $(\boldsymbol{i}, \boldsymbol{j}, \boldsymbol{k})$. In this framework, the Coriolis force is expressed as

$$\boldsymbol{F_C} = (-f_* w + f v)\boldsymbol{i} - f u \boldsymbol{j} + f_* u \boldsymbol{k}, \tag{2.2}$$

where u, v and w are the components of the velocity vector $\boldsymbol{u}$ in the x-, y- and z-directions, respectively, and $f = 2\Omega \sin\varphi$ is the *Coriolis parameter*, whereas $f_* = 2\Omega \cos\varphi$ is the *reciprocal Coriolis parameter*. In the northern hemisphere, f is positive; it is zero at the equator and negative in the southern hemisphere. In contrast, f_* is positive in both hemispheres, but it vanishes at the poles. Generally, the f-terms are important, whereas the f_*-terms can be neglected (Cushman-Roisin (1994)). Thus in the preceding framework, the Coriolis force is simply

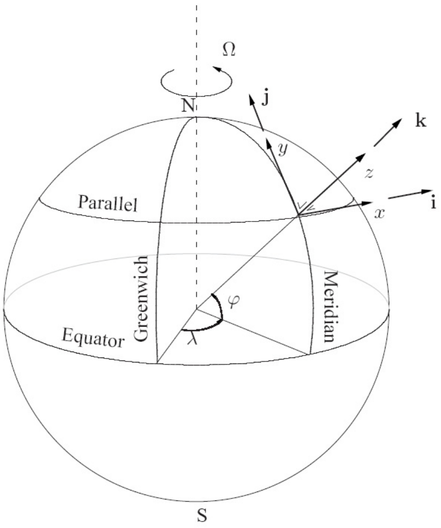

Figure 2.3: Definition of a local Cartesian framework of reference on a spherical Earth. The coordinate x is directed eastward, y northward, and z upward (from Cushman-Roisin (1994)).

$$\boldsymbol{F_C} = fv\boldsymbol{i} - fu\boldsymbol{j}. \tag{2.3}$$

In the absence of boundaries, a gravity current is deflected from its initial course by the Coriolis force, to the right in the northern hemisphere, and to the left in the southern hemisphere and is constrained to form an eddy. A stationary equilibrium may be reached in which Coriolis forces balance the radial pressure gradient[†]. This is called *geostrophic balance*, the circulating region of the gravity current is called a geostrophic eddy. Further release of potential energy is only possible through instability processes or through viscous dissipation (Griffiths (1986) and Hacker (1996)). The familiar "highs" and "lows" of weather maps are examples of geostrophic eddies in the atmosphere; similar flows occur in the oceans (although on a smaller scale) and are called mesoscale eddies. The process described above through which a geostrophic flow may be established, is called Rossby or "geostrophic" adjustment (Rossby (1938)).

In the vicinity of a boundary, velocities normal to the boundary, and hence Coriolis forces parallel to the boundary, must vanish. The constraints of the rotation are broken, and a gravity current flows along the boundary (Griffiths

---

[†] This is strictly the case if the radius of curvature of the region of the gravity current is large; otherwise centrifugal forces are also important in the final balance.

(1986)). Boundaries may be mountain ranges, coastlines, or a sloping ocean bottom. River outflows are localized sources of fresh, less dense water that (in the absence of advecting currents) are confined by Coriolis forces to spread in only one direction along the coast. The coast may have any orientation, but the gravity current must have the coast on its right-hand side when looking in the direction of the flow in the northern hemisphere, or on its left in the southern hemisphere. When the gravity current is stable, the flow approaches a state of geostrophic equilibrium and the interface at the edge of the region of fresh fluid slopes in order to provide a hydrostatic pressure gradient to balance the Coriolis force exerted on the flow.

2.2 Potential vorticity

The Rossby adjustment process may also be understood in terms of the conservation of the potential vorticity (Hacker (1996)). In fluid dynamics, vorticity is the curl of the fluid velocity. In the simplest sense, vorticity is the tendency for elements of the fluid to "spin". More formally, vorticity can be related to the amount of "circulation" or "rotation" (or more strictly, the local angular rate of rotation) in a fluid. In the study of geostrophic flows, since the horizontal flow field has no depth-dependence, there is no vertical shear and no eddies with horizontal axes (Cushman-Roisin (1994)). Thus, the absolute vorticity of a fluid particle, for a geostrophic flow, is

$$f + \xi \tag{2.4}$$

where f is the ambient vorticity and $\xi = \frac{\partial v}{\partial x} - \frac{\partial u}{\partial y}$ is the relative vorticity of the fluid particle. The vorticity vector is strictly vertical, and the preceding expression merely shows this vertical component. The potential vorticity, q, of a fluid parcel is the ratio of its absolute vorticity to its height, h:

$$q = \frac{f + \xi}{h}. \tag{2.5}$$

From the momentum and continuity equations of geostrophic flows, it can be shown that, in the absence of dissipation, the fluid parcel's volume and its circulation are conserved, implying the conservation of their ratio defined as the potential vorticity, q (Cushman-Roisin (1994)). Thus, the potential vorticity can be interpreted as the circulation per unit volume at a point in a fluid flow field.

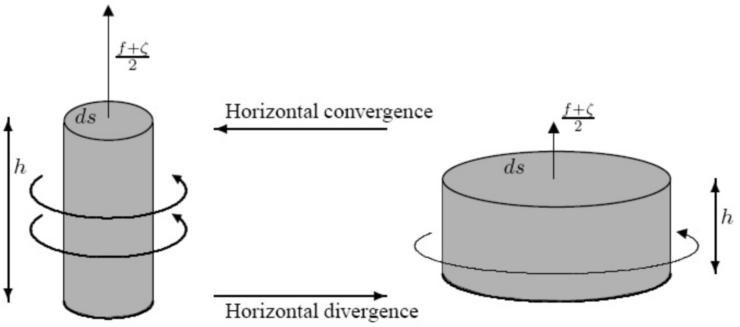

Figure 2.4: Conservation of volume and circulation of a fluid parcel undergoing squeezing or stretching, implying conservation of potential vorticity (from Cushman-Roisin (1994).

The best example to explain this conservation principle is that of a ballerina spinning on her toes; with her arms stretched out, she spins slowly, but with her arms brought against her body, she spins more rapidly. Likewise in homogeneous geophysical flows, when a parcel of fluid is squeezed laterally (its cross-sectional area ds decreasing), its vorticity must increase $(f + \varphi$ increasing) to conserve circulation (see figure 2.4).

2.3 Governing non-dimensional parameters

The length scale R_D, called the Rossby radius of deformation, and defined as

$$R_D = \frac{\sqrt{g\prime H}}{f}, \tag{2.6}$$

where f is the Coriolis parameter, $g\prime$ is defined in (2.1) and H is the height scale of the flow, is the fundamental length scale in all problems involving buoyancy forces and background rotation, since it is the length scale over which a density interface will slope in order to balance a buoyancy driven flow. In the Rossby adjustment process, R_D indicates the distance over which the fluid spreads before balance between the pressure gradient and Coriolis forces is obtained. The width of a gravity oceanic coastal current is expected to scale on R_D.

The associated dimensionless number is the Rossby number, Ro, defined as

$$Ro = \frac{U}{fL}, \tag{2.7}$$

where U and L are, respectively, characteristic velocity and horizontal length scales of the flow. Ro compares inertial to Coriolis forces and is fundamental in geophysical fluid dynamics, where it characterizes the importance of Coriolis accelerations arising from planetary rotation. For a fluid system strongly affected by Coriolis forces, $Ro << 1$.

The relative importance of friction is measured by the Ekman number, Ek, which is the ratio of viscous to Coriolis forces. This number is defined as

$$Ek = \frac{\nu}{fD}, \tag{2.8}$$

where ν is the kinematic viscosity and D is a characteristic (horizontal or vertical) length scale of the flow. It gives a measure at which stresses at a boundary are communicated to the fluid interior. For geophysical flows, this number is exceedingly small; it is very small even in the laboratory.

The Reynolds number, Re, which compares inertial to viscous forces, is defined as

$$Re = \frac{UD}{\nu}. \tag{2.9}$$

In most cases of geophysical interest, the Reynolds number is quite large. The densimetric Froude number, Fr, defined as

$$Fr = \frac{U}{\sqrt{g\prime H}}, \tag{2.10}$$

is a ratio of inertial to buoyancy forces. Finally, the Burger number, Bu, defined as

$$Bu = (\frac{Ro}{Fr})^2, \tag{2.11}$$

indicates the importance of the stratification of the flow. This number is often of order one for many atmospheric phenomena, meaning that both stratification and rotation play nearly equal roles in governing vertical and other motions in the fluid.

CHAPTER 3

Overview of prior studies

Buoyant outflows occur commonly and have been studied in various localities throughout the world. They can be formed from processes other than river discharges: for example, outflows from oceanic straits in which there are significant density differences can also form coastal currents. Many field investigations have been carried out during the last century along coastlines throughout the world to study the dynamics of these currents and understand the impacts they can have on near shore marine activities and biological population. Examples of buoyancy-driven coastal currents include the Columbia River Plume (Hickey *et al.* (1998)), the Delaware Coastal Current ((Munchow & Garvine, 1993a;b)), the Hudson River outflow (Chant *et al.* (2008)) and the Algerian Current (Obaton *et al.* (2000)), among others. The reader is referred to Chant (2011) for a detailed review of the systems observed and their properties.

Garvine (1995) developed a classification of buoyant outflows as either "small-scale" or "large-scale" dependent upon the cross-shore Kelvin number, K, the ratio of the plume width to the baroclinic Rossby radius, R_D. "Small-scale" outflows, with Kelvin numbers less than 1, are those in which inertial effects are greater than rotation, and outflows tend to spread laterally and to be trapped by advection near the source. An example of this type of "small-scale" outflow is the Connecticut river plume (Garvine (1977)). "Large-scale" outflows have a Kelvin number on the order 1 or greater; such outflows are dominated by the Earth's rotation and form coastally trapped currents that flow in the direction of Kelvin wave propagation. It is this latter category with which this study is concerned. Figure 3.1, from Chant *et al.* (2008), illustrates some of the observed properties of "large-scale" river plumes for the case of the Hudson River. Note in particular the presence of the bulge of buoyant water near the estuary mouth and the narrow coastal current emanating from it. The coastal current flows in the direction of Kelvin wave propagation, that is with the coast on its right (northern hemisphere).

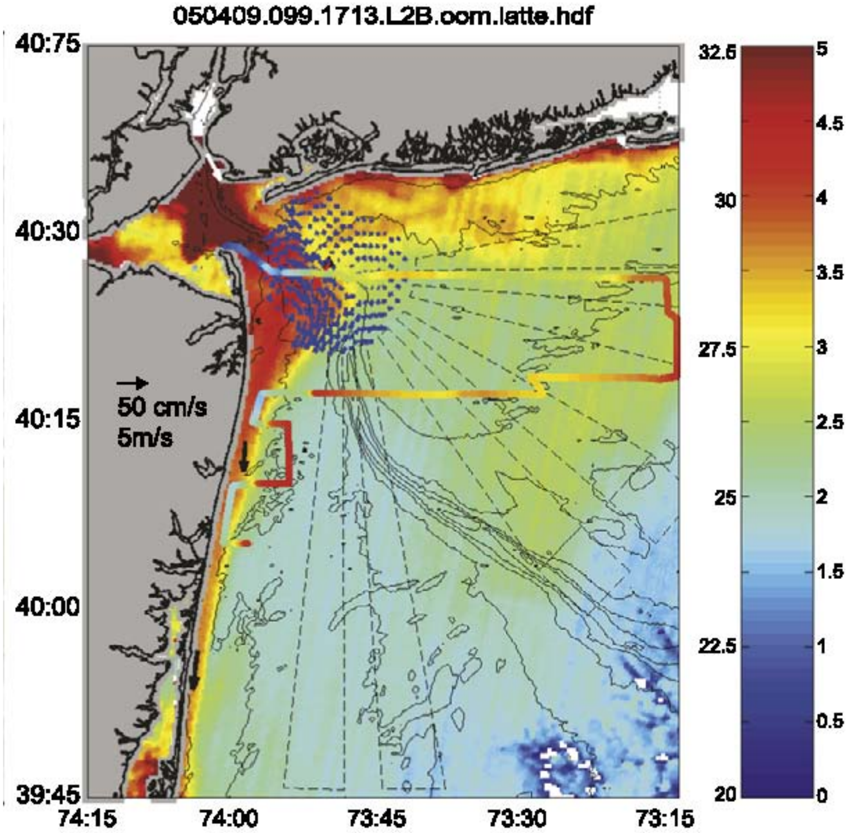
050409.099.1713.L2B.oom.latte.hdf
40:75
40:30
40:15
40:00
39:45
74:15
74:00
73:45
73:30
73:15
50 cm/s
5m/s
32.5
30
27.5
25
22.5
20
5
4.5
4
3.5
3
2.5
2
1.5
1
0.5
0

Figure 3.1: Hudson river outflow. The image was obtained from *MODIS* at 17 : 13 *GMT*. Blue arrows show *CODAR* field, black arrows result from shelf moorings and white arrows from *NOAA* mooring at the Narrows. The color bar (right side) is for surface salinity from the shiptrack shown in the figure (from Chant *et al.* (2008)).

3.1 Prior studies on coastal current dynamics

The coastal current is the most common structure observed in field studies (e.g. Figure 3.1). It is a region of downshelf transport of buoyant fluid (downshelf is defined as the direction of Kelvin wave propagation). Previous laboratory and numerical studies have examined the dynamics of the coastal currents.

Early laboratory experiments (e.g. Stern *et al.* (1982)) examined the propagation of a coastal current formed from a dam-break. The study of Stern *et al.* (1982) focused primarily on the geometry and propagation of the leading edge (nose) of the coastal current. Thomas & Linden (2007) investigated the dynamics of a coastal current when the freshwater was discharged continuously from a point source. In their experimental study, the width, the depth and the propagation speed of coastal currents moving along a vertical wall were determined. The experimental data were compared to their theoretical model based on geostrophy, continuity and conservation of potential vorticity (described in greater detail in Chapter 4). Overall, good agreement between the experiments of Thomas & Linden (2007) and their theory was obtained.

On the numerical side, many studies found that the coastal current was largely in geostrophic equilibrium. Chao & Boicourt (1986) divided the plume into two dynamically distinct regions: a bulge region near the estuary mouth and a downstream coastal current. They looked at the dynamics at the river mouth. Chao & Boicourt (1986) found that the nose of the coastal current advances faster in the estuary region than down the coast and suggested that mixing near the estuary mouth was responsible for the coastal current slowing down.

Whitehead & Chapman (1986) conducted experiments of a coastal current propagating along a vertical wall which ultimately encountered a sloping bottom and continued to flow along the sloping wall. They observed that the sloping bottom had a dynamically significant effect on the evolution of the coastal current: indeed coastal currents were seen to decelerate and widen in the region of the sloping bottom. However, Whitehead & Chapman (1986) did not offer a dynamical explanation for their results.

Attempts to classify the dynamics of coastal currents have been undertaken. With their numerical study, Chao (1988) proposed a classification scheme based upon an internal Froude number and a dissipation parameter. Csanady (1984) and Wright (1989) simulated a surface-to-bottom density front (i.e. plumes from which the buoyant water is in contact with the bottom, also referred to as bottom-advected plumes (Figure 3.2(b))) over a sloping bottom and a flat continental shelf, respectively, and noted that offshore transport of buoyant water in the bottom boundary layer contributed to the cross shelf movement of bottom advected plumes. Pursuing this result, Chapman & Lentz (1994) examined the role of bottom friction on the development of a coastal current. They suggested that the along-shore flow of the coastal current produced a bottom Ekman layer. This

Ekman layer may transport fluid offshore, and the coastal current may spread offshore to the point at which the along-shore velocity, and therefore the bottom Ekman layer flux, would decrease to zero.

Yankovsky & Chapman (1997) produced a scaling for a gravity current flowing over a continental shelf which distinguishes a surface-advected gravity current (Figure 3.2(a)), which is isolated from the bottom, with a bottom-trapped gravity current (Figure 3.2(b)), for which the buoyant water is in contact with the bottom and bottom friction is important in the establishment of the coastal current. They showed that in equilibrium the depth where the front intersects the bottom is the same depth as the depth for a gravity current flowing along a vertical wall. However, Yankovsky & Chapman (1997) examined whether the structure of a gravity current more closely resembles the surface-trapped or slope-controlled case for the region near the source and not for the coastal current away from the source. To investigate this latter issue, Lentz & Helfrich (2002) proposed a scaling theory for gravity currents flowing over a sloping bottom. Lentz & Helfrich (2002) also simulated gravity currents flowing along an inclined coastline in the laboratory : their experimental results were found to be consistent with their scaling theory.

Avicola & Huq (2002) simulated in the laboratory surface-advected and bottom-trapped plumes flowing over a continental shelf. They derived a theoretical model based on the assumption that the frontal dynamics are those of a Margules front. The theoretical expressions obtained by Avicola & Huq (2002) are similar to those obtained by Thomas & Linden (2007) (who assumed geostrophic equilibrium). Avicola & Huq (2002) classified the dynamics of coastal currents into a two-variable non-dimensional parameter space comprising an ambient depth parameter and a bottom slope parameter. Their resulting parameter space was found to delineate surface-advected currents to bottom-trapped currents.

3.2 Prior studies on the bulge region

The recirculating bulge region can be described as a large (relative to the coastal current width) freshwater lens rotating clockwise (in the northern hemisphere) located downstream to the source region. These features are rarely seen in nature (e.g. Figure 3.1), although they are quite common in numerical and laboratory experiments.

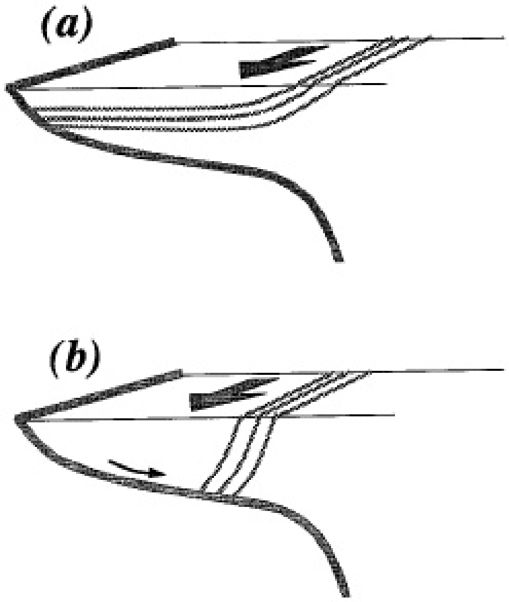

Figure 3.2: Sketches depicting (a) a surface-advected plume and (b) a bottom-trapped plume. The large arrows indicate the direction of the coastal plumes and the small arrow represents offshore transport in the bottom Ekman layer (from Chapman & Lentz (1994)).

Yankovsky & Chapman (1997) used a gradient wind balance* to predict the maximum size of the recirculating bulge. They predicted a maximum recirculating bulge radius for surface-advected plumes. Nof & Pichevin (2001) analytically hypothesized a mechanism for the bulge growth rate, based upon momentum conservation arguments.

For his numerical simulations, Garvine (2001) noted that a buoyant outflow in deep water will form a recirculating bulge and a coastal current, while an outflow in shallow water will form an upshelf intrusion and a coastal current. Avicola & Huq (2003a) experimentally examined the growth and characteristics of a recirculating bulge formed from a surface-advected plume exiting a strait or an estuary. When recirculating bulges formed, Avicola & Huq (2003a) determined that the freshwater storage within the bulge was approximately 60% to 70% of the source freshwater flux. Similarly, Horner-Devine *et al.* (2006) found that the growth of the bulge and the accumulation of fluid within it coincided with a reduction in the coastal current transport to approximately 50% of the inflow discharge. They further determined that the freshwater transport varied inversely proportional with the inflow Rossby number. Avicola & Huq (2003b) attempted to explain the role of the bay exit geometry in the formation of the recirculating bulge by varying the bay exit angle and the radius of curvature.

---

*Gradient wind balance is a balance between Coriolis, centrifugal and pressure gradient forces.

Fong & Geyer (2002) found that in the absence of an ambient flow field, the downstream coastal current carried a portion of the freshwater, while the freshwater remaining recirculated in a continually growing bulge in the vicinity of the estuary mouth. With the support of another set of numerical simulations,Fong & Geyer (2002) concluded that an external forcing agent (like an ambient current) was required for transporting all the discharged freshwater downstream.

3.3 Prior studies on the stability of a coastal current

It is important to understand the mechanisms driving the stability of coastal currents because in oceanography they establish the exchanges between the coast and the open sea. For instance, the circulation of the Western Mediterranean is influenced by instabilities of the Algerian Current (Figure 3.3), which are manifested in the form of mesoscale meanders and vortices.

Griffiths & Linden (1981a) studied the stability of an axisymmetric gravity current along a vertical wall. The wavelength and phase velocities of the disturbances observed by Griffiths & Linden (1981a) agreed with their baroclinic instability model of two-layer flow, which takes frictional dissipation caused by Ekman layers into account. Griffiths & Linden (1981b) defined θ as the square of the ratio of the internal Rossby radius of deformation to the horizontal length scale of the flow, and δ as the fraction of the total fluid depth occupied by the layer inside the front. They argued that for $\theta >> 1$ and $\delta > 0.1$, unstable disturbances obtain most of their energy from the potential energy of the flow, while for $\delta < 0.1$, extraction of the kinetic energy from the shear becomes the dominant driving mechanism.

Chabert D'Hières *et al.* (1991) investigated the stability of density-driven boundary currents and compared the results obtained with the Algerian current. For large Burger numbers, the gravity currents simulated by Chabert D'Hières *et al.* (1991) were stable, but as the Burger number decreased, increasing numbers of anticyclonic disturbances developed and grew along the axis of the currents. Rivas *et al.* (2005) showed that the presence of an inclined bottom stabilizes

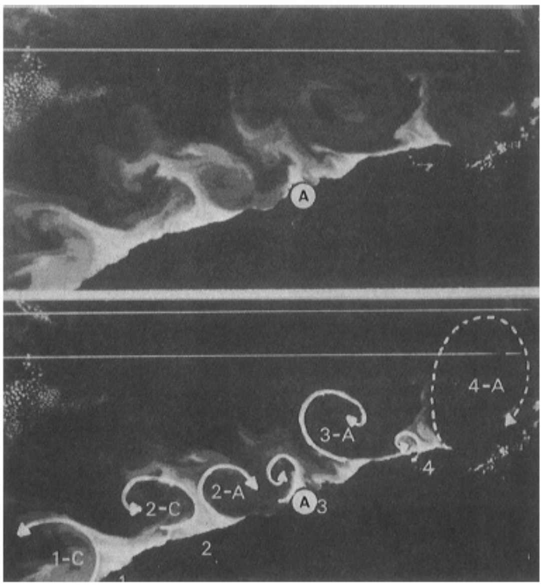

Figure 3.3: Advanced very high resolution radiometer ($AVHRR$) IR image on 22 July 1980, showing a series of well-developed cyclonic and anticyclonic eddies $\sim$ 50 km in diameter. In both figures, A stands for Algiers. The eddies are underlined and labelled in the bottom view to show that, going eastward, the cyclones (C) decrease while the anticyclones (A) increase (From Millot (1985)).

gravity currents.

Many additional processes (e.g., wind forcing, coastline irregularities, and bottom boundary layers) may modify the evolution and properties of buoyancy-driven coastal currents (Chant (2011)). However, the concern of this PhD research is to study the dynamics of surface-advected and bottom-trapped coastal plumes moving along straight and inclined coastlines in the absence of wind forcing.

Part II

Methods

CHAPTER 4

Geostrophic Theory

In this chapter, a theoretical analysis is performed to derive a set of equations giving the profile of gravity-driven coastal currents simulated in the laboratory. An ideal fluid system is considered, consisting of two moving layers, stacked one upon the other, each having a uniform density. The upper layer of freshwater, with density ρ_1, flows above the ambient salt water layer of density ρ_2. Since only processes in the coastal current are investigated herein, the lowest layer will be assumed to be deep and at rest.

4.1 Summary of the results for coastal currents flowing along a vertical coastline

Thomas & Linden (2007) considered gravity-driven coastal currents flowing along a vertical coastline. Their flow geometry and the nomenclature employed in the analysis of the problem are illustrated in Figure 4.1.

The curvature of the circular wall is neglected and a Cartesian coordinate system ($\boldsymbol{x}$, $\boldsymbol{y}$, $\boldsymbol{z}$) is introduced. The origin of the coordinate system coincides with the outlet of the source from which the buoyant freshwater discharges. It is assumed that the velocity components in the y- and z-directions are negligible in comparison to the velocity component, u, in the x-direction. All variations in the x-coordinate direction are also neglected so that $\frac{\partial}{\partial x} = 0$. Therefore the plume velocity is expressed as $\boldsymbol{u} = (u(y, z), 0, 0)$.

Frictional effects are ignored and the plume is assumed to be steady and in geostrophic balance; that is, the Coriolis acceleration term in the cross-plume direction is balanced by the cross-plume pressure gradient component. The pressure is considered to be hydrostatic, and, as the freshwater is released from a

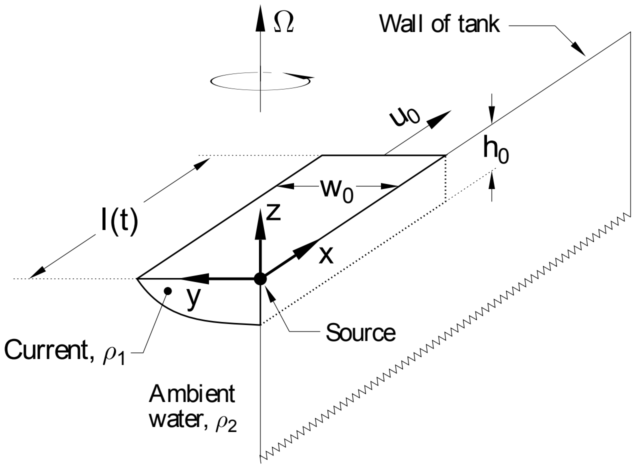

Figure 4.1: Sketch illustrating the nomenclature employed to develop the theoretical model for coastal currents flowing along a vertical wall (from Thomas & Linden (2007)).

continuous point source, it is further assumed that it is released with zero potential vorticity.

Using conservation of mass, angular momentum and potential vorticity, the detailed analysis in Thomas & Linden (2007) shows that the current width, w_0, its depth, h_0, its length, $l(t)$, and its constant propagation speed, $u_0 = l/t$, are given respectively by

$$w_0 = (\frac{g' q_0}{\Omega^3})^{\frac{1}{4}} \ , \ h_0 = (\frac{4\Omega q_0}{g'})^{\frac{1}{2}} \ , \ l = \frac{3}{4}(q_0 g' \Omega)^{\frac{1}{4}} t \ , \ u_0 = \frac{3}{4}(q_0 g' \Omega)^{\frac{1}{4}} \ , \tag{4.1}$$

where q_0 is the constant volumetric discharge rate at the source, Ω is the rotation rate of the turntable and $g\prime$ is defined in (2.1). As discussed in Thomas & Linden (2007), w_0 is equivalent to the Rossby deformation radius, R_D, based on the depth of the coastal current. The results of (4.1a-d) can be expressed in dimensionless form by non-dimensionalizing all lengths by w_0 and by introducing the non-dimensional time $T = \Omega t$. Using capital letters to denote non-dimensional variables, one obtains:

$$W = 1 \ , \ H = 2I^{\frac{5}{4}} \ , \ L = \frac{3}{4}T \ , \ U_0 = \frac{L}{T} = \frac{3}{4} \ , \tag{4.2}$$

where

$$I = \frac{\Omega q_0^{\frac{1}{5}}}{g'^{\frac{3}{5}}} \tag{4.3}$$

is a dimensionless parameter. Reference to (4.2b) reveals that $H = h_0/w_0$; therefore, the parameter I characterizes the height-to-width aspect ratio of the coastal current (see Thomas & Linden (2007)). Note that I also characterizes the isopycnal slope separating the two layers. Thomas & Linden (2007) noted that coastal currents with low I values (low Ω, q_0 with high g'), thus coastal currents with a small isopycnal slope, are wide and shallow, while coastal currents with high I values (high Ω, q_0 with low g'), thus coastal currents with a large isopycnal slope, are deep and narrow.

The Rossby number, R_0, is defined as:

$$R_0 = \frac{u_0}{f w_0} = \frac{3}{8}, \tag{4.4}$$

the Froude number, Fr, as:

$$Fr = \frac{u_0}{\sqrt{g\prime h_0}} = \frac{3}{4\sqrt{2}}, \tag{4.5}$$

the Burger number, Bu, as:

$$Bu = (\frac{Ro}{Fr})^2 = \frac{1}{2}, \tag{4.6}$$

the Reynolds number, Re, as:

$$Re = \frac{u_0 w_0}{\nu} = \frac{3 q_0^{1/2} g\prime^{1/2}}{4 \nu \Omega^{1/2}}, \tag{4.7}$$

the horizontal Ekman number, Ek_H, as:

$$Ek_H = \frac{\nu}{f w_0^2} = \frac{\nu \Omega^{1/2}}{2 q_0^{1/2} g\prime^{1/2}}, \tag{4.8}$$

and finally, the vertical Ekman number, Ek_V, as:

$$Ek_V = \frac{\nu}{f h_0^2} = \frac{\nu g\prime}{8 \Omega^2 q_0}, \tag{4.9}$$

using (4.1a-b-d) and $\nu = 0.01\ cm^2\ s^{-1}$ for the kinematic viscosity of water. Equations (4.7) and (4.8) give

$$Re = \frac{3}{8Ek_H}. \tag{4.10}$$

Thus the Reynolds number, Re, and the horizontal Ekman number, Ek_H, are inversely proportional. In the whole study presented here, the use of the horizontal Ekman number, Ek_H, is preferred to the use of the Reynolds number, Re, as the fluid system is assumed to be in geostrophic equilibrium and thus, Coriolis forces are assumed to be dominant. The non-dimensional ambient depth parameter (Avicola & Huq (2002)) is defined as

$$\frac{h_0}{H_D}, \tag{4.11}$$

where h_0 is the theoretical vertical-wall coastal current height defined in (4.1(b)). H_D is the coastal wall depth if the coastline is a simple vertical wall, that is, H_D is just the height of the ambient salt water, H_{SW}, in the circular tank. If the coastline is an inclined wall of slope, α, with the horizontal, $H_D = \alpha w_0$, where w_0 is the theoretical vertical-wall coastal current width defined in (4.1(a)). When the topography is a bottom slope, $h_0/H_D = H/\alpha$, where H is the theoretical non-dimensional coastal current height defined in (4.2(b)). The h_0/H_D ratio, for an inclined coastline, is also the ratio of the isopycnal slope, H, of the coastal current with the bottom slope, α.

4.2 Generalization of the analysis to coastal currents flowing along inclined boundaries

Here the problem and the nomenclature of Thomas & Linden (2007) are generalized to the case of coastal currents flowing over an inclined coastline as illustrated in Figure 4.2. For the inclined-wall case in Figure 4.2, the flow geometry has two distinct regions. Region A is the zone where the coastal current depth is simply determined by the solid boundary of the incline, while region B is the zone where the coastal current depth is determined by the interface between the buoyant outflow and the ambient water.

As in Thomas & Linden (2007), the curvature of the circular wall is neglected. Two Cartesian coordinate systems ($\boldsymbol{x}$, $\boldsymbol{y}$, $\boldsymbol{z}$) and ($\boldsymbol{x'}$, $\boldsymbol{y'}$, $\boldsymbol{z'}$) are introduced as illustrated in Figure 4.2. The origin of the coordinate system ($\boldsymbol{x}$, $\boldsymbol{y}$, $\boldsymbol{z}$) coincides with the outlet of the source from which the buoyant, freshwater discharges while the coordinate system ($\boldsymbol{x'}$, $\boldsymbol{y'}$, $\boldsymbol{z'}$) is a translation of the coordinate system ($\boldsymbol{x}$, $\boldsymbol{y}$, $\boldsymbol{z}$) along the y-axis such that $y = w_A + y'$, where w_A is the coastal current width in region A. The width of region B is referred to as w_B. The fluid heights in regions A and B are $h_A(y)$ and $h_B(y')$, respectively.

It is assumed that the velocity components in the y-, y'- and z-, z'-directions are negligible in comparison to the velocity component in the x-, x'-direction. Furthermore, all variations in the x-, x'-coordinate direction are ignored so that $\frac{\partial}{\partial x} = \frac{\partial}{\partial x'} = 0$. Therefore $\boldsymbol{u_A} = (u_A(y,z), 0, 0)$ and $\boldsymbol{u_B} = (u_B(y',z'), 0, 0)$, where $\boldsymbol{u_A}$ and $\boldsymbol{u_B}$ are the fluid velocities in regions A and B respectively, and u_A and u_B are their component in the x-, x'-direction.

As in Thomas & Linden (2007), frictional effects are ignored and it is assumed that the coastal current is in geostrophic balance.

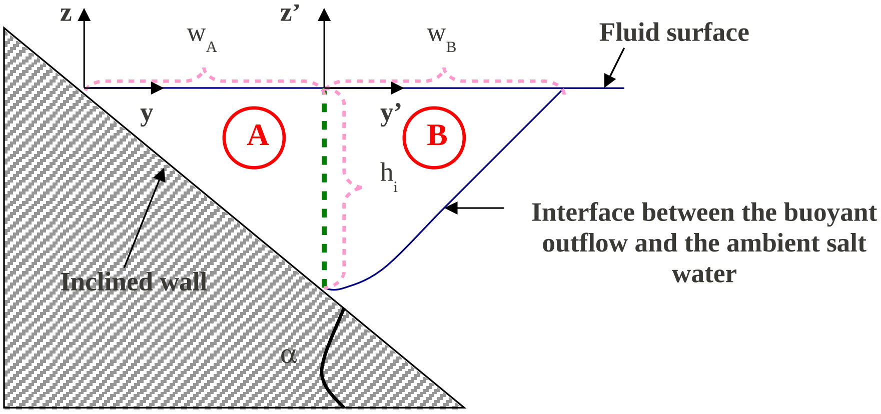
z
z'
w_A
w_B
Fluid surface
y
y'
A
B
h_i
Interface between the buoyant outflow and the ambient salt water
Inclined wall
α

Figure 4.2: Schematic of the view, along the across-shore direction, of a coastal current flowing over an inclined wall in the laboratory.

The potential vorticity, q, defined by

$$q = \frac{f - \frac{\partial u_A}{\partial y}}{h_A}, \tag{4.12}$$

in region A, and

$$q = \frac{f - \frac{\partial u_B}{\partial y'}}{h_B}, \tag{4.13}$$

in region B, is conserved by vertical fluid columns (Cushman-Roisin (1994)). Thus:

$$\frac{\partial q}{\partial t} = 0, \tag{4.14}$$

everywhere in the coastal current. Furthermore, as the freshwater is released from a continuous point source, one can subsequently assume that it is released with zero potential vorticity (Griffiths (1986) and Thomas & Linden (2007)). Hence

$$q = 0, \tag{4.15}$$

in the buoyant outflow. Using (4.12) and (4.13), (4.15) implies

$$\frac{\partial u_A}{\partial y} = f, \tag{4.16}$$

and

$$\frac{\partial u_B}{\partial y'} = f. \tag{4.17}$$

Integrating equations (4.16) and (4.17) over y and y' respectively gives

$$u_A = fy + K, \tag{4.18}$$

and

$$u_B = fy' + L. \tag{4.19}$$

where K and L are constants. Conservation of angular momentum requires that $u_A = 0$ at $y = 0$ (Thomas & Linden (2007))[*], thus $K = 0$. Furthermore, by continuity, the flow velocity in region A must be equal to the flow velocity in region B at the point of the intersection, $y = w_A$, equivalent to $y' = 0$, hence $L = fw_A$. Finally, one obtains:

$$u_A = fy, \tag{4.20}$$

and

---

[*] As the fresh water is injected vertically upwards, its alongshore and across-shore velocity components are zero at the source and thus, the buoyant outflow has zero angular momentum at the source. Due to conservation of angular momentum, the buoyant outflow should have zero angular momentum when returning back to the outer boundary and hence, the alongshore velocity should be zero at the wall.

$$u_B = f(y' + w_A). \tag{4.21}$$

In region B, the fluid system consists of the two layers of fluid. Thus the model can be represented as a single moving layer above a motionless abyss. From Cushman-Roisin (1994), the reduced-gravity shallow water model can describe the fluid system, and is reduced, with the previous assumptions, to:

$$fu_B = -g'\frac{\partial h_B}{\partial y'}, \tag{4.22}$$

where $f = 2\Omega$ is the Coriolis parameter. Differentiating with respect to y' (4.22), substituting for $\frac{\partial u_B}{\partial y'}$ in (4.17) and integrating twice over y' gives:

$$h_B = -\frac{f^2}{2g'}y'^2 + My' + N, \tag{4.23}$$

where M and N are constants. However at $y' = 0$, $h_B = h_i$, where h_i is the height at which the interface between the freshwater and the ambient salt water intersects the sloping bottom.Therefore:

$$h_B = -\frac{f^2}{2g'}y'^2 + My' + h_i. \tag{4.24}$$

Differentiating (4.24) with respect to y' and substituting for $\frac{\partial h_B}{\partial y'}$ in (4.22) and for u_B in (4.21) gives:

$$M = -\frac{f^2 w_A}{g'}. \tag{4.25}$$

With (4.25), (4.24) shows that the interface between the current in region B and the ambient water is given by:

$$h_B = -\frac{f^2}{2g'}y'^2 - \frac{f^2 w_A}{g'}y' + h_i, \tag{4.26}$$

Assuming that the width and depth of the coastal current at any downstream location remain constant in time, continuity requires that the volumetric flow rate, q_0, from the source must equal the volumetric flow rate across any cross-section of the coastal current. Then:

$$q_0 = \int_0^{w_A} h_A(y)u_A(y)dy + \int_0^{w_B} h_B(y')u_B(y')dy'. \tag{4.27}$$

Substituting (4.20),(4.21),(4.26) and,

$$h_A(y) = \tan(\alpha) y, \tag{4.28}$$

in (4.27), and using

$$w_A = \frac{h_i}{\tan(\alpha)}, \tag{4.29}$$

after integration, one obtains:

$$q_0 = \frac{f {h_i}^3}{3\tan^2(\alpha)} + \frac{g' {h_i}^2}{2f}. \tag{4.30}$$

Since (4.30) is a third-order polynomial, the solutions for h_i can only be obtain numerically. However from Yankovsky & Chapman (1997) and Lentz & Helfrich (2002), $h_i = h_0$, defined in (4.1b), which is the coastal current depth (see Figure 4.1) obtained by Thomas & Linden (2007) for coastal currents flowing along vertical walls. In order to compare h_i from (4.30) to h_0 from (4.1b), the ratio h_i/h_0 was numerically computed using (4.30) and (4.1b) with the values for the rotation rate, Ω, the flow rate, q_0, the reduced gravity, g', and the sloping angle, α, being the values used in the large-scale inclined-wall experiments presented in section 5.2 (for which the coastal current depth was measured). An average of the h_i/h_0 values found was then calculated with the standard deviation to obtain $h_i/h_0 = 0.76 \pm 0.2$. The inclined-wall depth, h_i, is then estimated to be the three-quarters of the vertical-wall depth, h_0. However, the experimental data presented in section 9.3 yield experimental evidence that the depth for coastal currents flowing along an inclined wall is better predicted by the vertical-wall depth, h_0, rather than by the inclined-wall depth, h_i. Therefore, similarly to Yankovsky & Chapman (1997) and Lentz & Helfrich (2002), it is assumed from here that $h_i = h_0$, and from (4.26), the interface between the coastal current in region B and the ambient water is thus given by:

$$h_B = -\frac{f^2}{2g'} y'^2 - \frac{f^2 w_A}{g'} y' + h_0, \tag{4.31}$$

with

$$w_A = \frac{h_0}{\tan(\alpha)}. \tag{4.32}$$

With (4.32) and the fact that, for a vertical-wall coastline, $\tan(\alpha) \to \infty$, the equation (3.10) of Thomas & Linden (2007), describing the depth profile of a coastal current flowing along a vertical wall, is recovered from (4.31).

The width of a coastal current flowing along an inclined wall, w_i, is simply $w_i = w_A + w_B$. The value of w_B is found from the condition, in (4.31), $h_B(w_B) = 0$, which yields:

$$0 = w_B^2 + 2w_A w_B - \frac{2g'h_0}{f^2}. \tag{4.33}$$

This leads to a quadratic equation with two solutions for w_B. It turns out that one of the two solutions always yields negative values for w_B. Hence, this solution has no physical relevance. Consequently, the other solution must be the correct one:

$$w_B = -w_A + \sqrt{w_A^2 + w_0^2}, \tag{4.34}$$

where w_0, defined in (4.1a), is the coastal current width (see Figure 4.1) obtained by Thomas & Linden (2007) for coastal currents flowing along vertical walls. Using (4.32) and (4.2b), (4.34) can be written as:

$$w_B = -w_A + w_0\sqrt{\left(\frac{H}{\tan(\alpha)}\right)^2 + 1}. \tag{4.35}$$

From (4.35) and the fact that $w_i = w_A + w_B$, the width, w_i, of a coastal current flowing along an inclined wall can be expressed as:

$$w_i = w_0\sqrt{\left(\frac{H}{\tan(\alpha)}\right)^2 + 1}. \tag{4.36}$$

For a vertical-wall coastline, $w_i = w_0$ is recovered.

The total volume, V, of the coastal current of length, l_i, is given by:

$$V = l_i \int_0^{w_A} h_A(y)dy + l_i \int_0^{w_B} h_B(y')dy'. \tag{4.37}$$

Substituting (4.31) and (4.28) in (4.37), after integration, one obtains:

$$V = l_i(\frac{\tan(\alpha)}{2}w_A^2 - \frac{f^2}{6g'}w_B^3 - \frac{f^2}{2g'}w_B^2 w_A + h_0 w_B). \tag{4.38}$$

From the condition, in (4.31), $h_B(w_B) = 0$, w_A can be rewritten as:

$$w_A = -\frac{w_B}{2} + \frac{g' h_0}{f^2 w_B}. \tag{4.39}$$

Replacing (4.39) in the third term of (4.38) gives:

$$V = l_i\left(\frac{\tan(\alpha)}{2} w_A^2 + \frac{f^2}{12g'} w_B^3 + \frac{h_0}{2} w_B\right). \tag{4.40}$$

From (4.40) and the fact that $V = q_0 t$, the nose displacement of the coastal current is:

$$l_i = \frac{q_0 t}{\left(\frac{\tan(\alpha)}{2} w_A^2 + \frac{f^2}{12g'} w_B^3 + \frac{h_0}{2} w_B\right)}. \tag{4.41}$$

For a vertical-wall case, the equation (3.19) of Thomas & Linden (2007) describing the length of a coastal current flowing along a vertical wall (see Figure 4.1) is recovered from (4.41).

Equation (4.41) implies that the coastal current head travels at constant speed, u_i, given by:

$$u_i = \frac{l_i}{t} = \frac{q_0}{\left(\frac{\tan(\alpha)}{2} w_A^2 + \frac{f^2}{12g'} w_B^3 + \frac{h_0}{2} w_B\right)}. \tag{4.42}$$

For a vertical-wall case, $u_i = u_0$, defined in (4.1d), which is the head propagation speed for coastal currents flowing along vertical walls obtained by Thomas & Linden (2007) (see Figure 4.1).

The above results can be conveniently expressed in dimensionless forms. As in Thomas & Linden (2007), the non-dimensional time $T = \Omega t$ is used and all lengths are non-dimensionalized by w_0. Using capital letters to denote non-dimensional variables, (4.41) is written as:

$$L_i = \frac{T}{-\frac{H}{\tan(\alpha)}\left(\frac{4}{3}\left(\frac{H}{\tan(\alpha)}\right)^2 + 1\right) + \frac{4}{3}\left(\left(\frac{H}{\tan(\alpha)}\right)^2 + 1\right)^{\frac{3}{2}}}, \tag{4.43}$$

where H, defined in (4.2b), is the dimensionless depth obtained by Thomas & Linden (2007) for coastal currents flowing along vertical walls. Thus, the dimensionless propagation speed, U_i, is:

$$U_i = \frac{1}{-\frac{H}{\tan(\alpha)}\left(\frac{4}{3}\left(\frac{H}{\tan(\alpha)}\right)^2+1\right)+\frac{4}{3}\left(\left(\frac{H}{\tan(\alpha)}\right)^2+1\right)^{\frac{3}{2}}}. \tag{4.44}$$

The dimensionless width, W_i, is then given by:

$$W_i = \sqrt{\left(\frac{H}{\tan(\alpha)}\right)^2+1}, \tag{4.45}$$

and the dimensionless depth, H_i, is simply:

$$H_i = H. \tag{4.46}$$

The horizontal lengths can also be non-dimensionalized by w_i. In this case, (4.41) is written as:

$$(L_i)_{w_i} = \frac{L_i}{\sqrt{\left(\frac{H}{\tan(\alpha)}\right)^2+1}}, \tag{4.47}$$

the dimensionless propagation speed, $(U_i)_{w_i}$, is:

$$(U_i)_{w_i} = \frac{U_i}{\sqrt{\left(\frac{H}{\tan(\alpha)}\right)^2+1}}, \tag{4.48}$$

and the dimensionless width, $(W_i)_{w_i}$, is simply:

$$(W_i)_{w_i} = 1. \tag{4.49}$$

From equations (4.43), (4.47), (4.44), (4.48) and (4.45), the non-dimensional coastal current lengths, L_i and $(L_i)_{w_i}$, propagation velocities, U_i and $(U_i)_{w_i}$, and width, W_i, respectively, are all functions of $H/\tan(\alpha)$. However, for small values of α, $H/\tan(\alpha) \sim H/\alpha$. Therefore, for coastlines with small inclination angles, α, the non-dimensional coastal current lengths, L_i and $(L_i)_{w_i}$, propagation velocities, U_i and $(U_i)_{w_i}$, and width, W_i, are expected to depend on the ambient depth parameter, h_0/H_D $(= H/\alpha)$.

4.3 Predictions of the inclined-wall model

4.3.1 Variations of the non-dimensional theoretical inclined-wall velocity U_i

Figures 4.3(a)-(b) display the non-dimensional theoretical inclined-wall coastal current velocity, U_i, as a function of the bottom slope, α (for different values of H), and, as a function of the non-dimensional coastal current height H, defined in (4.2b) (for different values of α), respectively.

Figures 4.3(a)-(b) show that the non-dimensional theoretical inclined-wall coastal current speed, U_i, has a maximum value, independent of the experimental conditions. In order to find where the maximum of U_i is, the sign of its partial derivatives with respect to H and α needs to be studied to find where the partial derivatives cancel. The denominator in (4.44) is always different from zero, thus U_i is well defined. Differentiating U_i with respect to α gives:

$$\frac{\partial U_i}{\partial \alpha} = \frac{\frac{-4H^3}{\sin^2(\alpha)\tan^2(\alpha)} - \frac{H}{\sin^2(\alpha)} + \frac{4H^2}{\tan(\alpha)\sin^2(\alpha)}\left(\left(\frac{H}{\tan(\alpha)}\right)^2+1\right)^{\frac{1}{2}}}{\left(-\frac{H}{\tan(\alpha)}\left(\frac{4}{3}\left(\frac{H}{\tan(\alpha)}\right)^2+1\right)+\frac{4}{3}\left(\left(\frac{H}{\tan(\alpha)}\right)^2+1\right)^{\frac{3}{2}}\right)^2}. \tag{4.50}$$

The denominator in (4.50) is squared, therefore it is always positive. Hence, the partial derivative (4.50) has the same sign as its numerator. Thus:

$$\frac{\partial U_i}{\partial \alpha} \geq 0 \tag{4.51}$$

$$\Rightarrow \frac{4H^2}{\tan(\alpha)\sin^2(\alpha)}\left(\left(\frac{H}{\tan(\alpha)}\right)^2+1\right)^{\frac{1}{2}} \geq \frac{4H^3}{\sin^2(\alpha)\tan^2(\alpha)} + \frac{H}{\sin^2(\alpha)}. \tag{4.52}$$

Multiplying both sides of the inequality in (4.52) by $\tan^2(\alpha)\sin^2(\alpha)$ and taking the square gives:

$$\left(4H^2\tan(\alpha)\left(\left(\frac{H}{\tan(\alpha)}\right)^2+1\right)^{\frac{1}{2}}\right)^2 \geq \left(4H^3 + H\tan^2(\alpha)\right)^2. \tag{4.53}$$

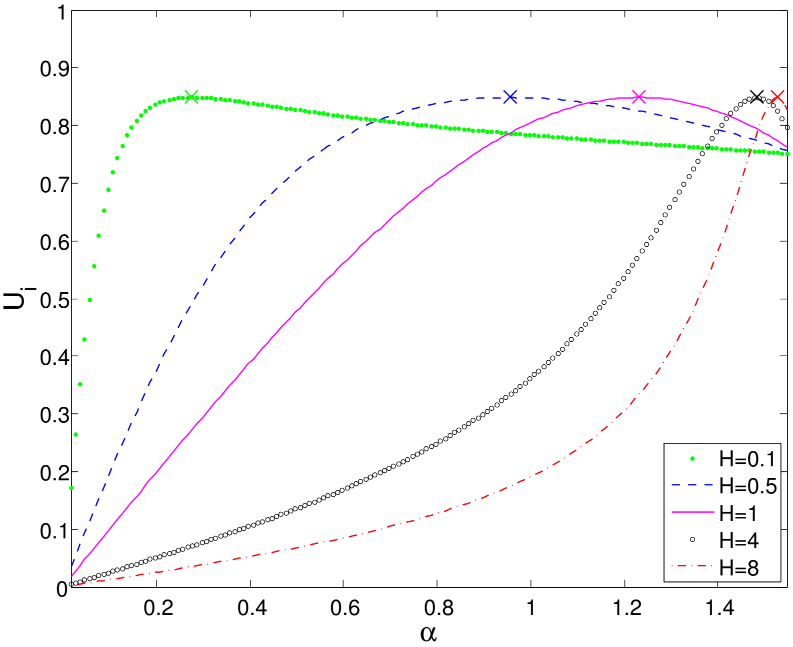

(a) U_i as a function of α, for different values of H. Crosses indicate the maxima of U_i, found at $\alpha = \arctan(2\sqrt{2}H)$, for the different values of H.

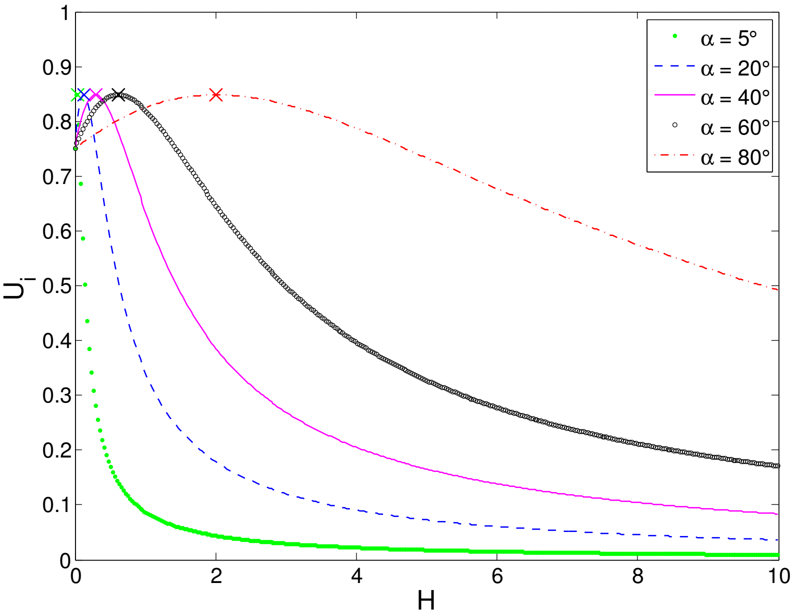

(b) U_i as a function of H, for different values of α. Crosses indicate the maxima of U_i, found at $H = \tan(\alpha)/2\sqrt{2}$, for the different values of α.

Figure 4.3: Variations of the non-dimensional theoretical inclined-wall coastal current velocity, U_i, as a function of the bottom slope, α, and, the non-dimensional height, H.

Using the fact that $H > 0$, $\tan(\alpha) > 0$ and that the functions root and *arctan* monotonically increase, (4.53) yields:

$$\alpha \leq \arctan(2\sqrt{2}H). \tag{4.54}$$

Therefore, with H held constant, the non-dimensional propagation speed, U_i, of a coastal current flowing over an inclined coastline increases until α reaches the maximum value $\arctan(2\sqrt{2}H)$ (because $\partial U_i/\partial\alpha \geq 0$ for $\alpha \leq \arctan(2\sqrt{2}H)$). After α has reached this maximum value, U_i decreases (because $\partial U_i/\partial\alpha \leq 0$ for $\alpha \geq \arctan(2\sqrt{2}H)$).

Similarly, by differentiating U_i with respect to H, one finds:

$$\frac{\partial U_i}{\partial H} = \frac{\frac{4H^2}{\tan^3(\alpha)} + \frac{1}{\tan(\alpha)} - \frac{4H}{\tan^2(\alpha)}\left(\left(\frac{H}{\tan(\alpha)}\right)^2 + 1\right)^{\frac{1}{2}}}{\left(-\frac{H}{\tan(\alpha)}\left(\frac{4}{3}\left(\frac{H}{\tan(\alpha)}\right)^2 + 1\right) + \frac{4}{3}\left(\left(\frac{H}{\tan(\alpha)}\right)^2 + 1\right)^{\frac{3}{2}}\right)^2}. \tag{4.55}$$

The denominator in (4.55) is squared, therefore it is always positive. Hence, the partial derivative (4.55) has the same sign as its numerator.

$$\frac{\partial U_i}{\partial H} \geq 0 \tag{4.56}$$

$$\Rightarrow \frac{4H^2}{\tan^3(\alpha)} + \frac{1}{\tan(\alpha)} \geq \frac{4H}{\tan^2(\alpha)}\left(\left(\frac{H}{\tan(\alpha)}\right)^2 + 1\right)^{\frac{1}{2}}. \tag{4.57}$$

Multiplying both sides of the inequality in (4.57) by $\tan^3(\alpha)$ and taking the square gives:

$$\left(4H^2 + \tan^2(\alpha)\right)^2 \geq \left(4H\tan(\alpha)\left(\left(\frac{H}{\tan(\alpha)}\right)^2 + 1\right)^{\frac{1}{2}}\right)^2. \tag{4.58}$$

Using the fact that $H > 0$, $\tan(\alpha) > 0$ and that the function root monotonically increases, (4.58) yields:

$$H \leq \frac{\tan(\alpha)}{2\sqrt{2}}. \tag{4.59}$$

Therefore, with α held constant, the non-dimensional propagation speed, U_i, of a coastal current flowing over an inclined coastline increases until H reaches the maximum value $\tan(\alpha)/2\sqrt{2}$ (because $\partial U_i/\partial\alpha \geq 0$ for $H \leq \tan(\alpha)/2\sqrt{2}$). After H has reached this maximum value, U_i decreases (because $\partial U_i/\partial\alpha \leq 0$ for $H \geq \tan(\alpha)/2\sqrt{2}$). It is interesting to note that:

$$\alpha = \arctan(2\sqrt{2}H) \Leftrightarrow H = \frac{\tan(\alpha)}{2\sqrt{2}}. \tag{4.60}$$

The crosses on Figures 4.3(a)-(b) indicate the maxima of U_i found at $\alpha = \arctan(2\sqrt{2}H)$ (for the different values of H) and at $H = \tan(\alpha)/2\sqrt{2}$ (for the different values of α). After calculation, the value of the non-dimensional theoretical inclined-wall coastal current speed, U_i, at the maximum is found to be 0.8485.

Using (4.2b) and (4.3), one can rewrite (4.44) in terms of the experimental parameters Ω, q_0 and g':

$$U_i = \frac{1}{-\frac{2\Omega^{\frac{5}{4}} q_0^{\frac{1}{4}}}{\tan(\alpha) g'^{\frac{3}{4}}} \left(\frac{4}{3} \left(\frac{2\Omega^{\frac{5}{4}} q_0^{\frac{1}{4}}}{\tan(\alpha) g'^{\frac{3}{4}}} \right)^2 + 1 \right) + \frac{4}{3} \left(\left(\frac{2\Omega^{\frac{5}{4}} q_0^{\frac{1}{4}}}{\tan(\alpha) g'^{\frac{3}{4}}} \right)^2 + 1 \right)^{\frac{3}{2}}}. \tag{4.61}$$

Figures 4.4(a)-(c) display the non-dimensional theoretical inclined-wall coastal current velocity, U_i, as a function of the rotation rate, Ω (for different values of α, with $q_0 = 20\ cm^3\ s^{-1}$ and $g' = 5\ cm\ s^{-2}$), as a function of the flow rate, q_0 (for different values of α, with $\Omega = 1.5\ rad\ s^{-1}$ and $g' = 5\ cm\ s^{-2}$), and as a function of the reduced-gravity, g' (for different values of α, with $\Omega = 0.5\ rad\ s^{-1}$ and $q_0 = 20\ cm^3\ s^{-1}$).
After differentiating (4.61) with respect to the different experimental parameters and studying the sign of each partial derivative, one obtains:

$$\frac{\partial U_i}{\partial \Omega} \geq 0 \quad \Rightarrow \quad \Omega \leq \frac{(\tan(\alpha))^{\frac{4}{5}} g'^{\frac{3}{5}}}{4 q_0^{\frac{1}{5}}}, \tag{4.62}$$

$$\frac{\partial U_i}{\partial q_0} \geq 0 \quad \Rightarrow \quad q_0 \leq \frac{(\tan(\alpha))^4 g'^3}{2^{10}\Omega^5}, \tag{4.63}$$

$$\frac{\partial U_i}{\partial g'} \geq 0 \quad \Rightarrow \quad g' \leq \frac{2^{\frac{10}{3}} \Omega^{\frac{5}{3}} q_0^{\frac{1}{3}}}{(\tan(\alpha))^{\frac{4}{3}}}. \tag{4.64}$$

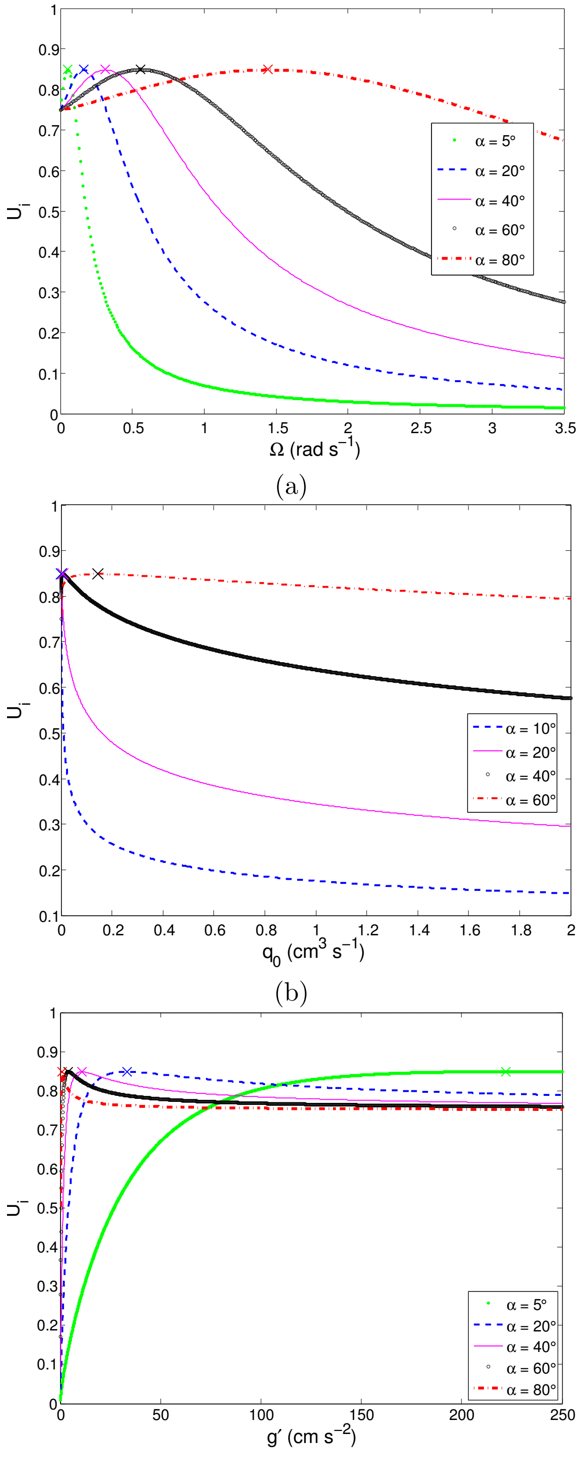

(a)

(b)

(c)

Figure 4.4: Variations of U_i, as a function of (a) Ω, for different values of α, with $q_0 = 20\ cm^3\ s^{-1}$ and $g\prime = 5\ cm\ s^{-2}$,(b) q_0, for different values of α, with $\Omega = 1.5\ rad\ s^{-1}$ and $g\prime = 5\ cm\ s^{-2}$, (c) $g\prime$, for different values of α, with $\Omega = 0.5\ rad\ s^{-1}$ and $q_0 = 20\ cm^3\ s^{-1}$. Crosses indicate the maxima of U_i, found at (a) $\Omega = (\tan(\alpha))^{4/5} g\prime^{3/5}/4q_0^{1/5}$, (b) $q_0 = (\tan(\alpha))^4 g\prime^3/2^{10}\Omega^5$, (c) $g\prime = 2^{10/3}\Omega^{5/3} q_0^{1/3}/(\tan(\alpha))^{4/3}$.

Thus, when looking at U_i as a function of Ω (with q_0, g' and α kept constant), U_i has a maximum at $\Omega = (\tan(\alpha))^{\frac{4}{5}} g'^{\frac{3}{5}}/(4q_0^{\frac{1}{5}})$. Similarly, when looking at U_i as a function of q_0 (with Ω, g' and α kept constant), U_i has a maximum at $q_0 = (\tan(\alpha))^4 g'^3/(2^{10}\Omega^5)$ and when looking at U_i as a function of g' (with Ω, q_0 and α kept constant), U_i has a maximum at $g' = 2^{\frac{10}{3}}\Omega^{\frac{5}{3}} q_0^{\frac{1}{3}}/(\tan(\alpha))^{\frac{4}{3}}$. The crosses on Figures 4.4(a)-(c) indicate the maxima of U_i found at $\Omega = (\tan(\alpha))^{\frac{4}{5}} g'^{\frac{3}{5}}/(4q_0^{\frac{1}{5}})$ (for the different values of α, with $q_0 = 20\ cm^3\ s^{-1}$ and $g' = 5\ cm\ s^{-2}$), at $q_0 = (\tan(\alpha))^4 g'^3/(2^{10}\Omega^5)$ (for the different values of α, with $\Omega = 1.5\ rad\ s^{-1}$ and $g' = 5\ cm\ s^{-2}$) and at $g' = 2^{\frac{10}{3}}\Omega^{\frac{5}{3}} q_0^{\frac{1}{3}}/(\tan(\alpha))^{\frac{4}{3}}$ (for the different values of α, with $\Omega = 0.5\ rad\ s^{-1}$ and $q_0 = 20\ cm^3\ s^{-1}$).

From Figures 4.3(a)-(b) and Figures 4.4(a)-(c), the non-dimensional inclined-wall coastal current velocity, U_i, after having reached its maximum value, decreases and approaches zero for very large values of H (see Figure 4.3b), Ω (see Figure 4.4a) and q_0 (see Figure 4.4b), while it approaches 0.75 (that is, the value of the non-dimensional vertical-wall coastal current velocity, U_0, of Thomas & Linden (2007) from (4.2d)) for very large values of α (see Figure 4.3a) and g' (see Figure 4.4c).

4.3.2 Comparison between the inclined-wall velocity, u_i, and the vertical-wall velocity, u_0

To compare the difference between the theoretical inclined-wall and vertical-wall coastal current velocities, their ratio, u_i/u_0, which is equivalent to $U_i/U_0 = (4/3)U_i$ (using (4.2d)), is studied. Therefore, the u_i/u_0 ratio varies similarly to U_i (the same variations and the same maxima). Using (4.44), one obtains:

$$\frac{u_i}{u_0} = \frac{1}{-\frac{H}{\tan(\alpha)}\left(\left(\frac{H}{\tan(\alpha)}\right)^2 + \frac{3}{4}\right) + \left(\left(\frac{H}{\tan(\alpha)}\right)^2 + 1\right)^{\frac{3}{2}}}. \tag{4.65}$$

Figures 4.5(a)-(b) display the ratio, u_i/u_0, of the predicted inclined-wall coastal current speed to the predicted vertical-wall coastal current speed as a function of the bottom slope, α (for different values of H), and, as a function of the non-dimensional coastal current height, H (for different values of α). The crosses on Figures 4.5(a)-(b) indicate the maxima of u_i/u_0 found at $\alpha = \arctan(2\sqrt{2}H)$ (for the different values of H) and at $H = \tan(\alpha)/2\sqrt{2}$ (for the different values of α). The solid line in Figures 4.5(a)-(b) identifies $u_i = u_0$, *i.e* when inclined-wall coastal currents propagate at same speed as vertical-wall coastal currents.

Figures 4.5(a)-(b) reveal that inclined-wall coastal currents can be faster or slower than their counterparts, or can have same speed as vertical-wall coastal currents. Inclined-wall coastal currents are faster than the vertical-wall coastal currents ($u_i/u_0 > 1$) at higher α (Figure 4.5a) and at lower H values (Figure 4.5b), thus for steep angles and, wide and shallow coastal currents (lower H values). At lower α (Figure 4.5a) and at higher H values (Figure 4.5b), thus for gentle slopes and, narrow and deep coastal currents (larger H values), inclined-wall coastal currents are slower than vertical-wall coastal currents. The extent of the α-interval for which inclined-wall coastal currents are faster than vertical-wall coastal currents decreases with increasing H values (Figure 4.5a). Similarly, the extent of the H-interval for which inclined-wall coastal currents are faster than vertical-wall coastal currents decreases with decreasing α values (Figure 4.5b). The value of the speed ratio, u_i/u_0, at the maximum, independent of the experimental conditions, is found after calculation to be equal to 1.1314.

Figures 4.6(a)-(c) display the ratio, u_i/u_0, of the predicted inclined-wall coastal current speed to the predicted vertical-wall coastal current speed as a function of the rotation rate, Ω (for different values of α, with $q_0 = 20\ cm^3\ s^{-1}$ and $g\prime = 5\ cm\ s^{-2}$), as a function of the flow rate, q_0 (for different values of α, with $\Omega = 1.5\ rad\ s^{-1}$ and $g\prime = 5\ cm\ s^{-2}$), and as a function of the reduced-gravity, $g\prime$ (for different values of α, with $\Omega = 0.5\ rad\ s^{-1}$ and $q_0 = 20\ cm^3\ s^{-1}$). The solid line in Figures 4.6(a)-(c) identifies $u_i = u_0$.

In terms of the experimental parameters Ω, q_0 and $g\prime$, inclined-wall coastal currents are faster than vertical-wall coastal currents at lower Ω (Figure 4.6(a)), lower q_0 (Figure 4.6(b)) and higher $g\prime$ values (Figure 4.6(c)). Figures 4.6(a)-(c) and figures similar to Figures 4.6(a)-(c) show that the extent of the Ω-interval for which inclined-wall coastal currents are faster than vertical-wall coastal currents decreases with decreasing α (Figure 4.6a), decreasing $g\prime$ and increasing q_0, the extent of the q_0-interval for which inclined-wall coastal currents are faster than vertical-wall coastal currents decreases with decreasing α (Figure 4.6b), increasing Ω and decreasing $g\prime$, and finally, the extent of the $g\prime$-interval for which inclined-wall coastal currents are faster than vertical-wall coastal currents decreases with decreasing α (Figure 4.6c), increasing Ω and increasing q_0.

From Figures 4.5(a)-(b) and Figures 4.6(a)-(c), after the u_i/u_0 ratio has reached its maximum value, it decreases and approaches zero for very large values of H (Figure 4.5b), Ω (Figure 4.6a) and q_0 (Figure 4.6b), while it ap-

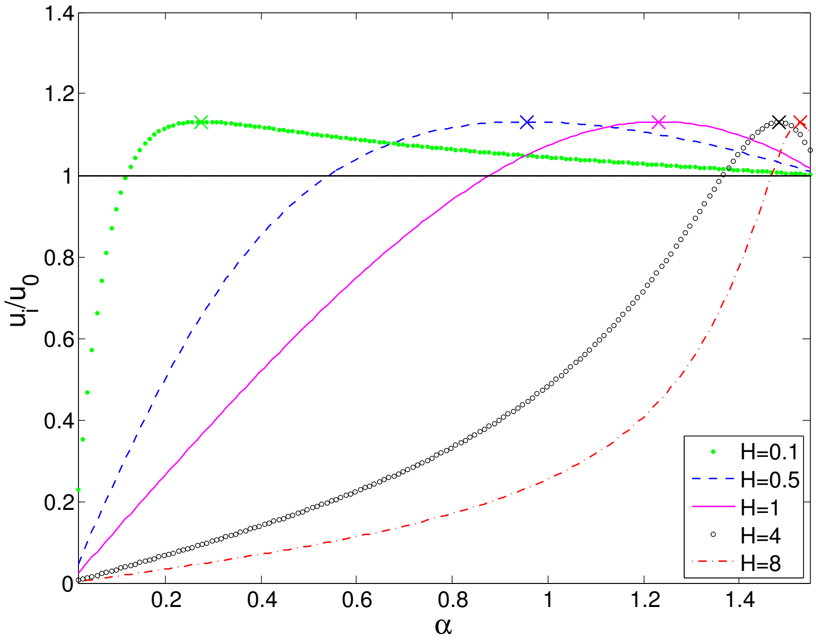

(a) u_i/u_0 as a function of α, for different values of H. Crosses indicate the maxima of u_i/u_0 found at $\alpha = \arctan(2\sqrt{2}H)$, for the different values of H.

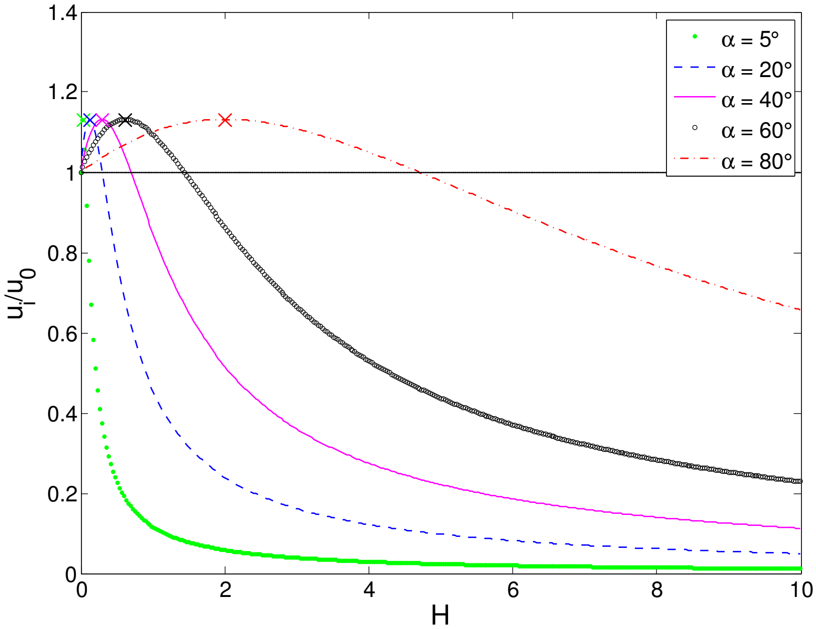

(b) u_i/u_0 as a function of H, for different values of α. Crosses indicate the maxima of u_i/u_0 found at $H = \tan(\alpha)/2\sqrt{2}$, for the different values of α.

Figure 4.5: Variations of the ratio, u_i/u_0, of the predicted inclined-wall coastal current speed to the predicted vertical-wall coastal current speed as a function of the bottom slope, α, and, the non-dimensional height, H.

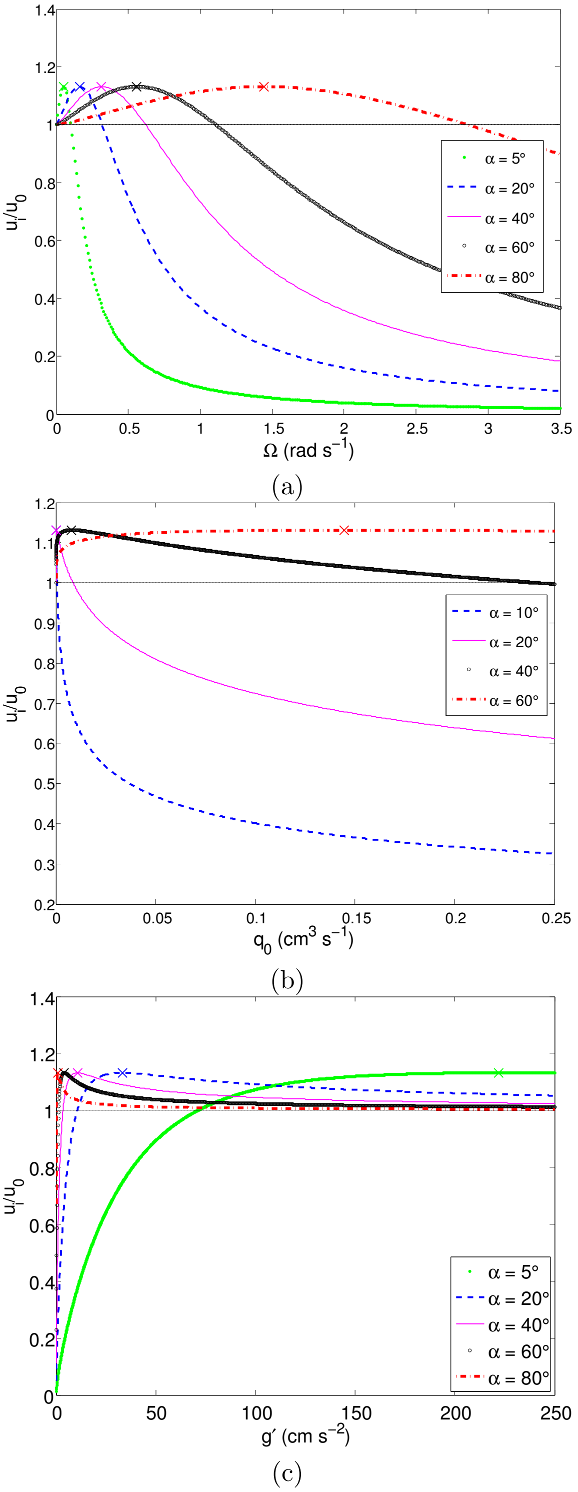

Figure 4.6: Variations of u_i/u_0 as a function of (a) Ω, for different values of α, with $q_0 = 20\ cm^3\ s^{-1}$ and $g\prime = 5\ cm\ s^{-2}$,(b) q_0, for different values of α, with $\Omega = 1.5\ rad\ s^{-1}$ and $g\prime = 5\ cm\ s^{-2}$, (c) $g\prime$, for different values of α, with $\Omega = 0.5\ rad\ s^{-1}$ and $q_0 = 20\ cm^3\ s^{-1}$. Crosses indicate the maxima of u_i/u_0, found at (a) $\Omega = (\tan(\alpha))^{4/5} g\prime^{3/5}/4q_0^{1/5}$, (b) $q_0 = (\tan(\alpha))^4 g\prime^3/2^{10}\Omega^5$, (c) $g\prime = 2^{10/3}\Omega^{5/3}q_0^{1/3}/(\tan(\alpha))^{4/3}$.

proaches 1, that is $u_i \backsim u_0$ and thus inclined-wall coastal currents have same propagation speed than vertical-wall coastal currents, for very large values of α (Figure 4.5a) and $g\prime$ (Figure 4.6c). Therefore, the inclined-wall coastal current velocity is found to approach zero and to be much lower than the vertical-wall coastal current velocity for the gentlest slopes and, the narrowest and deepest coastal currents, while the inclined-wall coastal current velocity approaches the vertical-wall coastal current velocity for the steepest slopes and, the widest and shallowest coastal currents.

CHAPTER 5

Experimental methods

The utility of the scaling analysis was examined through a program of two complementing sets of experiments, using different experimental facilities. The two facilities had substantially different spatial scales enabling the investigation of a wide range of the independent experimental parameters. Small-scale laboratory experiments were conducted at the *Fluid Dynamics Research Center* (School of Engineering, University of Warwick, United Kingdom) on a rotating turntable supporting a 1 m diameter fluid-filled tank. Large-scale experiments were conducted at the *Norwegian University of Science and Technology (NTNU)* (Trondheim, Norway) using the 5 m Coriolis turntable. The experimental procedures and techniques are described in detail below. The experimental set-up at the *NTNU* was designed to mirror the small-scale study on a larger scale.

5.1 Small-scale experiments

The goal of the experiments was to simulate estuarine discharges of buoyant freshwater into an environment of salty, denser ocean water along an inclined coastline. The arrangement of the experimental small-scale facility is shown in Figure 5.1.

The experiments were carried out in a transparent, circular acrylic tank with a radius of 0.5 m. The tank was placed on a rotating turntable to simulate the rotation of the Earth and introduce Coriolis effects on the flow. An inclined wall of slope α (represented in Figure 4.2), where α is the angle between the inclined wall and the horizontal bottom of the tank , was installed into the tank. Two different inclined walls, made from *PETG Copolyester sheet*, were used for this study and can be seen in Figures 5.2(a)-(b).

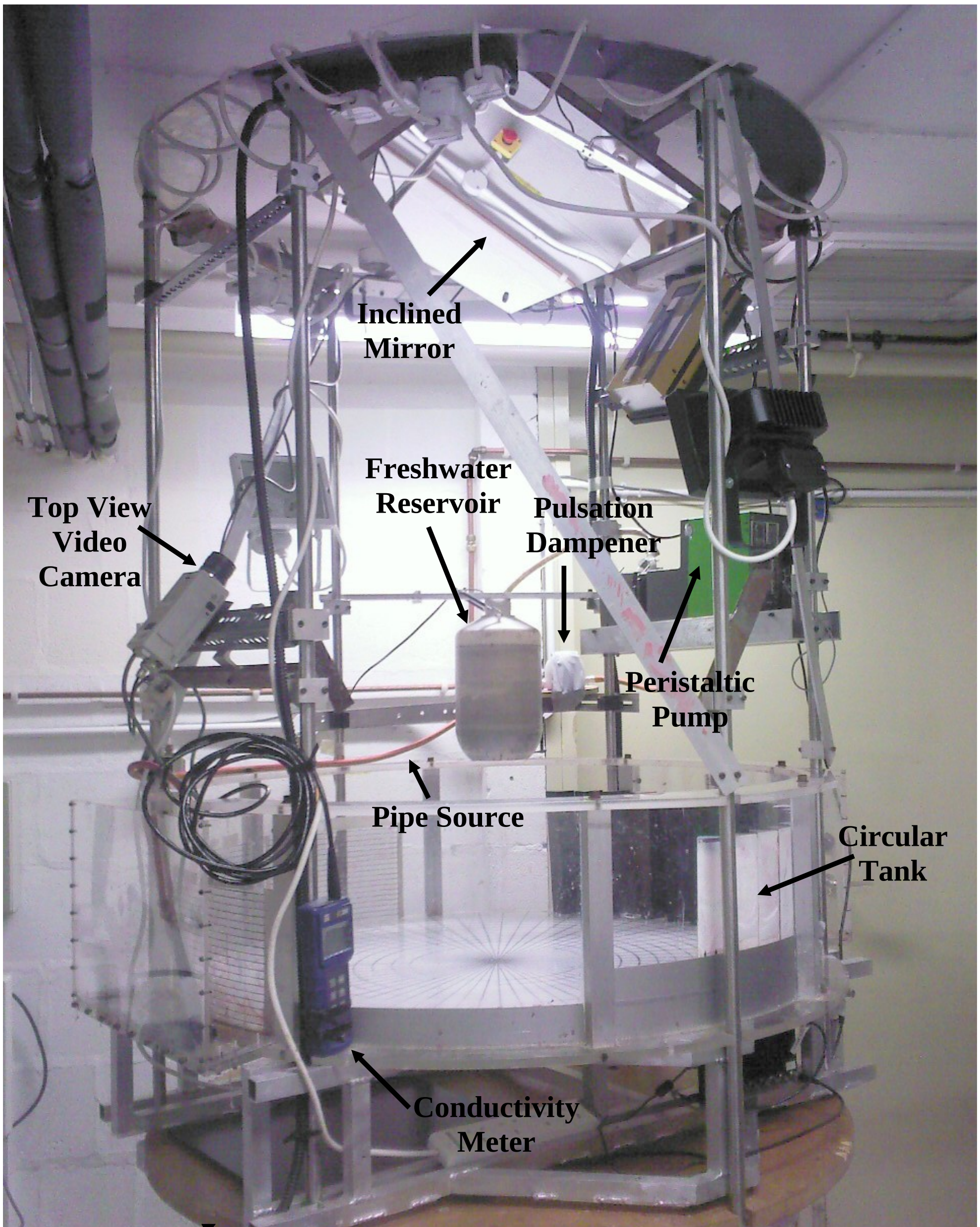
Inclined Mirror
Freshwater Reservoir
Top View Video Camera
Pulsation Dampener
Peristaltic Pump
Pipe Source
Circular Tank
Conductivity Meter
Rotating Turntable

Figure 5.1: Small-scale turntable at the *Fluid Dynamics Research Center* (University of Warwick).

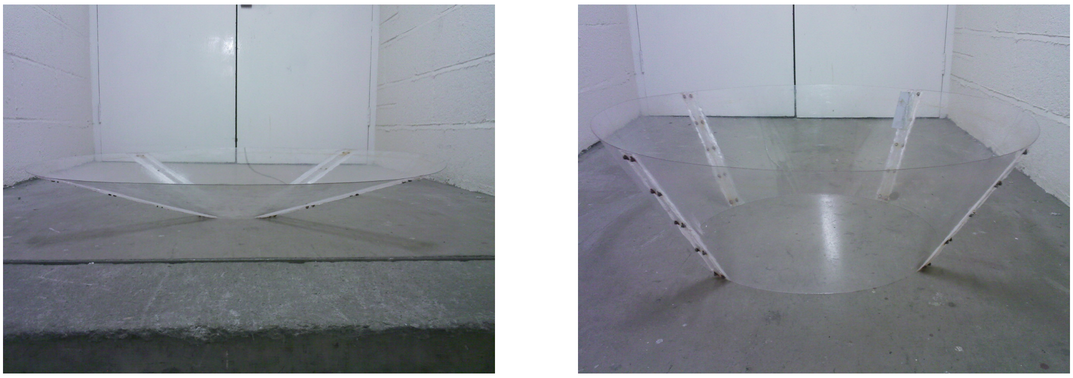

(a) $\alpha = 18.5\,^{\circ}$ (b) $\alpha = 59.2\,^{\circ}$

Figure 5.2: The two inclined walls for the small-scale experimental study

The tank was filled with salt water of a specified density ρ_2 representing ocean water, while freshwater of density ρ_1, with $\rho_1 < \rho_2$, was stored in a separate, co-rotating smaller reservoir mounted on the turntable. The freshwater was supplied from the reservoir to the source by means of a calibrated peristaltic pump ($505Di/L$ microprocessor controlled high-accuracy dispenser 350 rpm, *Watson-Marlow*). The accuracy of the pump was ± 0.5%. A pulsation dampener (*Cole-Parmer*) was used to reduce the pulsations produced by the pump on the buoyant outflow. The source, for these experiments, was a pipe with a diameter of 0.7 cm, which was adjusted to be level with the surface of the dense salt water. Gauze was added at the source outlet to diffuse the fresh fluid. The buoyant outflow, simulating estuarine discharges, was released continuously and with a constant specific volumetric discharge rate q_0. Similarly to Thomas & Linden (2007), the fluid was discharged vertically upwards, rather than horizontally as would be the case in the natural environment. The purpose of the vertical discharge direction was to minimize momentum flux effects and mixing of freshwater and salt water near the source (Thomas & Linden (2007)).

An $YSI\ EC300$ conductivity/temperature meter (*Cole-Parmer*) was employed to measure the salinity and the temperature of the salt water prior to the start of the experiment. The salinity and temperature accuracies were ± 0.2% and $\pm\ 0.2\,^{\circ}C$, respectively. The density of the salt water was determined from both its salinity and its temperature. The density difference between the freshwater and the salt water was characterized in terms of the reduced gravity, g', defined previously in equation (2.1). The turntable was set to a specified rotation

	Small-scale vertical-wall experiments	Small-scale inclined-wall experiments
α	90°	18.5°, 59.2°
Ω	$0.491\ rad\ s^{-1} \leq \Omega \leq 1.525\ rad\ s^{-1}$	$0.49\ rad\ s^{-1} \leq \Omega \leq 1.515\ rad\ s^{-1}$
$g\prime$	$2.92\ cm\ s^{-2} \leq g\prime \leq 18.77\ cm\ s^{-2}$	$2.98\ cm\ s^{-2} \leq g\prime \leq 18.85\ cm\ s^{-2}$
q_0	$3.17\ cm^3\ s^{-1} \leq q_0 \leq 28.28\ cm^3\ s^{-1}$	$3.11\ cm^3\ s^{-1} \leq q_0 \leq 28.29\ cm^3\ s^{-1}$
H_D	$2.3\ cm \leq H_D \leq 12.4\ cm$	$0.55\ cm \leq H_D \leq 8.43\ cm$
I	$0.109 \leq I \leq 1.52$	$0.107 \leq I \leq 1.508$
Ek_H	$1.55 \times 10^{-4} \leq Ek_H \leq 1.67 \times 10^{-3}$	$1.53 \times 10^{-4} \leq Ek_H \leq 2 \times 10^{-3}$
Ek_V	$5.87 \times 10^{-5} \leq Ek_V \leq 2.89 \times 10^{-2}$	$5.92 \times 10^{-5} \leq Ek_V \leq 3.09 \times 10^{-2}$
Re	$230 \leq Re \leq 2419$	$187 \leq Re \leq 2452$
h_0/H_D	$0.06 \leq h_0/H_D \leq 2.04$	$0.12 \leq h_0/H_D \leq 6.77$

Table 5.1: Summary of the ranges of the independent parameters in the small-scale experiments.

rate Ω before each experiment, to within a $\Delta\ T = 0.1\ s$. Depending upon the rotation period of an experiment, this corresponds to a relative rotation error of between 0.0038 and 0.0372 rad s^{-1}. The ambient ocean fluid was allowed to reach solid body rotation before each experiment was begun. The table spun in a clockwise direction; thus, f was negative and the coastal current moved along the inclined wall by keeping the coast to its left. Experiments were terminated before the coastal current was allowed to reach the source. Griffiths & Hopfinger (1983) found that a covering lid was unnecessary as any motions induced by evaporative convection and surface wind stress were not detectable in their long-time-exposure photographs of particle motions. Therefore no cover over the turntable was used in the experiments. Water temperature was allowed to equilibrate to room temperature before experiments to minimize thermal differences.

In total, five parameters were varied for these experiments: the rotation rate, Ω, the flow rate at the source, q_0, the reduced gravity, g', the total depth of the salt water in the tank, H_{SW}, and the bottom slope, α. The purpose of varying the total depth of the salt water in the tank was to study the depth at which the bottom of the tank would interact with the coastal current and which effects it would cause on it. To this end, some vertical wall experiments were also carried out. Table 5.1 summarizes the range of the values of the relevant parameters for the small-scale experiments. Velocities and geometrical information of coastal currents were measured with time from video records by two means: dye visualization and PIV methods.

5.1.1 Dye visualization of coastal currents

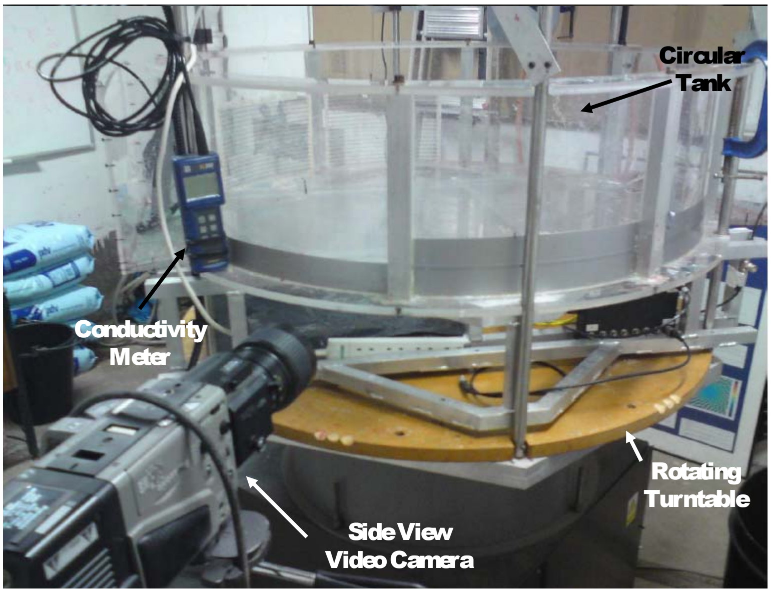

Figure 5.3: Side-view video camera for capturing the coastal current height profile.

The buoyant outflow was marked using small concentrations of food coloring, while the ambient water was clear, in order to facilitate visualization of the coastal current.

The experiments were filmed with two video cameras simultaneously. One color video camera (model $TK-C1481BEG$, JVC) was rigidly mounted on the superstructure of the rotating turntable and filmed the coastal current through a large mirror mounted at the top of the tank (Figure 5.1). This camera provided information on the general aspect of the coastal current and its nose displacement as a function of time. The second color video camera (model $WV-F15HSE$, $Panasonic$) was positioned next to the turntable and filmed the flow through the transparent side wall of the acrylic tank (Figure 5.3). This camera scanned the coastal current height at the wall of the tank once per turntable revolution.

A white calibration disc, made from *PETG Copolyester sheet*, was fixed to the bottom of the tank. Radial lines, all spaced 0.1 radians apart (except the last one which was spaced $\sim$ 0.08 radians away), and circumferential lines, spaced 3 cm apart, were drawn on it. This allowed for coastal current length measurements from the top-view video camera. Details for each experiment are provided in Appendix B.

The coastal current width was not inferred from dye concentrations, as dye concentrations can vary from experiment to experiment. Also, the use of dye concentrations to infer width is ambiguous because dye may occupy regions that are not dynamically active (e.g., the dye may be advected or mixed to a region in which the velocities and pressure gradients are small) (Avicola & Huq (2002)). Thomas & Linden (2007) discuss in greater detail in their Section 4.5 why dye measurements are not a good indicator for coastal current width and give error estimates for dye measurement of the coastal current width. Rather, width information was determined using Particle Image Velocimetry techniques (PIV) (see Brend (2009) for a good literature review on PIV).

5.1.2 Particle Image Velocimetry Measurements

Measurements of the coastal current width and its surface velocities were made using a 2-component PIV system shown in Figure 5.4. This consisted of a *pco.*2000 2048 x 2048 pixel CCD camera (*PCO A.G.*), and a triggerable MS 300 stroboscope (*IMPO Electronic A/S*). The camera was fitted with a $f : 1.4$ 50 mm lens and was aimed upwards at a large mirror mounted at the top of the tank. The stroboscope was mounted at the top of the tank, aimed directly towards the area being viewed by the camera. Both devices were triggered by a $microPulse$ timing generator, under the control of *proControl* software (*Etalon Research Ltd.*). This allowed simple adjustment of the inter-frame pulsing period ($\Delta\ t$), with values of between 80 - 190 ms used for the majority of the experiments.

100 micrometers diameter white polyamide seeding particles were mixed into the ambient salt water, then allowed to float on top of the surface water. The freshwater was free from particles as they would obstruct the source outlet. The salt water was dyed dark blue using food coloring to obtain a good contrast between the particles and the background. To avoid coagulation of the floating particles, they were first mixed with a small quantity of antistatic wetting agent ($TETENAL$ *Mirasol* 2000 *Antistatic*), prior to being added to the salt water. Care was taken to avoid excessive amounts of foam being generated, and any bubbles that formed on the water surface were burst prior to recording the PIV images. At a high rotation rate (*i.e* for $\Omega > 1\ rad\ s^{-1}$), the salt water surface tilted sufficiently, due to the centrifugal forces, to bring the majority of the particles in the ambient water near the wall. Therefore, when discharging the freshwater in the tank, particles mixing in the coastal current were concentrated

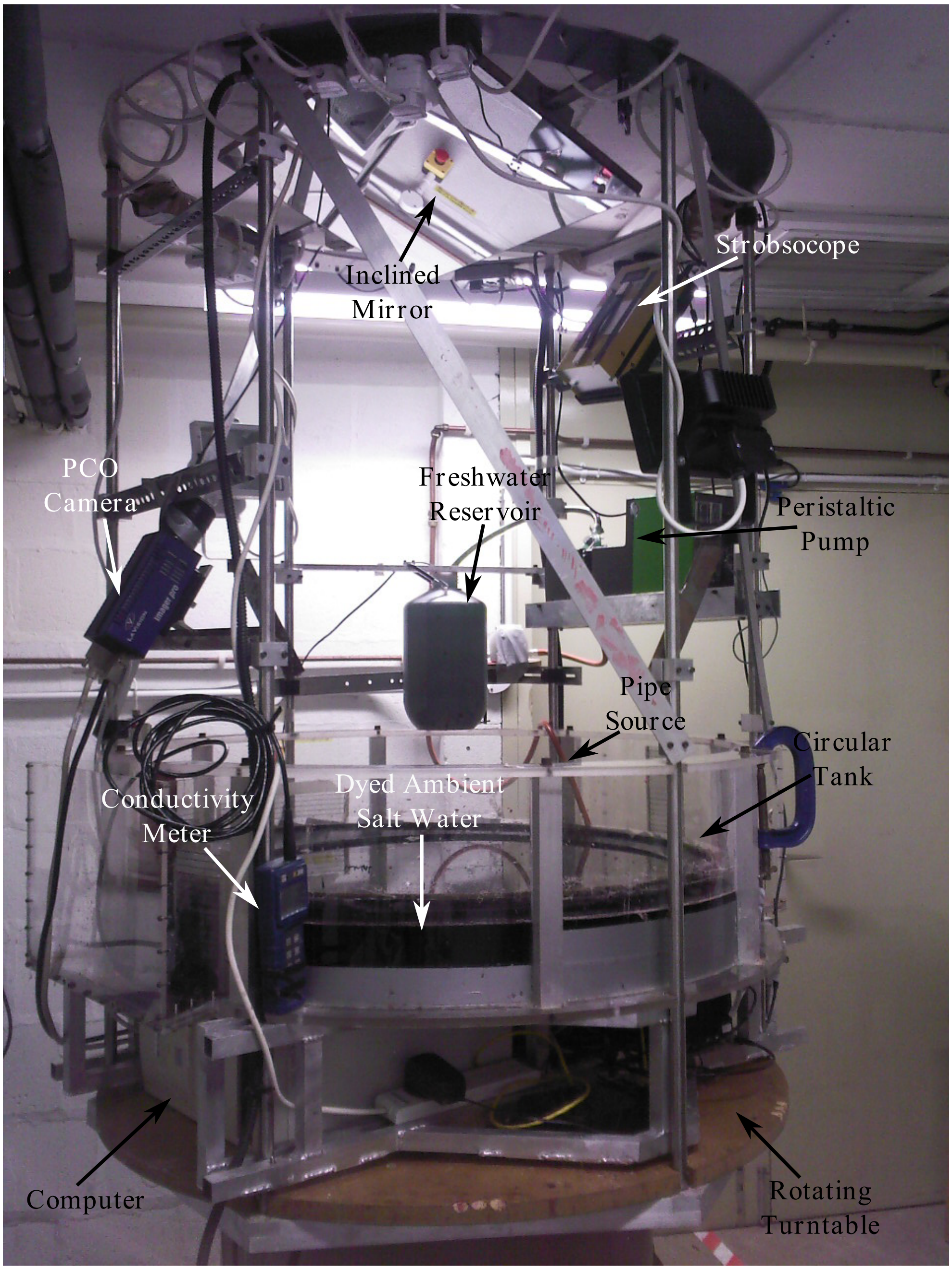
Inclined
Mirror
Strobsocope
PCO
Camera
Freshwater
Reservoir
Peristaltic
Pump
Pipe
Source
Circular
Tank
Conductivity
Meter
Dyed Ambient
Salt Water
Computer
Rotating
Turntable

Figure 5.4: *PIV* setup.

only in the portion of the coastal current next to the wall, giving poor quality measurements. Due to the lack of seeding in the coastal currents at a high rotation rate, the PIV experiments were limited to low rotation rate conditions ($i.e$ $\Omega \leq 1\ rad\ s^{-1}$). Two series of PIV measurements were made for each experimental condition, at a rate of either 1 or 2 Hz: the first series of measurements (called experiments D, C and B) were taken between 63 cm and 187 cm downstream from the source while the second series of measurements (called experiments J, H and F) were done between 43 cm and 115 cm downstream from the source. The second series of measurements are preferred to the first ones as more data can be extracted (due to the measurements position from the source). Details for each PIV condition are provided in Appendix D.

The optical system was spatially calibrated using a thick black plastic target sheet, which was placed at the bottom of the tank. This was covered with white crosses on a 40 mm grid (with the central position differentiated by a circle); these marks were in turn used to calculate a polynomial camera calibration model. The captured PIV images were processed in $DaVis$ 7.1 ($LaVision\ GmBH$), using multi-pass cross-correlation with a final window size of 32 pixels and 50% overlap. The PIV measurements produced a time-series of "vector maps", which were approximately 279 x 275 vectors in size, each comprising two-component velocity measurements, recorded in Cartesian coordinates. Sixty-one profiles (each containing 150 samples) stretched towards the tank wall in the radial direction were extracted from each map, and the tangential and radial components of velocity at each point along the profile computed. The profiles covered the range $r = 0$ to 52 cm (the tank radius was 50 cm), with 2° spacing between profiles. Therefore 1/3 of the tank was covered by the PIV measurements, with the coastal current source positioned further upstream. The profiles were next grouped into 3 "sectors" (each covering a 40° segment of the tank), and the velocity profiles within each sector were averaged.

Variations in the surface velocity values were observed in the PIV data. These variations were suggested to be caused by tank "sloshing" (they were found to be periodic, with a period matching the turntable rotation period). Tank sloshing may have occurred because of poor turntable motor drive-train or by off-centre mounting of experimental materials on the turntable. In order to estimate the frequency of the disturbances introduced by the tank sloshing, a FFT was calculated using data extracted from the spatially averaged time-series data. Then the data were smoothed in the time-domain using a sliding-window averaging-filter whose size was equal to the wavelength of the temporal disturbance. Figure 5.5 illustrates the improvement on the along-shore velocity profiles after time and spatial averages were made: it displays, in order, a raw single profile, a spatial averaged profile, and a spatial and temporal averaged profile for the along-shore velocity from the PIV experiment $J07$ (listed in Table D.2) extracted at the fixed along-shore distance, d_S, downstream from the source with $d_S = 77.5$ cm.

To obtain the width, one needs to identify the seaward limit of the coastal current. Some of the measurements for the coastal current width were inferred using the position of the maximum value for the gradient of the azimuthal velocity in the across-shore direction. The velocity value found at this position defined a velocity threshold value and the coastal current location was then determined wherever the velocity value was greater than the threshold value. This method did not work for all experiments, as spatial perturbations in some experiments were sufficiently important to disturb the width measurements: indeed in some experiments, the velocity threshold value was not found at the front of the coastal current but farther away in the ambient salt water. Thus, for these experiments, a velocity threshold value was chosen (after several tests) and after examination, was found to be approximately 35% of the value for the maximum velocity in the coastal current. Coastal current widths measured with this latter method were found to be similar to the coastal current width obtained using the maximum value for the gradient of the azimuthal velocity in the across-shore direction (when this last method worked).

Figure 5.6 illustrates the second width extraction method for the PIV experiments. The top image displays the azimuthal velocity for one PIV experiment (experiment $J10$ listed in table D.2), measured at a fixed distance downstream from the source, $d_s = 77.5$ cm, as a function of time (the color bar next to the top image represents velocity ($cm\ s^{-1}$)). The y-axis represents the radial position. The velocity threshold value is chosen to be 1.7 $cm\ s^{-1}$, thus all the velocity values from the top image above the value of 1.7 $cm\ s^{-1}$ determine the coastal current and are displayed in the bottom image of figure 5.6 (the velocity threshold value of the coastal current from figure 5.6 is $\sim 34\%$ of the maximum speed, $u_{max} = 5.04$ $cm\ s^{-1}$).

The acquisition and processing of the PIV data was performed in conjunction with Dr. Andrew Skeen. The next section describes the large-scale experiments. They were conducted in a similar manner as the small-scale experiments; therefore only the differences are highlighted.

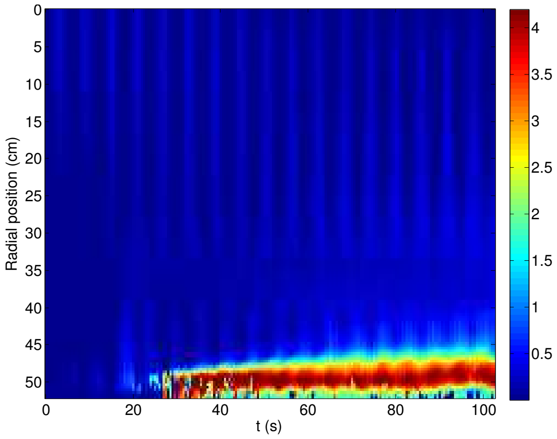

(a) Raw single along-shore velocity profile.

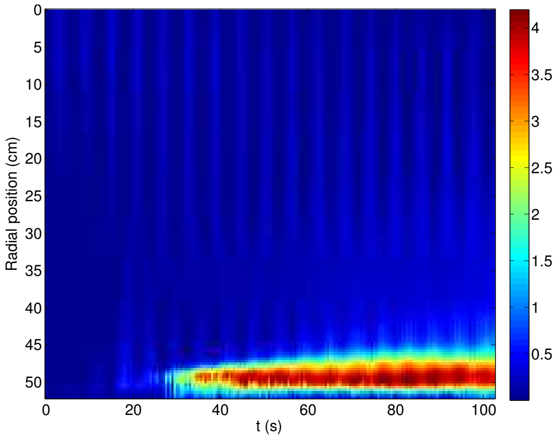

(b) Spatial averaged along-shore velocity profile.

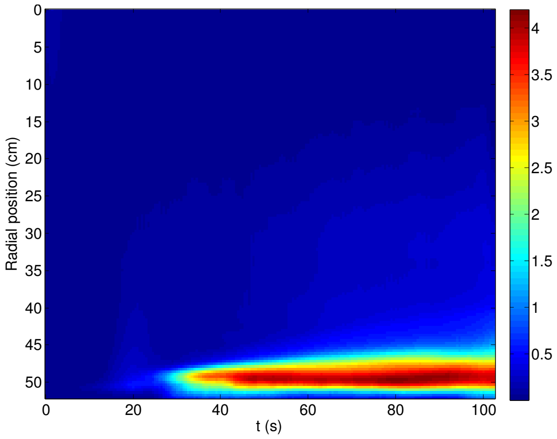

(c) Spatial and temporal averaged along-shore velocity profile.

Figure 5.5: Results of the spatial and time averages on a single along-shore velocity profile extracted from the PIV experiment $J07$ at the fixed distance, d_S, downstream from the source with $d_S = 77.5cm$. The colour bar on the figures is for velocity $(cm\ s^{-1})$.

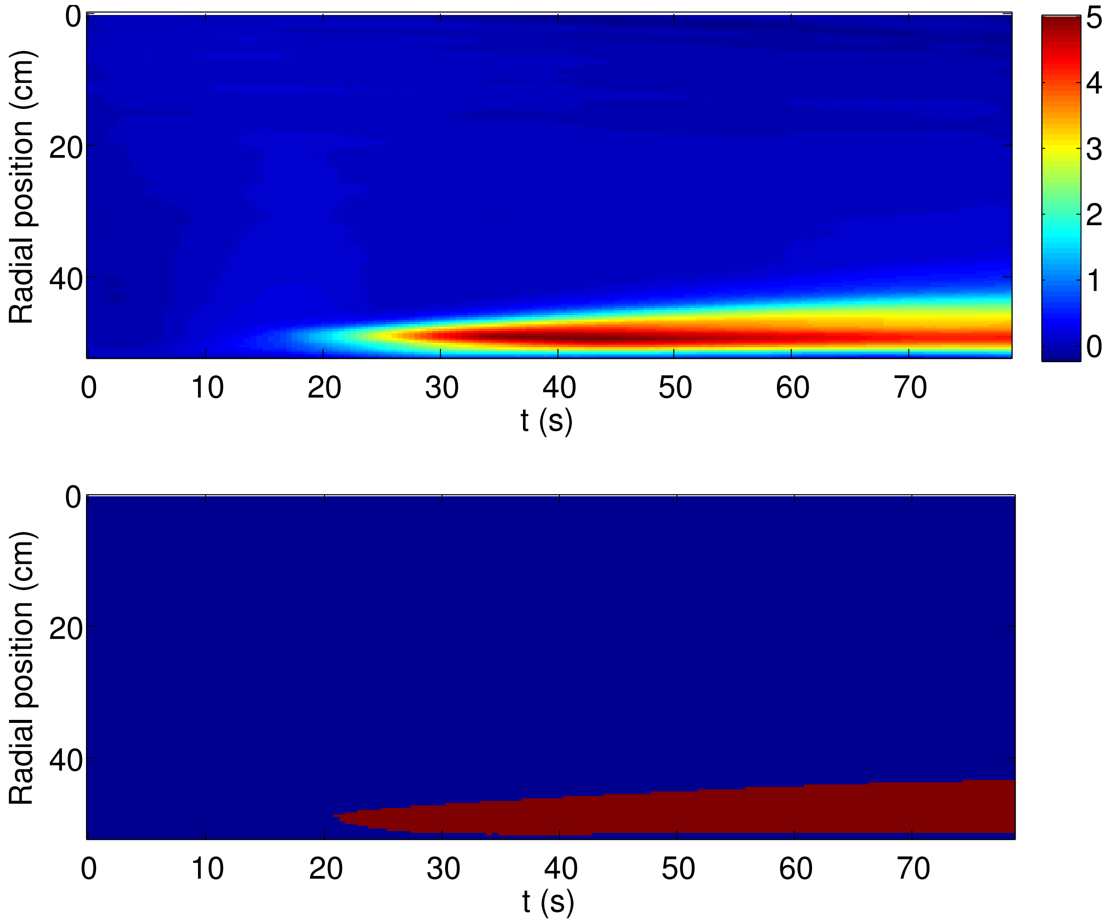

Figure 5.6: PIV width extraction method (the colour bar on the top image represents velocity ($cm\ s^{-1}$)).

5.2 Large-scale experiments

The rotating basin at the *NTNU* in Trondheim is shown in Figure 5.7. It has a diameter of 5 m and a depth of 50 cm. Three independent sources of water with different salinities allow the simulation of stratified, rotational geophysical flows. Rotation periods can be chosen from 10 s to 27 h.

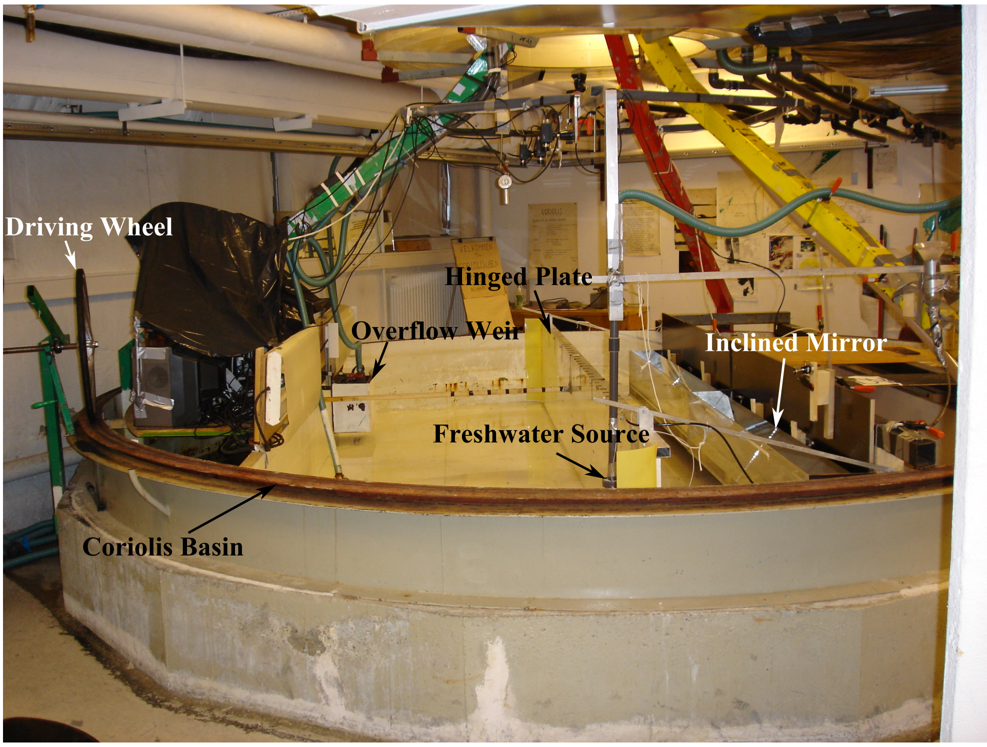

Figure 5.7: Picture of the Coriolis basin.

Figure 5.8 shows the construction of the rotating turntable in the cross-section. Three beams rising in a pyramid from the platform support the upper part. The unique feature of the design is that it is suspended like a horizontal wheel, with one axle in the ceiling and one in the floor. The weight is reduced by means of a hydraulic air cushion under a submerged skirt. With this arrangement, the forces are reduced to a minimum and it is not necessary to use thrust bearings. It is possible to align the axis to within 2×10^{-5} radians from the vertical. Vertical motions induced by shifting weights do not affect the simulation as long as the accelerations are much less than gravity (Vinger & McClimans (1980)). The water and electricity supply systems are also shown in Figure 5.8. There are four circular troughs mounted to the ceiling, intended for salt and

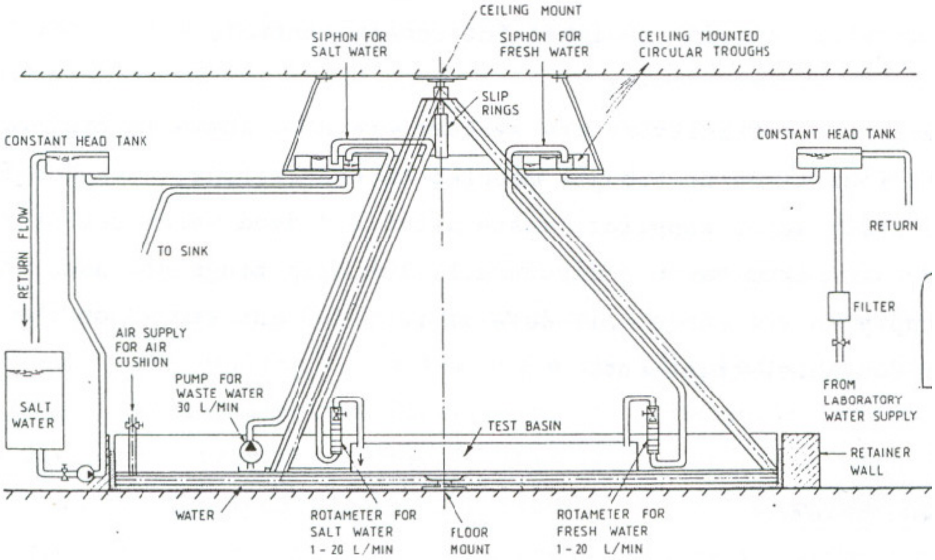
CEILING MOUNT
SIPHON FOR SALT WATER
SIPHON FOR FRESH WATER
CEILING MOUNTED CIRCULAR TROUGHS
SLIP RINGS
CONSTANT HEAD TANK
CONSTANT HEAD TANK
RETURN FLOW
TO SINK
RETURN
FILTER
AIR SUPPLY FOR AIR CUSHION
PUMP FOR WASTE WATER 30 L/MIN
SALT WATER
TEST BASIN
FROM LABORATORY WATER SUPPLY
RETAINER WALL
WATER
ROTAMETER FOR SALT WATER 1-20 L/MIN
FLOOR MOUNT
ROTAMETER FOR FRESH WATER 1-20 L/MIN

Figure 5.8: A cross-section of the 5 m diameter rotating turntable at the *NTNU* in Trondheim (from Vinger & McClimans (1980)).

freshwater supplies, waste water and dyed water for studying the dispersion from various discharges. The slip rings are used for power supply to the table. All data are recorded and stored on the platform for later treatment.

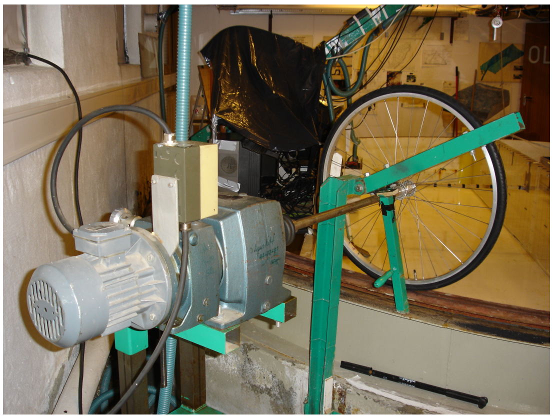

Figure 5.9: Turntable drive mechanism.

The arrangement of the experiments is illustrated in Figure 5.7. In order to facilitate experiments with different coastline inclination angles, a hinged transparent acrylic plate was mounted across the diameter of the Coriolis tank. Again, the inclination angle, α, is the angle between the plate and the horizontal bottom of the Coriolis basin. The rotational speed of the basin was varied by means of a Kopp variable speed drive and one rim-drive positive traction wheel (Figure 5.9). With normal operating conditions, the rotational velocity was controlled to within 2%. The supply of freshwater to the rotating basin was measured by means of a standard rotameter (shown in Figure 5.10). The accuracy of this flow measurement was estimated to be ± 3%. Freshwater was released continuously, with a constant volumetric discharge rate, from a small source, with a diameter of 7.6 cm, mounted on the inclined plate as illustrated in Figure 5.11. The Coriolis basin was filled with salt water to a height $H_{SW} = 40$ cm.

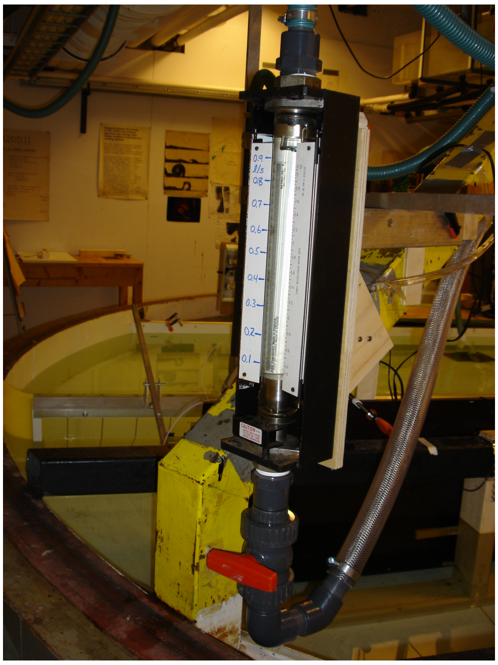

Figure 5.10: Rotameter for measuring the flow rate, q_0, at the source.

The compensation source of entrained seawater was supplied through a sponge at the bottom of the basin, along the left-hand wall (when looking through Figure 5.7). An overflow weir, seen in Figure 5.7, was mounted along the left wall closer to the near end of the basin. The height of the weir regulates the water depth in the basin with the given flow. At the start of each run, the water level in the sump was the same as the final equilibrium. The pump was turned on when the nose of the coastal current was within 50 cm from the sink. The outflow was pumped up along the green leg to a trough at the ceiling. This procedure enabled the flow to reach a steady state.

The table spun in an anti-clockwise direction; thus, f was positive and the

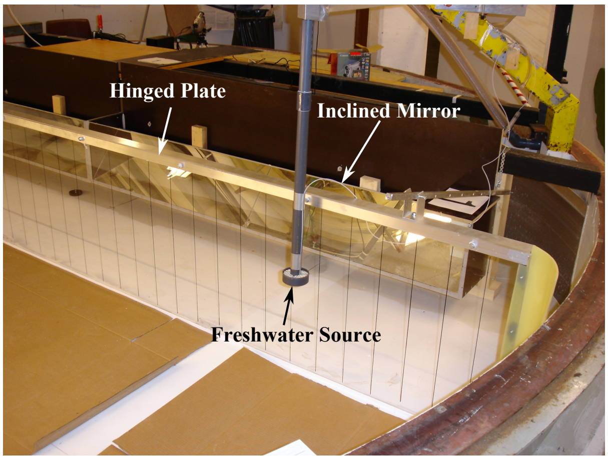

Figure 5.11: Freshwater Source.

coastal current moved along the plate by keeping the coast to its right. For visualization purposes, the freshwater discharged at the source was dyed while the ambient salt water was clear. The experiments were filmed with a number of video cameras simultaneously. One overhead video camera, mounted near the ceiling, with a wide-angle lens, viewed the entire diameter of the tank. This enabled viewing the general aspect of the coastal current and measuring its nose displacement as a function of time. Lines were drawn every 10 cm on the hinged plate (Figure 5.11) to serve as length scales for the coastal current length measurement. The width of the coastal current was additionally filmed with higher spatial resolution by a second overhead video camera viewing an enlarged section of the coastal currents located just downstream of the centre of the tank. A stick with ticks every centimetre was disposed above the water surface within the field of view of the second video camera to evaluate the coastal current width. The width was only estimated with dye visualizations as PIV experiments were not possible when these large-scale experiments were carried out. The coastal current depth, h_i, was measured as illustrated in Figure 5.12. Mirrors slanting 45 ° from the vertical, placed along the coast, allowed for the visual observation of the thickness of the coastal current through the transparent inclined plate which had ticks in the vertical direction every centimetre. An overhead camera, shown in Figure 5.13, filmed h_i' from which $h_i = h_i' \sin\alpha$ is obtained. Experiments for four different inclination angles α were conducted at Trondheim. The ranges over which the independent experimental parameters varied are summarized in Table 5.2. The details of each experiment are provided in Appendix C.

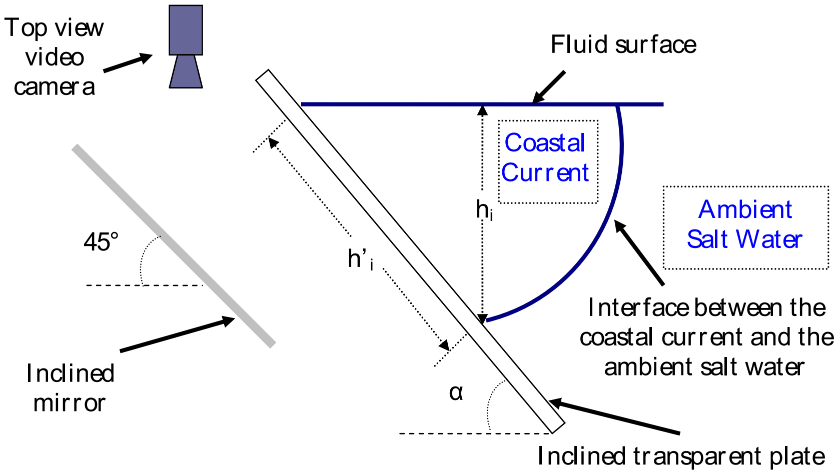
Top view
video
camera
Fluid surface
Coastal
Current
h_i
Ambient
Salt Water
45°
h'_i
Interface between the
coastal current and the
ambient salt water
Inclined
mirror
α
Inclined transparent plate

Figure 5.12: Illustration of the method to measure the coastal current depth.

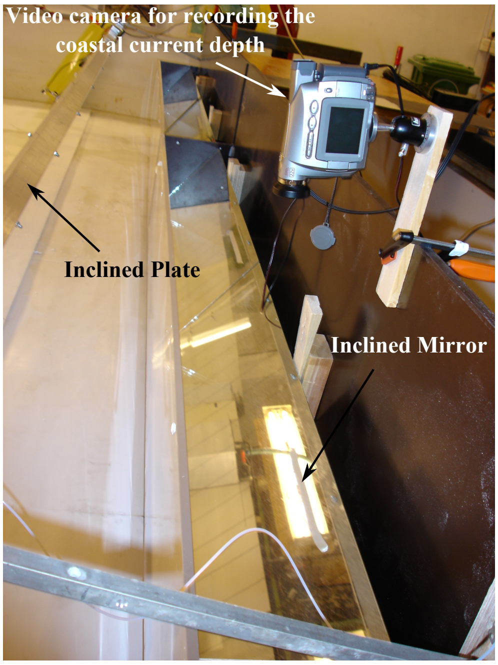
Video camera for recording the
coastal current depth
Inclined Plate
Inclined Mirror

Figure 5.13: Camera recording the coastal current depth.

	Large-scale vertical-wall experiments	Large-scale inclined-wall experiments
α	$90°$	$25.9°$, $40°$, $50°$, $60°$
Ω	$0.105\ rad\ s^{-1} \leq \Omega \leq 0.608\ rad\ s^{-1}$	$0.104\ rad\ s^{-1} \leq \Omega \leq 0.621\ rad\ s^{-1}$
$g\prime$	$2.84\ cm\ s^{-2} \leq g\prime \leq 21.39\ cm\ s^{-2}$	$2.7\ cm\ s^{-2} \leq g\prime \leq 21.35\ cm\ s^{-2}$
q_0	$110\ cm^3\ s^{-1} \leq q_0 \leq 920\ cm^3\ s^{-1}$	$100\ cm^3\ s^{-1} \leq q_0 \leq 920\ cm^3\ s^{-1}$
H_D	$40\ cm$	$3.85\ cm \leq H_D \leq 49.1\ cm$
I	$0.173 \leq I \leq 1.172$	$0.042 \leq I \leq 1.164$
Ek_H	$2.74 \times 10^{-5} \leq Ek_H \leq 1.24 \times 10^{-4}$	$1.86 \times 10^{-5} \leq Ek_H \leq 2.26 \times 10^{-4}$
Ek_V	$1.57 \times 10^{-5} \leq Ek_V \leq 1.24 \times 10^{-3}$	$1.64 \times 10^{-5} \leq Ek_V \leq 2.4 \times 10^{-2}$
Re	$3026 \leq Re \leq 13676$	$1661 \leq Re \leq 20120$
h_0/H_D	$0.13 \leq h_0/H_D \leq 0.57$	$0.04 \leq h_0/H_D \leq 3.47$

Table 5.2: Summary of the ranges of the independent parameters in the large-scale experiments.

CHAPTER 6

Numerical methods

The circulation model used in this study, to reproduce the vertical-wall coastal currents simulated in the small-scale study of Thomas & Linden (2007) and in the small-scale experiments described in Section 5.1.2, is the Regional Ocean Modeling System (*ROMS*, `http://marine.rutgers.edu/po/index.php?model=roms`), which has been developed and is supported by a consortium of institutions including Rutgers University and *UCLA*[*]. *ROMS* has been developed for, and applied to, a wide variety of coastal marine applications, including studies of buoyancy-driven coastal currents (e.g., the idealized studies of the Hudson River by Zhang *et al.* (2009) and the realistic simulations of the Columbia River plume by Liu *et al.* (2009)). The current chapter, Chapter 7 and Chapter 8 have been published in Grégorio *et al.* (2011). Section 6.1, describing the configuration of *ROMS*, was written for and contributed to Grégorio *et al.* (2011) by Prof. Dale Haidvogel[†].

6.1 Numerical configuration

ROMS utilizes consistent temporal averaging of the barotropic mode to guarantee both exact conservation and constancy preservation properties for tracers and therefore more accurately resolves barotropic processes, while preventing aliasing of unresolved barotropic signals into the slow baroclinic motions. Accuracy of the mode-splitting is further enhanced due to redefined barotropic pressure-gradient terms to account for the local variations in the density field (i.e., the pressure-gradient truncation error is greatly reduced). Vertical interpolation is based on conservative parabolic splines. Finally, *ROMS* uses orthogonal curvilinear coordinates in the horizontal, an essential feature here, as described below. Shchepetkin & McWilliams (2005) describe in detail the algorithms that comprise the ROMS computational kernel, and Haidvogel *et al.* (2007) discuss the validation of ROMS in a variety of oceanic settings.

---

[*] University of California, Los Angeles, USA

[†] Institute of Marine and Coastal Sciences, Rutgers University, New Brunswick, NJ 08901, USA

The *ROMS* model employs the hydrostatic approximation in the vertical equation of motion, traditional in models of the large-scale ocean circulation. This assumption is not problematic, as this study is based on a rotationally dominated regime. However it does introduce one complication. This has to do with the method of injection of buoyant fluid. In the laboratory setting, this is accomplished via direct vertical insertion. This option is not readily available to *ROMS*, wherein the hydrostatic assumption precludes independent specification of vertical fluid motion.

In configuring *ROMS* for these simulations, several alternatives were therefore considered for introduction of buoyancy. These options included the addition of light fluid via a specified rain field, the use of nudging (a relaxation term in the density equation), and horizontal injection of light fluid via an attached estuary. A hybrid of the latter two approaches was eventually adopted, as shown schematically in Figure 6.1.

The annular geometry of the laboratory experiments is reproduced easily in *ROMS* by choosing a polar coordinate system, and adopting periodic boundary conditions at the matching edge in the azimuthal direction. A singularity at the center of the circle is avoided by cutting away a small section in the center, yielding a donut shape (Figure 6.1a). A small estuary containing buoyant (density ρ_1) fluid at the surface, is attached to the sidewall of the donut which is itself initially filled with denser fluid ($\rho_2 > \rho_1$). A strong nudging term within the estuary (but not within the annulus!) maintains a supply of light water within the estuary throughout the simulation.

For consistency with the laboratory experiments, in which no horizontal momentum is introduced with the light water, the injection of buoyant fluid in *ROMS* is allowed to take place by gravitational adjustment. At the initial instant, there exists a vertical density front between the cap of fresh water in the estuary and the adjacent dense water in the annulus. This front is gravitationally unstable and, once allowed to evolve in time, slumps into the annulus, producing

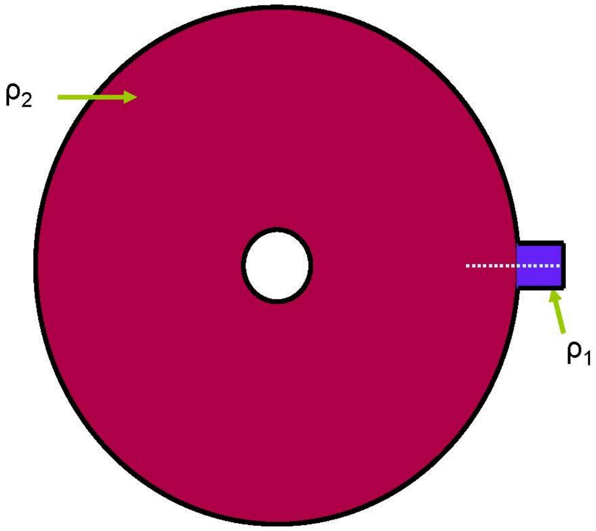

(a) Top view of the *ROMS* configuration.

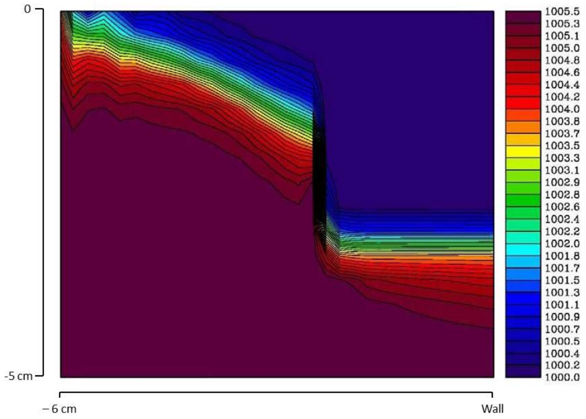

(b) Vertical section of density taken along the dashed line in Figure 6.1a. The x-axis is along the radial direction, and the y-axis is along the vertical direction. Color bar is for density (in $kg\ m^{-3}$). Only the upper 5 cm of the water column is shown.

Figure 6.1: *ROMS* configuration.

a source of buoyancy just outside the mouth of the estuary[‡] (Figure 6.1b). The rate of buoyancy injection (i.e., the analogue of q_0 in the laboratory frame) is therefore not an independently specified parameter in this approach. However, it may be determined *a posteriori*[§].

As discussed further below, simulations with *ROMS* were conducted both with and without explicit levels of horizontal viscosity (The value of diffusivity in the density equation was set to zero in all cases.). The sidewall boundary conditions in the momentum equations are either free-slip (without viscosity) or no-slip (non-zero viscosity). No-flux sidewall boundary conditions are applied in the density equation.

The *ROMS* simulations were conducted at Rutgers University by Pr. Dale Haidvogel and Dr. Ezgi Taskinoglu[¶], however the data analysis of the numerical simulations was performed by the author of this thesis. The numerical solutions are obtained on a polar grid having 128 points (stretched towards the outer annular wall) in the radial direction and 512 points around the circumference; 60 equally spaced levels are used in the vertical direction. The finest resulting grid spacing is of order two millimeters. The required time step used for the simulations was two milliseconds. This is the smallest-scale application thus far produced with *ROMS*.

6.2 Flow rate extraction

As was specified in 6.1, the volumetric flow rate in *ROMS* is not an independent specified parameter. Thus, its value has to be determined from the output data files for the different simulations. To get a value for the flow rate, the volume-averaged density, ρ_{mean}, has to be computed first, from the output data files, in the annulus (excluding the estuary) as a function of time. With this quantity, the volume of buoyant freshwater added in the annulus can be found.

Assuming that an equal amount of dense water is being subtracted while the buoyant water is added, at any given time, the volume-averaged density, ρ_{mean}, is given by:

[‡] Note that there is no net source of mass, as in the laboratory setting. Buoyant fluid is discharged from the estuary at the surface, and denser ambient water enters the estuary at depth. Surface density in the estuary is kept fresh by the density nudging term.

[§] Since the rate of buoyancy injection is not independently prescribed, the values of the dimensionless parameter I cannot be matched *a priori* to those of the laboratory experiments.

[¶] SRA International, Inc., 1201 New Road, Linwood, NJ 08221, USA

$$\rho_{mean} = \frac{(V - dV)\rho_2 + dV\rho_1}{V}, \tag{6.1}$$

where V is the volume in the annulus (excluding the estuary), dV is the volume of buoyant freshwater added in the annulus, ρ_2 and ρ_1 are the density values for the dense and buoyant waters, respectively.

By rearranging (6.1), the volume of freshwater added in the annulus at a given time is expressed as:

$$dV = V\left(\frac{\rho_2 - \rho_{mean}}{\rho_2 - \rho_1}\right). \tag{6.2}$$

With this information, the rate at which the freshwater is added per unit of time can be estimated. Figures 6.2a-c display the volume-averaged density, ρ_{mean}, departing from its background value as a function of time, the volume of freshwater, dV, added in the annulus as a function of time, and the rate, Q_{FW}, at which the freshwater is added in the annulus as a function of time, respectively, for one specific run.

In each laboratory experiment, the flow rate is kept constant. In order to compare *ROMS* with the laboratory experiments and therefore to have a constant value characterising the flow rate in the different simulations, the mean of the flow rate, Q_{FW}, for each run, is taken to be this constant value.

6.3 Data extraction methods

In the next chapter, the results for the plume length, width and velocity obtained in the *ROMS* simulations are presented and compared to laboratory experiments.

The nose displacement of the coastal currents in *ROMS* was extracted from the surface density field, as follows. First, the background density value was subtracted from the surface density field, for each time step. Thus non-zero values of the density anomaly on the surface defined the coastal current. Then, for each time step, the maximum azimuthal location of a negative density anomaly, proceeding in the direction of plume propagation, defined the azimuthal location of the plume head. The *ROMS* plume length data are compared to the small-scale experimental data of Thomas & Linden (2007) (see their paper for data extraction details for the plume length).

The width of the coastal plumes in *ROMS* was extracted in a similar fashion

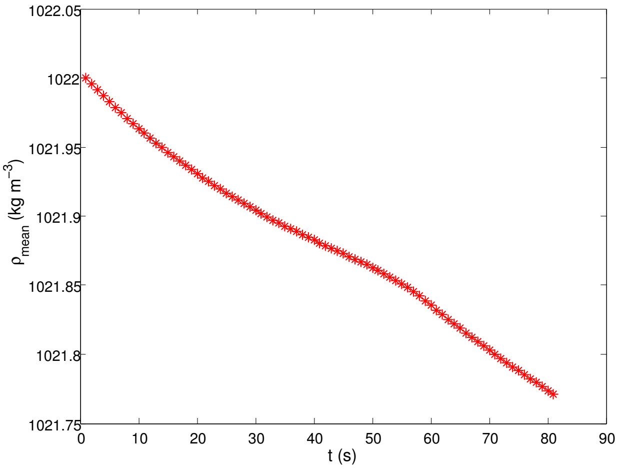

(a) Volume-averaged density, ρ_{mean}, departing from its background value as a function of time, t.

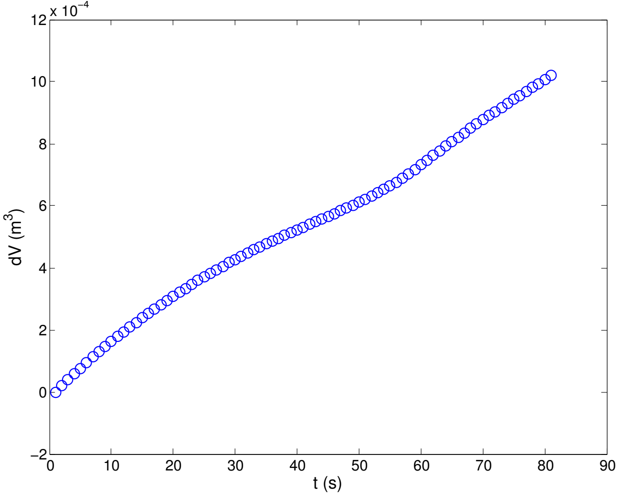

(b) Volume of freshwater, dV, added in the annulus as a function of time, t.

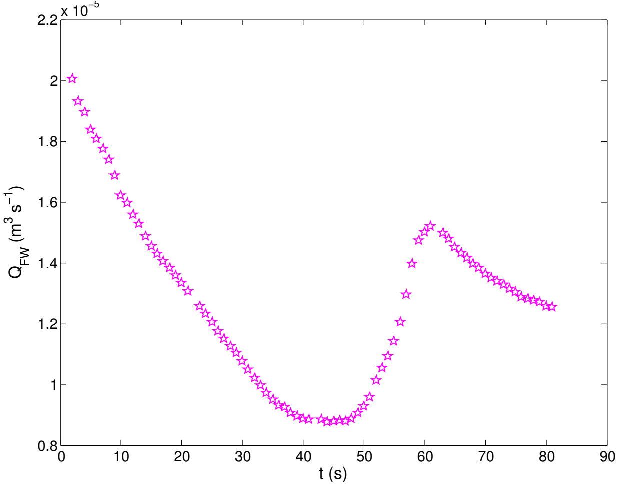

(c) Rate, Q_{FW}, at which the freshwater is added in the annulus as a function of time, t.

Figure 6.2: The different steps to find the flow rate in the *ROMS* simulations; the figures display results for one specific run (plume 153, Table 7.1).

to the length, that is, from the surface density field. First, the background density value was subtracted from the surface density field, for each time step. Then, at one fixed azimuthal position, for each time step, the maximum radial location of a negative density anomaly, proceeding in the direction of the annulus center, defined the width. The $ROMS$ plume width and surface velocity data are compared to the PIV experimental data presented in 5.1.2.

6.4 Comparison between the numerical, experimental and theoretical approaches

The geostrophic theory, the laboratory experiments and the numerical simulations all differ somewhat in their formulation and assumptions. For example, the theory is for steady, inviscid flow, makes no specification of how the buoyant water is introduced, and ignores bulge formation entirely. The laboratory and numerical models are both able to offer a more complete picture of the combined bulge / coastal current system, but they too differ in several respects, most notably in how they introduce their buoyant flows. Table 6.1 summaries several specific attributes of the three approaches. An interesting issue addressed in the next chapter is just how robust the plume properties are in the face of these differing methodological choices and assumptions.

Method	Theory	Experiment	$ROMS$
Forcing	Unspecified	Vertical injection	Estuarine adjustment
Specified mass flux?	yes $\int u \times area\ plume$	yes	no
Specified buoyancy rate?	yes	yes	no
Dynamics	Geostrophic	Real fluid	Discretized hydrostatic PE
Viscosity	Inviscid	Finite Ekman number	Inviscid or finite Ekman number

Table 6.1: Summary of the characterizations for the theory, the laboratory experiments and the $ROMS$ simulations.

Part III

Numerical Study

CHAPTER 7

ROMS simulations

The theory of Thomas & Linden (2007) assumes an inviscid ocean. To begin, *ROMS* was therefore configured with zero explicit horizontal viscosity (By virtue of its spatial and temporal discretization, *ROMS* carries some implicit smoothing. It is therefore possible to conduct simulations with explicit values of horizontal viscosity and diffusivity set to zero.). Ten "inviscid" experiments were run. In order to match the laboratory experiments, simulations with the lateral viscosity set to the molecular value of 10^{-2} cm^2 s^{-1} were also conducted. Seven "viscous" experiments were carried out. These seven numerical simulations precisely duplicate seven of the inviscid simulations, except for the inclusion of lateral viscosity. The parameters for the *ROMS* experiments are summarized in Table 7.1 and their values, listed in order, are the bottom slope, α (°), the Coriolis parameter, f (s^{-1}), the reduced gravity anomaly, $g\prime$ (cm s^{-2}), the averaged flow rate, q_0 (cm^3 s^{-1}), the ambient ocean depth, H_D (cm), the theoretical plume depth, h_0 (cm), the theoretical plume width, w_0 (cm), the dimensionless parameter, I, the horizontal Ekman number, Ek_H, the vertical Ekman number, Ek_V, the Reynolds number, Re, and the non-dimensional ambient depth parameter, h_0/H_D. The ambient ocean depth, H_D, in the inviscid and viscous numerical simulations was sufficient (except for the simulation number 136) to ensure that the plume properties were not affected by the bottom of the annulus. Therefore this chapter is only concerned about the simple case of a surface-advected plume moving along a straight coastline.

Plume	118	120	125	126	128	130
α	90	90	90	90	90	90
f	1	1	2	3	3	3
g'	5.4	21.6	5.4	5.4	21.6	43.2
q_0	9	20.97	5.03	3.54	11.12	22.17
H_D	12.5	12.5	12.5	12.5	12.5	12.5
h_0	1.83	1.39	1.93	1.98	1.76	1.75
w_0	4.44	7.76	2.28	1.54	2.9	4.1
I	0.282	0.145	0.502	0.702	0.384	0.291
Ek_H	0	0	0	0	0	0
Ek_V	3×10^{-3}	5.15×10^{-3}	1.34×10^{-3}	8.47×10^{-4}	1.08×10^{-3}	1.08×10^{-3}
Re	∞	∞	∞	∞	∞	∞
h_0/H_D	0.15	0.11	0.15	0.16	0.14	0.14
Plume	131	132	134	136	148 (126)	149 (131)
α	90	90	90	90	90	90
f	1	2	2	3	3	1
g'	43.2	43.2	21.6	32.4	5.4	43.2
q_0	30.54	28.97	15.91	10.27	3.5	31.23
H_D	12.5	12.5	12.5	3	12.5	12.5
h_0	1.19	1.64	1.72	1.38	1.97	1.2
w_0	10.14	5.95	4.31	3.15	1.54	10.19
I	0.103	0.205	0.275	0.297	0.701	0.104
Ek_H	0	0	0	0	1.41×10^{-3}	9.63×10^{-5}
Ek_V	7.07×10^{-3}	1.86×10^{-3}	1.7×10^{-3}	1.75×10^{-3}	8.57×10^{-4}	6.92×10^{-3}
Re	∞	∞	∞	∞	266	3896
h_0/H_D	0.1	0.13	0.14	0.11	0.16	0.1
Plume	150 (134)	151 (125)	152 (118)	153 (128)	155 (130)	
α	90	90	90	90	90	
f	2	2	1	3	3	
g'	21.6	5.4	5.4	21.6	43.2	
q_0	16.2	5.04	9.47	12.76	15.97	
H_D	12.5	12.5	12.5	12.5	12.5	
h_0	1.73	1.93	1.87	1.88	1.49	
w_0	4.32	2.28	4.5	3.01	3.78	
I	0.276	0.502	0.285	0.395	0.273	
Ek_H	2.67×10^{-4}	9.59×10^{-4}	4.94×10^{-4}	3.69×10^{-4}	2.33×10^{-4}	
Ek_V	1.67×10^{-3}	1.34×10^{-3}	2.85×10^{-3}	9.4×10^{-4}	1.5×10^{-3}	
Re	1403	391	759	1017	1609	
h_0/H_D	0.14	0.15	0.15	0.15	0.12	

Table 7.1: Experimental parameters of the *ROMS* simulations: plumes 118 to 136 have no lateral viscosity while plumes 148 to 155 have the lateral viscosity set to the molecular value of 10^{-2} cm^2 s^{-1}.

7.1 Introductory Remarks

As discussed in Section 6.2, *ROMS* internally determines its own buoyancy injection rate, the analogue of q_0*. One can anticipate that the value of q_0 in *ROMS* will depend on the values of the other experimental parameters, the rotation rate, Ω, and the reduced gravity, $g\prime$. From Table 7.1, q_0 is seen to increase as Ω decreases and as $g\prime$ increases. One final experiment, plume 136, was conducted in which the depth of the annulus/estuary was reduced from 12.5 *cm* to 3.0 *cm*, with no accompanying reduction in the thickness of the freshwater cap in the estuary. The resulting value of q_0 (Table 7.1) is suggestive of a dependence on depth. However, this possibility has not been pursued. The value of the flow rate did not change appreciably by the addition of lateral viscosity.

7.2 Qualitative aspects of the coastal currents

Figure 7.1(a) is a picture of a laboratory experiment from Thomas & Linden (2007), obtained with the video camera mounted on the rotating turntable, which shows a plume viewed from above the circular tank, looking vertically downwards onto the fluid surface. The dyed coastal current appears dark on the picture. Figure 7.1(b) is a picture from an inviscid numerical simulation, which displays the density field at the surface. A comparison of the pictures in Figures 7.1(a)-(b) reveals a great degree of qualitative similarity. The buoyancy-driven flows are, in both cases, characterized by a stationary “bulge” of fresh water retained near the buoyant outflow, and a propagating plume of fresh water. In both settings, the Coriolis parameter is positive; therefore the turntables rotate cyclonically, as do the plumes, keeping the wall to their right.

In both the laboratory and numerical observations, when the source is turned on a buoyant outflow disperses along the coastline. This outflow can be decomposed into a growing anti-cyclonic bulge and a coastal plume flowing downstream of the bulge. For some experimental parameters combinations, the rate of elongation of the plumes shows little decrease during the whole experiment, while for some other experimental parameter combinations, the coastal plume is observed to accelerate at the start of the experiment, then to decelerate to a nearly constant propagation speed. Finally, for some experiments, instabilities are seen to form

---

*Henceforth, referred to this simply as q_0.

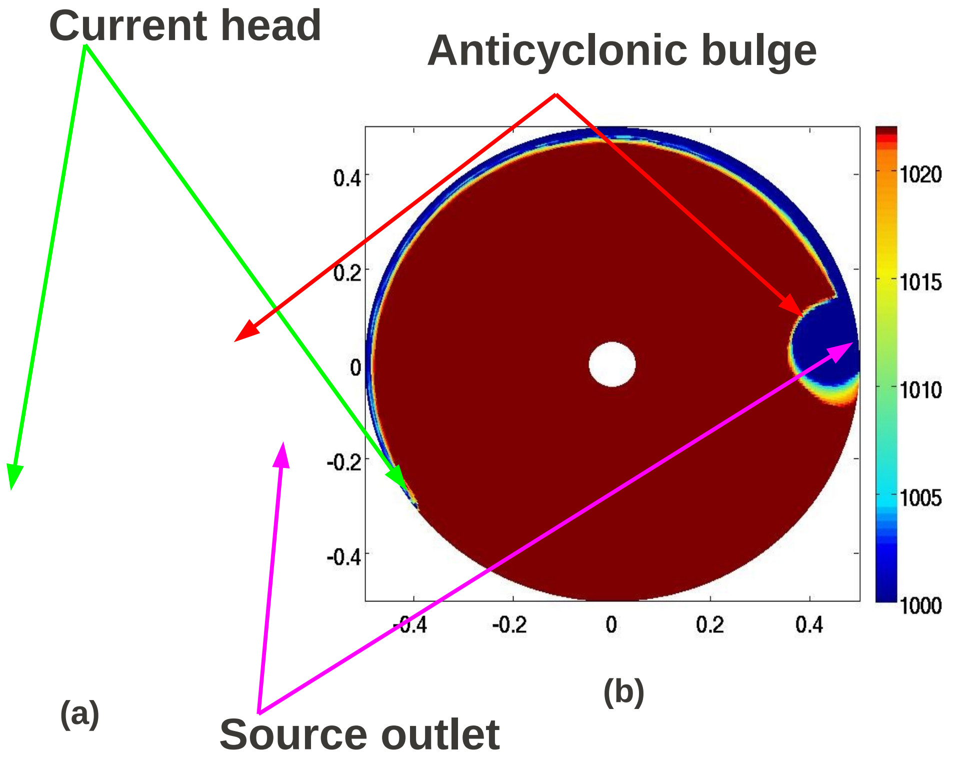

Figure 7.1: Top view of a coastal current simulated, (a) in the laboratory, (b) numerically. The images are taken at T=30. $I = 0.301 \pm 0.026$, $Ek_V = (1.4 \pm 0.3) \times 10^{-3}$, $ROMS$: $Ek_H = 0$, Laboratory experiment: $Ek_H = 2.68 \times 10^{-4}$. In (b), the color bar is for density(in $kg\ m^{-3}$).

and evolve along the edge of the buoyant plumes. These features are illustrated next, and their dynamical implications are pursued below in Chapter 8.

7.3 Coastal current length

Figure 7.2a and Figure 7.3a show raw data for the plume length, l, as a function of time, t, for the inviscid and viscous numerical experiments, respectively, while Figure 7.2b and Figure 7.3b redisplay the data in non-dimensional form. In Figure 7.2b and Figure 7.3b, data are non-dimensionalized by w_0 and the solid line superposed on the figures is the theoretical prediction of Thomas & Linden (2007), namely, $L = (3/4)T$. The majority of the numerical experiments were terminated when the plume nose got back to the source. The remaining cases – plumes 118, 125, 126, 148 and 152 – were stopped before the plume re-entered the source region.

The experiments of Thomas & Linden (2007) showed that the plume speed increases when increasing the values of the flow rate, q_0, the rotation rate, Ω, and the reduced gravity, $g\prime$. From Figure 7.2a and Figure 7.3a, and from Table 7.1, increasing the values of $g\prime$ and q_0 increases the plume speed, in agreement with theory.

A comparison between Figure 7.2 and Figure 7.3 reveals that while in Figure 7.2 the velocity of all the plumes shows little diminution during the plume propagation along the annulus, the plume velocity in Figure 7.3 is consistently higher in the vicinity of the source than further downstream (as it was also observed in the simulations of Chao & Boicourt (1986)) and plumes slow down substantially during the simulations (especially for the plumes 148 and 151 which have the lowest flow rate, in agreement with the experimental findings of Thomas & Linden (2007)).

Figure 7.4 compares the simulations with lateral viscosity to their corresponding inviscid numerical simulations and to the small-scale laboratory experiments and the geostrophic model of Thomas & Linden (2007) for the non-dimensional plume length, L. Experiments with similar values for the parameter I, the horizontal and vertical Ekman numbers, Ek_H and Ek_V, respectively, are expected to be analogous. Details of the small-scale experiments of Thomas & Linden (2007) are listed in Appendix A. The non-dimensionalizing factor of Ω for the time was different in the *ROMS* and laboratory experiments shown in Figure 7.4b, thus

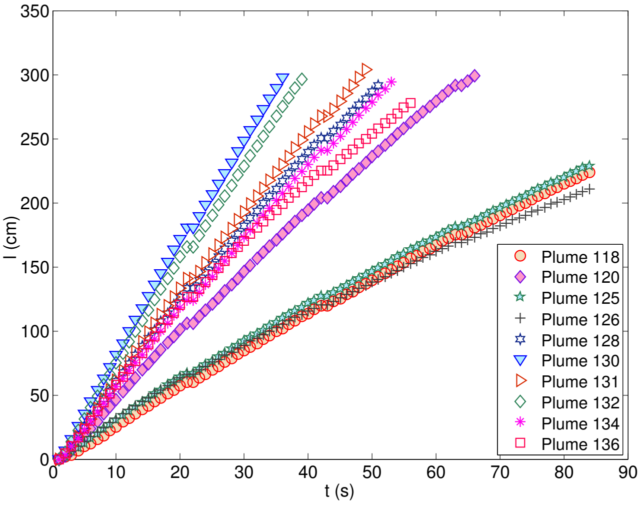

(a) Summary of the plume length, l, as a function of time, t.

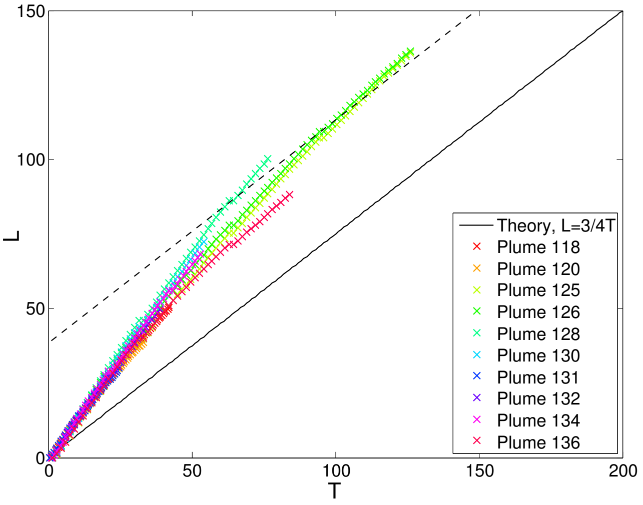

(b) Summary of the non-dimensional plume length, L, as a function of the non-dimensional time, T. The solid line represents the theoretical prediction, $L = (3/4)T$, of Thomas & Linden (2007). The dashed line is parallel to the theoretical prediction, shifted upwards to facilitate visual comparison with the numerical results.

Figure 7.2: Nose propagation of the inviscid plumes.

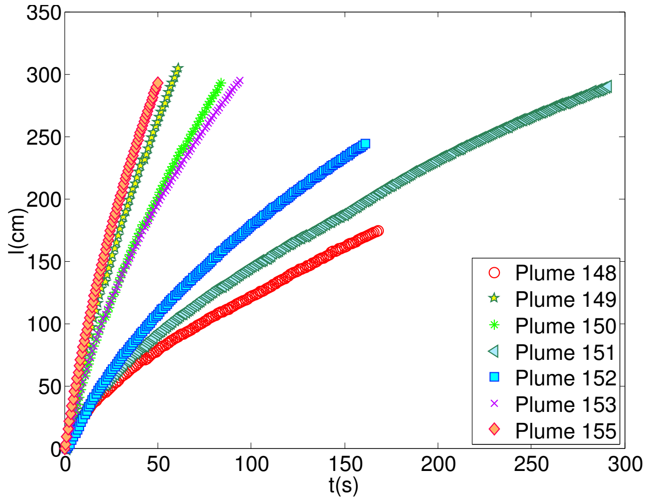

(a) Summary of the plume length, l, as a function of time, t.

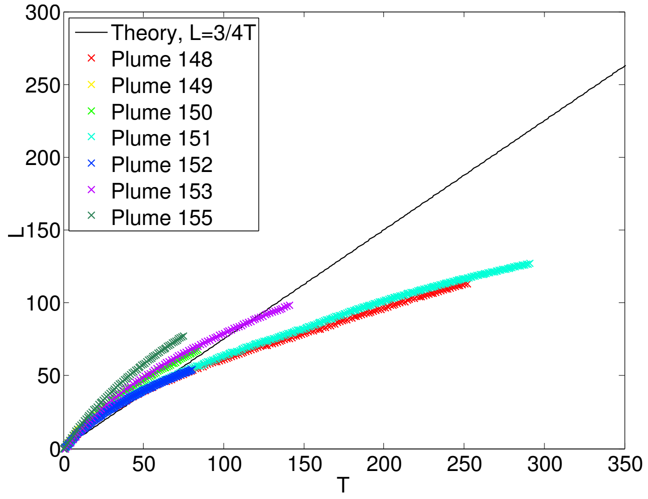

(b) Summary of the non-dimensional plume length, L, as a function of the non-dimensional time, T. The solid line represents the theoretical prediction, $L = (3/4)T$, of Thomas & Linden (2007).

Figure 7.3: Nose propagation of the viscous plumes.

explaining why the curves of the *ROMS* experiments for the plume length are shorter than the curve of the laboratory experiment.

From Figure 7.2b and Figure 7.4, two conclusions may be drawn. First, the rate of elongation of the plumes in the inviscid simulations always exceeds the estimate given by the geostrophic theory. Second, the non-dimensional plume lengths in the inviscid simulations are comparable to the laboratory experiments with very low values for the horizontal Ekman number, however plumes from the inviscid simulations have a more rapid rate of elongation than plumes from the laboratory experiments (Figure 7.4a).

To quantify the speed at which the inviscid plumes advance, a single data fit of the form $L = a + bT$ for the dimensionless time, T, was computed for four of the ten numerical simulations, when the plume flows at a nearly constant speed. The constant b in the fit is simply the plume speed. The plumes reach a nearly steady velocity around $T = 60$. Therefore the fit was computed for the four numerical simulations for which data exists for $T \geq 60$. From the values determined for a and b, averages and associated standard deviations were then calculated to find an averaged fit, $L = (21.32 \pm 3.75) + (0.91 \pm 0.12)T$. The value of the constant b, for the fit $L = a + bT$ in the *ROMS* inviscid numerical simulations, differs from the theoretical value of 3/4 by approximately +20%.

From Figure 7.3b and Figure 7.4, the simulations with the lateral viscosity set to the molecular value no longer follow the geostrophic theory, but rather reproduce the results of the laboratory experiments. The discrepancies between the geostrophic model and the viscous numerical simulations (and therefore the laboratory experiments) are most significant when the lateral viscous forces are the greatest (that is for high values of the horizontal Ekman number, Ek_H).

7.4 Coastal current width

Figures 7.5(a)-(b) display the non-dimensional plume width, W, as a function of the dimensionless time, T, measured at the non-dimensional distance, D_S, downstream from the source, with $D_S = 12$, for all the inviscid and viscous numerical simulations, respectively, while Figure 7.6 displays the non-dimensional plume width, W, as a function of the dimensionless time, T, measured at the distance, d_S, downstream from the source, with $d_S = 57.8\ cm$, for all the *PIV* vertical-wall experiments. Width data are non-dimensionalized by w_0. The width

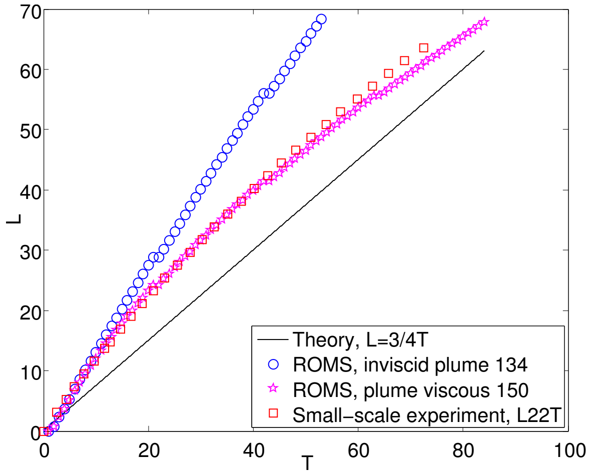

(a) $I = 0.3 \pm 0.033$, $Ek_V = (1.46 \pm 0.32) \times 10^{-3}$, L22T & plume 150: $Ek_H = (2.73 \pm 0.06) \times 10^{-4}$, plume 134 : $Ek_H = 0$.

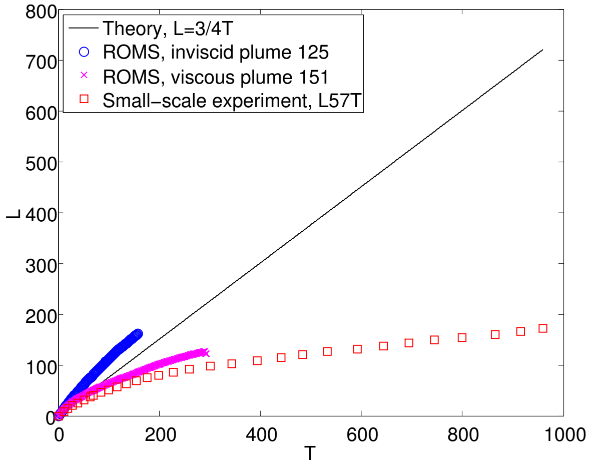

(b) $I = 0.542 \pm 0.057$, $Ek_V = (1.26 \pm 0.03) \times 10^{-3}$, L57T & plume 151: $Ek_H = (1.16 \pm 0.2) \times 10^{-3}$, plume 125 : $Ek_H = 0$.

Figure 7.4: Comparison of the non-dimensional plume length, L, as a function of the non-dimensional time, T, for inviscid and viscous numerical simulations, and laboratory experiments of Thomas & Linden (2007). The solid line represents the theoretical prediction, $L = (3/4)T$.

measurements for the laboratory experiments were done at a fixed (dimensional) distance downstream from the source (instead of a fixed non-dimensional distance downstream from the source as for the numerical simulations) to facilitate data extraction and comparison between each laboratory experiment. For some numerical and laboratory experiments, width measurements were stopped before the end of the experiments due to the presence of instabilities in the plumes. Width data from two laboratory experiments are not displayed in Figure 7.6 as one experiment was too unstable and width extraction was not possible, and one experiment had data not usable.

In the majority of the laboratory and numerical experiments, the plume widths continue to increase and do not approach a steady value over the duration of each experiment. From Figures 7.5(a)-(b) and Figure 7.6, the non-dimensional width measurements closely cluster around a single curve, growing as $T^{\frac{1}{2}}$ (as Lentz & Helfrich (2002) and Thomas & Linden (2007) also found).

Of the ten inviscid numerical simulations and of the seven viscous numerical simulations, nine inviscid numerical simulations and six viscous numerical simulations could be compared to the PIV experiments as one inviscid and one viscous simulation had no available laboratory experiment comparable to it. Figures 7.7(a)-(b) show the non-dimensional plume width, W, as a function of the dimensionless time, T, measured at the non-dimensional distance, D_S, downstream from the source, with $D_S = 28.8$ and $D_S = 10$, respectively, for one inviscid simulation, one viscous simulation, and one PIV laboratory experiment. In Figure 7.7a, the laboratory and numerical experiments have a large Ek_H value while in Figure 7.7b, the laboratory and numerical experiments have a small Ek_H value. The width measurements of the numerical and laboratory experiments from Figure 7.7a were stopped before the end of the experiments due to the presence of instabilities in the plumes. The non-dimensionalizing factor of Ω for the time was different in some of the compared cases, thus leading to different non-dimensional curve lengths for the width. The overall agreement between the inviscid and viscous simulations and the laboratory experiments is found to be quite good (even if the plumes with high Ek_H values from the numerical simulations cross the measurement position before the plumes from the laboratory experiments). A comparison between the non-dimensional widths for the inviscid and viscous numerical simulations reveals that adding lateral viscosity does not change very much the plume width, but it seems that at later times, plume width in the viscous simulations grows larger than plume width in the inviscid

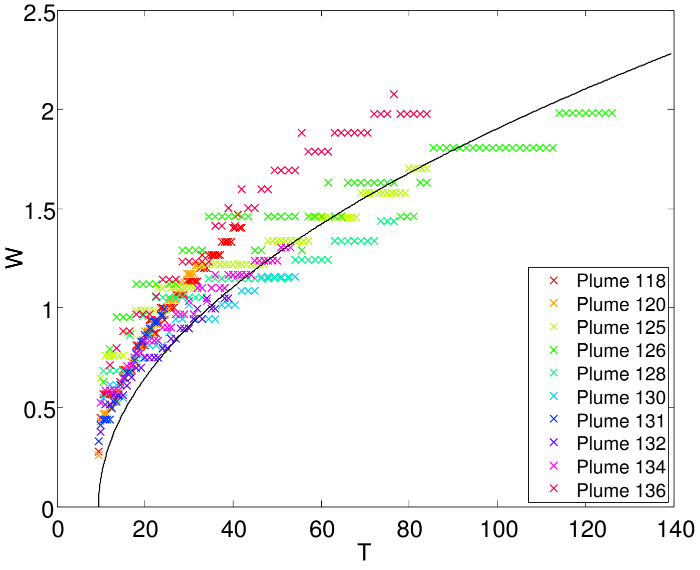

(a)

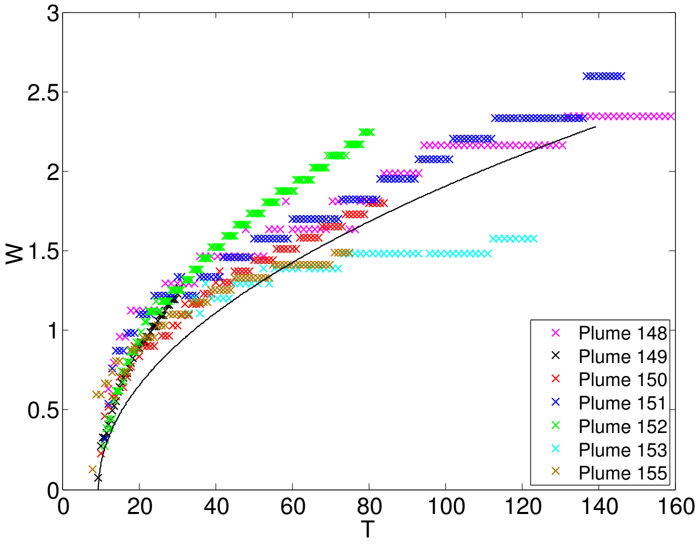

(b)

Figure 7.5: Summary of the non-dimensional plume width, W, as a function of the dimensionless time, T, for (a) all the inviscid numerical simulations and (b) all the viscous numerical simulations. The width was measured at the non-dimensional distance, D_S, downstream from the source, with $D_S = 12$. The black curve on the figures of equation $0.2(T)^{\frac{1}{2}}$ is just to show that plume widths grow as $T^{\frac{1}{2}}$.

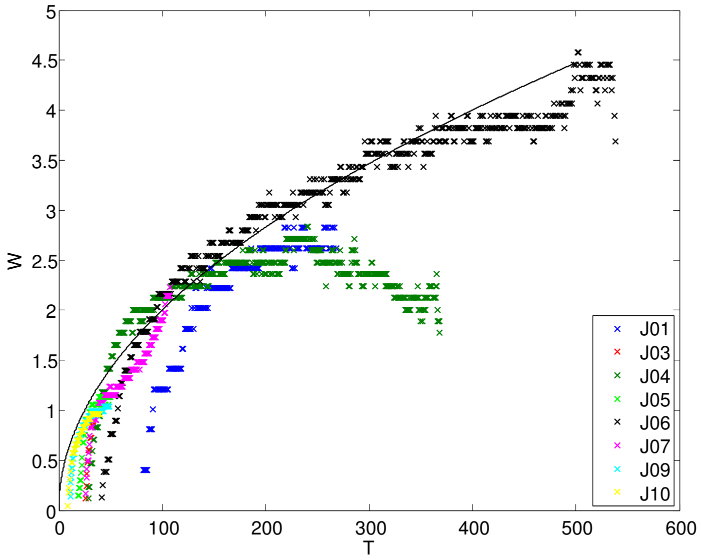

Figure 7.6: Summary of the non-dimensional plume width, W, as a function of the dimensionless time, T, for the PIV vertical-wall experiments. The width was measured at the distance, d_S, downstream from the source, with $d_S = 57.8\ cm$. The black curve on the figure of equation $0.2(T)^{\frac{1}{2}}$ is just to show that plume widths grow as $T^{\frac{1}{2}}$.

simulations.

Figures 7.8(a)-(b) display a summary of the values for the non-dimensional plume width, W, as a function of the dimensionless parameter, I, and the horizontal Ekman number, Ek_H, respectively, for the inviscid and viscous $ROMS$ simulations from Figures 7.5(a)-(b), and for the PIV laboratory experiments from Figure 7.6. The black line on the figures identifies $W = 1$, $i.e$ agreement between experiments and theory. To quantify the non-dimensional plume width, W, in Figures 7.8(a)-(b), W was averaged for each experiment from the last data point to the data point such that the non-dimensional time interval, ΔT, of the measurements, was $10 < \Delta T < 60$ in the numerical simulations and $10 < \Delta T < 250$ in the laboratory experiments (the non-dimensional time interval length depended on the experiment duration). The standard deviation was calculated for each value found for W.

From Figures 7.8(a)-(b), W increases as I and Ek_H increase. Despite the important experimental data scatter, best agreement between the theory and, the laboratory and numerical experiments, for the plume width, is found for plumes with low I and Ek_H values. These results are consistent with the results of Thomas & Linden (2007) who also found that the best agreement between

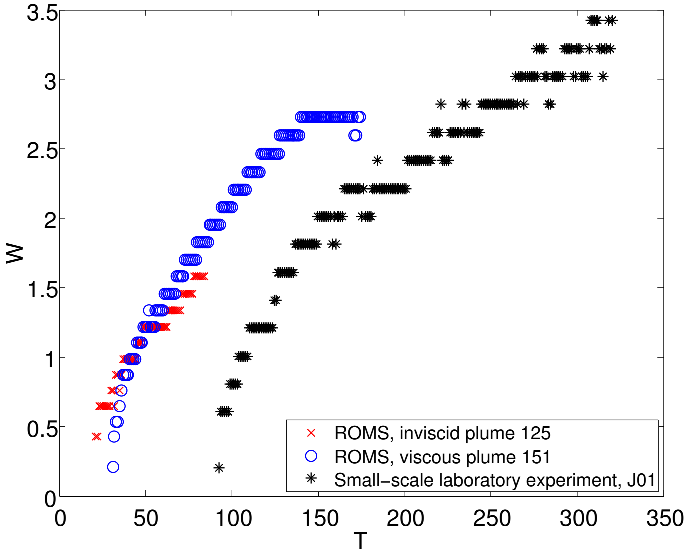

(a) $I = 0.558 \pm 0.08$, $Ek_V = (1.26 \pm 0.11) \times 10^{-3}$, Inviscid simulation: $Ek_H = 0$, Viscous simulation and laboratory experiment: $Ek_H = (1.29 \pm 0.34) \times 10^{-3}$.

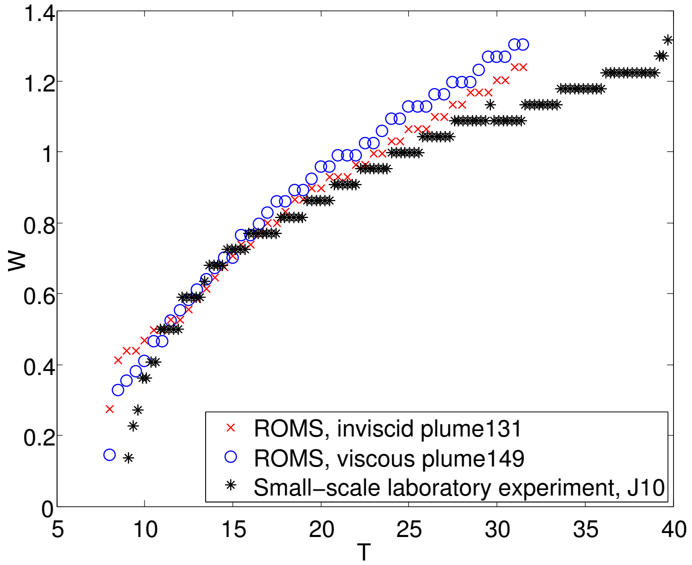

(b) $I = 0.126 \pm 0.03$, $Ek_V = (5.73 \pm 1.79) \times 10^{-3}$, Inviscid simulation: $Ek_H = 0$, Viscous simulation and laboratory experiment: $Ek_H = (1.26 \pm 0.29) \times 10^{-4}$.

Figure 7.7: Comparison of the non-dimensional plume width, W, as a function of the dimensionless time, T, between one inviscid numerical simulation, one viscous numerical simulation and one laboratory experiments. The width was measured at the non-dimensional distance, D_S, downstream from the source, with (a) $D_S = 28.8$ and (b) $D_S = 10$.

their small-scale experiments and their theory for the plume width was met for plumes with low I values and large Re values (at least for the largest Re values from their small-scale study), where Re is the Reynolds number defined in (4.7). However from (4.10), large Re value is equivalent to small Ek_H value (as Re is inversely proportional to Ek_H). This study using PIV measurements for the plume width recovers the same results than the study of Thomas & Linden (2007) who used dye visualization for the plume width measurements.

7.5 Coastal current velocity

In order to compare the theoretical geostrophic velocity to the inviscid and viscous numerical simulations, one look at the ratio, $U_{max} = \frac{u_{max}}{u_0}$, of the numerical/experimental maximum surface velocity, u_{max}, to the theoretical velocity, u_0. The maximum surface velocity, u_{max}, is measured at a fixed azimuthal position downstream from the source, for each time step. Thus at early time, the maximum surface velocity is extracted from the plume nose and at later time, it is extracted from the coastal plume. The measurement position is far enough from the source so by the time the plume crosses it, the plume is supposed in geostrophic equilibrium.

Figures 7.9(a)-(b) display the maximum non-dimensional plume velocity, U_{max}, as a function of the dimensionless time, T, measured at the surface and at the non-dimensional distance, D_S, downstream from the source, with $D_S = 12$, for all the inviscid and viscous numerical simulations, respectively, while Figures 7.10(a)-(b) display the maximum non-dimensional plume velocity, U_{max}, as a function of the dimensionless time, T, measured at the surface and at the distance, d_S, downstream from the source, with $d_S = 57.8\ cm$, for all the PIV vertical-wall experiments of Figure 7.6. The PIV experiments were divided in two figures (Figure 7.10(a) for the short experiments and Figure 7.10(b) for the long experiments).

From Figures 7.9(a)-(b), one can see that the maximum value for U_{max} is in the front of the coastal current for the inviscid and viscous numerical simulations, and is much larger than 1 (thus the maximum surface velocity for the numerical simulations is much larger than the geostrophic prediction in the coastal current nose). For some numerical simulations (e.g. plumes 118, 152), U_{max} decreases along the whole plume, while for some other numerical simulations (e.g. plumes

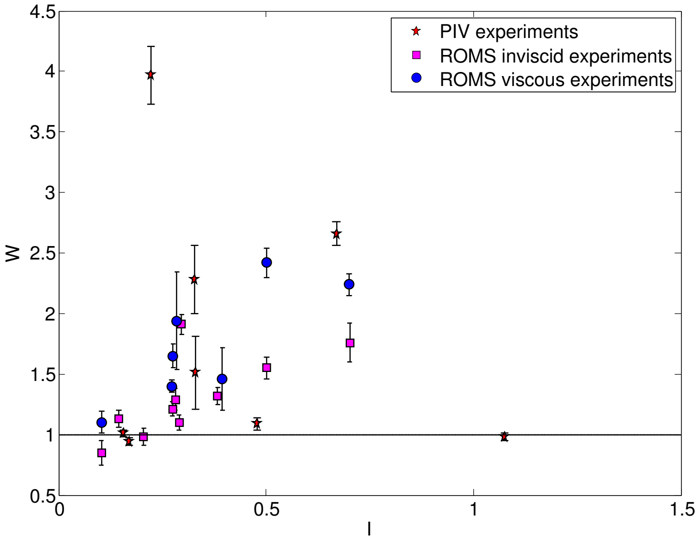

(a)

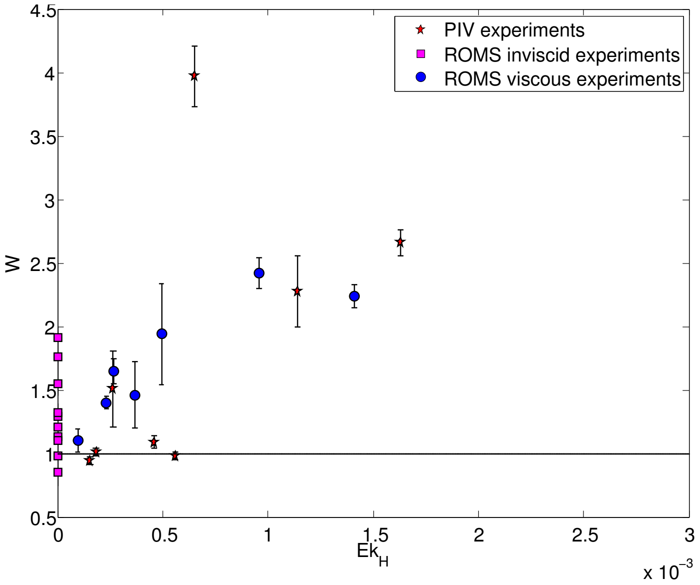

(b)

Figure 7.8: Summary of the (averaged) non-dimensional plume width, W, as a function of (a) the dimensionless parameter, I, and (b) the horizontal Ekman number, Ek_H, respectively, for the viscous and inviscid numerical simulations, and for the PIV laboratory experiments. The black line on the figures identifies $W = 1$, that is agreement between experiments and theory. The error bars are standard deviation errors of the averaged non-dimensional plume width.

136, 153), U_{max} decreases until it reaches a nearly constant value located inside the coastal current. In contrast to the numerical results, the minimum value of U_{max} for the laboratory experiments (minimum value which is much smaller than 1) is found in the coastal current nose (Figures 7.10(a)-(b)) and there U_{max} increases until it reaches its maximum value located just behind the nose. After U_{max} has reached its maximum value, for some laboratory experiments (*e.g* experiment $J04$) U_{max} decreases along the whole plume while for some other laboratory experiments (e.g. experiments $J01$, $J07$) U_{max} decreases to attain a nearly constant value. For the unstable numerical and laboratory experiments (e.g. plumes 126, 151 or experiments $J03$, $J05$), the maximum velocity does not reach a constant value but instead is seen to fluctuate along the coastal current.

Figure 7.11 displays the maximum non-dimensional plume speed, U_{max}, as a function of the dimensionless time, T, measured at the dimensionless distance, D_S, downstream from the source, with $D_S = 10$, for one inviscid and one viscous simulation, and for one PIV laboratory experiment. The measurements were taken at the freshwater surface for the laboratory experiment and the viscous simulation, and at the freshwater surface ($N = 60$) and around 9 mm below the freshwater surface ($N = 56$) for the inviscid simulation.

For plumes with lower values for the horizontal Ekman number (e.g., plume 149 in Figure 7.11), adding lateral viscosity in the simulations does not significantly influence the value of the maximum velocity, U_{max}, as T evolves. For plumes with higher values for the horizontal Ekman number (e.g. plume 125 in Figure 7.9a and plume 151 in Figure 7.9b), adding lateral viscosity changes the value of the maximum velocity considerably as T evolves: plumes with lateral viscosity have values for U_{max} much lower than the inviscid plumes.

For all the inviscid simulations and for the viscous simulations with the lowest values for the horizontal Ekman number, the maximum velocity is larger than the theoretical prediction at the surface (Figures 7.9(a)-(b)). The value of the maximum velocity was investigated at different vertical levels, and was found to approach the geostrophic velocity, u_0, inside the plume just below the water surface (around 9 mm below the freshwater surface in Figure 7.11). Thus the value of the maximum velocity of the plumes from the inviscid simulations and from the viscous simulations with the lowest values for the horizontal Ekman number lies near the value of the theoretically predicted geostrophic velocity just below the freshwater surface inside the coastal current.

Nine of the ten inviscid numerical simulations and six of the seven viscous

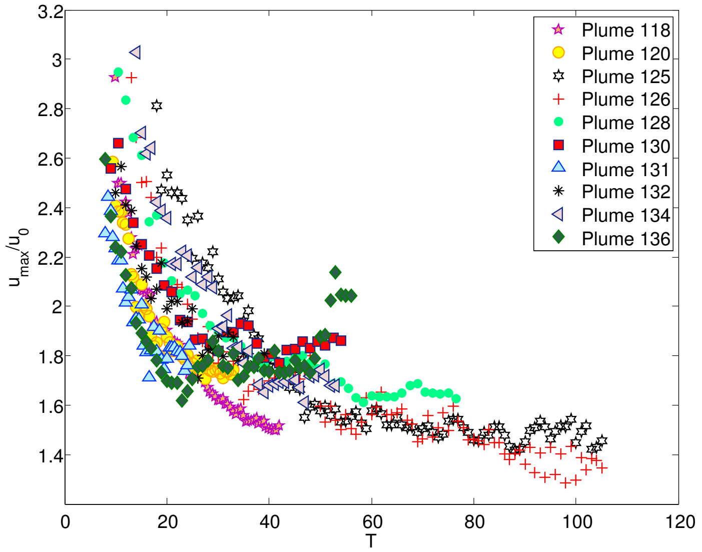

(a)

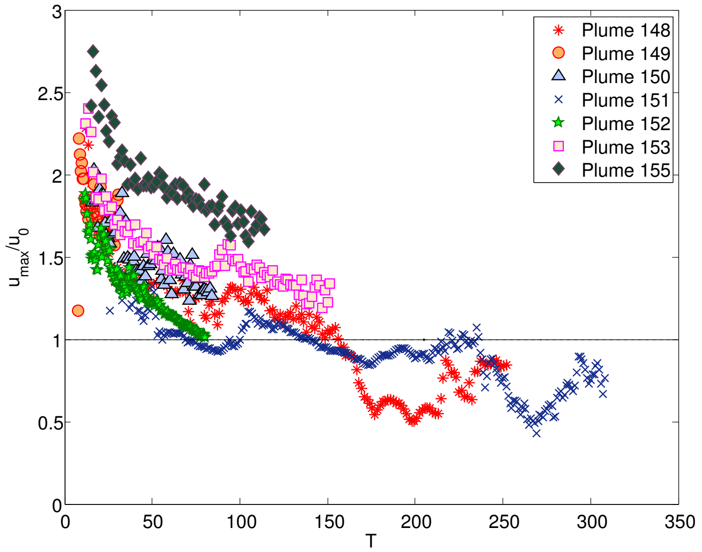

(b)

Figure 7.9: Summary of the maximum non-dimensional plume speed, U_{max}, as a function of the dimensionless time, T, for (a) all the inviscid numerical simulations and (b) all the viscous numerical simulations. U_{max} was measured at the non-dimensional distance, D_S, downstream from the source, with $D_S = 12$. The black line on the Figure 7.9b identifies $U_{max} = 1$, that is agreement between experiments and theory.

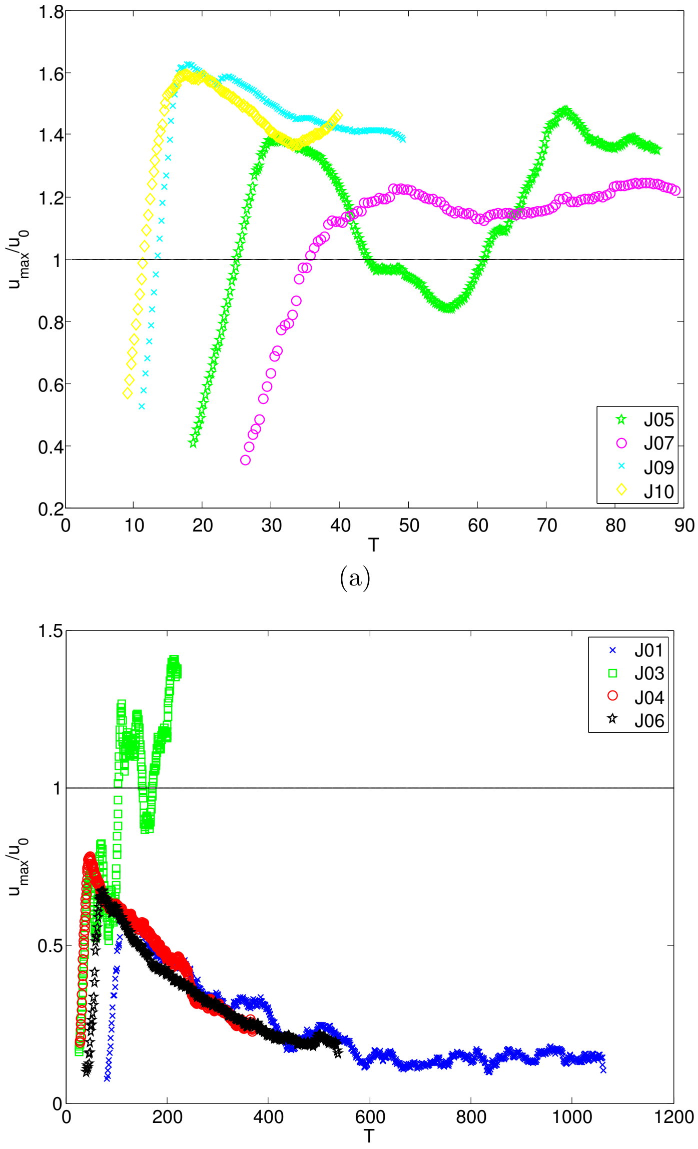

(a)

(b)

Figure 7.10: Summary of the maximum non-dimensional plume speed, U_{max}, as a function of the dimensionless time, T, for the PIV vertical-wall experiments. U_{max} was measured at the distance, d_S, downstream from the source, with $d_S = 57.8\ cm$. The black line on the figures identifies $U_{max} = 1$, that is agreement between experiments and theory.

numerical simulations could be compared to the PIV laboratory experiments. For plumes with the lowest values of the horizontal Ekman number, reasonably good agreement for the maximum velocity is found between the inviscid and viscous simulations, and the laboratory experiments, inside the coastal current (Figure 7.11). As relatively good agreement was found between laboratory experiments and numerical simulations for the maximum plume velocity inside the coastal plume, one might expect from the prior discussion that the maximum velocity from the laboratory experiments with the lowest values for the horizontal Ekman number will also approach the geostrophic velocity just below the water surface. It is interesting to see that the geostrophic equilibrium is obtained (*i.e.* that the maximum velocity reaches a nearly constant value) at the same non-dimensional time in the plume for the inviscid and viscous simulations, and for the corresponding laboratory experiment (Figure 7.11). Less good agreement is found between the inviscid numerical simulations and the laboratory experiments with the highest Ek_H values.

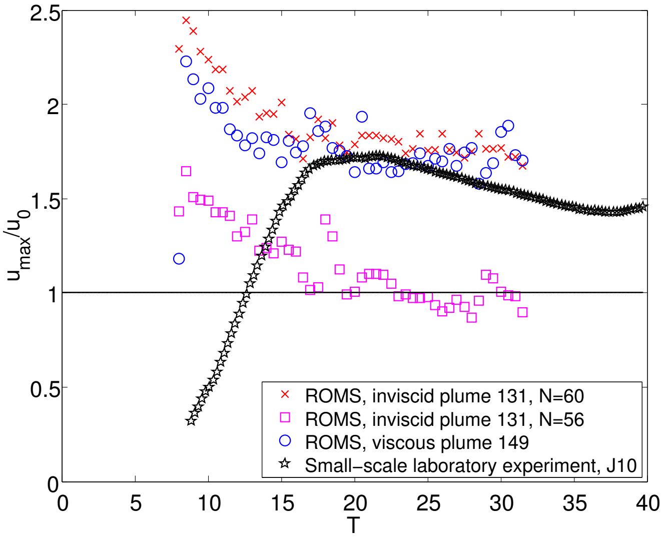

Figure 7.11: Maximum non-dimensional plume speed, U_{max}, as a function of the dimensionless time, T, measured at the non-dimensional distance, D_S, downstream from the source, with $D_S = 10$, for one inviscid simulation, one viscous simulation and one laboratory experiment. U_{max} was measured at the surface for the laboratory experiment and the viscous simulation, and, at the surface ($N = 60$) and around 9 mm below the surface ($N = 56$) for the inviscid simulation. $I = 0.126 \pm 0.03$, $Ek_V = (5.73 \pm 1.79) \times 10^{-3}$, Inviscid simulation: $Ek_H = 0$, Viscous simulation and laboratory experiment: $Ek_H = (1.26 \pm 0.29) \times 10^{-4}$.

Figures 7.12(a)-(b) display a summary of the values for the maximum non-dimensional plume speed, U_{max}, as a function of the dimensionless parameter, I, and the horizontal Ekman number, Ek_H, respectively, for the inviscid and viscous $ROMS$ simulations from Figures 7.9(a)-(b), and for the PIV laboratory experiments from Figures 7.10(a)-(b). The black line on the figures identifies $U_{max} = 1$, *i.e* agreement between experiments and theory. To quantify the maximum non-dimensional plume speed, U_{max}, in Figures 7.12(a)-(b), U_{max} was averaged for each experiment from the last data point to the data point such that the non-dimensional time interval, ΔT, of the measurements, was $15 < \Delta T < 240$ in the numerical simulations and $15 < \Delta T < 200$ in the laboratory experiments (in Figure 7.9, U_{max} for the plume from the laboratory experiment was averaged from $T = 25$, while U_{max} for the plumes from the inviscid and viscous numerical simulations was averaged from $T = 20$.). The standard deviation was calculated for each value found for U_{max}.

Figures 7.12(a)-(b) suggest an underlying dependence on the parameters I and Ek_H, although the dependence on Ek_H is tighter and scatter in the PIV experiments is great in both cases. From the PIV laboratory experiments and most clearly from the viscous numerical simulations displayed in Figure 7.12a, the value of U_{max} decreases as I increases[†].

From Figure 7.12b, it is clear that U_{max} decreases as Ek_H increases. For high values of the horizontal Ekman number, plumes are slower than the theoretical prediction while for very low Ek_H values, the plumes are faster than the theory (in particular, all the inviscid plumes (for which $Ek_H = 0$) are faster than the theory). Figure 7.12b confirms the results obtained in Section 7.3. Combining the results of this section with the preceding section, plumes with large I and Ek_H values, that is deep and narrow plumes in a fluid system in which viscous forces are important, are slower and larger than the theoretical geostrophic prediction, and plumes with small I and Ek_H values, that is wide and shallow plumes in a fluid system in which viscous forces are negligible, are faster than the theoretical prediction.

[†] A figure similar to Figure 7.12a can be constructed from the experiments of Thomas & Linden (2007) for the experimental mean velocity, u_{mean}. Experimental mean plume speed of Thomas & Linden (2007) is found to be slower than the theoretical prediction for the largest values of I (that is for the deepest and the narrowest plumes).

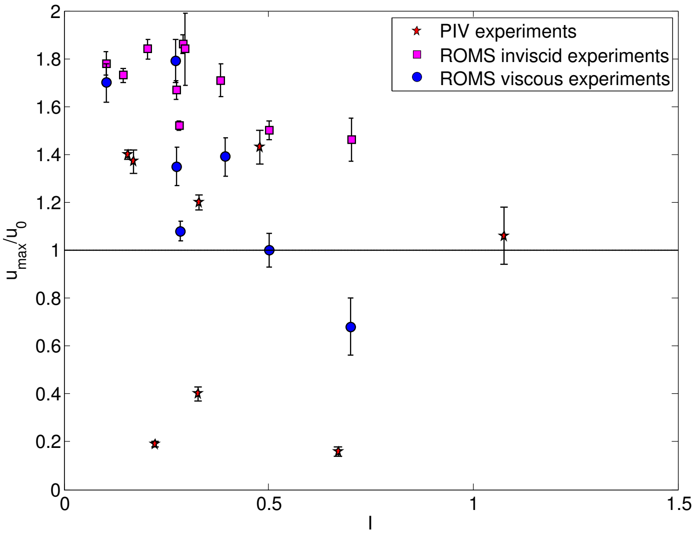

(a)

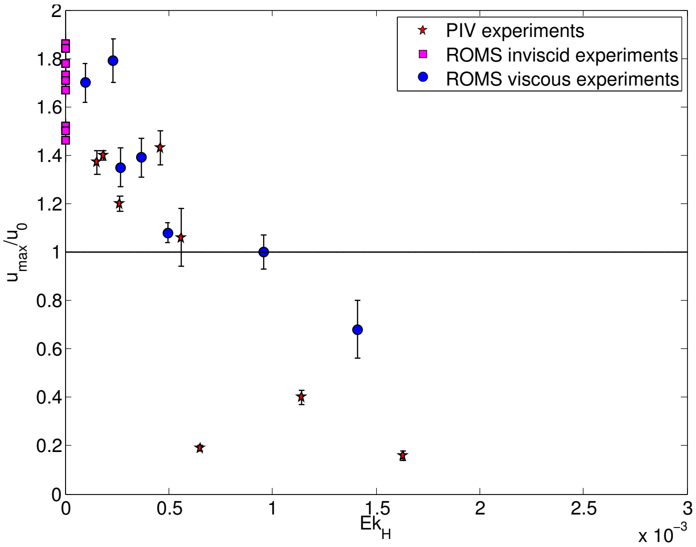

(b)

Figure 7.12: Summary of the (averaged) maximum non-dimensional plume speed, U_{max}, as a function of (a) the dimensionless parameter, I, and (b) the horizontal Ekman number, Ek_H, respectively, for the viscous and inviscid numerical simulations, and for the PIV laboratory experiments. The black line on the figures identifies $U_{max} = 1$, that is agreement between experiments and theory. The error bars are standard deviation errors of the averaged maximum non-dimensional plume speed.

7.6 Plume-edge instabilities

As mentioned in 7.2, instabilities along the outer plume edge were seen to develop in some of the numerical and laboratory experiments. Figure 7.13 shows the surface density field taken at the non-dimensional time $T = 168$ for the unstable plumes 148 and 151 from the viscous numerical simulations. Well-developed instabilities are seen along the plume edge. One can see from Figure 7.13 the rapid mixing of fresh and ambient waters within the growing instabilities.

Figure 7.14 displays an I-Ek_H diagram summarizing the stability properties of the plumes simulated in the inviscid and viscous numerical simulations, and in the *PIV* laboratory experiments. The formation of instabilities is shown to depend on the magnitude of the parameters I and Ek_H. In particular, for finite Ek_H values, plumes with an I value greater than approximately 0.3 are unstable. Interestingly, the range of instability for the lowest Ek_H values (e.g., the inviscid *ROMS* simulations) is somewhat reduced, with instabilities appearing for values of I greater than approximately 0.6.

The dimensionless parameter I is the ratio of the theoretical plume height to the theoretical plume width; it therefore characterizes the isopycnal slope. Large values of I imply plumes that are deep and narrow. Plumes with high I values will have therefore potential energy available to be released into the growing disturbances observed in the experiments. This suggests that the instabilities observed for experiments with high I values are predominantly baroclinic, as the energy source for baroclinic instabilities is the potential energy in the fluid system.

From Griffiths & Linden (1981b), unstable disturbances are expected to be baroclinic for $\theta >> 1$ and $\delta > 0.1$, where θ is the square of the ratio of the internal Rossby radius of deformation to the horizontal length scale of the flow, and δ is the fraction of the total fluid depth occupied by the layer inside the front. Here, the internal Rossby radius of deformation, R, is equal to $\sqrt{2}w_0$, where w_0 is the theoretical plume width of Thomas & Linden (2007). Figures 7.5(a)-(b) and Figure 7.6 reveal that the measured width of the unstable coastal currents from the laboratory and numerical simulations were larger than w_0 and R, giving $\theta > 1$ for all the unstable experiments presented in this chapter. Furthermore, by inspecting the ratio of the plume depth to the total fluid depth for all the numerical and laboratory unstable experiments, this ratio is found to be always greater than 0.1. Thus the two criteria of Griffiths & Linden (1981b) to have

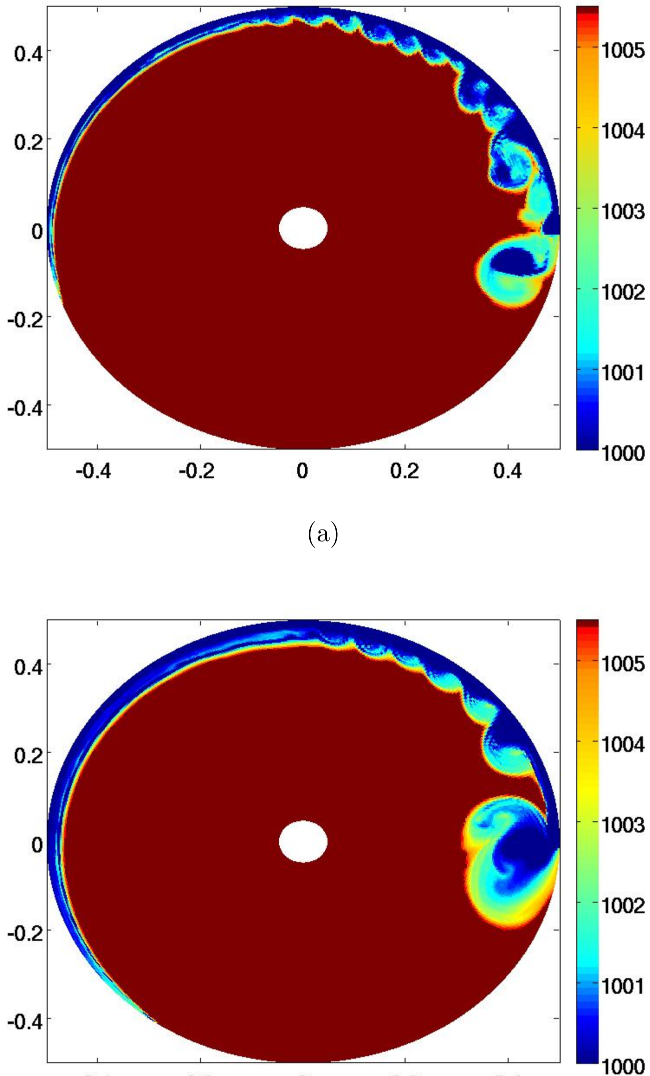

(a)

(b)

Figure 7.13: Surface density field showing the unstable plumes (a) 148 and (b) 151 from the viscous numerical simulations. Color bar is for density (in $kg\ m^{-3}$).

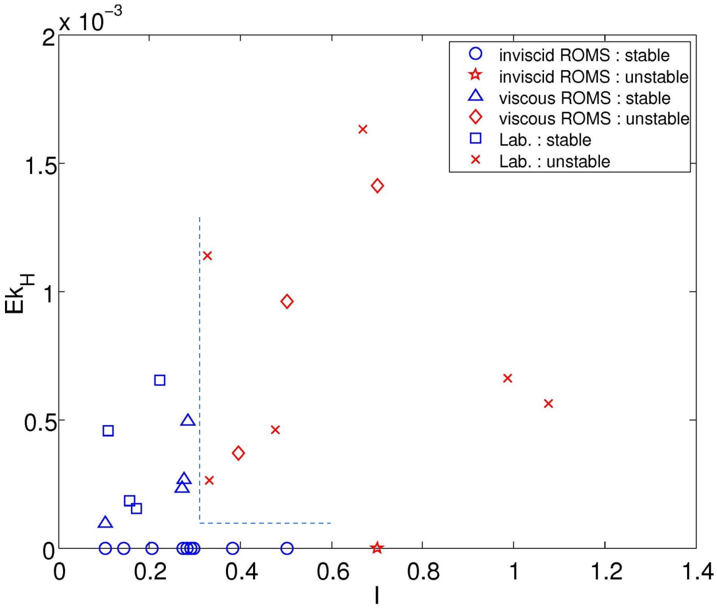

Figure 7.14: I-Ek_H diagram displaying the parametric locations where the plumes are found to be stable/unstable. The dashed line is suggestive of the stability boundary.

baroclinic disturbances are met in the laboratory and numerical unstable simulations presented here. By considering also that these numerical and laboratory unstable experiments produced quite deep (and narrow) plumes (medium to large I values), which thus have available potential energy (which is the energy source of baroclinic instabilities) to be released into the disturbances observed, one may conclude that the instabilities observed in the plumes simulated in this study are baroclinic.

CHAPTER 8

Departures from the theory: Internal structure and dynamics

The geostrophic theory of Thomas & Linden (2007) assumes that the buoyant plume is steady, x-invariant and inviscid. It further requires the plume velocity to vanish at the coast, and to achieve its maximum strength where the density front intersects the surface. Although the bulk properties of the plumes observed in the laboratory and simulated in ROMS are in generally good agreement with the theoretical predictions, some departures from the theory are nonetheless evident. Some of these are explored next.

8.1 Internal velocity structure and momentum balances

The geostrophic theory is clearly not meant to represent the early evolution of the bulge and developing plume. Therefore it is perhaps not surprising that the early-time properties of the plume may differ from the theoretical predictions. One advantage of the $ROMS$ numerical simulations is that the internal structure of the plumes and the accompanying dynamical balances may be readily investigated.

Figures 8.1(a)-(c) and Figures 8.1(b)-(d) display cross-sections in the y-z plane of the time-averaged non-dimensional Coriolis term in the v-momentum equation, and the time-averaged non-dimensional pressure gradient term in the v-momentum equation, respectively, taken at the alongshore distance upstream from the nose, $d_N = 5\ cm$, and at the times, $t = 4.25\ s$ (Figures 8.1(a)-(b)) and $t = 36.25\ s$ (Figures 8.1(c)-(d)), for the viscous plume 150. The Coriolis and pressure gradient terms in Figure 8.1 are non-dimensionalized by (fu_0) where f

is the Coriolis parameter and u_0 is the theoretical geostrophic velocity. The time average in Figure 8.1 is taken over 0.5 seconds.

At $t = 4.25\ s$, the flow is already nearly geostrophic; the Coriolis and pressure gradient terms in the cross-shore momentum equation nearly balance (Figures 8.1(a)-(b)). At later time, the Coriolis and pressure gradient terms still nearly balance but the magnitude of the Coriolis and pressure gradient terms is smaller than at early time, especially in the viscous simulations (Figures 8.1(c)-(d)). The next largest terms are those making up the total time rate of change (local acceleration and advection; not shown), but these are much smaller and have no clear spatial pattern. Lastly, explicit viscous forces are smaller by one to two orders of magnitude. The dynamical balance was only available for viscous simulations (and their inviscid companion) with a low Ek_H value. A numerical simulation with a high Ek_H value is expected to have the magnitude of the lateral viscous forces getting greater at later time.

Figures 8.2(a)-(c) and Figures 8.2(b)-(d) display cross-sections in the y-z plane of the time-averaged non-dimensional alongshore velocity, U, for the inviscid plume 134 and the viscous plume 150, and the time-averaged density field for the inviscid plume 134 and the viscous plume 150, respectively, taken at the alongshore distance upstream from the nose, $d_N = 5\ cm$, and at the time, $t = 4.25\ s$. Figures 8.3(a)-(c) and Figures 8.3(b)-(d) display cross-sections in the y-z plane of the non-dimensional alongshore velocity, U, for the inviscid plume 125 and the viscous plume 151, and the density field for the inviscid plume 125 and the viscous plume 151, respectively, taken at the alongshore distance upstream from the nose, $d_N = 5\ cm$, and at the time, $t = 4\ s$. The time average in Figure 8.2 is taken over 0.5 seconds. The along-shore velocity in Figures 8.2(a)-(c) and Figures 8.3(a)-(c) is non-dimensionalized by the theoretical geostrophic velocity, u_0.

The initial structure of the density field within the developing plume has a strong sloping front. The isopycnal slope is rather linear for the simulations with low Ek_H values (and their inviscid companion, Figures 8.2(b)-(d)), while it is more quadratic for the simulations with large Ek_H values (and their inviscid companion, Figures 8.3(b)-(d)). At early time, stratification occurs mainly in the coastal current coincident with the strong coastal jet. The accompanying alongshore velocity (Figures 8.2(a)-(c) and Figures 8.3(a)-(c)) exceeds the theoretical estimate by a factor larger than two and does not go to zero at the wall (as required by the theory), instead the alongshore velocity has a maximum value at

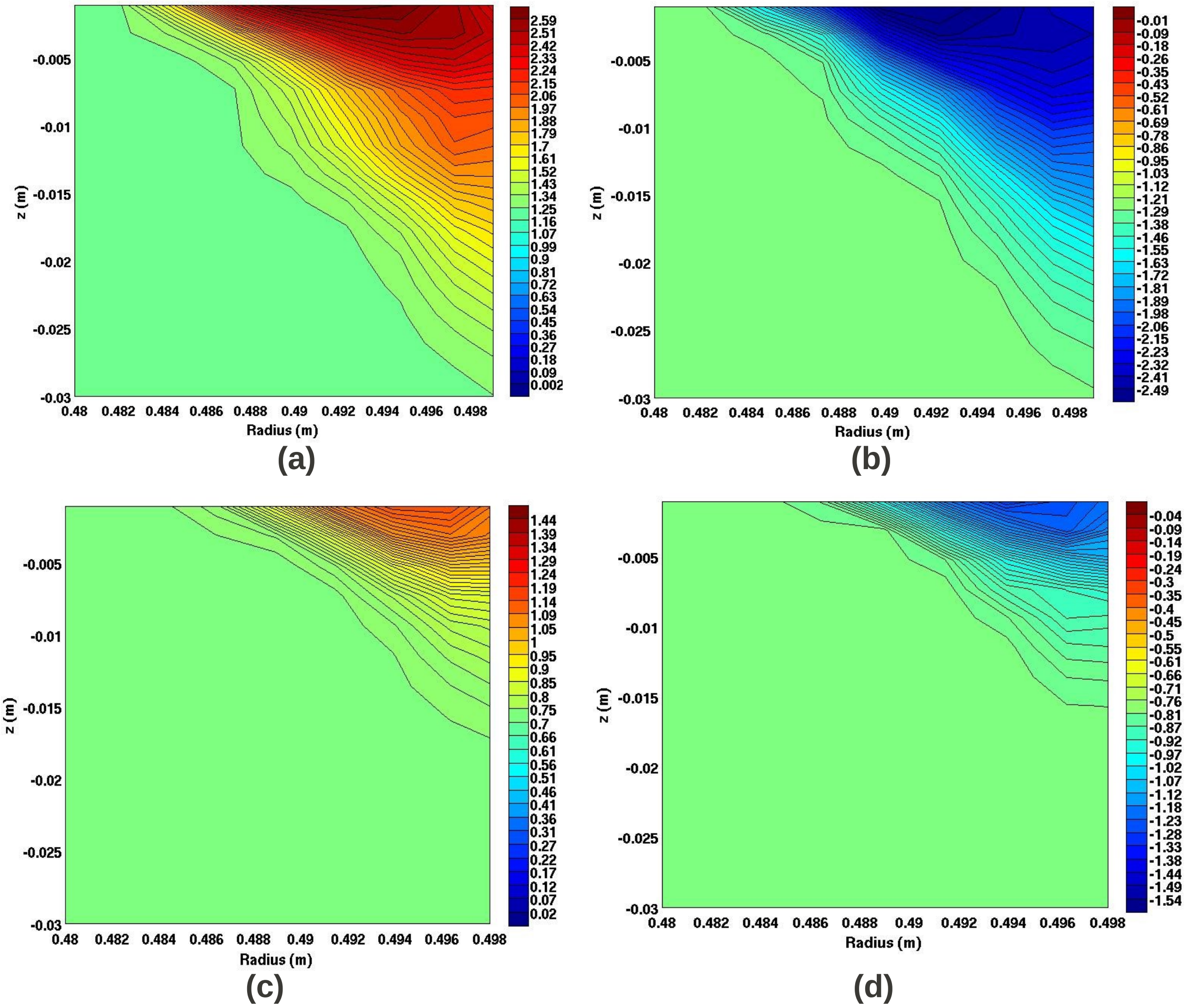

Figure 8.1: Cross-section in the y-z plane of (a)-(c) the non-dimensional Coriolis term in the v-momentum equation, and (b)-(d) the non-dimensional pressure gradient term in the v-momentum equation, taken at the alongshore distance upstream from the nose, $d_N = 5\ cm$, and at the times (a)-(b) $t = 4.25\ s$ and (c)-(d) $t = 36.25\ s$ for the viscous plume 150.

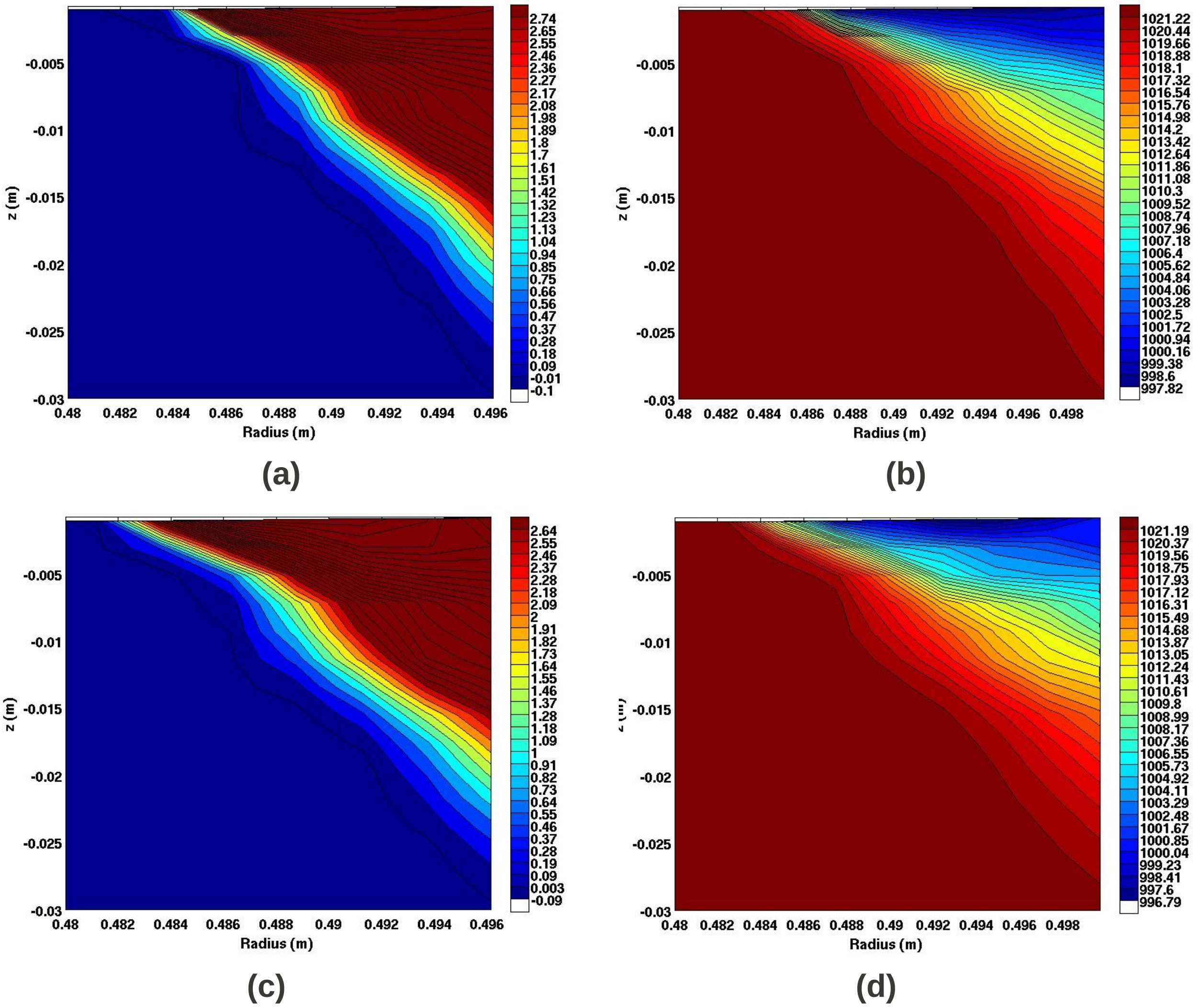

(a) (b)

(c) (d)

Figure 8.2: Cross-section in the y-z plane of (a)-(c) the non-dimensional alongshore velocity, U, for the inviscid plume 134 and the viscous plume 150, respectively, and (c)-(d) the density field for the inviscid plume 134 and the viscous plume 150, respectively, taken at the alongshore distance upstream from the nose, $d_N = 5\ cm$, and at the time, $t = 4.25\ s$. The color bar in the right images is for density (in $kg\ m^{-3}$).

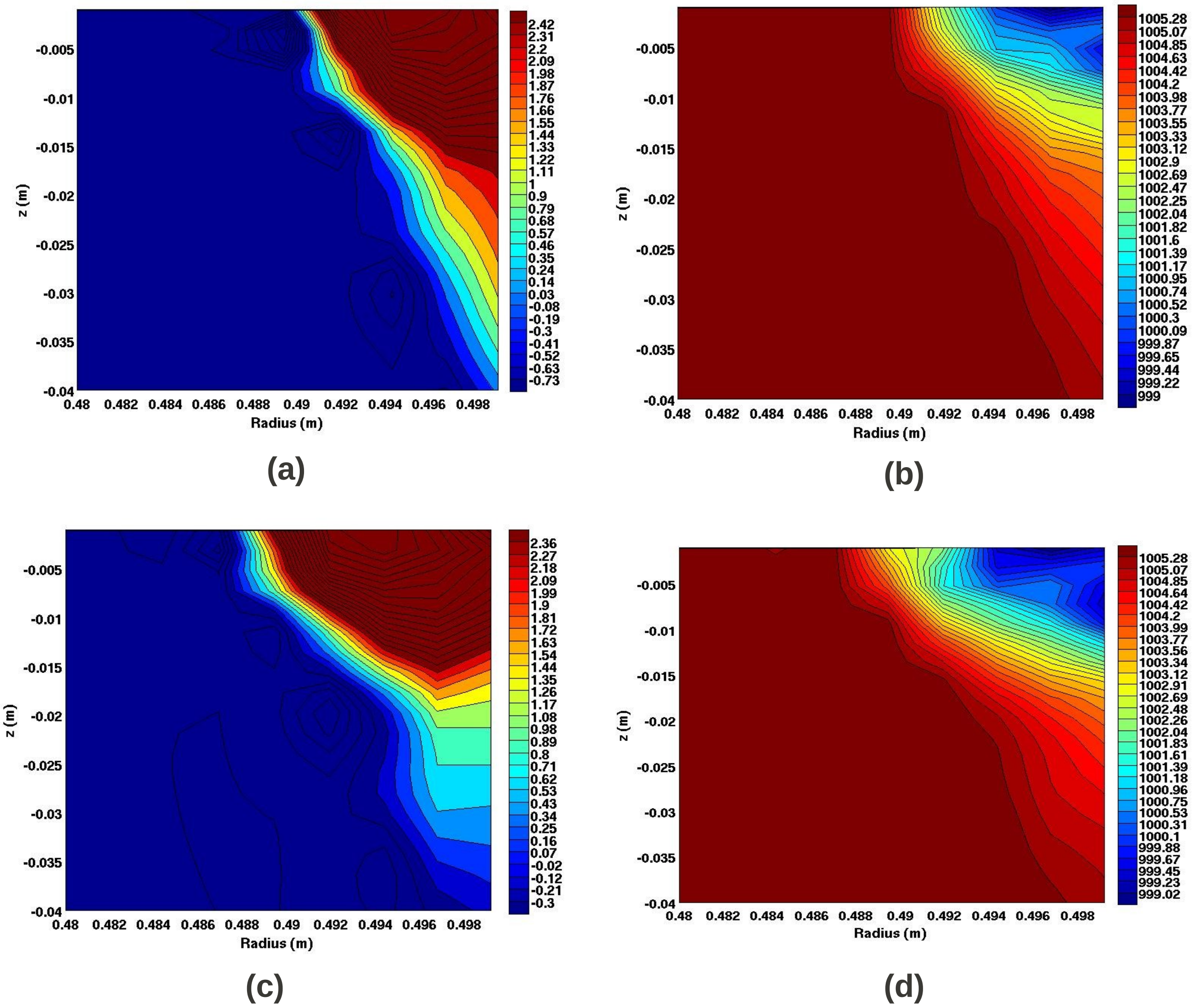

Figure 8.3: Cross-section in the y-z plane of (a)-(c) the non-dimensional alongshore velocity, U, for the inviscid plume 125 and the viscous plume 151, respectively, and (c)-(d) the density field for the inviscid plume 125 and the viscous plume 151, respectively, taken at the alongshore distance upstream from the nose, $d_N = 5\ cm$, and at the time, $t = 4\ s$. The color bar in the right images is for density (in $kg\ m^{-3}$).

the wall.

Figures 8.4(a)-(c) and Figures 8.4(b)-(d) display cross-sections in the y-z plane of the time-averaged non-dimensional alongshore velocity, U, for the inviscid plume 134 and the viscous plume 150, and the time-averaged density field for the inviscid plume 134 and the viscous plume 150, respectively, taken at the alongshore distance upstream from the nose, $d_N = 5\ cm$, and at the time, $t = 36.25\ s$. The time average is taken over 0.5 seconds and the along-shore velocity is non-dimensionalized by the theoretical geostrophic velocity, u_0.

A comparison between Figure 8.2 and Figure 8.4 reveals that at later time, plumes are shallower and narrower. The alongshore velocity is also smaller at later time, especially for the viscous simulations (Figure 8.4(c)). Stratification appears to be confined to the seaward edge of the jet.

Figures 8.5(a)-(c) and Figures 8.5(b)-(d) display cross-sections in the y-z plane of the non-dimensional alongshore velocity, U, for the viscous plumes 150 and 151, and the density field for the viscous plumes 150 and 151, respectively, taken at the alongshore distance upstream from the nose, $d_N = 50\ cm$, and at the time, $t = 36\ s$. The along-shore velocity is non-dimensionalized by the theoretical geostrophic velocity, u_0.

Farther from the coastal current nose, the frontal structure accompanying the plume is both wider and deeper (from a comparison between Figure 8.4(d) and Figure 8.5(b)). Furthermore, in the viscous simulations, the azimuthal velocity structure is a U-shape (Figures 8.4(a)-(c)) with a boundary layer at the wall in which the alongshore velocity vanishes for the plumes with large Ek_H values (Figure 8.4(c)), in agreement with theory.

Figure 8.6 and Figure 8.7 display the variations along the radial position of the alongshore velocity, u (Figure 8.6a and Figure 8.7a), the across-shore velocity, v (Figure 8.6b and Figure 8.7b), and the vertical velocity, w, (Figure 8.6c and Figure 8.7c), taken at the free surface, at different alongshore distances upstream from the plume nose, d_N, and at the time, $t = 40\ s$, for the inviscid plume 134 and the viscous plume 150, respectively.

An examination of the cross-section in the y-z plane for the radial and vertical velocity components reveal that the magnitude of the across-shore and vertical velocities is much smaller than the magnitude of the alongshore velocity, in agreement with Thomas & Linden (2007) assumptions (even if the across-shore and vertical velocities are found to be the largest in the plume nose region, their magnitude is still below 20% of the magnitude for the azimuthal velocity (Figure 8.6

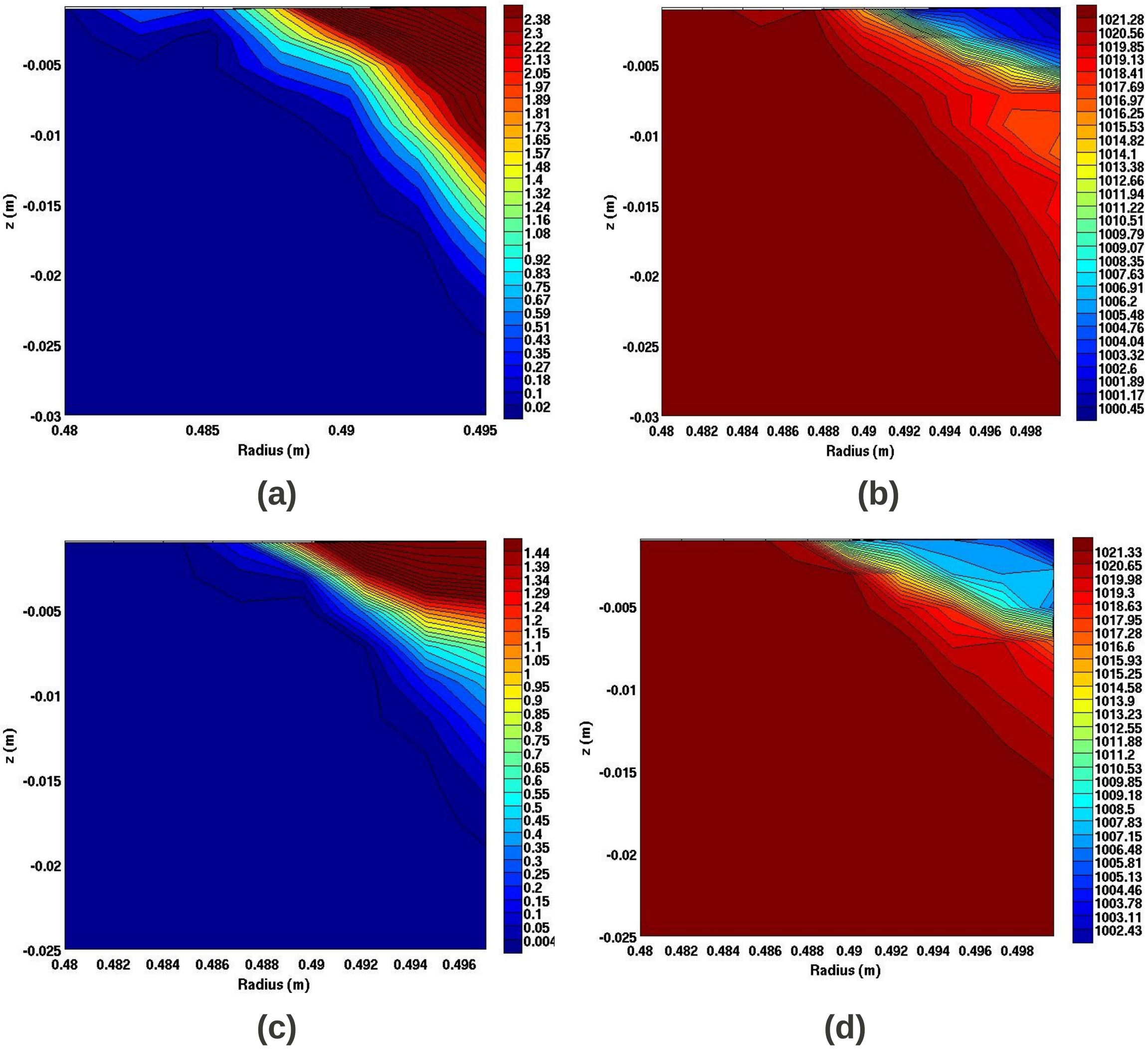

(a) (b)

(c) (d)

Figure 8.4: Cross-section in the y-z plane of (a)-(c) the non-dimensional alongshore velocity, U, for the inviscid plume 134 and the viscous plume 150, respectively, and (c)-(d) the density field for the inviscid plume 134 and the viscous plume 150, respectively, taken at the alongshore distance upstream from the nose, $d_N = 5\ cm$, and at the time, $t = 36.25\ s$. The color bar in the right images is for density (in $kg\ m^{-3}$).

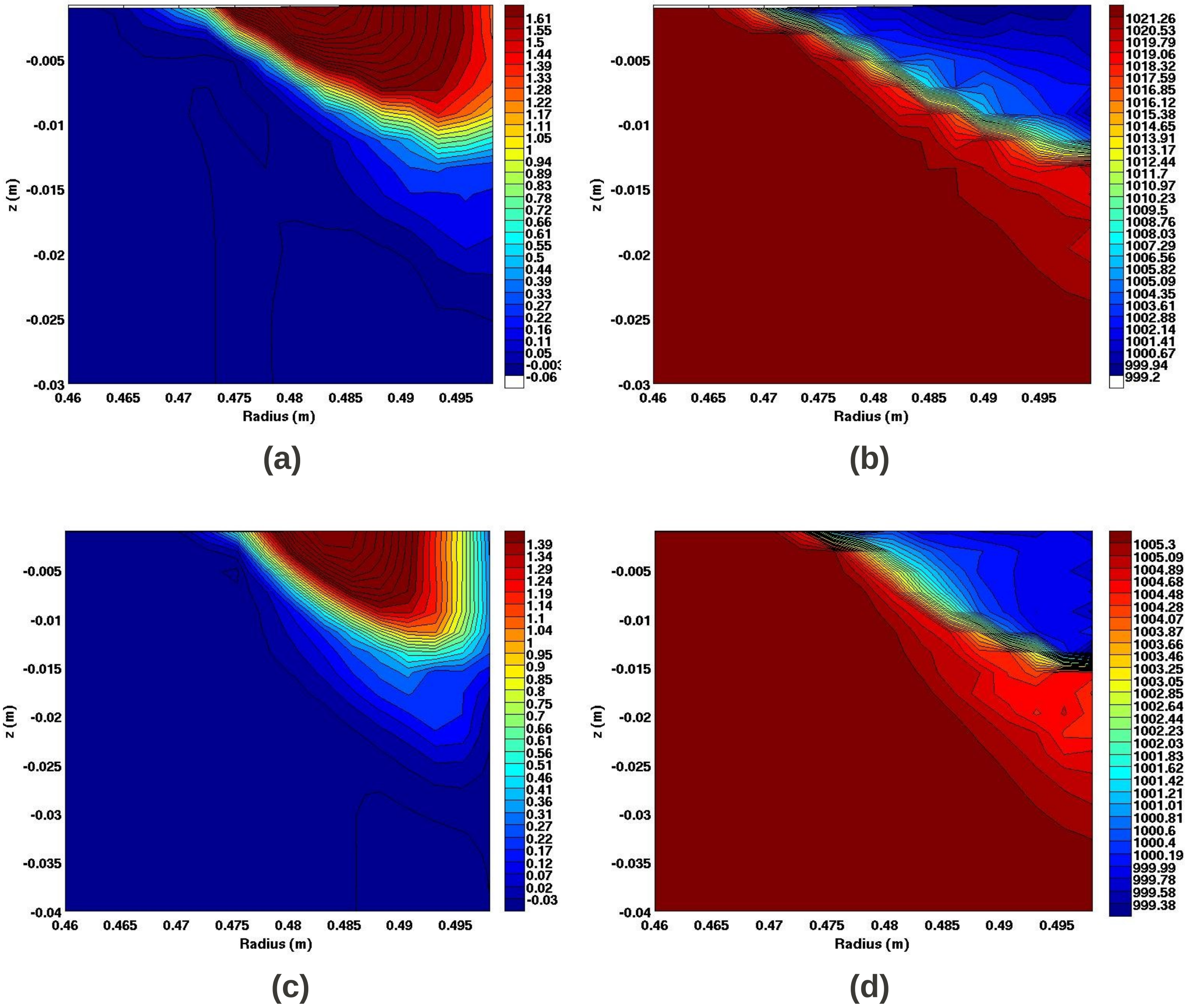

Figure 8.5: Cross-section in the y-z plane of (a)-(c) the non-dimensional alongshore velocity, U, for the viscous plumes 150 and 151, respectively, and (c)-(d) the density field for the viscous plumes 150 and 151, respectively, taken at the alongshore distance upstream from the nose, $d_N = 50\ cm$, and at the time, $t = 36\ s$. The color bar in the right images is for density (in $kg\ m^{-3}$).

and Figure 8.7)). In agreement with the previous observations from this section, the surface alongshore velocity has its maximum value at or near the wall in the inviscid numerical simulations (Figure 8.6(a)). In the viscous numerical simulations, the surface alongshore velocity approaches zero when getting farther from the plume nose (Figure 8.7(a)) and when increasing the value of the horizontal Ekman number (Figure 8.5(c)). In some numerical simulations, large across-shore velocity magnitudes were observed (of the order of the magnitude for the azimuthal velocity) but these large radial velocities were due to the presence of instabilities in the plumes.

Figures 8.8(a)-(b) display the cross-section in the x-z plane of the density field taken at 4.8 mm from the wall and at the time $t = 50$ s, for the inviscid plume 134 and the viscous plume 150, respectively. The azimuthal profile of the plume depth displayed in Figures 8.8(a)-(b) reveals that the plume depth decreases along the wall but only in the final plume length, contradicting Thomas & Linden (2007) who suggested that plumes decreased in depth linearly along the coastal wall.

8.2 Mixing in the plumes

It is interesting to inquire whether the mixing associated with the plume-edge instabilities in the numerical simulations can be quantified. One way to approach this is to measure, as a function of time, the rate of production of intermediate water, that is, water with a value of density intermediate between that of the ambient and buoyant fluids. As viscous effects are confined to the wall boundary layer (and explicit diffusivity is omitted), mixing of density in the numerical plumes arises solely from two sources: implicit smoothing due to discretization, and the mixing associated with the plume-edge instabilities, should the latter arise.

Figures 8.9(a)-(b) display the non-dimensional volume of intermediate water in the gravity plume and bulge system as a function of the dimensionless time, T, and the non-dimensional plume length, L, extracted from Figure 7.2b and Figure 7.3b, for the inviscid and viscous simulations. The volume of intermediate water in Figure 8.9 is non-dimensionalized by (q_0/Ω). The range of the density values for the intermediate water in each experiment was chosen to extend from $(1000 + 0.46 * \Delta(\rho))$ to $(1000 + 0.82 * \Delta(\rho))$, thereby occupying 36% of the total range of the density in the experiments.

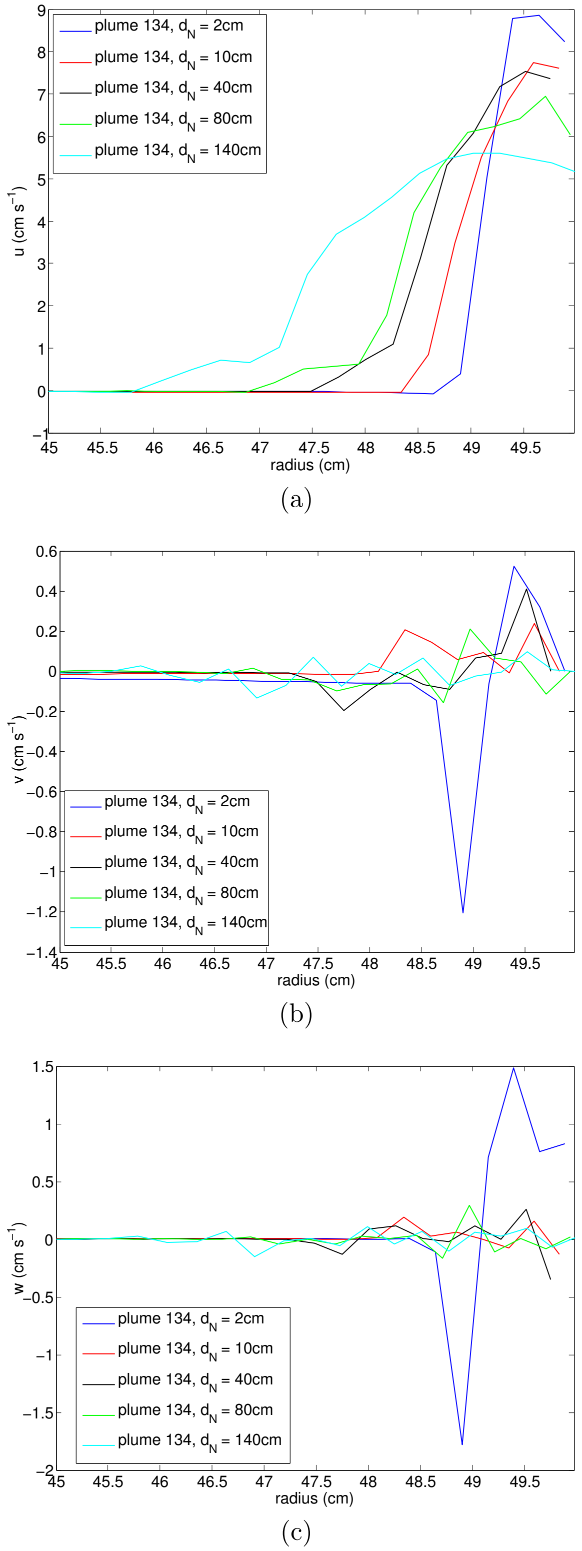

Figure 8.6: Variations along the radial position of (a) the alongshore velocity, u, (b) the across-shore velocity, v, and (c) the vertical velocity, w, taken at the free surface, at different alongshore distances upstream from the plume nose, d_N, and at the time, $t = 40\ s$, for the inviscid plume 134.

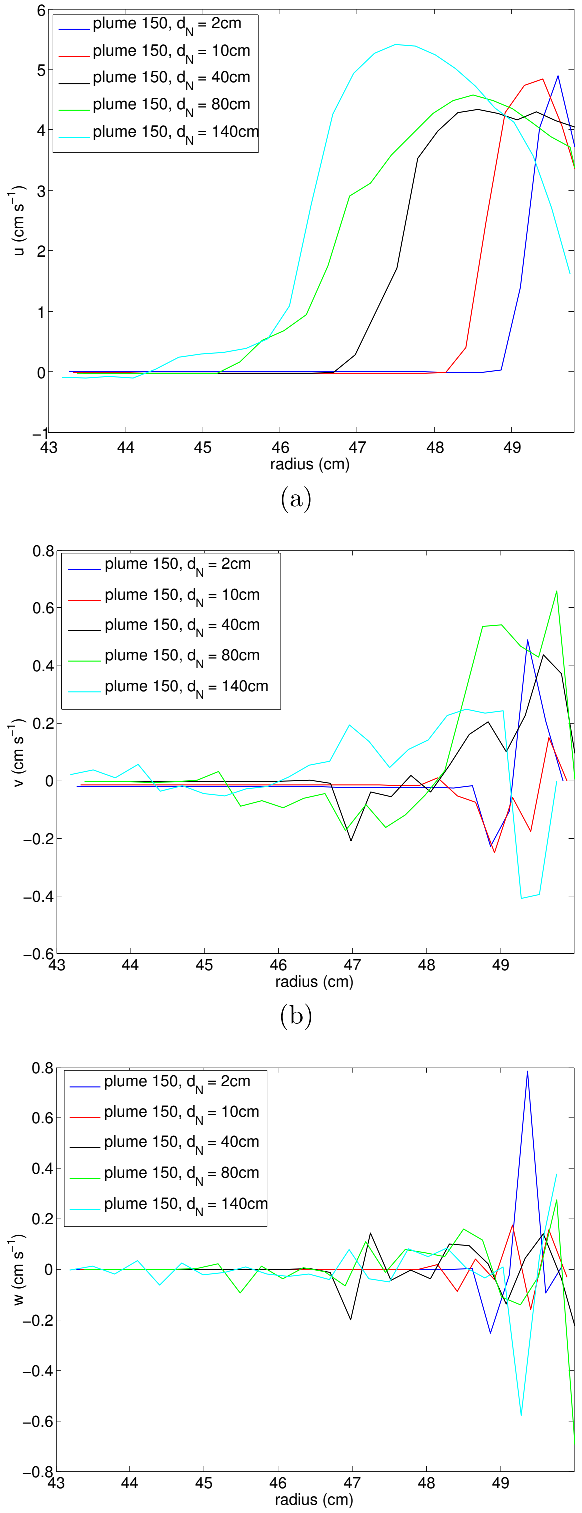

(a)

(b)

(c)

Figure 8.7: Variations along the radial position of (a) the alongshore velocity, u, (b) the across-shore velocity, v, and (c) the vertical velocity, w, taken at the free surface, at different alongshore distances upstream from the plume nose, d_N, and at the time, $t = 40\ s$, for the viscous plume 150.

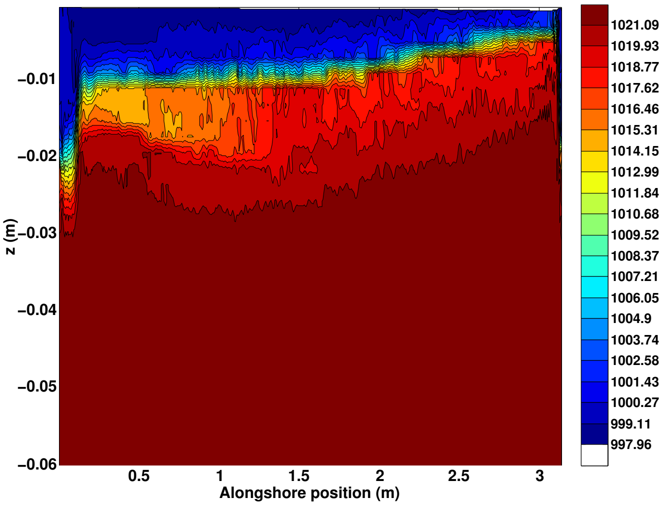

(a)

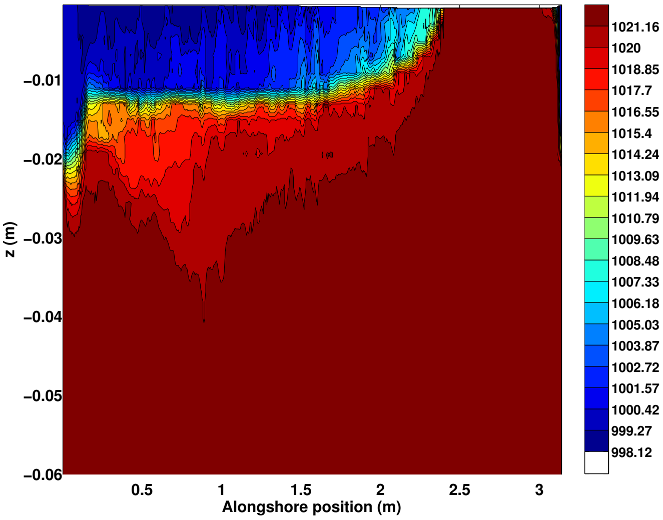

(b)

Figure 8.8: Cross-section in the x-z plane of the density field taken at 4.8 mm from the wall and at the time $t = 50$ s for the inviscid plume 134 and the viscous plume 150, respectively.

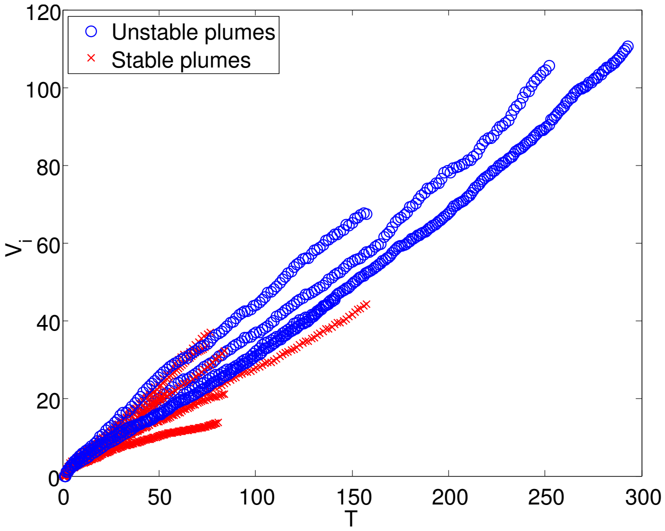

(a)

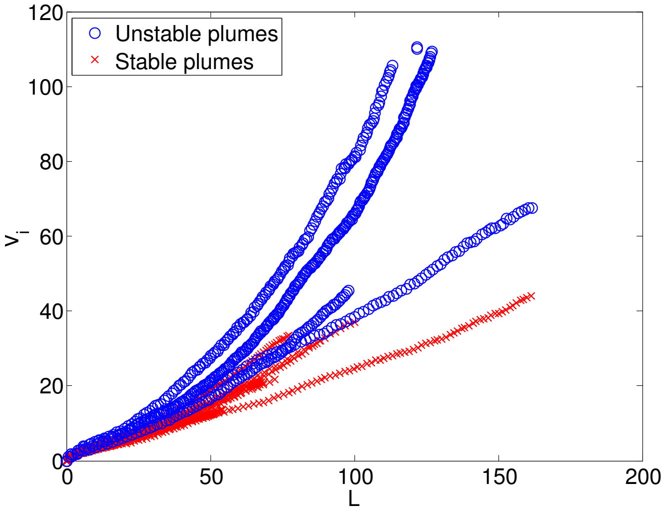

(b)

Figure 8.9: Non-dimensional volume, V_i, of intermediate water in the coastal plume and bulge system, as a function of (a) the dimensionless time, T, and (b) the non-dimensional plume length, L, for the inviscid and viscous numerical simulations.

Figures 8.9(a)-(b) show that the non-dimensional rates at which intermediate water is formed have some interesting, and perhaps non-intuitive, dependencies. Figure 8.9a, in which the rate of mixing is plotted against the non-dimensional time, T, suggests a time rate of mixing that is rather similar across all numerical simulations. In particular, the range of values for these *rates* do not appear to depend importantly on whether the plumes are stable or unstable. Despite this, Figure 8.9a does make clear that the *total amount of mixing* undergone in a single experiment is much greater for the unstable experiments. The explanation is, of course, that the viscous plumes are advancing more slowly and therefore take more time to complete a circuit about the annulus.

If one plots the volume of intermediate water against *distance travelled* (Figure 8.9b), a different picture emerges. The unstable plumes are clearly more effective at mixing *per unit distance travelled*. One recalls from Section 7.6 that the addition of viscosity increased the region in I parameter space in which instabilities were observed to occur. The addition of viscosity also acts to decelerate the plumes. The observation that total mixing is enhanced within the slow-moving plumes therefore appears to be at least consistent with the results presented above. However, whether the enhanced region of instability accompanying the addition of viscosity is due to the physics or the numerics (or both) is not immediately obvious.

8.3 Theoretical considerations

As the foregoing sections and chapters illustrate, the assumptions underlying the geostrophic theory of Thomas & Linden (2007) are only approximately met in the laboratory experiments and the numerical simulations. Perhaps the most obvious disagreement pertains to the role of lateral viscosity. Whereas the geostrophic theory envisions an inviscid ocean, both the laboratory and numerical results underscore the importance of lateral viscous forces. In particular, the speed of the buoyant plume is observed to depend on the magnitude of the viscous forces as measured by the horizontal Ekman number, Ek_H.

Figure 8.10 shows the departure of the non-dimensional plume length given by the viscous simulations with $ROMS$ from that predicted by the geostrophic theory. As noted above, the initial displacement of the plume is faster than the theory would provide. However, the plumes eventually decelerate and reach a

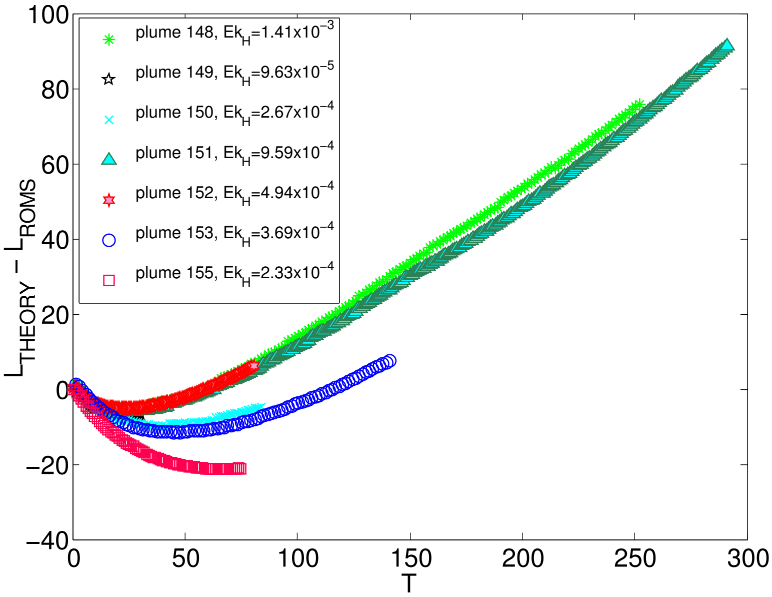

Figure 8.10: Difference between the non-dimensional plume length, L, for the viscous simulations, and the theory of Thomas & Linden (2007), $L = (3/4)T$.

nearly constant speed that is less than the theoretical value. This suggests that viscosity is providing a nearly constant decelerating force that partially offsets the action of the geostrophic pressure gradient.

Linear fits are produced to the curves in Figure 8.10 for $T \geq 50$. The slopes given by these fits represent estimates of the velocity discrepancy between the geostrophic theory and each of the simulations. Figure 8.11 shows the resulting estimates of velocity discrepancy plotted against the horizontal Ekman number. An approximate dependence on the horizontal Ekman number to the one-half power is observed.

Grégorio *et al.* (2011) examined the potential role of the viscous forces by a slight modification of the theory proposed by Thomas & Linden (2007), retaining many of their original assumptions – i.e., x-invariant, rotationally dominated, steady flow – but introducing molecular viscous forces in the cross-plume direction. Grégorio *et al.* (2011) obtained that the velocity discrepancy was proportional to the square root of the horizontal Ekman number (in agreement with the results from Figure 8.11).

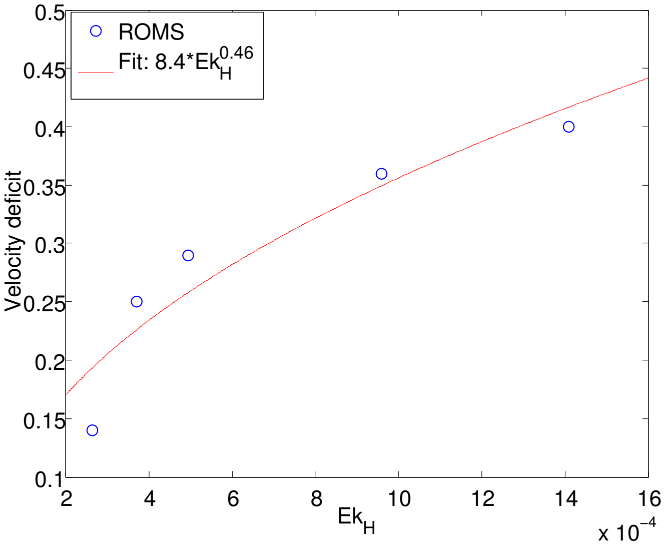

Figure 8.11: Velocity deficit as a function of the horizontal Ekman number, Ek_H. The curve is the best fit for the data of equation $8.4 \times (Ek_H)^{0.46}$. The velocity deficits are simply the slope of the best linear fits for the curves of Figure 8.10 computed from $T \geq 50$.

Part IV

Experimental Study

CHAPTER 9

The effect of sloping bottom on coastal current evolution

Gravity currents in the ocean typically flow along a coast with variable topography rather than a vertical wall. In this chapter, experimental results for plumes flowing along a more realistic topography of an inclined coastline are presented and compared to the theory described in Chapter 4 and to experimental results for coastal currents flowing along a vertical coastline. Therefore this chapter is concerned about the case of surface-advected and bottom-trapped plumes propagating along a sloping bottom.

9.1 Introductory remarks

A typical coastal current flowing along an inclined coastline in the large-scale Coriolis facility is shown in Figure 9.1. The coastal current flows along the plate keeping the boundary to its right, and looks qualitatively very similar to coastal currents flowing along vertical walls. Similar to vertical-wall coastal currents, a gyre develops near the source region. Aspects relating to the gyre were already discussed in Thomas & Linden (2007). In their vertical-wall experiments, Thomas & Linden (2007) observed that the gyre usually surrounds the source extending into the region just downstream of it. In the inclined-wall experiments however, there is a trend for the gyre position to slightly shift just upstream of the source as is the case in Figure 9.1. As for vertical-wall coastal currents, for some experimental parameters combinations, the rate of elongation of the plumes flowing along an inclined coastline shows little decrease during the whole experiment, while for some other experimental parameters combinations, the coastal plumes are observed to accelerate at the start of the experiment, then to decelerate to a nearly constant propagation speed. Finally for some inclined-wall experiments, instabilities are seen to develop along the edge of the plume (as in Figure 9.2).

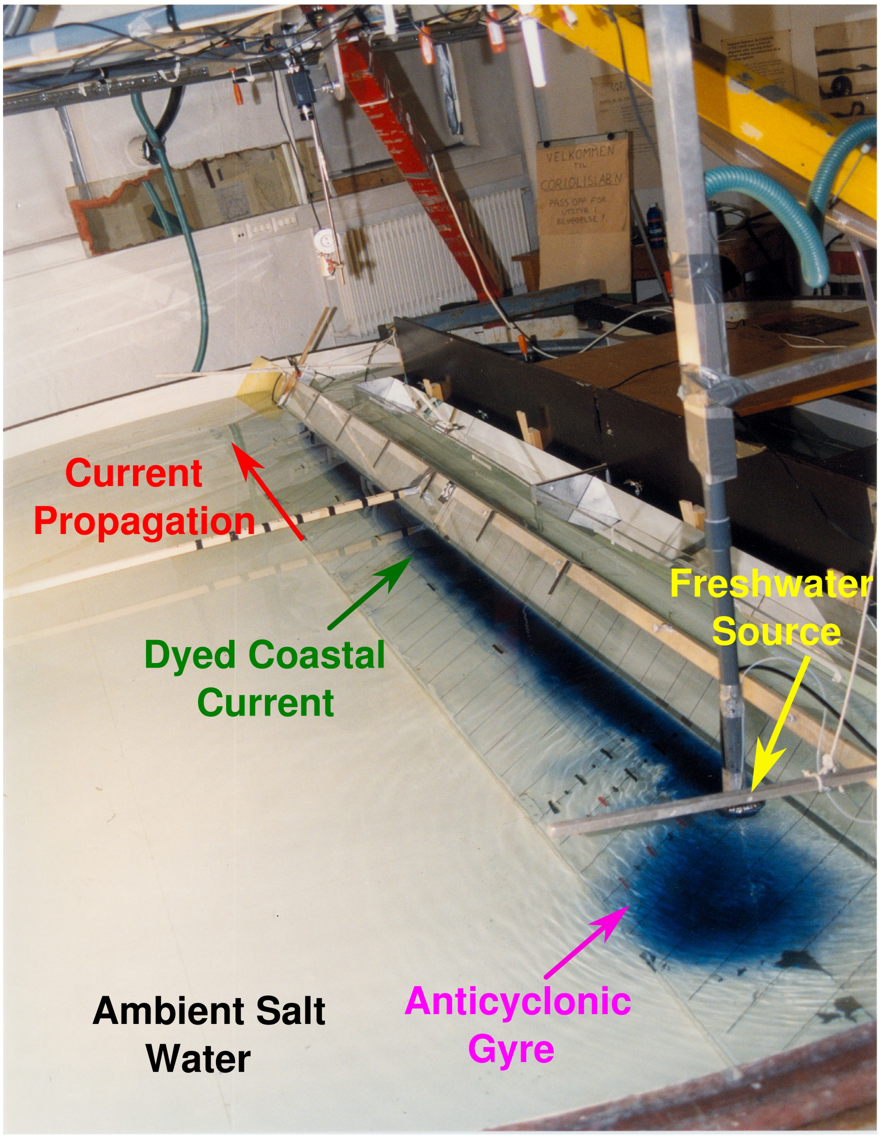
VELKOMMEN
TIL
CORIOLISLAB'N
Current
Propagation
Freshwater
Source
Dyed Coastal
Current
Ambient Salt
Water
Anticyclonic
Gyre

Figure 9.1: A typical coastal current (experiment $T35$) flowing along an inclined plate mounted across the diameter of the Coriolis tank at Trondheim. $\alpha = 50°$, $I = 0.292$, $Ek_V = 6.6 \times 10^{-4}$, $Ek_H = 1.21 \times 10^{-4}$, $h_0/H_D = 0.49$.

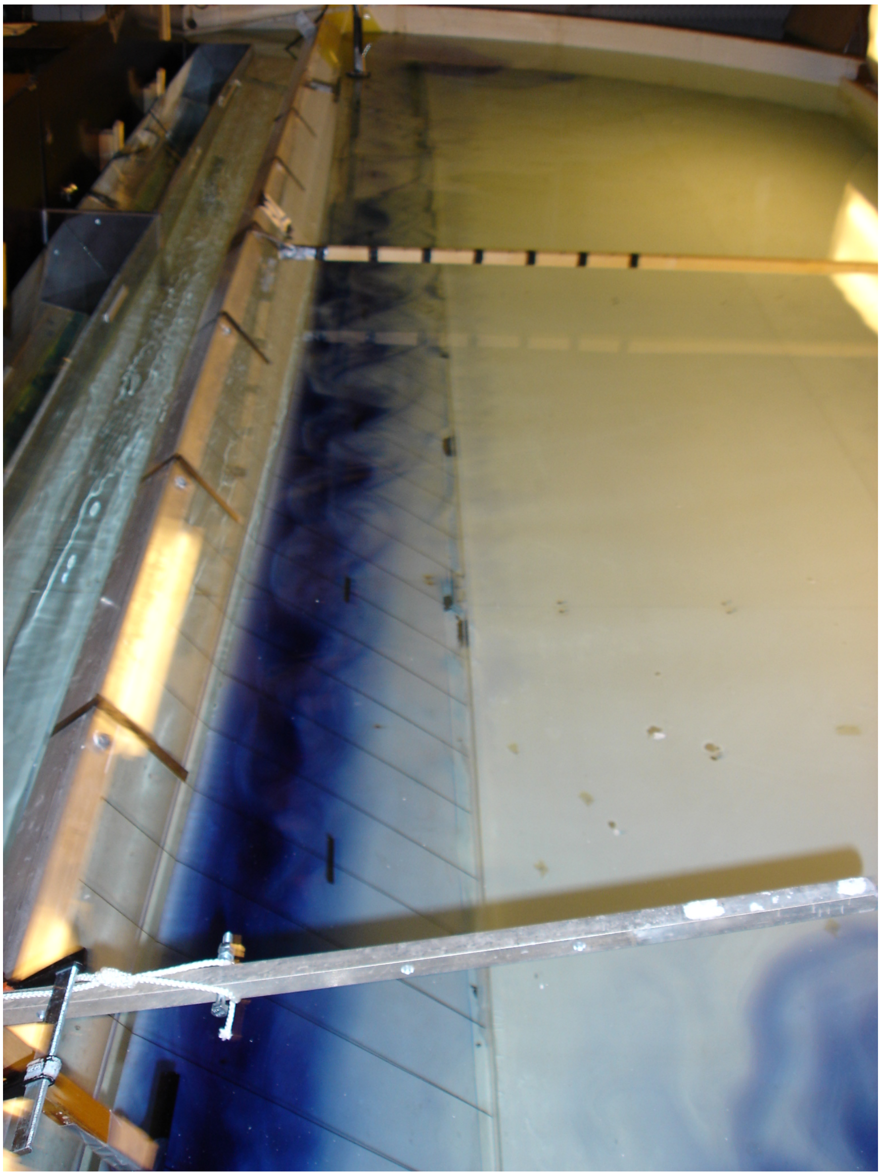

Figure 9.2: An unstable coastal current (experiment $T32$) flowing along an inclined wall in the large-scale Coriolis tank at Trondheim. $\alpha = 50°$, $I = 0.481$, $Ek_V = 2.43 \times 10^{-4}$, $Ek_H = 1.56 \times 10^{-4}$, $h_0/H_D = 0.92$.

9.2 Coastal current length and propagation velocity

9.2.1 Comparison between inclined-wall and vertical-wall experiments

31 small-scale and 56 large-scale experiments were performed in order to investigate the effect of an inclined coastline on coastal current evolution. A further 13 control large-scale experiments were carried out for coastal currents flowing along a vertical wall. The latter set of experiments was conducted to obtain reference data for comparison with the 56 inclined-wall large-scale experiments. Details of the small-scale experiments are summarized in Tables B.2, B.3 and B.4 of Appendix B while details of the large-scale experiments are listed in Appendix C.

Figures 9.3(a)-(c) show typical small-scale data for the non-dimensional plume length, L_i, as a function of the dimensionless time, T. On each figure, experiments have equal rotation rate, Ω, equal flow rate, q_0, equal reduced gravity, $g\prime$, but different sloping angles, α. Experiments with a sloping angle $\alpha = 90°$ are small-scale experiments of Thomas & Linden (2007). They are compared to small-scale experiments with sloping angles $\alpha = 59.2°$ and $\alpha = 18.5°$. Details of the small-scale experiments of Thomas & Linden (2007) are listed in Appendix A.

Figures 9.4(a)-(c) show typical large-scale data for the non-dimensional plume length, L_i, as a function of the dimensionless time, T. On each figure, experiments have similar values for the dimensionless parameter I, the horizontal and vertical Ekman numbers, Ek_H and Ek_V, respectively; only the sloping angle, α, differs. During the large-scale experiments with the bottom slope $\alpha = 25.9°$, a camera was recording the plume width through a mirror mounted on the turntable at angle 45° with the horizontal. The mirror was in the field of view of the camera recording the plume length. This set-up explains why some length data for the coastal currents flowing along the inclined coastline $\alpha = 25.9°$ are unavailable on Figures 9.4(a)-(c). Data for the plume length in Figures 9.3(a)-(c) and Figures 9.4(a)-(c) are non-dimensionalized by w_0.

In Figure 9.3a, at early time, the coastal current flowing over the sloping wall propagates faster than the coastal current flowing over the vertical wall. Then from $T \sim 6$, the plume flowing over the sloping wall starts to decelerate to finally propagate from $T \sim 13$ at same (constant) speed as the plume flowing along the vertical wall (which, conversely to the plume flowing over the inclined wall, propagates at nearly constant speed during the whole experiment). In

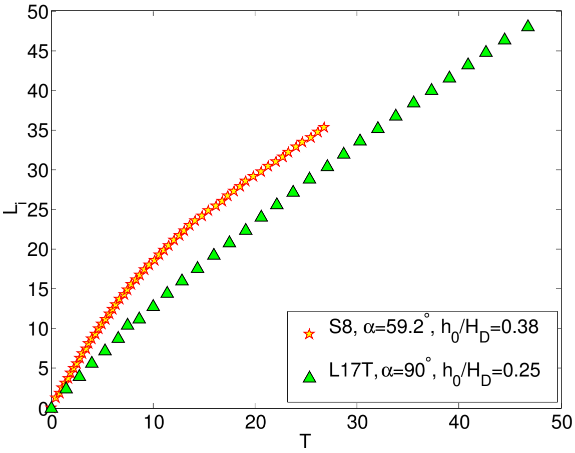

(a) $I = 0.288 \pm 0.018$, $Ek_V = (1.72 \pm 0.18) \times 10^{-3}$, $Ek_H = (3.03 \pm 0.16) \times 10^{-4}$.

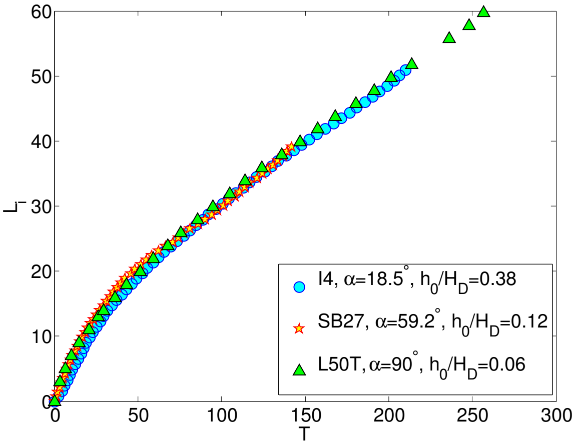

(b) $I = 0.111 \pm 0.005$, $Ek_V = (2.83 \pm 0.21) \times 10^{-2}$, $Ek_H = (4.66 \pm 0.21) \times 10^{-4}$.

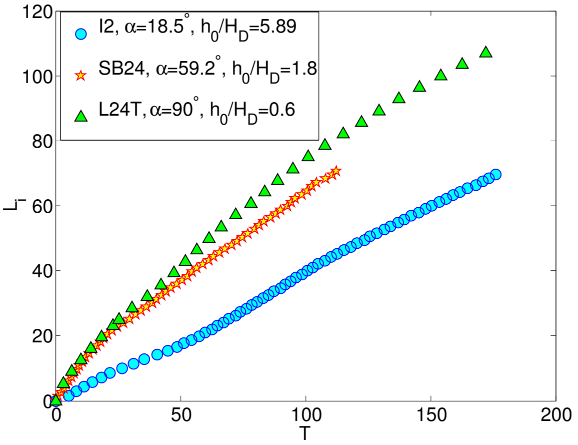

(c) $I = 1.038 \pm 0.12$, $Ek_V = (1.63 \pm 0.28) \times 10^{-4}$, $Ek_H = (6.98 \pm 0.69) \times 10^{-4}$.

Figure 9.3: Comparison of the non-dimensional plume length, L_i, as a function of the dimensionless time, T, for small-scale experiments with different sloping angles, α.

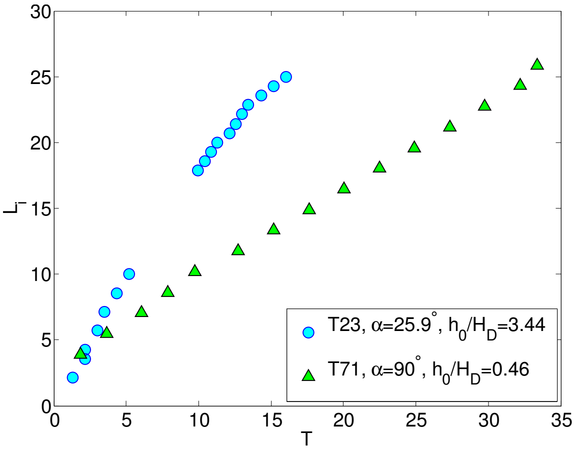

(a) $I = 0.794 \pm 0.022$, $Ek_V = (2.43 \pm 0.01) \times 10^{-5}$, $Ek_H = (5.48 \pm 0.41) \times 10^{-5}$.

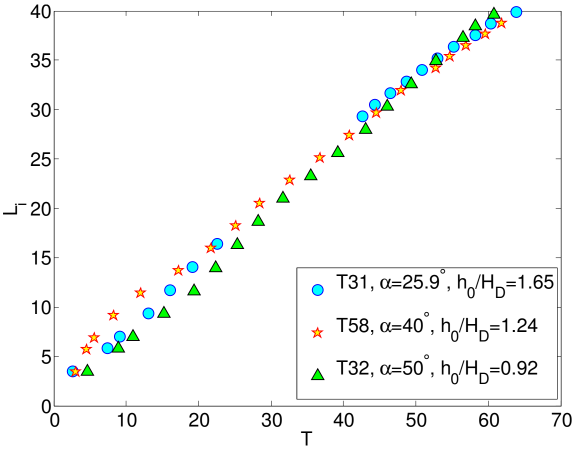

(b) $I = 0.482 \pm 0.024$, $Ek_V = (2.53 \pm 0.24) \times 10^{-4}$, $Ek_H = (1.62 \pm 0.08) \times 10^{-4}$.

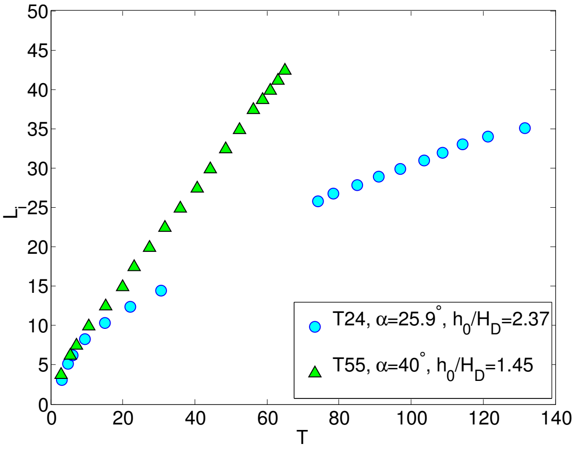

(c) $I = 0.592 \pm 0.013$, $Ek_V = (1.44 \pm 0.36) \times 10^{-4}$, $Ek_H = (1.53 \pm 0.3) \times 10^{-4}$.

Figure 9.4: Comparison of the non-dimensional plume length, L_i, as a function of the dimensionless time, T, for large-scale experiments with different sloping angles, α.

Figure 9.4a, the coastal plume flows faster on the sloping wall than on the vertical wall. In Figure 9.3b and Figure 9.4b, the introduction/variation of the sloping wall does not change the rate of elongation of the plumes. In Figure 9.3c, the plume flowing on the incline 18.5° propagates slower than the plumes flowing on the higher incline and on the vertical wall. In Figure 9.4c, at early time, the plume flowing over the incline 25.9° propagates as the plume flowing over the incline 40°, and from $T \sim 8$, the plume flowing over the incline 25.9° slows down to finally propagate at a nearly constant speed, slower than the speed of the plume flowing over the incline 40°.

From experimental observations, introducing an inclined wall (or varying its sloping angle) can increase (Figure 9.4a) or decrease (Figure 9.3c) the plume propagation speed. It can also make no difference at all on the whole evolution of the coastal current (Figure 9.3b). Surprisingly, the introduction of a sloping wall does not necessarily slow down the coastal current propagation (as noted for e.g. Whitehead & Chapman (1986)).

9.2.2 Comparison of inclined-wall experiments with inclined-wall theory

Figures 9.5(a)-(b) and Figures 9.6(a)-(b) compare small-scale and large-scale data, respectively, for the non-dimensional plume length, L_i, as a function of the dimensionless time, T, with the theoretical prediction for the different sloping angles according to (4.43). Data for the plume length are non-dimensionalized by w_0. On each figure, experiments have similar values for the dimensionless parameter I, the horizontal and vertical Ekman numbers, Ek_H and Ek_V, respectively.

First of all, the theory developed in Chapter 4 predicts a constant propagation speed for a coastal current. However, as it was discussed in the previous section, and similarly to vertical-wall coastal currents, in some experiments, coastal currents are seen to propagate at a nearly constant speed (Figure 9.6a), while in some other experiments, the coastal plumes are observed to accelerate at the start of the experiments, then to decelerate to a nearly constant propagation speed (Figure 9.5a).

For some experimental parameters combinations, agreement between experiments and theory was found to be quite good (see Figure 9.5b and Figure 9.6b). However, for some other experimental parameters combinations (usually exper-

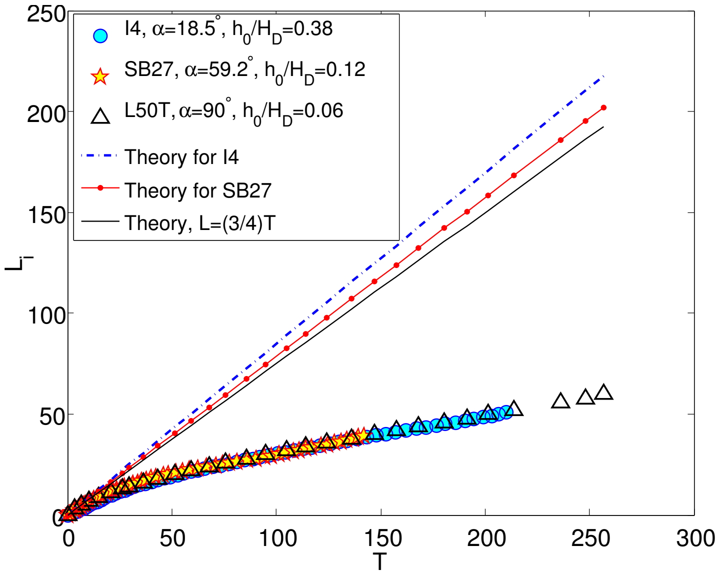

(a) $I = 0.111 \pm 0.005$, $Ek_V = (2.83 \pm 0.21) \times 10^{-2}$, $Ek_H = (4.66 \pm 0.21) \times 10^{-4}$.

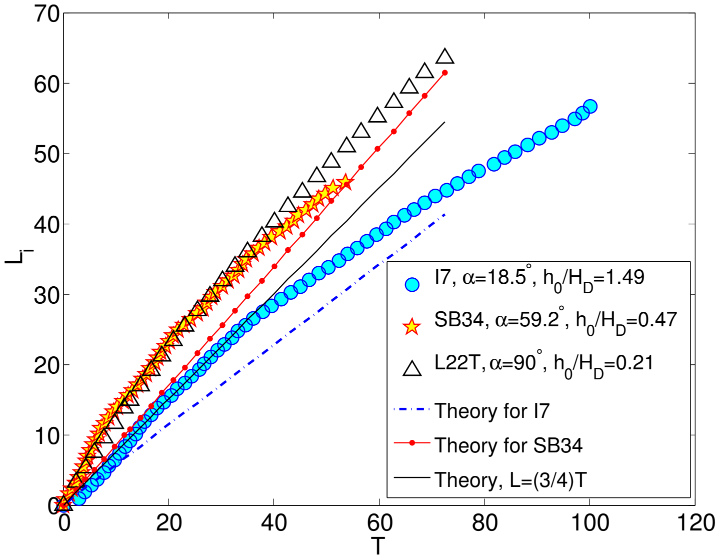

(b) $I = 0.331 \pm 0.011$, $Ek_V = (1.08 \pm 0.06) \times 10^{-3}$, $Ek_H = (2.69 \pm 0.08) \times 10^{-4}$.

Figure 9.5: Comparison of the non-dimensional plume length, L_i, as a function of the non-dimensional time, T, for small-scale experiments with different sloping angles, α. The solid lines represent the theoretical predictions for the different sloping angles according to (4.43).

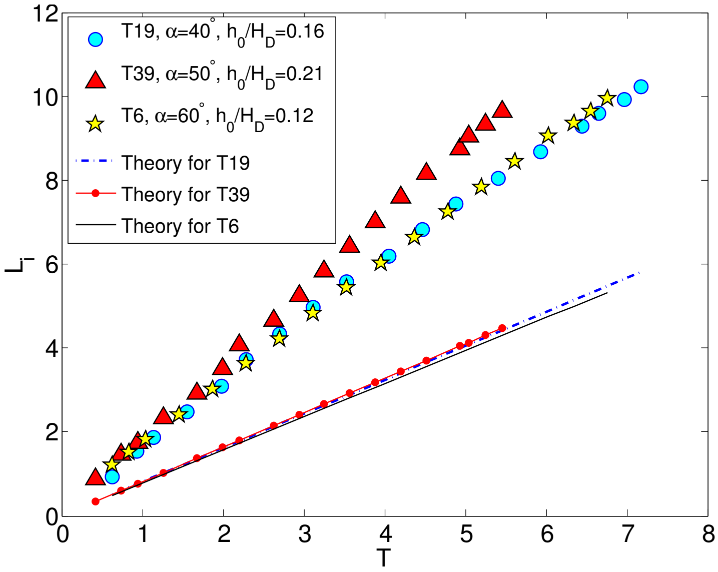

(a) $I = 0.118 \pm 0.023$, $Ek_V = (2.68 \pm 1.14) \times 10^{-3}$, $Ek_H = (4.35 \pm 0.23) \times 10^{-5}$.

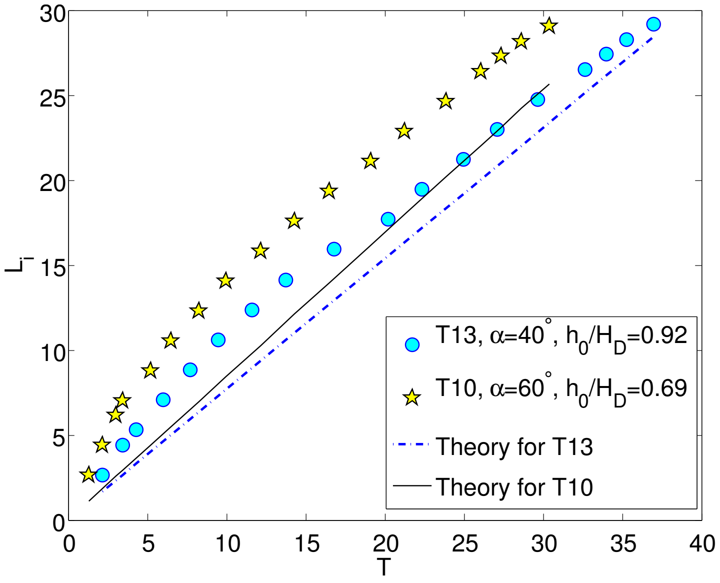

(b) $I = 0.423 \pm 0.02$, $Ek_V = (1.95 \pm 0.24) \times 10^{-4}$, $Ek_H = (9.01 \pm 0.08) \times 10^{-5}$.

Figure 9.6: Comparison of the non-dimensional plume length, L_i, as a function of the non-dimensional time, T, for large-scale experiments with different sloping angles, α. The solid lines represent the theoretical predictions for the different sloping angles according to (4.43).

iments with low flow rate), the coastal currents slowed down during the experiments to finally propagate at a constant speed smaller than the theoretical prediction (mostly observed in the small-scale study, see Figure 9.5a). Finally, some coastal currents were seen to propagate faster than the theory (mostly observed in the large-scale study, see Figure 9.6a).

The easiest way to compare theory and experiments for the plume nose propagation is to examine the plume mean velocity. The measured mean velocity, u_i^{exp}, of the plumes during their propagation from the source along the inclined wall can be calculated from the last data point for each run as $u_i^{exp} = l_i(t_{end})/t_{end}$. Hence, using $U_i = L_i/T$, $L_i = l_i/w_0$ and $T = t\Omega$, one gets $U_i = u_i/(\Omega w_0)$.

Figure 9.7 summarizes the values of the non-dimensional measured mean speed, U_i^{exp}, for the plumes flowing along an inclined wall, as a function of the non-dimensional theoretical inclined-wall plume speed , U_i^{th} (from (4.44)), for the small-scale and large-scale studies. The solid line in Figure 9.7 identifies $U_i^{exp} = U_i^{th}$, *i.e* agreement between the prediction and the corresponding experimental data point, while the dashed line identifies the best linear fit given by $0.62\ U_i^{th} + 0.51$ with a correlation of 0.21.

From Figure 9.7, and as it was noted just above, for some experimental parameters combinations, good agreement is found between experiments and theory, while for some other experimental parameters combinations, experimental velocities are overestimated or underestimated by the theory. Nonetheless, in the overall experimental results, the agreement between experimental and theoretical propagation velocities is quite poor. From Figure 9.7, the coastal currents with the propagation velocity smaller than the theoretical prediction are mainly simulated in the small-scale study while the plumes with the propagation velocity larger than the theory are modelled in the large-scale study. The discrepancy between the experiments and the theory for the plume propagation speed occurs for any coastline angle, thus the disagreement between experiments and theory does not seem to be induced by the value of the coastline angle.

In order to find whether or not the different dimensionless numbers characterizing the plume dynamics (I, h_0/H_D, Ek_V and Ek_H) have an impact on the discrepancy between the theoretical and experimental plume propagation velocities, the difference between the non-dimensional experimental and theoretical velocities is examined. Figures 9.8(a)-(b) and Figures 9.9(a)-(b) summarize the values of the difference between the non-dimensional measured mean inclined-wall speed, U_i^{exp}, and the non-dimensional predicted inclined-wall speed, U_i^{th}, as a function

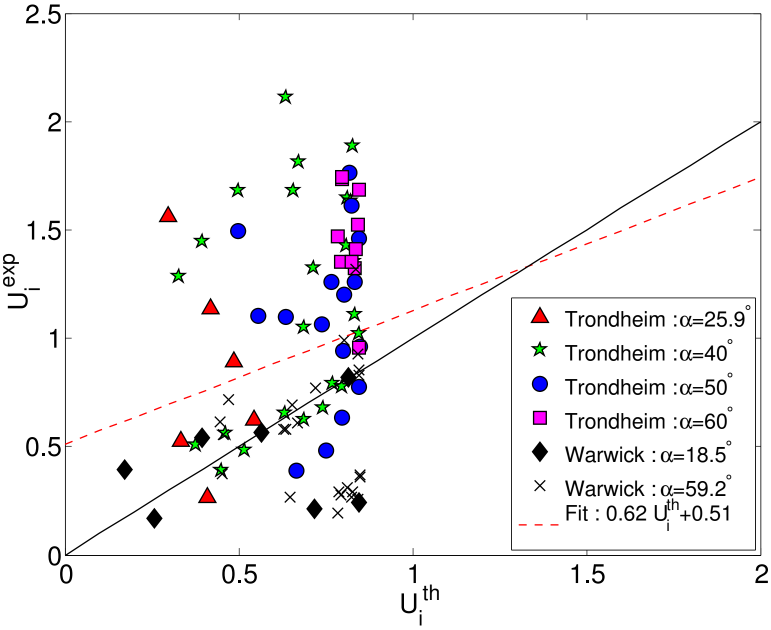

Figure 9.7: Non-dimensional measured mean inclined-wall velocity, U_i^{exp}, as a function of the non-dimensional theoretical inclined-wall velocity, U_i^{th}, for the small-scale and large-scale inclined-wall experiments. The solid line identifies $U_i^{exp} = U_i^{th}$, while the dashed line identifies the best linear fit given by $0.62\ U_i^{th} + 0.51$ with a correlation of 0.21.

of the dimensionless parameter, I (defined in (4.3)), the non-dimensional ambient depth parameter, h_0/H_D (defined in (4.11)), the horizontal Ekman number, Ek_H (defined in (4.8)), and the vertical Ekman number, Ek_V (defined in (4.9)) respectively, for the small-scale and large-scale inclined-wall experiments. The solid line on the figures identifies $U_i^{exp} = U_i^{th}$, *i.e.* agreement between theory and experiments.

Figures 9.8(a)-(b) and Figure 9.9(b) reveal that the dimensionless parameter, I, the non-dimensional ambient depth parameter, h_0/H_D, and the vertical Ekman number, Ek_V, seem to have no influence on the difference between experimental and theoretical plume velocities. On the other hand, from Figure 9.9(a), there appears to exist a dependency between the values of $(U_i^{exp} - U_i^{th})$ and the values of the horizontal Ekman number, Ek_H: except for few data points, the $(U_i^{exp} - U_i^{th})$ values increase as the Ek_H values decrease. The plumes simulated in the laboratory are found to be faster than the theoretical prediction $((U_i^{exp} - U_i^{th}) > 0)$ when the values of their horizontal Ekman number, Ek_H, are very small, that is when the viscous forces are the most negligible in the fluid system. Conversely, the plumes are slower than the theory $((U_i^{exp} - U_i^{th}) < 0)$ when the Ek_H values are large, that is when the viscous forces become important. These results are consistent with the results found in the numerical Sections 7.3 and 7.5 (one notes that the inviscid numerical simulations (for which $Ek_H = 0$) are expected to reproduce the best plumes with very low Ek_H values therefore plumes simulated in the large scale study). Thus, the magnitude of the lateral viscous forces seems to have a major impact as well on the propagation speed of coastal plumes flowing along a sloping wall.

In order to take into account in the velocity discrepancy the fact that for some experiments, the coastal currents do not propagate at a constant speed, linear fits are produced, in a similar fashion to Section 8.3, to the curves displaying the difference between the non-dimensional plume length, ${L_i}^{exp}$, for the small-scale and large-scale inclined-wall experiments, and the inclined-wall theory, ${L_i}^{th}$, according to (4.43), from the non-dimensional time, T, for which the coastal plumes propagate at a nearly constant speed. The slopes given by these fits represent estimates of the velocity discrepancy between the geostrophic theory for inclined-wall plumes and each of the inclined-wall laboratory experiments. Figure 9.10 shows the resulting estimates of the velocity discrepancy plotted against the horizontal Ekman number, Ek_H. Similarly to the previous observations of Figure 9.9(a) and to the results obtained in Section 8.3, a dependence on the horizontal Ekman

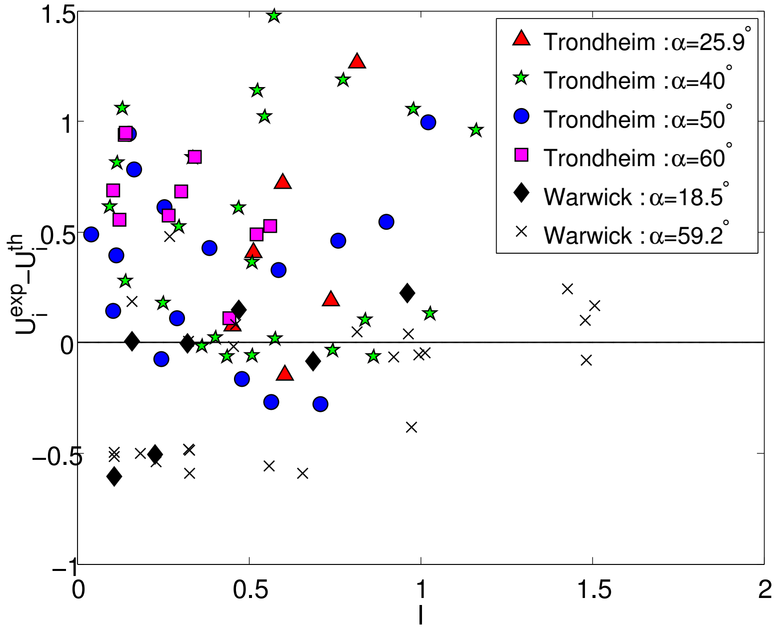

(a)

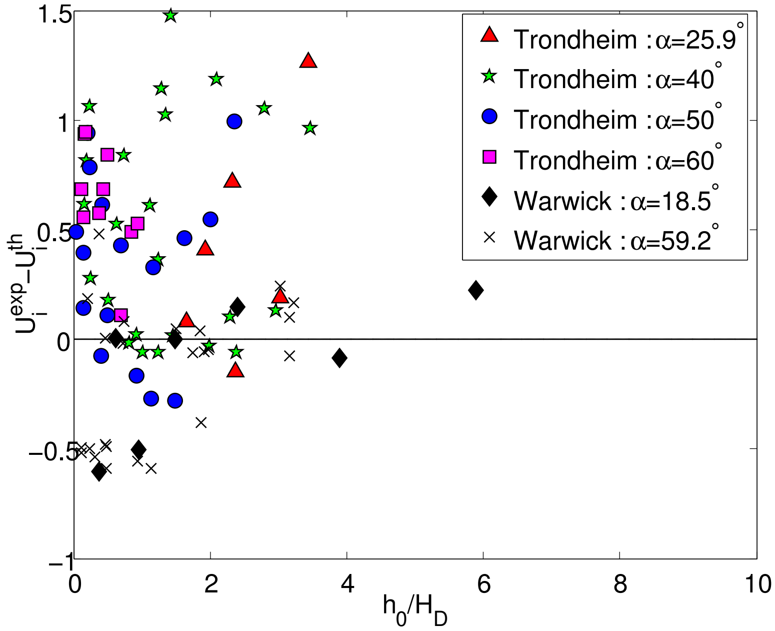

(b)

Figure 9.8: Difference between the non-dimensional measured mean inclined-wall speed, U_i^{exp}, and the non-dimensional predicted inclined-wall speed, U_i^{th}, as a function of (a) the dimensionless parameter, I, (b) the non-dimensional ambient depth parameter, h_0/H_D, for the small-scale and large-scale inclined-wall experiments. The solid line on each figure identifies $U_i^{exp} = U_i^{th}$.

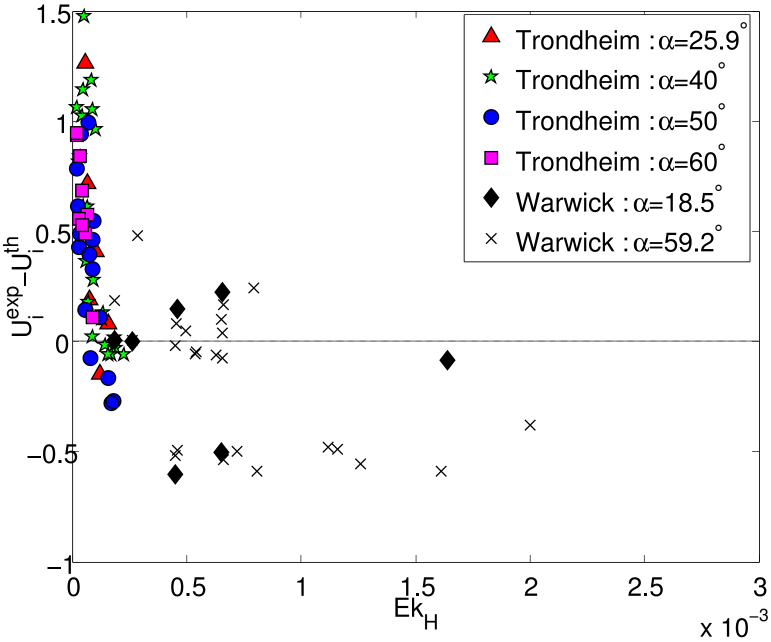

(a)

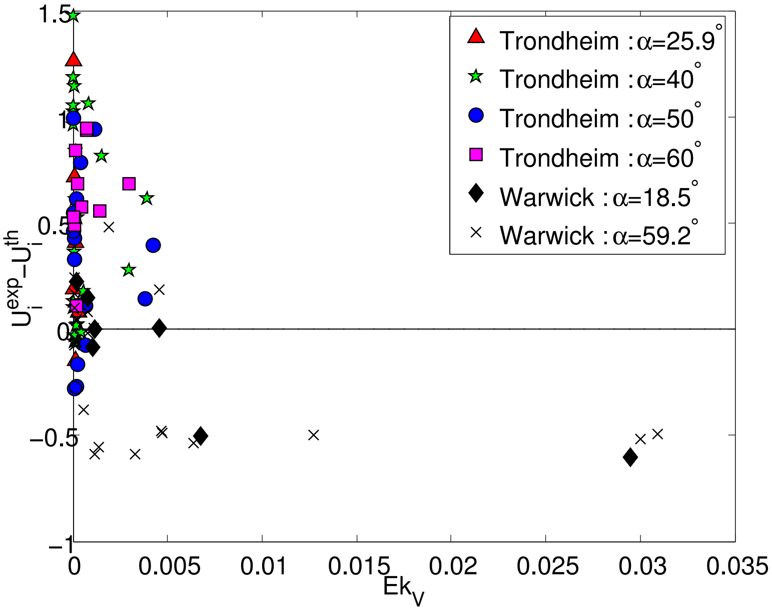

(b)

Figure 9.9: Difference between the non-dimensional measured mean inclined-wall speed, U_i^{exp}, and the non-dimensional predicted inclined-wall speed, U_i^{th}, as a function of (a) the horizontal Ekman number, Ek_H, (b) the vertical Ekman number, Ek_V, for the small-scale and large-scale inclined-wall experiments. The solid line on each figure identifies $U_i^{exp} = U_i^{th}$.

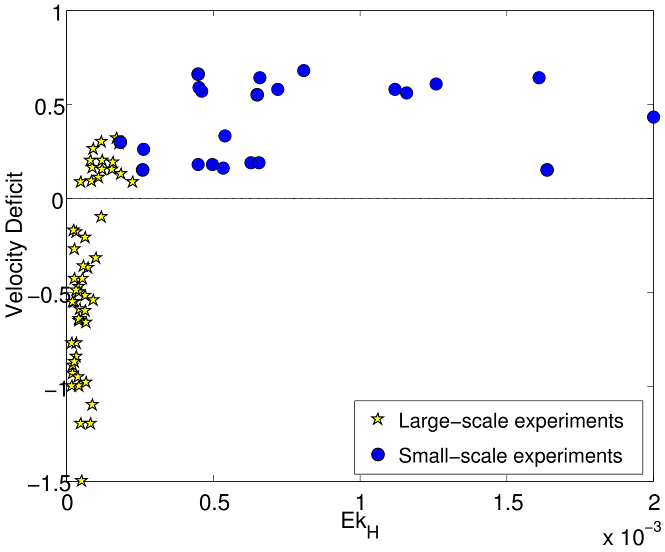

Figure 9.10: Velocity deficit for the small-scale and large-scale inclined-wall experiments as a function of the horizontal Ekman number, Ek_H.

number is observed. From Figure 9.10, and as it was noted previously in this section, gravity plumes with a very small Ek_H value (thus with a large Reynolds number, Re), are produced in the large-scale study and propagate faster than the geostrophic velocity, while plumes with a large Ek_H value, are simulated in the small-scale study and propagate slower than the geostrophic velocity. It is also worth to mention that the coastal plumes with very low Ek_H values (simulated in the large-scale study) propagate at a nearly constant speed, whereas the coastal plumes with large Ek_H values (simulated in the small-scale study) are seen to slow down during the experiments to finally propagate slower than the theoretical prediction, and as the Ek_H value increases, the magnitude of the plume deceleration gets more important.

From the numerical Sections 7.3 and 7.5, and from the results from this section, the coastal currents with very low Ek_H values are faster than the theoretical prediction while the coastal currents with high Ek_H values are slower than the theory. In this section, it was also observed that the coastal currents slower than the theory were mainly simulated in the small-scale study, while the coastal currents faster than the theory were modelled in the large-scale experiments. This observation can be explained by the size of the experimental facility. Indeed, in the small-scale study, the flow rate, q_0, never exceeded the value of 28.28 $cm^3\ s^{-1}$ and the rotation rate, Ω, never dropped off below the value of 0.49 $rad\ s^{-1}$, while in the large-scale study, q_0 never dropped off below the value of 100 $cm^3\ s^{-1}$ and Ω never exceeded the value of 0.621 $rad\ s^{-1}$. Then in the small-scale experiments, high Ω values and low q_0 values were used, giving large Ek_H values (thus coastal currents slower than the theory) whereas in the large-scale experiments, very small Ω values and very large q_0 values were used, giving very small Ek_H values (thus coastal currents faster than the theory). In addition, from Figures 9.9(a)-(b) and Figure 9.10, the coastal currents faster than the theory are found for the lowest values of their horizontal and vertical Ekman numbers, Ek_H and Ek_V, respectively. From the definitions of the horizontal Ekman number, Ek_H, in (4.8), and the vertical Ekman number, Ek_V, in (4.9), low Ek_H values imply high values for the reduced gravity, $g\prime$, and the flow rate, q_0, and low values for the rotation rate, Ω, whereas low Ek_V values imply low $g\prime$ values and high Ω and q_0 values. Thus, the coastal currents faster than the theoretical prediction are expected to be coastal currents with very large flow rate, q_0, but very large flow rates could be produced in the large-scale facility only.

Figure 9.11 displays the non-dimensional measured mean inclined-wall speed, U_i^{exp}, as a function of the horizontal Ekman number, Ek_H, for the small-scale and large-scale inclined-wall experiments. Figures displaying the non-dimensional measured mean inclined-wall speed, U_i^{exp}, as a function of the dimensionless parameter, I, the non-dimensional ambient depth parameter, h_0/H_D, and the vertical Ekman number, Ek_V, were omitted as they were similar to Figures 9.8(a)-(b) and Figure 9.9(b), respectively, and, therefore, did not show anything interesting. From Figure 9.11, the U_i^{exp} values clearly increase as the Ek_H values decrease.

In all the section, the plume length was non-dimensionalized by the theoretical vertical-wall plume width ,w_0, defined in (4.1a). It is interesting to see what would happen when non-dimensionalizing the plume length by the theoretical inclined-wall plume width, w_i, defined in (4.36). Figure 9.12 displays the values of the non-dimensional measured mean inclined-wall velocity, $(U_i^{exp})_{w_i}$, as a function of the non-dimensional theoretical inclined-wall velocity, $(U_i^{th})_{w_i}$, with $(U_i)_{w_i} = u_i/(\Omega w_i)$, for the small-scale and large-scale inclined-wall experiments. The solid line in Figure 9.12 identifies $(U_i^{exp})_{w_i} = (U_i^{th})_{w_i}$, while the dashed line identifies the best linear fit given by 1.19 $(U_i^{th})_{w_i}$ + 0.08 with a correlation of 0.64. A comparison between Figure 9.7 and Figure 9.12, and between the slopes of the best linear fits in each figure reveals that agreement between experiments and theory is much better when the plume length is non-dimensionalized by w_i.

The figures displaying the difference between the non-dimensional experi-

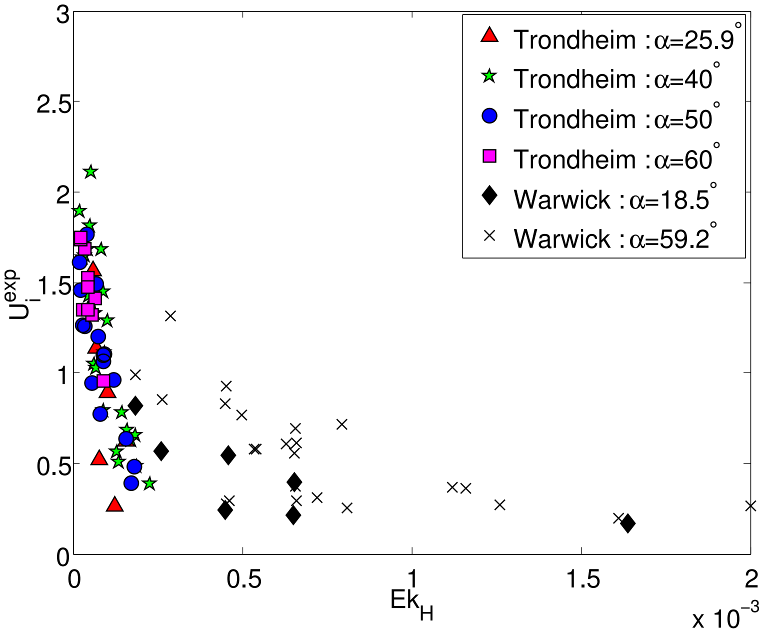

Figure 9.11: Non-dimensional measured mean inclined-wall speed, U_i^{exp}, as a function of the horizontal Ekman number, Ek_H, for the small-scale and large-scale inclined-wall experiments .

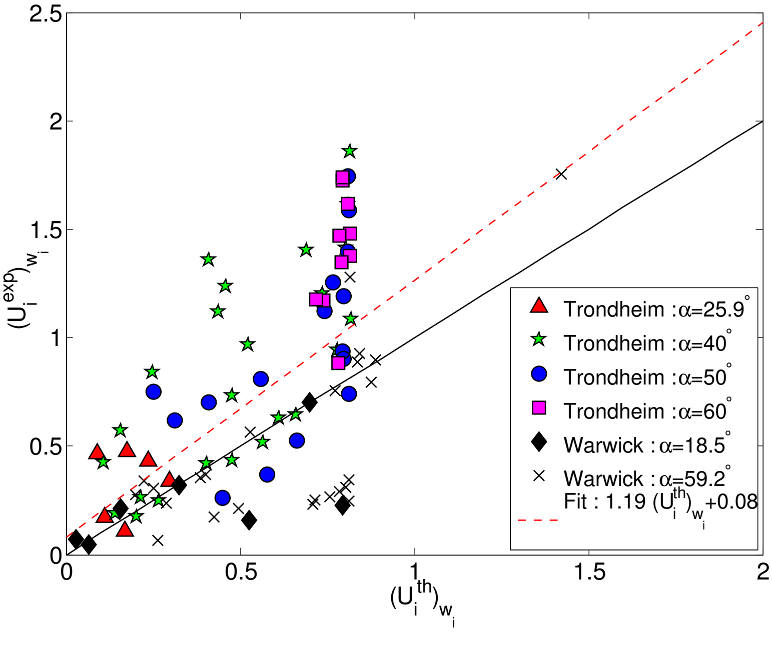

Figure 9.12: Non-dimensional measured mean inclined-wall velocity, $(U_i^{exp})_{w_i}$, as a function of the non-dimensional theoretical inclined-wall velocity, $(U_i^{th})_{w_i}$, for the small-scale and large-scale inclined-wall experiments. The solid line identifies $(U_i^{exp})_{w_i} = (U_i^{th})_{w_i}$, while the dashed line identifies the best linear fit given by $1.19\ (U_i^{th})_{w_i} + 0.08$ with a correlation of 0.64.

mental and theoretical plume velocities as a function of the different dimensionless numbers (I, h_0/H_D, Ek_V and Ek_H), when the plume length is non-dimensionalized by w_i, are not included as the figures obtained were very similar to Figures 9.8(a)-(b) and Figures 9.9(a)-(b).

Figures 9.13(a)-(b) display the values of the non-dimensional measured mean inclined-wall speed, $(U_i^{exp})_{w_i}$, as a function of the dimensionless parameter, I, and the non-dimensional ambient depth parameter, h_0/H_D, respectively, for the small-scale and large-scale inclined-wall experiments. When non-dimensionalizing the plume length by w_i, it seems to exist a dependency between the non-dimensional measured mean inclined-wall speed, $(U_i^{exp})_{w_i}$, and the dimensionless parameters, I and h_0/H_D (this dependency was not observed when the plume length was non-dimensionalized by w_0). From Figures 9.13(a)-(b), the $(U_i^{exp})_{wi}$ values decrease as both the I and h_0/H_D values increase. Also, and similarly to when data for the plume length were non-dimensionalized by w_0, the $(U_i^{exp})_{wi}$ values decrease as the Ek_H values increase (the figure is not displayed as it is similar to Figure 9.11).

From the Section 4.2, the non-dimensional theoretical velocities, U_i^{th} and $(U_i^{th})_{w_i}$, are functions of $H/\tan\alpha$ but $H/\tan\alpha$ is a function of I (from (4.2b)), and, for small values of α, $H/\tan\alpha \sim H/\alpha$. Thus U_i^{th} and $(U_i^{th})_{wi}$ are functions of I and H/α. Therefore a relation of dependence between the non-dimensional measured velocities, U_i^{exp} and $(U_i^{exp})_{w_i}$, and, the dimensionless numbers, I and h_0/H_D, should be found if, of course, agreement between experiments and theory is found: in the first case, that is for U_i^{exp}, the dependence relation is not observed at all, as the agreement between experiments and theory is quite poor (see Figure 9.7), while in the second case, that is for $(U_i^{exp})_{w_i}$, a dependence relation is partially observed (see Figures 9.13(a)-(b)), as the agreement between experiments and theory is partially found (see Figure 9.12).

9.3 Coastal current height

In this section, large-scale inclined-wall experimental results for the plume depth are presented and compared to the theoretical prediction from Chapter 4.

Thomas & Linden (2007) found that the depth of a plume flowing along a vertical wall decreases with distance from the source, and has a maximum height, h_m, just downstream of the source. Figure 9.14, taken from Thomas & Linden

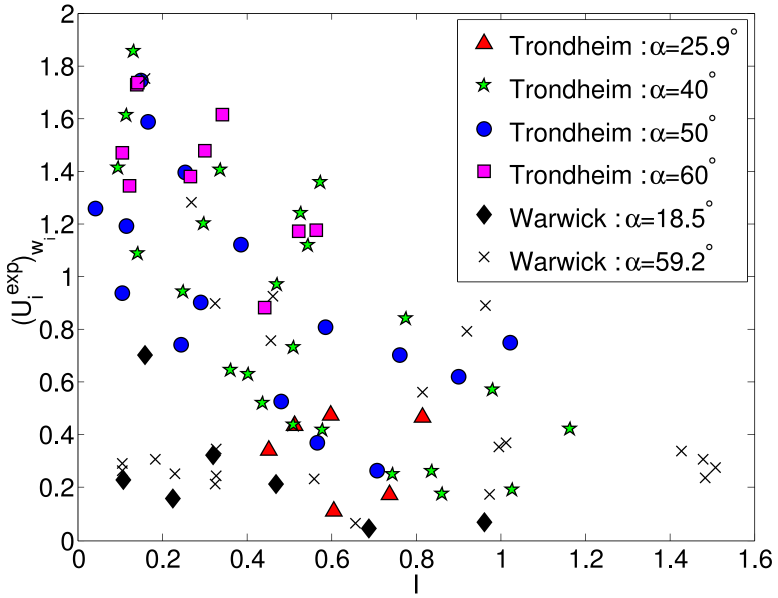

(a)

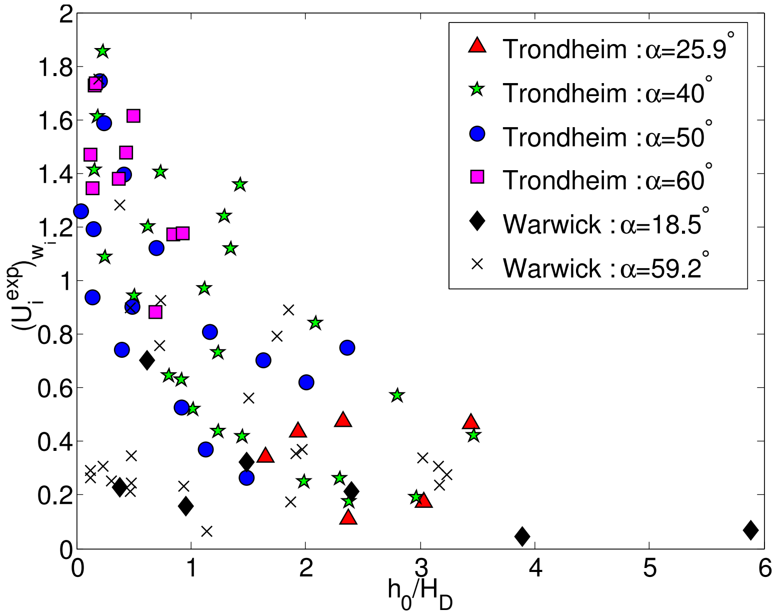

(b)

Figure 9.13: Non-dimensional measured mean inclined-wall speed, $(U_i^{exp})_{wi}$, as a function of (a) the dimensionless parameter, I, (b) the non-dimensional ambient depth parameter, h_0/H_D, for the small-scale and large-scale inclined-wall experiments.

(2007), illustrates the height profile of a plume at the wall ($y = 0$) in the x-z plane of Figure 4.1. Thomas & Linden (2007) compared the maximum depth, h_m, to their theoretical prediction, h_0, given in (4.1b), and found very good agreement between h_m and h_0.

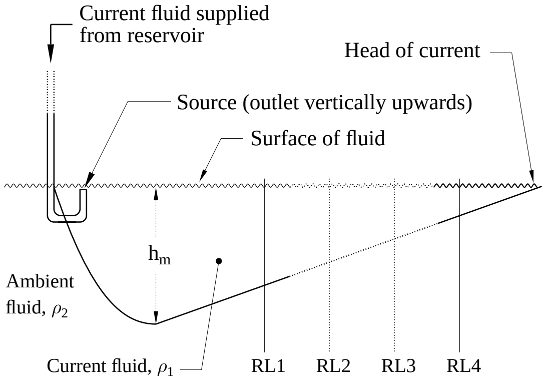

Figure 9.14: Sketch from Thomas & Linden (2007) illustrating a side-view of a plume.

In the present study, similarly to the vertical-wall plumes, the depth, h_i, of a plume flowing along an inclined wall was observed to decrease with the alongshore distance, from the source to the plume head, and to have a maximum value, h_{i_m}, a few centimetres downstream of the source. The value of h_{i_m} was monitored with the video camera shown in Figure 5.12 and Figure 5.13. The recordings yielded h'_{i_m} from which one finds $h_{i_m} = h'_{i_m} \sin\alpha$.

Figure 9.15 displays the maximum measured plume height, h_{i_m}, near the source, as a function of the theoretical predictions, h_0 and h_i, for the depth of a plume flowing along a vertical wall, and along an inclined coastline, respectively. The solid line in the figure identifies agreement between the experiments and the predictions, while the blue and red dashed lines identify the best linear fits given by 0.91 $h_0 + 2.52$ with a correlation of 0.88, and 1.51 $h_i + 0.7$ with a correlation of 0.8, respectively. Figure 9.15 shows that the maximum measured plume height, h_{i_m}, is better predicted by the theoretical vertical-wall height, h_0 (given in (4.1b)), rather than by the theoretical inclined-wall height, h_i (numerically computed from (4.30)). The data for the non-dimensional plume height, $H_i^{exp} = h_{i_m}/w_0$, are displayed in Figure9.16 as a function of the dimensionless parameter, I. The solid line included in the figure represents the theoretical prediction, $H = 2I^{5/4}$, from equations (4.46) and (4.2b). The dashed line is the best fit to the experimental

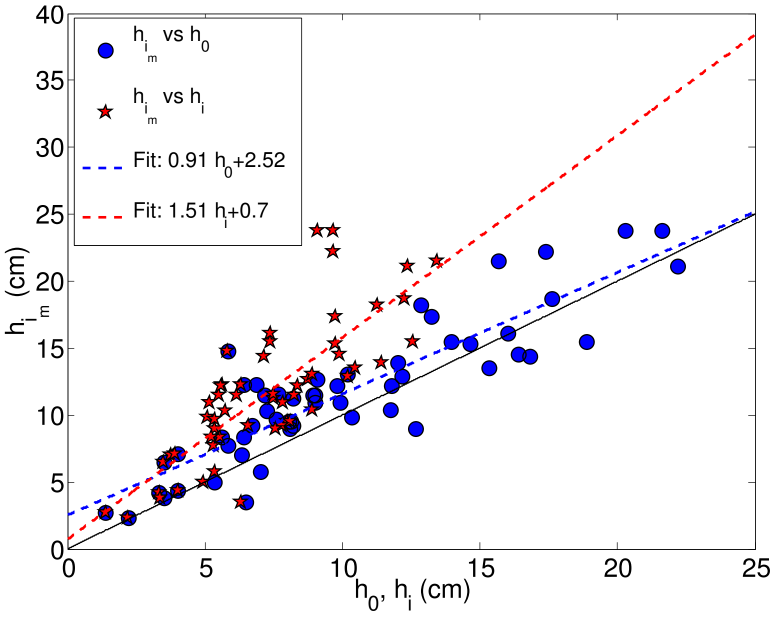

Figure 9.15: Maximum measured plume height, h_{i_m}, near the source, as a function of the theoretical heights, h_0 and h_i, for vertical-wall and inclined-wall plumes, respectively. The solid line identifies agreement between the experiments and the theories, while the blue and red dashed lines identify the best linear fits given by $0.91\ h_0 + 2.52$ with a correlation of 0.88, and $1.51\ h_i + 0.7$ with a correlation of 0.8, respectively.

data given by $2.22(I)^{1.15}$. Figure9.16 reveals a very good agreement between the theoretical values, H, and the experimental values, H_i^{exp}.

Hence, experiments show that the maximum depth, h_{i_m}, of inclined-wall plumes near the source is well predicted by the depth of vertical-wall plumes from the models of Thomas & Linden (2007) and Avicola & Huq (2002). For plumes flowing along inclined walls, Yankovsky & Chapman (1997) argued that, in equilibrium, the depth of a plume flowing along a vertical coastline should also be the depth where the front intersects the bottom; these data support the conclusion of Yankovsky & Chapman (1997).

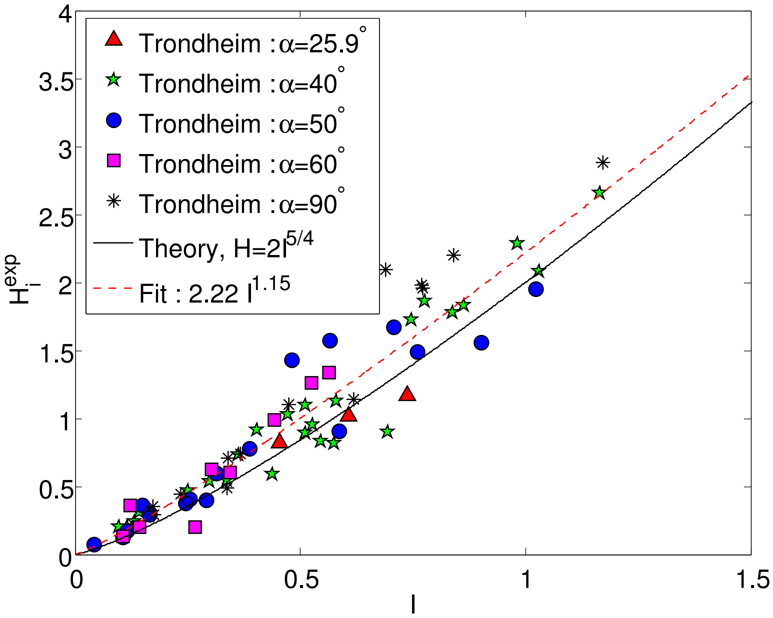

Figure 9.16: Non-dimensional maximum plume height, H_i^{exp}, near the source, as a function of the dimensionless parameter, I, for the large-scale inclined-wall experiments. The solid line represents the theoretical prediction, $H = 2I^{5/4}$, while the dashed line is the best fit line given by $2.22(I)^{1.15}$.

9.4 Coastal current width

In this section, PIV small-scale inclined-wall results for the plume width are presented and compared to the PIV small-scale vertical-wall results introduced in Section 7.4 and to the theoretical prediction from Chapter 4.

Figure 9.17 displays the non-dimensional plume width, W_i, as a function of the dimensionless time, T, measured at the distance, d_S, downstream from the source, with $d_S = 57.8\ cm$, for all the PIV vertical-wall and inclined-wall experiments. Width data are non-dimensionalized by w_0. The PIV inclined-wall experiments precisely duplicate the PIV vertical-wall experiments, except for the introduction of the sloping wall. For some experiments, width measurements were stopped before the end of the experiments due to the presence of instabilities in the plumes. Width data from two vertical-wall experiments are not displayed in Figure 9.17 as one experiment was too unstable and width extraction was not possible, and one experiment had data not usable. Width data from three inclined-wall experiments are also not displayed in Figure 9.17 as the data were not usable.

From Figure 9.17, for the vertical-wall experiments and for the majority of the inclined-wall experiments (except two of them) as well, the non-dimensional width measurements closely cluster around a single curve, growing as $T^{\frac{1}{2}}$ (as Lentz & Helfrich (2002) and Thomas & Linden (2007) also found). After examination of the experimental parameters, the two inclined-wall experiments, for which the width measurement expands the furthest offshore in Figure 9.17, have the largest value for the non-dimensional ambient depth parameter, h_0/H_D.

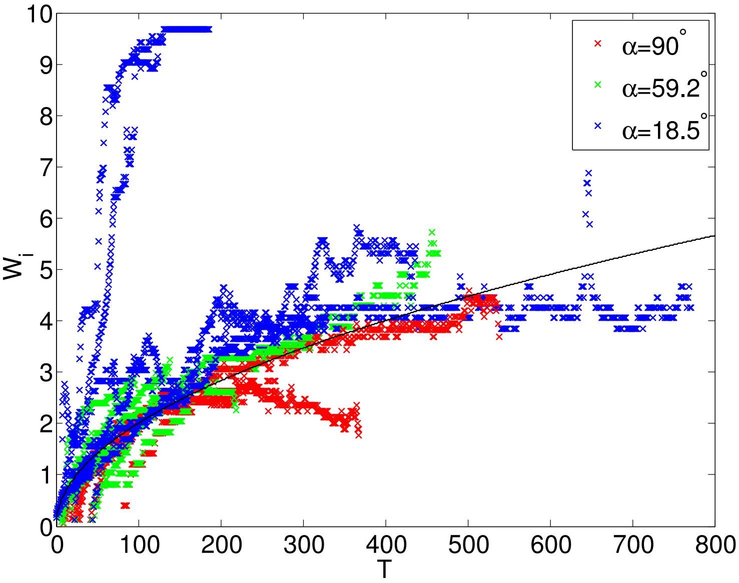

Figure 9.17: Summary of the non-dimensional plume width, W_i, as a function of the dimensionless time, T, for the PIV small-scale vertical-wall and inclined-wall experiments. The width was measured at the distance, d_S, downstream from the source, with $d_S = 57.8\ cm$. The black curve on the figure of equation $0.2(T)^{\frac{1}{2}}$ is just to show that the majority of the plume widths grows as $T^{\frac{1}{2}}$.

Figures 9.18(a)-(c) compare the non-dimensional plume width, W_i, as a function of the dimensionless time, T, measured at the distance, d_S, downstream from the source, with $d_S = 57.8\ cm$, for PIV small-scale experiments with different sloping angles. In some experiments, the introduction/variation of the sloping wall did not change drastically the plume width (Figure 9.18a), while in some other experiments, the coastal plumes became wider when flowing along a sloping wall (especially when flowing along a gentle slope, see Figure 9.18b).

Figure 9.19 and Figure 9.20 display a summary of the values for the non-dimensional plume width, W_i, as a function of $H/\tan(\alpha)$ and as a function of the non-dimensional ambient depth parameter, h_0/H_D, respectively, for the PIV inclined-wall experiments (and also for the PIV vertical-wall experiments in Figure 9.20). The solid line in Figure 9.19 represents the theoretical prediction, $W_i = \sqrt{(H/\tan(\alpha))^2 + 1}$, according to (4.45). To quantify the non-dimensional plume width, W_i, in Figure 9.19 and Figure 9.20, W_i was averaged for each experiment from the last data point to the data point such that the non-dimensional time interval, ΔT, of the measurements, was $10 < \Delta T < 500$ (the non-dimensional time interval length depended on the experiment duration). The standard deviation was calculated for each value found for W_i.

The data for the plume width in Figure 9.19 seem to follow the trend of the curve representing the theoretical prediction. It will be shown shortly that the best agreement between experiments and theory for the plume width is found for plumes with low Ek_H values. From Figure 9.20, it seems that the non-dimensional plume width, W_i, increases as the non-dimensional ambient depth parameter, h_0/H_D, increases (the h_0/H_D values increase as the sloping angle decreases). This last result is consistent with Whitehead & Chapman (1986) who observed that a coastal current was wider when flowing along an inclined coastline.

Figure 9.21 displays the non-dimensional plume width, $(W_i)_{w_i}$, as a function of the dimensionless time, T, measured at the distance, d_S, downstream from the source, with $d_S = 57.8\ cm$, for all the PIV vertical-wall and inclined-wall experiments from Figure 9.17. Width data in Figure 9.21 (and from now) are non-dimensionalized by the theoretical inclined-wall plume width, w_i, defined in (4.36). Similarly to Figure 9.17, the non-dimensional width measurements from Figure 9.21 for the vertical-wall experiments and for the majority of the inclined-wall experiments (except one of them) closely cluster around a single curve, growing as $T^{\frac{1}{2}}$. When non-dimensionalizing the width data by w_0, the

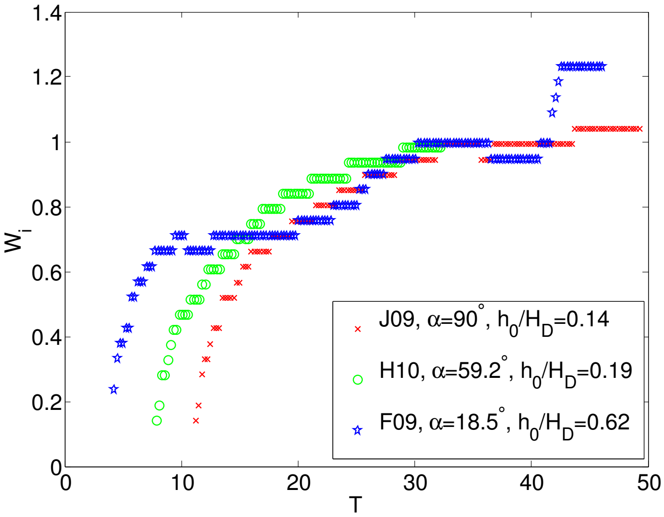

(a) $I = 0.157 \pm 0.001$, $Ek_V = (4.69 \pm 0.07) \times 10^{-3}$, $Ek_H = (1.83 \pm 0.01) \times 10^{-4}$.

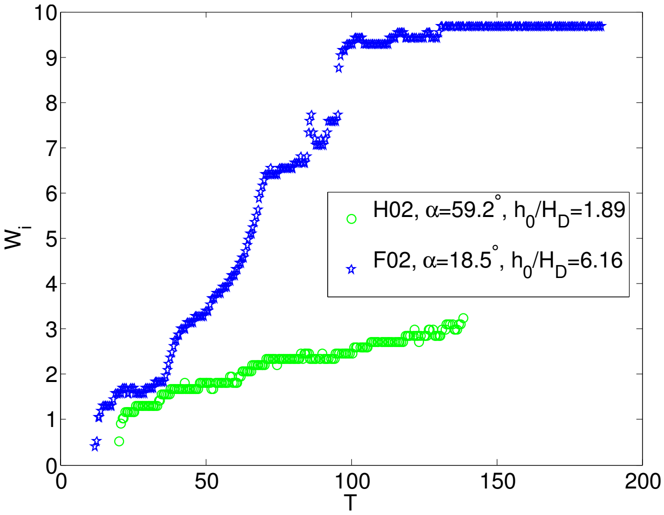

(b) $I = 0.99 \pm 0.007$, $Ek_V = (1.69 \pm 0.02) \times 10^{-4}$, $Ek_H = (6.62 \pm 0.02) \times 10^{-4}$.

Figure 9.18: Comparison of the non-dimensional plume width, W_i, as a function of the non-dimensional time, T, for PIV experiments with different sloping angles, α.

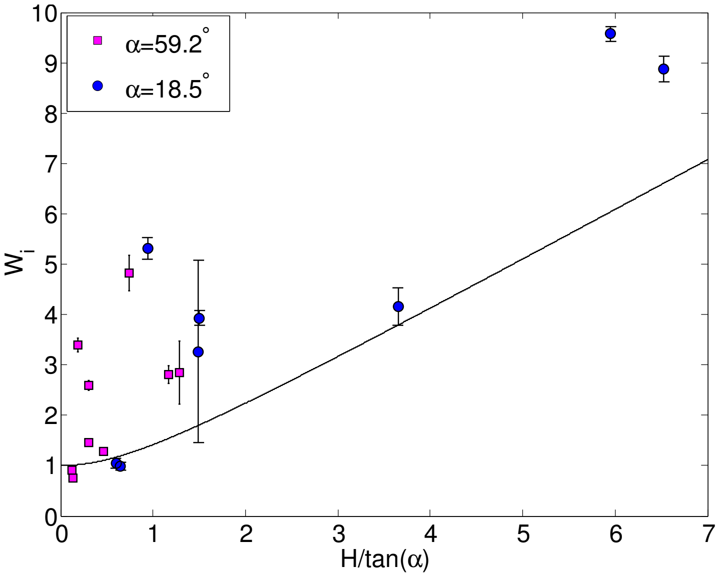

Figure 9.19: Summary of the (averaged) non-dimensional plume width, W_i, as a function of $H/\tan(\alpha)$ for the PIV small-scale inclined-wall experiments. The solid line represents the theoretical prediction, $W_i = \sqrt{(H/\tan(\alpha))^2 + 1}$. The error bars are standard deviation errors of the averaged non-dimensional plume width.

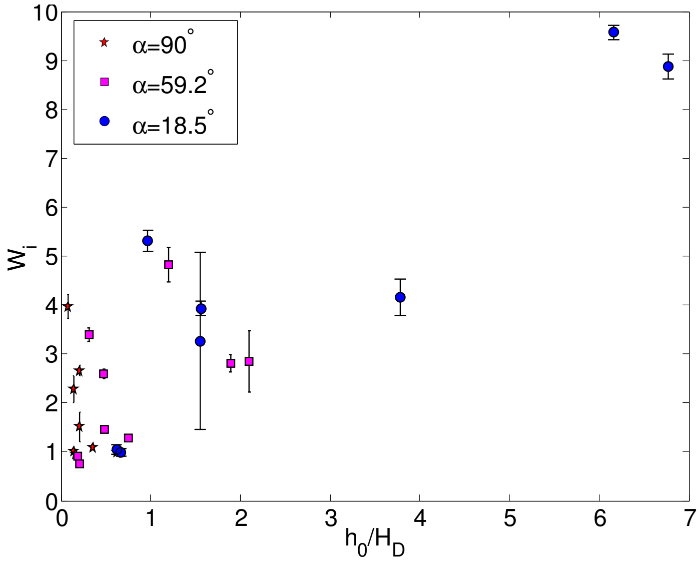

Figure 9.20: Summary of the (averaged) non-dimensional plume width, W_i, as a function of the non-dimensional ambient depth parameter, h_0/H_D, for the PIV small-scale vertical-wall and inclined-wall experiments. The error bars are standard deviation errors of the averaged non-dimensional plume width.

plume width measurements are greater for the plumes flowing along the incline $\alpha = 18.5°$ (Figure 9.17), while when non-dimensionalizing the width data by w_i (therefore when taking into account the topography in the non-dimensionalizing scheme), the plume width measurements are smaller for the plumes flowing along the incline $\alpha = 18.5°$ (Figure 9.21). After examination of the experimental parameters, the inclined-wall experiment, for which the width measurement expands the nearest inshore in Figure 9.21, has the largest value for the horizontal Ekman number, Ek_H, combined with a large value for the non-dimensional ambient depth parameter, h_0/H_D.

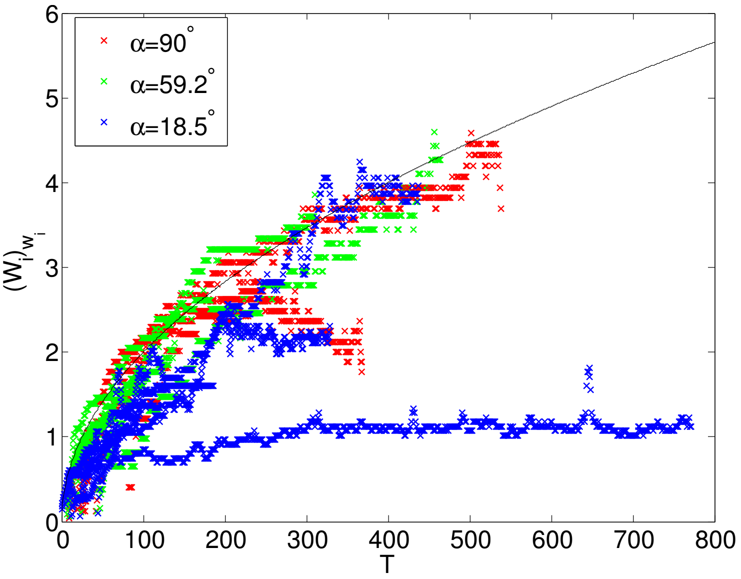

Figure 9.21: Summary of the non-dimensional plume width, $(W_i)_{w_i}$, as a function of the dimensionless time, T, for the *PIV* small-scale vertical-wall and inclined-wall experiments. The width was measured at the distance, d_S, downstream from the source, with $d_S = 57.8\ cm$. The black curve on the figure of equation $0.2(T)^{\frac{1}{2}}$ is just to show that the majority of the plume widths grows as $T^{\frac{1}{2}}$.

Figures 9.22(a)-(b) display a summary of the values for the non-dimensional plume width, $(W_i)_{w_i}$, as a function of the non-dimensional ambient depth parameter, h_0/H_D, and the horizontal Ekman number, Ek_H, respectively, for the *PIV* vertical-wall and inclined-wall experiments. The solid line on the Figures 9.22(a)-(b) identifies $(W_i)_{w_i} = 1$, that is agreement between experiments and theory. To quantify the non-dimensional plume width, $(W_i)_{w_i}$, in Figures 9.22(a)-(b), $(W_i)_{w_i}$ was averaged for each experiment from the last data point to the data point such that the non-dimensional time interval, ΔT, of the measurements, was

$10 < \Delta T < 500$. The standard deviation was calculated for each value found for $(W_i)_{w_i}$.

Despite the small data number, Figure 9.22a suggests that the value for the non-dimensional plume with, $(W_i)_{w_i}$, decreases as the value for the non-dimensional ambient depth parameter, h_0/H_D, increases. It seems also that for large h_0/H_D values, agreement between the theory and the experiments for the plume width is found. Although the important data scatter, but similarly to the results found in Section 7.4, Figure9.22b suggests that the $(W_i)_{w_i}$ values increase as the Ek_H values increase; best agreement between experiments and theory is found for small Ek_H values (except for plumes with large h_0/H_D values for which agreement between experiments and theory for the plume width seems to be found, whatever is the value of the horizontal Ekman number, Ek_H).

In the next chapter, results from other experimental studies and from oceanic observations are compared to the results presented in this chapter and to the theory from Chapter 4.

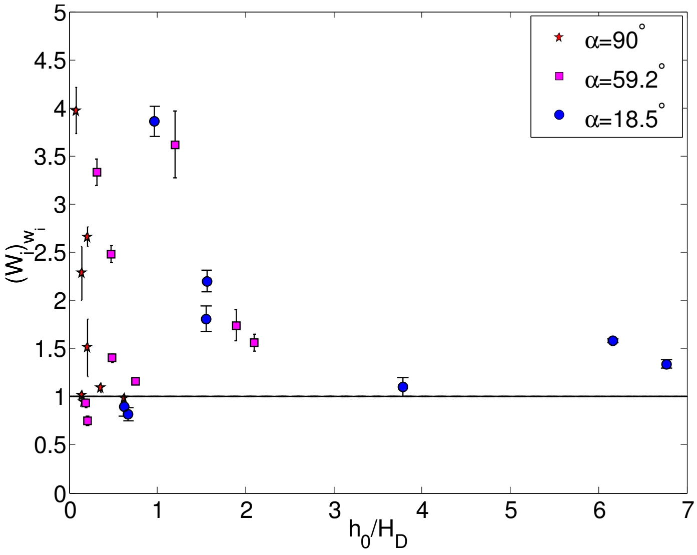

(a)

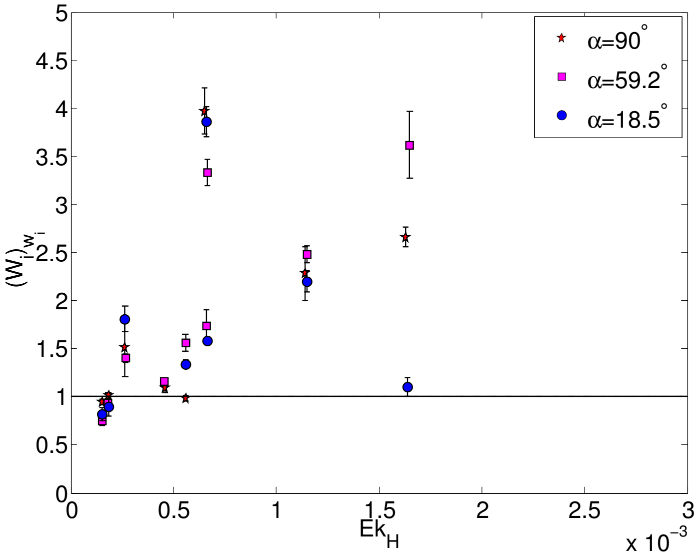

(b)

Figure 9.22: Summary of the (averaged) non-dimensional plume width, $(W_i)_{w_i}$, as a function of (a) the non-dimensional ambient depth parameter, h_0/H_D, and (b) the horizontal Ekman number, Ek_H, respectively, for the PIV small-scale vertical-wall and inclined-wall experiments. The solid line on the figures identifies $(W_i)_{w_i} = 1$, that is agreement between experiments and theory. The error bars are standard deviation errors of the averaged non-dimensional plume width.

CHAPTER 10

Comparison of the present theoretical and experimental results with other studies

In this chapter, the theory developed in Chapter 4 and the experimental results presented in Chapter 9 are compared to the experimental results of Whitehead & Chapman (1986) and Avicola & Huq (2002), and to the theoretical model and experimental results of Lentz & Helfrich (2002). Oceanic observations are also compared to the theory from Chapter 4 and to the theoretical model of Lentz & Helfrich (2002).

10.1 Summary of the experimental set-up of Whitehead & Chapman (1986), Avicola & Huq (2002) and Lentz & Helfrich (2002)

Whitehead & Chapman (1986), Avicola & Huq (2002) and Lentz & Helfrich (2002) conducted experiments for coastal plumes flowing along inclined coastlines. The experimental set-up of these three studies is briefly reviewed here.

10.1.1 Experiments of Whitehead & Chapman (1986)

Whitehead & Chapman (1986) performed three sets of experiments. In their first set of experiments (called "Experiment I"), buoyant dyed fluid was pumped into an 89.8 *cm* diameter rotating tank at a constant flow rate along a vertical wall. The resulting gravity current flowed along the wall, encountered a sloping bottom, with angle $\alpha = 11.5°$, and then flowed along the slope. The values of the rotation rate, Ω, and the reduced gravity, $g\prime$, were varied in 12 different runs. The arrival times of the gravity current nose at 10 *cm* increments along the slope over a distance of 50 *cm* were recorded and are listed in their Table 1. The plume propagation speed, u_i^{exp}, for their experiments was calculated from the last data point for each run. The plume width and depth were not recorded for these runs. Details of these 12 runs are listed in Table E.2 of Appendix E.

Their second and third sets of experiments were not considered here as the coastal current was generated differently than in the experiments presented in Chapter 5, that is by the release of a reservoir of buoyant fluid, *i.e* a dam break. Furthermore, their third set of experiments was exclusively conducted to measure the shelf-wave phase speeds observed during their experiments.

10.1.2 Experiments of Avicola & Huq (2002)

In their experimental study, Avicola & Huq (2002) used two tanks which were installed onto a 1.2 *m* diameter rotating turntable. They carried out 8 experiments, 3 using a tank with a flat bottom (named experiments D, E, F), and 5 using a tank with a bottom slope, with angle $\alpha = 19.1°$ (named experiments A, B, C, G, H). Dyed freshwater was injected at a constant flow rate. The values of the rotation rate, Ω, the flow rate, q_0, and the reduced gravity, $g\prime$, were varied in the different runs. Details of these 8 experiments are summarized in Table E.1 of Appendix E.

The difference between the inclined-wall experiments presented in this study, and the experiments of Avicola & Huq (2002) with their sloping bottom tank is that, instead of having a topography composed of a single sloping wall (as in this study ; see Figure 4.2 for a schematic of a side-view of a coastal current flowing along an inclined wall in the experiments presented in Chapter 5), Avicola & Huq (2002) had a continental shelf composed of a vertical wall, with a coastal wall depth, H_C, and a bottom slope extending offshore for 15 *cm* uniformly around the tank (see Figure 10.1 for a schematic of their experimental configuration using the sloping bottom tank). Then offshore of their continental shelf was a 15 *cm* abyss. The ocean ambient depth, H_D, for the experiments of Avicola & Huq (2002) with the sloping bottom tank was computed in Table E.2 as $H_D = H_C + \alpha w_0$, where H_C is the coastal wall depth, α is the sloping bottom angle and w_0 is the theoretical vertical-wall plume width defined in (4.1a).

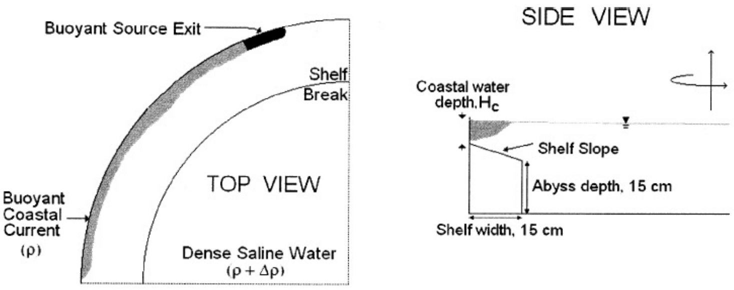

Figure 10.1: Schematic depicting the experimental configuration of Avicola & Huq (2002) using the sloping bottom tank (from Avicola & Huq (2002)).

Only the experiments G and H of Avicola & Huq (2002) from their 5 experiments with the continental shelf were compared to the theory and experiments of the present study because in the experiments A, B, C of Avicola & Huq (2002) with the continental shelf, the theoretical plume depth, h_0, was much smaller than the coastal wall depth, H_C, *i.e* $h_0/H_C < 0.15$, and therefore, from what will be demonstrated in Chapter 11, the plumes simulated in their experiments A, B, C should not feel any effect from the sloping bottom and should propagate as if they were flowing along a simple vertical coastline above a deep abyss. As the theoretical plume depth, h_0, for their experiments G and H is larger than the continental shelf, H_C, *i.e* $h_0/H_C > 1.35$, and in order to compare these experiments with the theory from Chapter 4, which was developed for a single inclined coastline (and not for a continental shelf), the topography in their experiments G and H is assumed to be a single slope with angle $\alpha = 19.1°$.

The data of Avicola & Huq (2002) were collected from their Figure 7 which summarizes the plume length and width as a function of time for their 8 runs. The non-dimensional data points for their experiments G and H were reproduced from enlarged copies of their Figures 7(e)-(f). Either the values of their scale width, R, tabulated for their experiments G and H in the Table 2 of Avicola & Huq (2002) are incorrect or some of the listed values for their reduced gravity, $g\prime$, their scale depth, h, and their Coriolis parameter, f, are incorrect. Calculating their scale width, R, for their experiments G and H with the values for $g\prime$, h and f listed in their Table 2 gives the values for R of 2.01 cm and 5.27 cm, respectively. These recalculated values of their scale width, R, were used to invert the non-dimensionalization scheme applied to the data points in the Figures 7(e)-(f) of

Avicola & Huq (2002) and to obtain the raw data for the plume length and width from their experiments G and H. Their plume propagation speed, u_i^{exp}, was afterwards calculated from the last data point for their experiments G and H. To quantify their plume width, averages of their width measurements were computed over the last five observations for their experiments G and H.

10.1.3 Experiments of Lentz & Helfrich (2002)

Lentz & Helfrich (2002) conducted 28 experiments, similar to the experiments presented in this study, investigating buoyant gravity currents flowing along sloping bottoms in a 2.1 m diameter rotating tank. The values of the rotation rate, Ω, the flow rate, q_0, the reduced gravity, $g\prime$, and the sloping angle, α, were varied. The data for their measured plume propagation speed and width are tabulated in the Table 2 of Lentz & Helfrich (2002) where they are referred to as ${c_p}^{obs}$ and ${W_p}^{obs}$, respectively. Their experimental parameters are listed in Tables E.3 and E.4 of Appendix E.

10.2 Comparison with other experimental study

In this section the experimental results of Avicola & Huq (2002), Lentz & Helfrich (2002) and Whitehead & Chapman (1986) are compared to the theoretical model developed in Chapter 4 and the experimental results presented in Chapter 9.

10.2.1 Coastal current propagation velocity

Figure 10.2 summarizes the values of the non-dimensional measured mean inclined-wall speed, U_i^{exp}, as a function of the non-dimensional theoretical inclined-wall speed , U_i^{th} (from (4.44)), for the experiments of Avicola & Huq (2002), Lentz & Helfrich (2002) and Whitehead & Chapman (1986) described in Section 10.1. Data for the plume velocity are non-dimensionalized by w_0 thus $U_i = u_i/(\Omega w_0)$. The solid line in Figure 10.2 identifies $U_i^{exp} = U_i^{th}$, *i.e* agreement between the prediction and the corresponding experimental data point, while the dashed line identifies the best linear fit given by 0.95 $U_i^{th} + 0.04$ with a correlation of 0.89.

A comparison between Figure 9.7 and Figure 10.2, and between the slope values for the best linear fits in Figure 9.7 and Figure 10.2 reveals that while poor agreement between the theoretical model from Chapter 4 and the experimental results presented in Chapter 9 is found, a very good agreement between the theory from Chapter 4 and the experiments of Avicola & Huq (2002), Lentz & Helfrich (2002) and Whitehead & Chapman (1986) is observed.

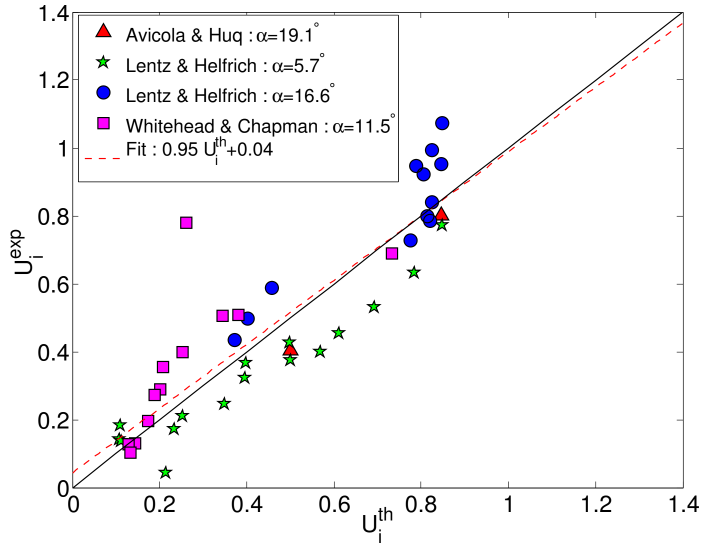

Figure 10.2: Non-dimensional measured mean inclined-wall velocity, U_i^{exp}, as a function of the non-dimensional theoretical inclined-wall velocity, U_i^{th}, for the experiments of Avicola & Huq (2002), Lentz & Helfrich (2002) and Whitehead & Chapman (1986). The solid line identifies $U_i^{exp} = U_i^{th}$, while the dashed line identifies the best linear fit given by 0.95 $U_i^{th} + 0.04$ with a correlation of 0.86.

Figure 10.3 resumes the values of the ratio, U_i^{exp}/U_0, of the non-dimensional measured mean inclined-wall velocity to the non-dimensional theoretical vertical-wall velocity, as a function of $H/\tan(\alpha)$, where H is defined in (4.2b), for the experiments of Avicola & Huq (2002), Lentz & Helfrich (2002) and Whitehead & Chapman (1986) displayed in Figure 10.2. Data for the plume velocity are non-dimensionalized by w_0. The solid line in Figure 10.3 represents the theoretical prediction according to (4.65). As above, the figure reveals a very good agreement between the theory and the experimental data. In particular, the experimental data points for the lower values of $H/\tan(\alpha)$ support the existence of the region where $U_i/U_0 > 1$, *i.e* a parameter region where the coastline inclination angle leads to plumes that propagate faster than their vertical-wall counterparts.

In Section 9.2.2, it was discussed that agreement between the theory and the experiments for the plume propagation velocity was better when non-dimensionalizing the data for the plume length by the theoretical inclined-wall plume width, w_i (*i.e* by taking into account the topography in the non-dimensionalizing scheme),

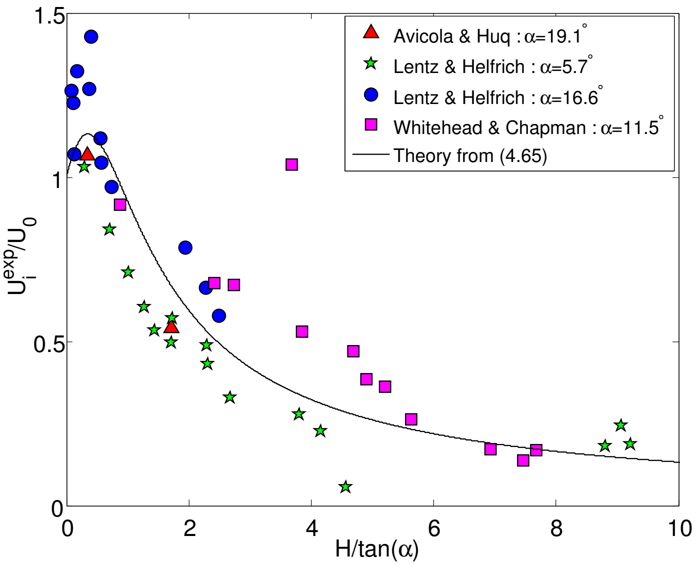

Figure 10.3: Ratio, U_i^{exp}/U_0, of the non-dimensional measured mean inclined-wall velocity to the non-dimensional theoretical vertical-wall velocity, as a function of $H/\tan(\alpha)$, for the experiments of Avicola & Huq (2002), Lentz & Helfrich (2002) and Whitehead & Chapman (1986). The solid line represents the theoretical prediction according to (4.65).

rather than by the theoretical vertical-wall plume width, w_0. Figure 10.4 displays the values of the non-dimensional measured mean inclined-wall velocity, $(U_i^{exp})_{w_i}$, as a function of the non-dimensional theoretical inclined-wall velocity, $(U_i^{th})_{w_i}$, for the experiments of Avicola & Huq (2002), Lentz & Helfrich (2002) and Whitehead & Chapman (1986) displayed in Figure 10.2. The solid line in Figure 10.4 identifies $(U_i^{exp})_{w_i} = (U_i^{th})_{w_i}$, while the dashed line identifies the best linear fit given by 1.04 $(U_i^{th})_{w_i} - 0.005$ with a correlation of 0.98. Data are non-dimensionalized by w_i in Figure 10.4 thus $(U_i)_{w_i} = u_i/(\Omega w_i)$. The agreement between the theory from Chapter 4 and the experiments of Avicola & Huq (2002), Lentz & Helfrich (2002) and Whitehead & Chapman (1986) is indeed better when the plume length data are non-dimensionalized by w_i rather than by w_0 (from a comparison between Figure 10.2 and Figure 10.4, and between the slope values for the linear fits in Figure 10.2 and Figure 10.4 and their coefficient of correlation).

From the discussion at the end of Section 9.2.2, one knows that if agreement between experiments and theory for the plume propagation speed is found, there will exist a relation of dependence between the non-dimensional measured mean inclined-wall velocity and, the dimensionless parameters, I and h_0/H_D. Fig-

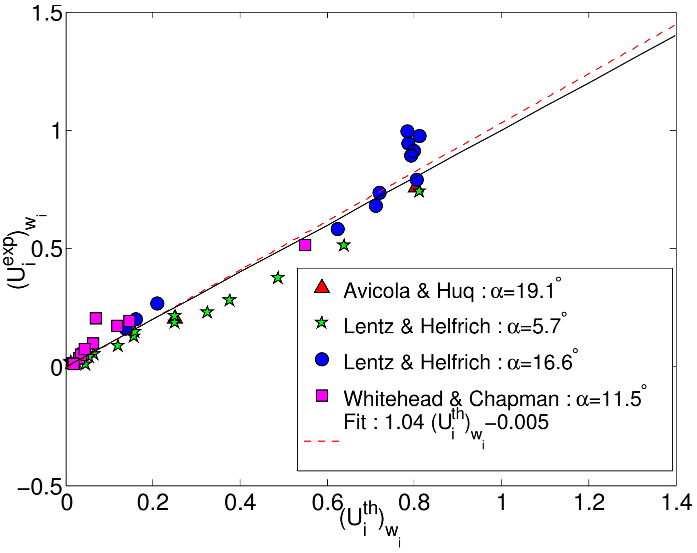

Figure 10.4: Non-dimensional measured mean inclined-wall velocity, $(U_i^{exp})_{w_i}$, as a function of the non-dimensional theoretical inclined-wall velocity, $(U_i^{th})_{w_i}$, for the experiments of Avicola & Huq (2002), Lentz & Helfrich (2002) and Whitehead & Chapman (1986). The solid line identifies $(U_i^{exp})_{w_i} = (U_i^{th})_{w_i}$, while the dashed line identifies the best linear fit given by 1.04 $(U_i^{th})_{w_i} - 0.005$ with a correlation of 0.98.

ures 10.5(a)-(b), displaying the values of the non-dimensional measured mean inclined-wall speed ,U_i^{exp}, as a function of the dimensionless parameters, I and h_0/H_D, respectively, for the experiments of Avicola & Huq (2002), Lentz & Helfrich (2002) and Whitehead & Chapman (1986) shows that the U_i^{exp} values depend on the I and h_0/H_D values (as expected due to the very good agreement found between the theory from Chapter 4 and the experiments of Avicola & Huq (2002), Lentz & Helfrich (2002) and Whitehead & Chapman (1986) for the plume propagation speed). From Figures 10.5(a)-(b), the U_i^{exp} values clearly decrease as the I and h_0/H_D values increase. Then shallow and wide plumes are faster than deep and narrow plumes (from Figure 10.5(a)) and surface-advected plumes are faster than bottom-trapped plumes (from Figure 10.5(b)).

The question now is to understand why a very good agreement is found between the theoretical model developed in Chapter 4 and the experiments of Avicola & Huq (2002), Lentz & Helfrich (2002) and Whitehead & Chapman (1986), whereas a poor agreement is found between the theory from Chapter 4 and the experiments presented in Chapter 9. Figures 10.6(a)-(b) and Figures 10.7(a)-(b) summarize the values of the difference between the non-dimensional measured

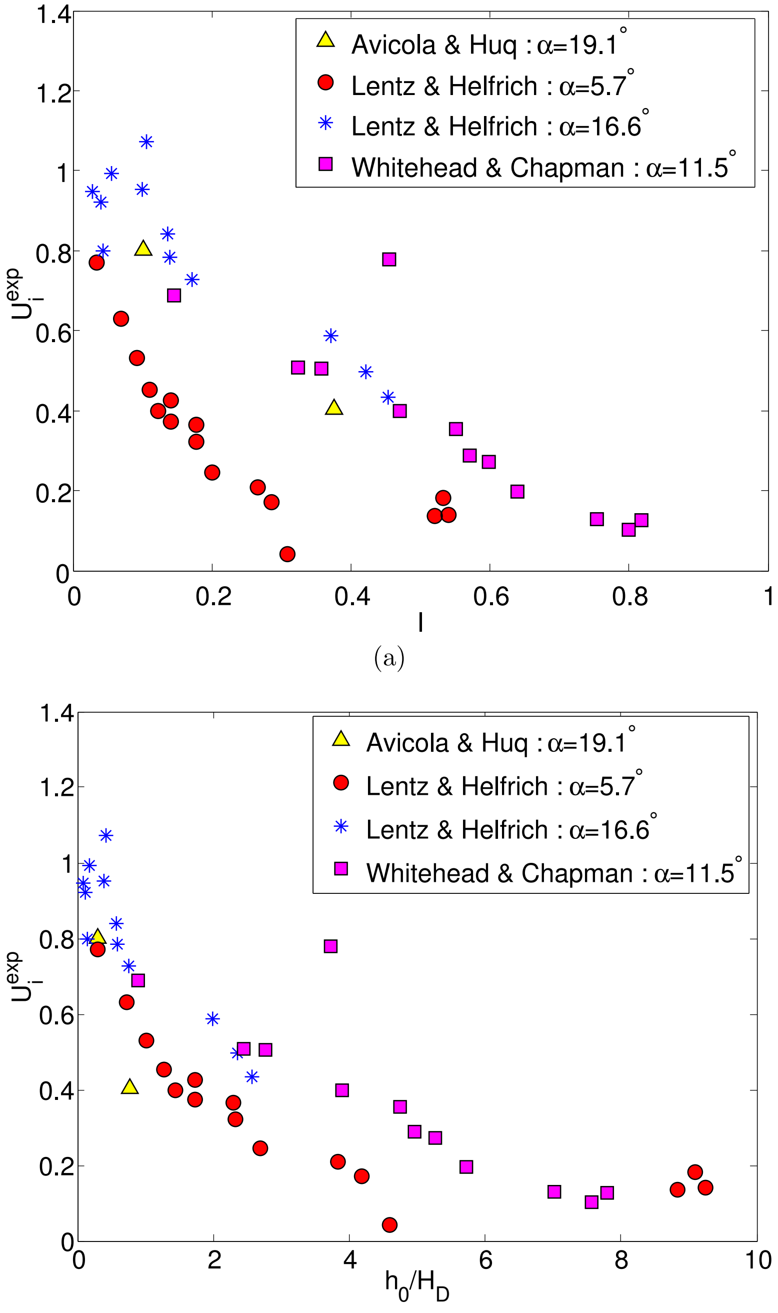

Figure 10.5: Non-dimensional measured mean inclined-wall speed, U_i^{exp}, as a function of (a) the dimensionless parameter, I, (b) the non-dimensional ambient depth parameter, h_0/H_D, for the experiments of Avicola & Huq (2002), Lentz & Helfrich (2002) and Whitehead & Chapman (1986).

mean inclined-wall speed, U_i^{exp}, and the non-dimensional predicted inclined-wall speed, U_i^{th}, as a function of the dimensionless parameter, I, the non-dimensional ambient depth parameter, h_0/H_D, the horizontal and vertical Ekman numbers, Ek_H and Ek_V, respectively, for the experiments presented in this study and for the experiments of Avicola & Huq (2002), Lentz & Helfrich (2002) and Whitehead & Chapman (1986). The solid line in Figures 10.6(a)-(b) and Figures 10.7(a)-(b) identifies $U_i^{exp} = U_i^{th}$, $i.e$ agreement between experiments and theory. Data in Figures 10.6(a)-(b) and Figures 10.7(a)-(b) are non-dimensionalized by w_0 thus $U_i = u_i/(\Omega w_0)$.

From Figure 10.6(a), the dimensionless parameter I seems to have no influence on the difference between the theoretical and experimental plume velocities. Figure 10.6(b) reveals that Lentz & Helfrich (2002) and Whitehead & Chapman (1986) used larger values for the non-dimensional ambient depth parameter, h_0/H_D, than the present study. Similarly, Figure 10.7(b) shows that Lentz & Helfrich (2002) employed larger values for the vertical Ekman number, Ek_V, than the present study. It seems from Figure 10.6(b) and Figure 10.7(b) that agreement between experiments and theory for the plume propagation velocity is found for experiments with very large h_0/H_D and Ek_V values.

In Chapter 7 and Chapter 9, it was found that for sufficiently large values of the horizontal Ekman number, Ek_H, the experimental plume propagation velocity was smaller than the theoretical plume propagation velocity, while for very small Ek_H values (obtained in the large-scale study), the plumes in the laboratory were much faster than the theoretical prediction. From Figure 10.7(a), Avicola & Huq (2002), Lentz & Helfrich (2002) and Whitehead & Chapman (1986) simulated coastal plumes with values for the horizontal Ekman number, Ek_H, in the range for which agreement between the experiments presented in this study and the inclined-wall theory was found. This result strengthens the results from Sections 7.3, 7.5 and 9.2.2: the difference between the experiments and the geostrophic theory for the plume propagation speed depends on the magnitude of the lateral viscous forces.

Figure 10.8 displays a (h_0/H_D)-Ek_H diagram summarizing the parametric locations where the plumes are found to be faster/slower than the theory, or to have same speed than the theory. To build Figure 10.8, plumes in the laboratory were considered slower than the theory when the difference between the non-dimensional experimental and theoretical velocities was smaller than -0.25, they were considered faster than the theory when the difference between the non-

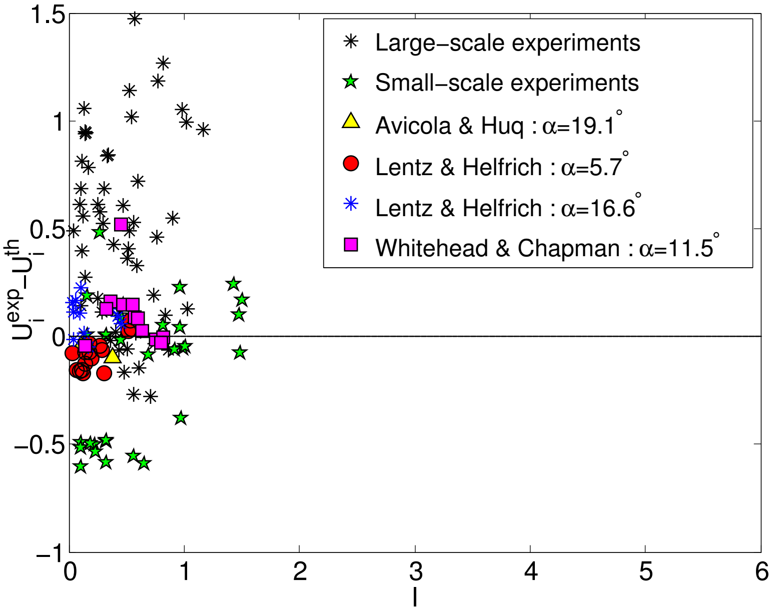

(a)

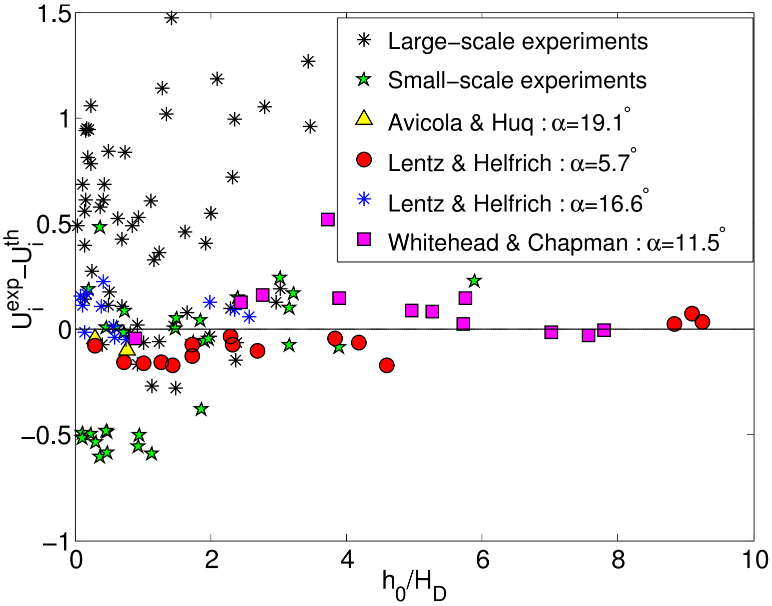

(b)

Figure 10.6: Difference between the non-dimensional measured mean inclined-wall speed, U_i^{exp}, and the non-dimensional predicted inclined-wall speed, U_i^{th}, as a function of (a) the dimensionless parameter, I, (b) the non-dimensional ambient depth parameter, h_0/H_D, for the large-scale and small-scale experiments of this study, and for the experiments of Avicola & Huq (2002), Lentz & Helfrich (2002) and Whitehead & Chapman (1986). The solid line on each figure identifies $U_i^{exp} = U_i^{th}$.

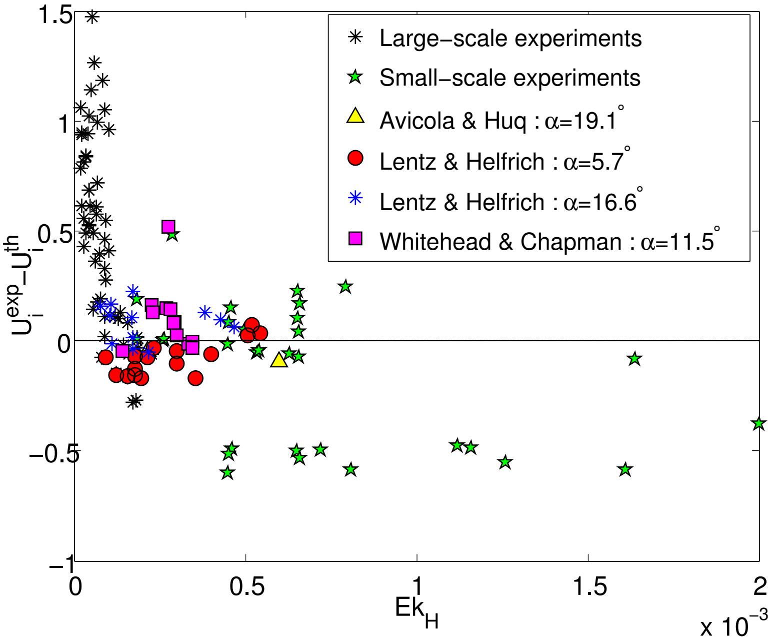

(a)

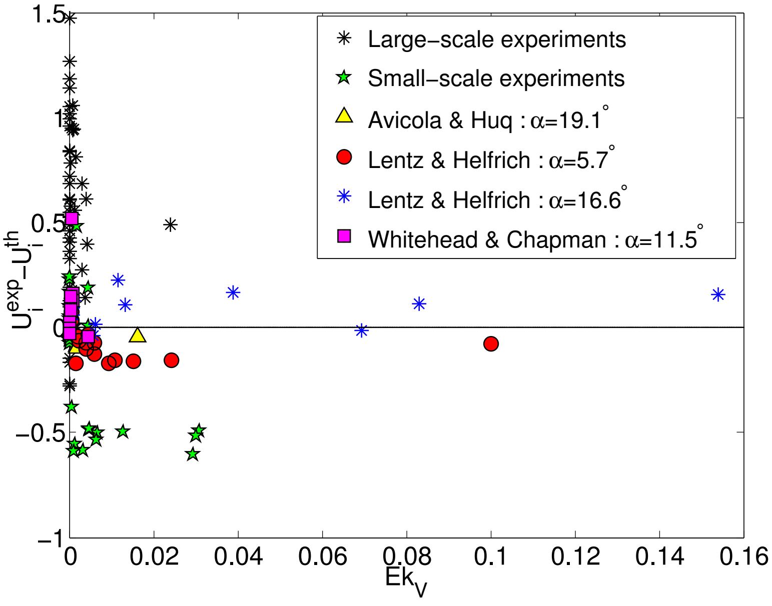

(b)

Figure 10.7: Difference between the non-dimensional measured mean inclined-wall speed, U_i^{exp}, and the non-dimensional predicted inclined-wall speed, U_i^{th}, as a function of (a) the horizontal Ekman number, Ek_H, (b) the vertical Ekman number, Ek_V, for the large-scale and small-scale experiments of this study, and for the experiments of Avicola & Huq (2002), Lentz & Helfrich (2002) and Whitehead & Chapman (1986). The solid line on each figure identifies $U_i^{exp} = U_i^{th}$.

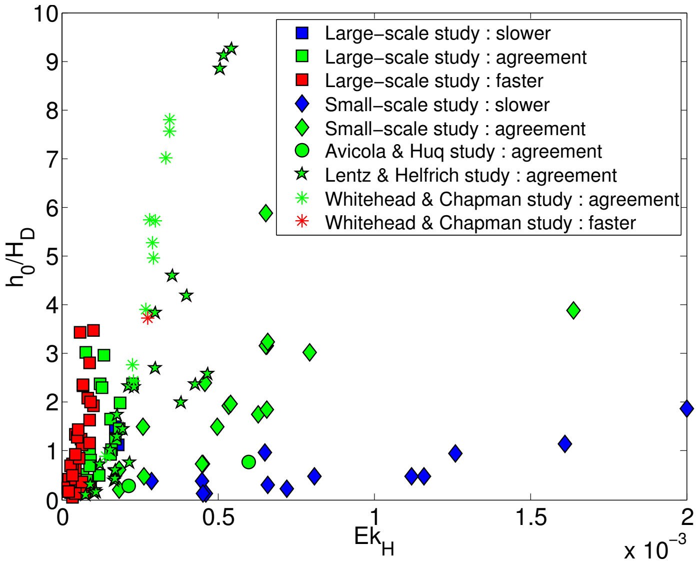

Figure 10.8: (h_0/H_D)-Ek_H diagram displaying the parametric locations where the plumes are found to be faster/slower than the theory, or to have same speed than the theory.

dimensional experimental and theoretical velocities was larger than 0.25, otherwise agreement between experiments and theory for the propagation speed was considered to be found. From figure 10.8, the plumes faster than the theoretical prediction are found for very low Ek_H values. For very low h_0/H_D values, the plumes are slower than the theory for medium to large Ek_H values. The extent of the Ek_H-interval for which agreement between the experiment and the theory is met seems to increase as the h_0/H_D value increases.

Figure 10.9 displays the non-dimensional measured mean inclined-wall speed, U_i^{exp}, as a function of the horizontal Ekman number, Ek_H, for the experiments presented in this study and for the experiments of Avicola & Huq (2002), Lentz & Helfrich (2002) and Whitehead & Chapman (1986). Figures displaying the non-dimensional measured mean inclined-wall speed, U_i^{exp}, as a function of the dimensionless parameter, I, the non-dimensional ambient depth parameter, h_0/H_D, and the vertical Ekman number, Ek_V, for the experiments presented in this study and for the experiments of Avicola & Huq (2002), Lentz & Helfrich (2002) and Whitehead & Chapman (1986) were omitted as they did not show anything new from what was seen in Chapter 9. Figure 10.9 confirms the observations from Section 9.2.2: the U_i^{exp} value increases as the Ek_H value decreases. Thus the plume propagation velocities are faster in a fluid system in which viscous forces are negligible, and get slower as the lateral viscous forces become important in the fluid system.

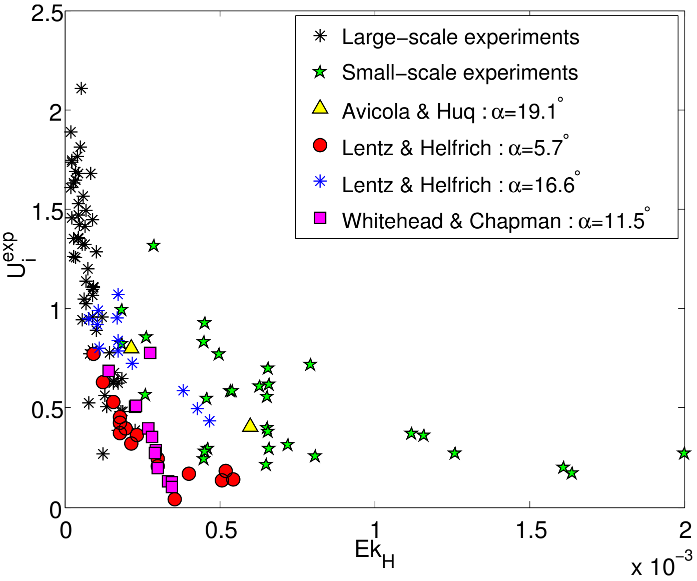

Figure 10.9: Non-dimensional measured mean inclined-wall speed, U_i^{exp}, as a function of the horizontal Ekman number, Ek_H, for the large-scale and small-scale experiments of this study and for the experiments of Avicola & Huq (2002), Lentz & Helfrich (2002) and Whitehead & Chapman (1986).

10.2.2 Coastal current width

Figure 10.10 displays the measured inclined-wall width, w_i^{exp}, as a function of the theoretical inclined-wall width, w_i^{th}, defined in (4.36), for the PIV small-scale inclined-wall experiments of this study and for the experiments of Avicola & Huq (2002) and Lentz & Helfrich (2002). The solid line on the figure identifies $w_i^{exp} = w_i^{th}$, *i.e* agreement between experiments and theory, while the dashed line identifies the best linear fit given by 0.95 w_i^{th} + 3.16 with a correlation of 0.9. The overall agreement between the experiments displayed in Figure 10.10 and the inclined-wall theoretical prediction for the plume width is found to be very good.

Figure 10.11 summarizes the values for the non-dimensional plume width, W_i, as a function of the non-dimensional ambient depth parameter, h_0/H_D, for the PIV small-scale inclined-wall experiments and for the experiments of Avicola & Huq (2002) and Lentz & Helfrich (2002). The data for the plume width in Fig-

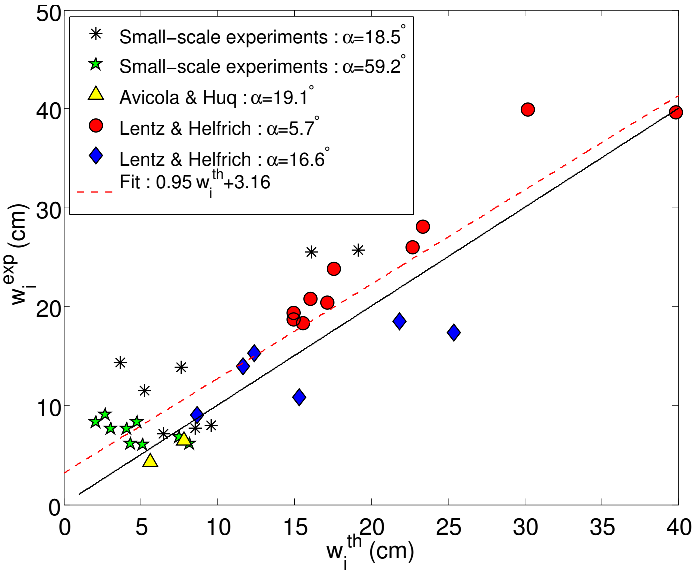

Figure 10.10: Measured inclined-wall width, w_i^{exp}, as a function of the theoretical inclined-wall width, w_i^{th}, for the PIV small-scale inclined-wall experiments and for the experiments of Avicola & Huq (2002) and Lentz & Helfrich (2002). The solid line identifies $w_i^{exp} = w_i^{th}$, while the dashed line identifies the best linear fit given by 0.95 $w_i^{th} + 3.16$ with a correlation of 0.9.

ure 10.11 are non-dimensionalized by the theoretical vertical-wall plume width, w_0, which is equivalent to the Rossby deformation radius. From Figure 10.11, despite the data scatter, the plume width values increase as the values for the non-dimensional ambient depth parameter, h_0/H_D, increase, thus bottom-trapped coastal plumes are the widest.

Figures 10.12(a)-(b) display a summary of the values for the non-dimensional plume width, $(W_i)_{w_i}$, as a function of (a) the non-dimensional ambient depth parameter, h_0/H_D, and (b) the horizontal Ekman number, Ek_H, respectively, for the PIV small-scale vertical-wall and inclined-wall experiments and for the experiments of Avicola & Huq (2002) and Lentz & Helfrich (2002). Data for the plume width in Figures 10.12(a)-(b) are non-dimensionalized by the theoretical inclined-wall width, w_i, defined in (4.36). The solid line on the figures identifies $(W_i)_{w_i} = 1$, that is agreement between experiments and theory. Similarly to the results found in Section 9.4, Figure 10.12a suggests that the value for the non-dimensional plume width, $(W_i)_{w_i}$, decreases as the value for the non-dimensional ambient depth parameter, h_0/H_D, increases, and that agreement is found for large h_0/H_D values. Although the great data scatter, Figure10.12b suggests that

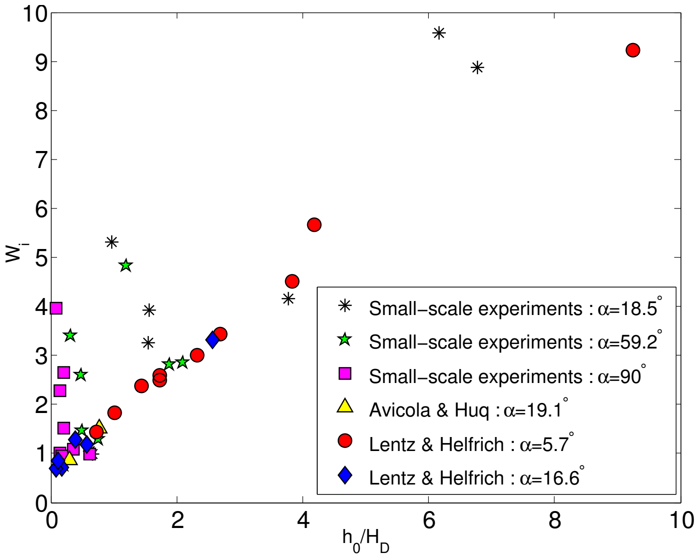

Figure 10.11: Summary of the non-dimensional plume width, W_i, as a function of the non-dimensional ambient depth parameter, h_0/H_D, for the PIV small-scale inclined-wall experiments and for the experiments of Avicola & Huq (2002) and Lentz & Helfrich (2002).

the $(W_i)_{w_i}$ values increase as the Ek_H values increase and that the best agreement between experiments and theory is found for small Ek_H values (except for plumes with large h_0/H_D values for which agreement between experiments and theory for the plume width seems to be found whatever is the Ek_H value). Therefore, the geostrophic model predicts the best the plume width for bottom-trapped coastal plumes whatever is the value of the horizontal Ekman number, and for surface-advected plumes in a fluid system in which the lateral viscous forces are small (low Ek_H values).

10.3 Comparison with the scaling of Lentz & Helfrich (2002)

In this section the scaling proposed by Lentz & Helfrich (2002) is compared to the theoretical model developed in Chapter 4. Lentz & Helfrich (2002) considered a gravity current propagating along a boundary with a uniform slope, α. They assume the coastal current in geostrophic balance, and that in equilibrium the depth where the front intersects the bottom is the same depth as the depth for a gravity current flowing along a vertical wall.

They found that the total width, w_p, of a gravity current flowing along an

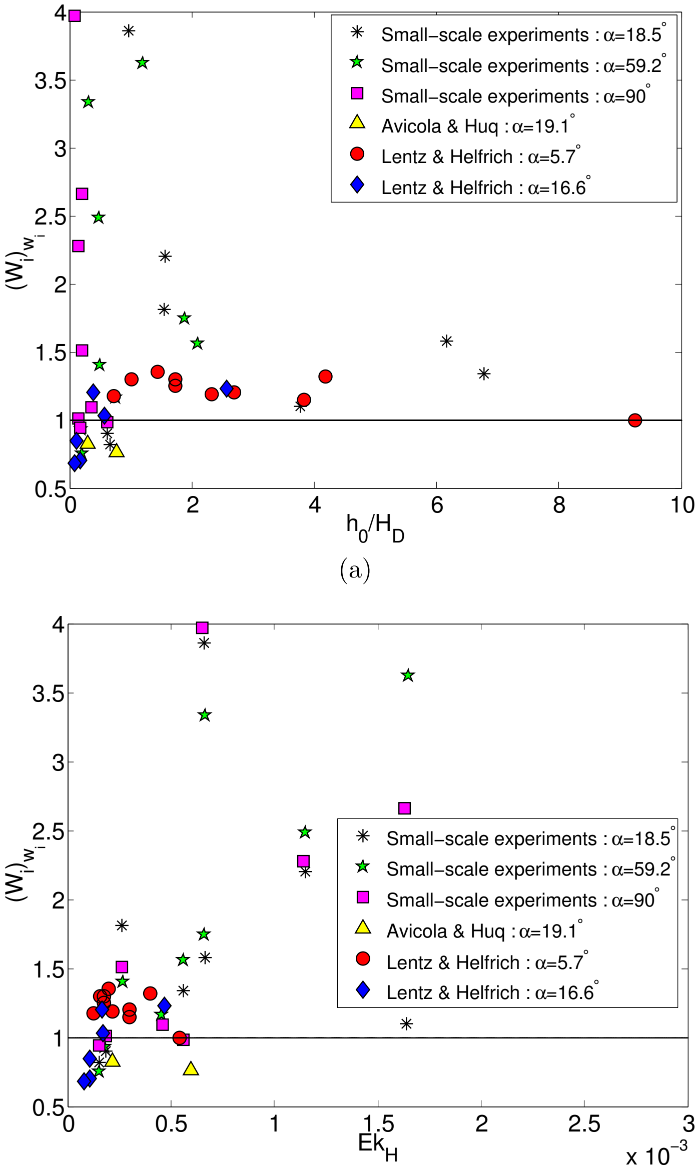

(a)

(b)

Figure 10.12: Summary of the non-dimensional plume width, $(W_i)_{w_i}$, as a function of (a) the non-dimensional ambient depth parameter, h_0/H_D, and (b) the horizontal Ekman number, Ek_H, respectively, for the PIV small-scale vertical-wall and inclined-wall experiments and for the experiments of Avicola & Huq (2002) and Lentz & Helfrich (2002). The solid line on the figures identifies $(W_i)_{w_i} = 1$, that is agreement between experiments and theory.

inclined coastline is given by:

$$w_p \sim \frac{\sqrt{g'h_0}}{f} + \frac{h_0}{\alpha}, \tag{10.1}$$

and that the propagation speed of the coastal current nose is:

$$c_p \sim \frac{1}{\frac{1}{\sqrt{g'h_0}} + \frac{f}{\alpha g'}}, \tag{10.2}$$

where h_0 is the theoretical depth, defined in (4.1(b)), for a plume flowing along a vertical coastline. In their study, Lentz & Helfrich (2002) found very good agreement between their experiments and their scaling theory when the coefficient multiplying the scaling values for w_p and c_p was 1. In order to compare the scaling of Lentz & Helfrich (2002) to the theory presented in Chapter 4, the scaling values for w_p and c_p from (10.1) and (10.2), respectively, are therefore multiplied by 1.

10.3.1 Coastal current propagation velocity

Figures 10.13(a)-(b) display the measured mean inclined-wall speed, u_i^{exp}, as a function of the theoretical inclined-wall speed, u_i^{th}, defined in (4.42), and the theoretical inclined-wall speed, c_p, of Lentz & Helfrich (2002), respectively, for the small-scale experiments of this study and for the experiments of Avicola & Huq (2002), Lentz & Helfrich (2002) and Whitehead & Chapman (1986). Figures 10.14(a)-(b) display similar results than Figures 10.13(a)-(b) for the large-scale experiments of this study. The solid line in Figure 10.13(a) and Figure 10.14(a) identifies $u_i^{exp} = u_i^{th}$, *i.e* agreement between the experiments and the theory of this study, while the solid line in Figure 10.13(b) and Figure 10.14(b) identifies $u_i^{exp} = c_p$, *i.e* agreement between the experiments and the theory of Lentz & Helfrich (2002). The dashed line in Figures 10.13(a)-(b) and Figures 10.14(a)-(b) identifies the best linear fit given by 0.89 $u_i^{th} + 0.08$ with a correlation of 0.75, 0.65 $c_p + 0.52$ with a correlation of 0.66, 1.65 $u_i^{th} + 0.35$ with a correlation of 0.73 and 1.17 $c_p + 2.13$ with a correlation of 0.63, respectively. A comparison between Figures 10.13(a)-(b) and Figures 10.14(a)-(b), and between the slopes of the best fit lines in each figure reveal that agreement between experiments and theory is best in the small-scale studies (Figures 10.13(a)-(b)) rather than in the large-scale study (Figures 10.14(a)-(b)) for both theories. Despite the theory of Lentz & Helfrich (2002) predicted the best the propagation speed for the plumes from the large-scale study, the agreement between the large-scale experiments and the theory is still quite poor. On the other hand, both theories predicted quite well the propagation speed for the plumes from the small-scale studies with a better agreement found with the theory from Chapter 4.

10.3.2 Coastal current width

Figure 10.15 displays the values of the measured inclined-wall width, w_i^{exp}, as a function of the theoretical inclined-wall width, w_p, of Lentz & Helfrich (2002), for the PIV small-scale inclined-wall experiments and for the experiments of Avicola & Huq (2002) and Lentz & Helfrich (2002). The solid line identifies $w_i^{exp} = w_p$, while the dashed line identifies the best linear fit given by $0.94\ w_p + 1.93$ with a correlation of 0.9. A comparison between Figure 10.10 and Figure 10.15 reveal that while good agreement between experiments and theory for the plume width is found for both theories, the best agreement is found for the theory of Lentz & Helfrich (2002).

Figures 10.16(a)-(b) summarize the values of the non-dimensional plume width, $(W_i)_{w_p}$, as a function of the non-dimensional ambient depth parameter, h_0/H_D, and the horizontal Ekman number, Ek_H, respectively, for the PIV small-scale vertical-wall and inclined-wall experiments and for the experiments of Avicola & Huq (2002) and Lentz & Helfrich (2002). The solid line on the figures identifies $(W_i)_{w_p} = 1$, that is agreement between the experiments and the theory of Lentz & Helfrich (2002). In Figures 10.16(a)-(b), the width data for the plumes flowing along a sloping bottom were non-dimensionalized by the theoretical inclined-wall width, w_p, of Lentz & Helfrich (2002), while the width data for the plumes flowing along the vertical-wall coastline were non-dimensionalized by the Rossby deformation radius, $R_D = \sqrt{g\prime h_0}/f$, used by Lentz & Helfrich (2002). Figures 10.16(a)-(b) confirm the results found in Section 10.2.2: the value for the non-dimensional plume width decreases as the value for the non-dimensional ambient depth parameter, h_0/H_D, increases and the value for the horizontal Ekman number,Ek_H, decreases. Agreement is found for small Ek_H values and for large h_0/H_D values (whatever is the Ek_H value).

10.4 Comparison with oceanic observations

Oceanic observations are now compared to the theoretical model developed in Chapter 4 and to the scaling of Lentz & Helfrich (2002). Parameters describing

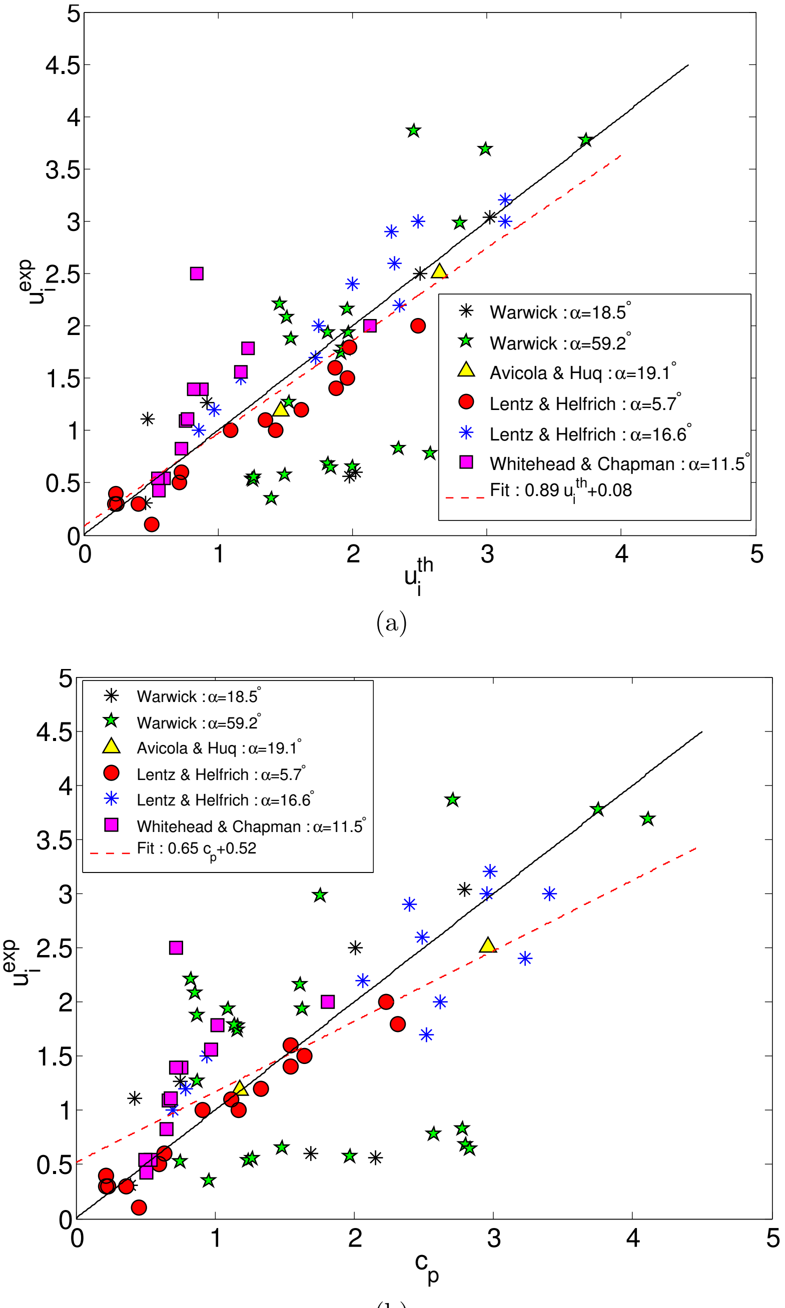

Figure 10.13: Measured mean inclined-wall speed, u_i^{exp}, as a function of (a) the theoretical inclined-wall speed, u_i^{th}, defined in (4.42), and (b) the theoretical inclined-wall speed, c_p, of Lentz & Helfrich (2002), for the small-scale experiments of this study and for the experiments of Avicola & Huq (2002), Lentz & Helfrich (2002) and Whitehead & Chapman (1986). The solid line in the figures identifies (a) $u_i^{exp} = u_i^{th}$ and (b) $u_i^{exp} = c_p$, while the dashed line identifies the best linear fit given by (a) 0.89 $u_i^{th} + 0.08$ with a correlation of 0.75 and (b)0.65 $c_p + 0.52$ with a correlation of 0.66.

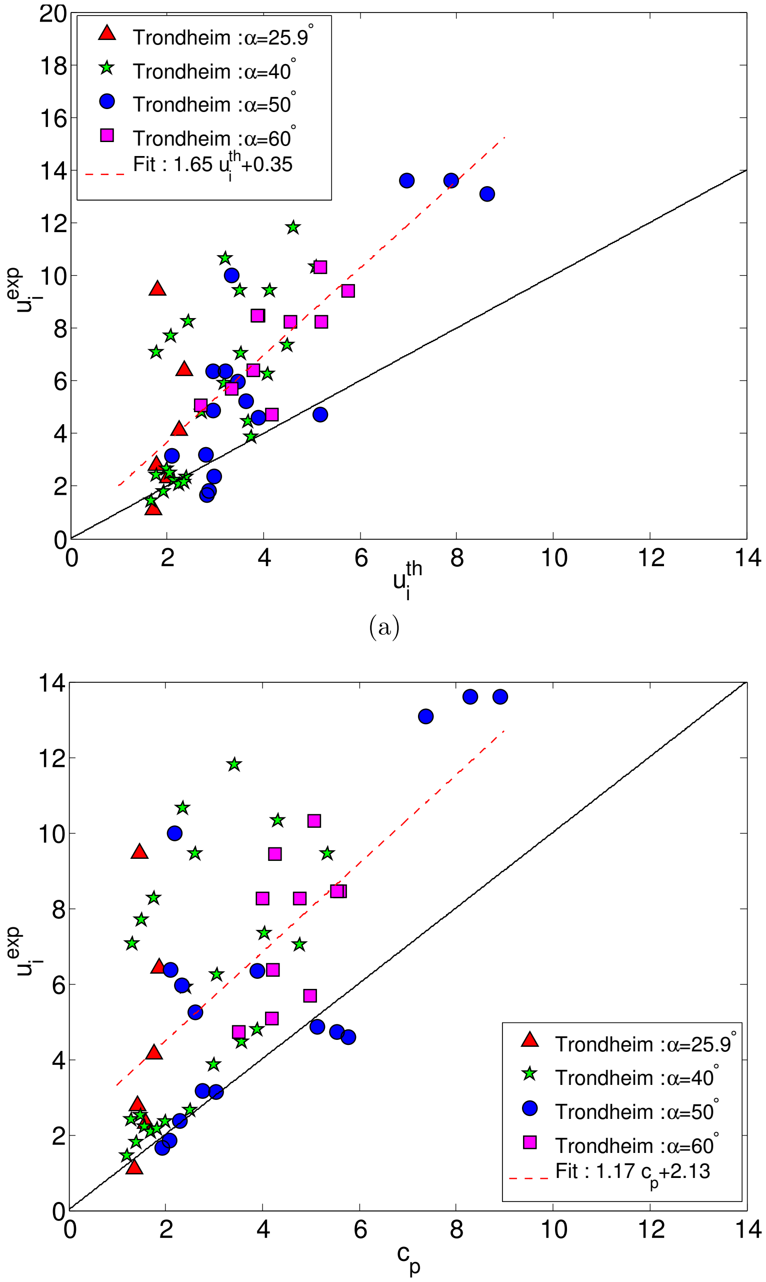

(a)

(b)

Figure 10.14: Measured mean inclined-wall speed, u_i^{exp}, as a function of (a) the theoretical inclined-wall speed, u_i^{th}, defined in (4.42), and (b) the theoretical inclined-wall speed, c_p, of Lentz & Helfrich (2002), for the large-scale experiments of this study. The solid line in the figures identifies (a) $u_i^{exp} = u_i^{th}$ and (b) $u_i^{exp} = c_p$, while the dashed line identifies the best linear fit given by (a) $1.65\ u_i^{th} + 0.35$ with a correlation of 0.73 and (b)$1.17\ c_p + 2.13$ with a correlation of 0.63.

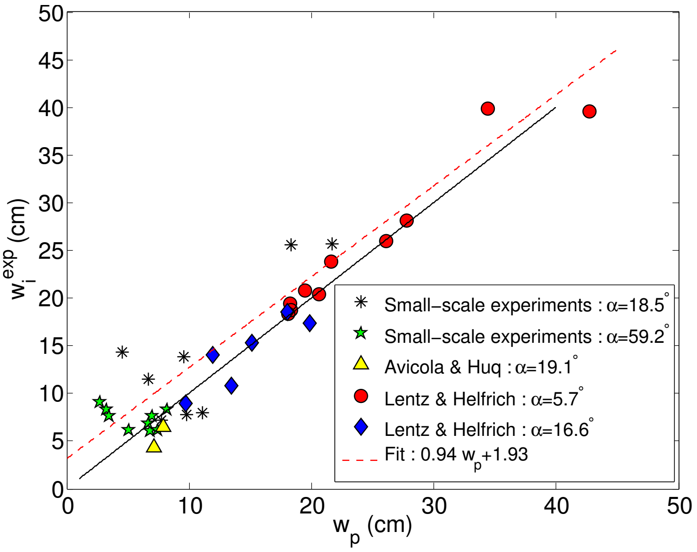

Figure 10.15: Measured inclined-wall width, w_i^{exp}, as a function of the theoretical inclined-wall width, w_p, of Lentz & Helfrich (2002), for the PIV small-scale inclined-wall experiments and for the experiments of Avicola & Huq (2002) and Lentz & Helfrich (2002). The solid line identifies $w_i^{exp} = w_p$, while the dashed line identifies the best linear fit given by 0.94 $w_p + 1.93$ with a correlation of 0.9.

some oceanic coastal currents are summarized in Table 10.1 and their values, listed in order, are the bottom slope, α (°), the Coriolis parameter, f (s^{-1}), the reduced gravity anomaly, $g\prime$ ($m\ s^{-2}$), the flow rate at the source, q_0 ($m^3\ s^{-1}$), the ambient ocean depth, H_D (m), the theoretical vertical-wall plume depth, h_0 (m), the theoretical vertical-wall plume width, w_0 (m), the observed plume width, w_i^{field} (m), the observed alongshore velocity, u_i^{field} ($m\ s^{-1}$), the dimensionless parameter, I, the horizontal Ekman number, Ek_H, the vertical Ekman number, Ek_V, the Reynolds number, Re, and the non-dimensional ambient depth parameter, h_0/H_D. From the eight buoyant outflow sources tabulated in Table 10.1, six are river systems (Chesapeake, Columbia, Delaware, Gaspé, Rhine and Rio de la Plata) and two are strait outflows (Soya and Tsugaru). The values for α, f, $g\prime$ and q_0 in Table 10.1 are taken from the Table 1 of Avicola & Huq (2002). Three of the river systems (Delaware, Rhine and Chesapeake) have been characterized by a non-zero coastal wall depth, H_C. This coastal wall depth, H_C, has been estimated at 10 m (Avicola & Huq (2002)). The ocean ambient depth, H_D, for these three river systems in Table 10.1 was then computed as $H_D = H_C + \alpha w_0$. As the value of the plume height, h_0, for these three river systems is equivalent to the value of their coastal wall depth, H_C, *i.e* $0.86 \leq h_0/H_C \leq 1.07$, and

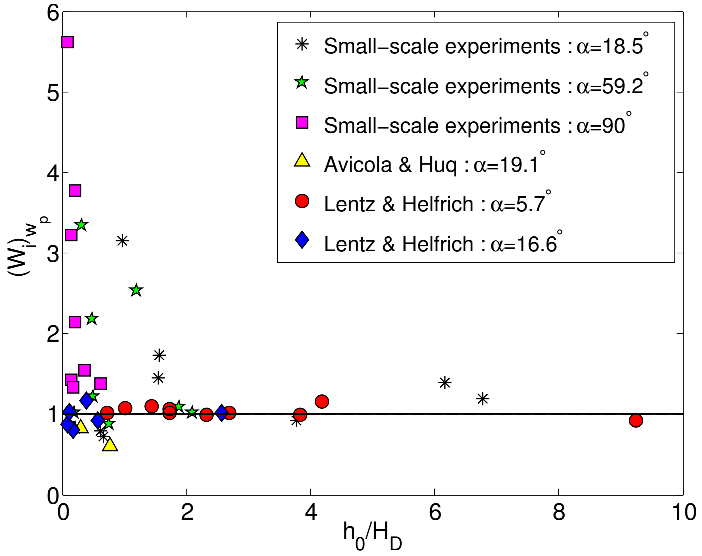

(a)

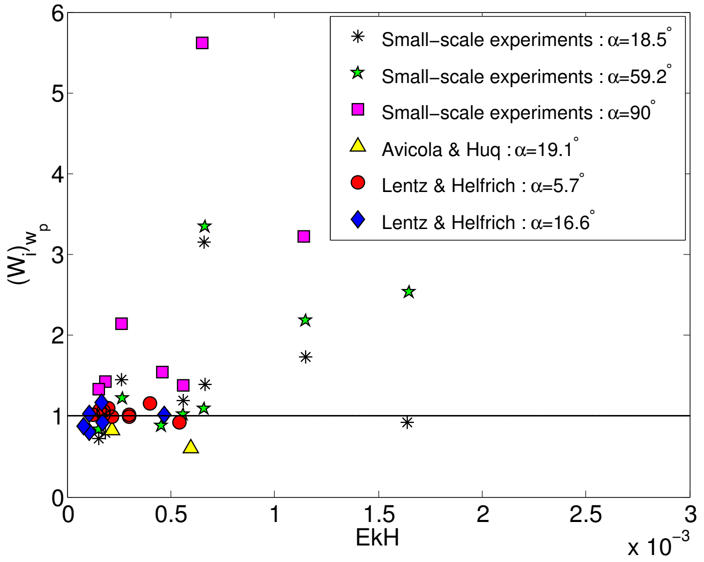

(b)

Figure 10.16: Summary of the non-dimensional plume width, $(W_i)_{w_p}$, as a function of (a) the non-dimensional ambient depth parameter, h_0/H_D, and (b) the horizontal Ekman number, Ek_H, for the PIV small-scale vertical-wall and inclined-wall experiments and for the experiments of Avicola & Huq (2002) and Lentz & Helfrich (2002). The solid line on the figures identifies $(W_i)_{w_p} = 1$, that is agreement between experiments and theory.

in order to compare these three river systems with the theory from Chapter 4, which was developed for a single inclined coastline (and not for a continental shelf), their topography is assumed to be a single slope with angle α, tabulated in Table 10.1. The values for the observed plume width and alongshore velocity, w_i^{field} and u_i^{field}, respectively, listed in Table 10.1, are taken from Munchow & Garvine (1993b) for the Delaware Plume, Framinan *et al.* (2008) for the Rio de la Plata Estuary, Simpson *et al.* (1993) for the Rhine Plume, Lentz *et al.* (2003) for the Chesapeake Plume, Hickey *et al.* (1998) (for the observed alongshore velocity value) and Thomas & Weatherbee (2006) (for the observed plume width value) for the Columbia Plume, Mertz *et al.* (1988) for the Gaspé Current, Matsuyama *et al.* (2006) for the Soya Current and Ito *et al.* (2003) for the Tsugaru Current.

Figures 10.17(a)-(b) display the observed alongshore speed, u_i^{field}, as a function of the theoretical inclined-wall speed, u_i^{th}, defined in (4.42), and the theoretical inclined-wall speed, c_p, of Lentz & Helfrich (2002), respectively, for the plumes tabulated in Table 10.1. The solid line in the figures identifies $u_i^{field} = u_i^{th}$ and $u_i^{field} = c_p$, respectively, while the dashed line identifies the best linear fit given by $1.04\, u_i^{th} + 0.06$, with a correlation of 0.79, and $0.48\, c_p + 0.25$, with a correlation of 0.55, respectively. Data for the plume velocity are non-dimensionalized by w_0. Figure 10.17a reveals that the inclined-wall theory developed in Chapter4 predicts quite well the propagation velocity of the plumes tabulated in Table 10.1. Agreement is not so good when comparing the propagation velocity of the plumes with the scaling of Lentz & Helfrich (2002) (see Figure 10.17b).

Figure 10.18 summarizes the values of the ratio, U_i^{field}/U_0, of the non-dimensional observed alongshore velocity, U_i^{field}, to the non-dimensional theoretical vertical-wall velocity, U_0, as a function of $H/\tan(\alpha)$, for the plumes tabulated in Table 10.1. The solid line on the figure represents the theoretical prediction according to (4.65). Data for the plume velocity are non-dimensionalized by w_0. Similarly to the experimental results presented in Section 10.2.1, the oceanic data points for the lower values of $H/\tan(\alpha)$ support the existence of the region where $U_i/U_0 > 1$, *i.e* a parameter region where the coastline inclination angle leads to plumes that propagate faster than their vertical-wall counterparts.

Figures 10.19(a)-(b) show the observed width, w_i^{field}, as a function of the theoretical inclined-wall width, w_i^{th}, defined in (4.36), and the theoretical inclined-wall width, w_p, of Lentz & Helfrich (2002), respectively, for the plumes tabulated in Table 10.1. The solid line in the figures identifies $w_i^{field} = w_i^{th}$ and $w_i^{field} = w_p$, respectively, while the dashed line identifies the best linear fit given by $0.85\, w_i^{th} +$

Outflow	Delaware	Rio de la Plata	Rhine	Chesapeake
α	0.04	0.04	0.017	0.057
f	9.09×10^{-5}	7.27×10^{-5}	1.15×10^{-4}	8.7×10^{-5}
g'	0.039	0.245	0.038	0.033
q_0	16000	25000	19000	18000
H_D	12.5	12.5	12.5	12.5
h_0	8.64	3.85	10.72	9.74
w_0	9029	18897	7850	9217
w_i^{field}	20000	38000	30000	5000
u_i^{field}	0.2	0.45	0.175[a]	0.5
I	0.002	0.001	0.003	0.002
Ek_H	1.35×10^{-10}	3.85×10^{-11}	1.41×10^{-10}	1.35×10^{-10}
Ek_V	1.47×10^{-4}	9.27×10^{-4}	7.56×10^{-5}	1.21×10^{-4}
Re	2.78×10^{9}	9.74×10^{9}	2.66×10^{9}	2.77×10^{9}
h_0/H_D	0.53	0.29	0.87	0.51
Outflow	Columbia	Gaspé	Soya	Tsugaru
α	0.206	0.687	0.16	1.089
f	1.05×10^{-4}	1.08×10^{-4}	1.02×10^{-4}	9.7×10^{-5}
g'	0.118	0.078	0.03	0.03
q_0	22000	60000	700000	1000000
H_D	12.5	12.5	12.5	3
h_0	6.26	12.89	68.99	80.42
w_0	11573	13130	19947	22645
w_i^{field}	10000	20000	32500[b]	32500[c]
u_i^{field}	0.4[d]	0.65[e]	1.15[f]	0.9[g]
I	0.001	0.002	0.006	0.006
Ek_H	7.11×10^{-11}	5.37×10^{-11}	2.46×10^{-11}	2.01×10^{-11}
Ek_V	2.43×10^{-4}	5.57×10^{-5}	2.06×10^{-6}	1.59×10^{-6}
Re	5.27×10^{9}	6.98×10^{9}	1.52×10^{10}	1.87×10^{10}
h_0/H_D	0.15	0.08	1.24	0.19

Table 10.1: Parameters used in describing some oceanic coastal currents.

---

[a] u_i^{field} has been averaged over [0.15; 0.2]

[b] w_i^{field} has been averaged over [30000; 35000]

[c] w_i^{field} has been averaged over [25000; 40000]

[d] u_i^{field} has been averaged over [0.3; 0.5]

[e] u_i^{field} has been averaged over [0.3; 1]

[f] u_i^{field} has been averaged over [1; 1.3]

[g] u_i^{field} has been averaged over [0.5; 1.3]

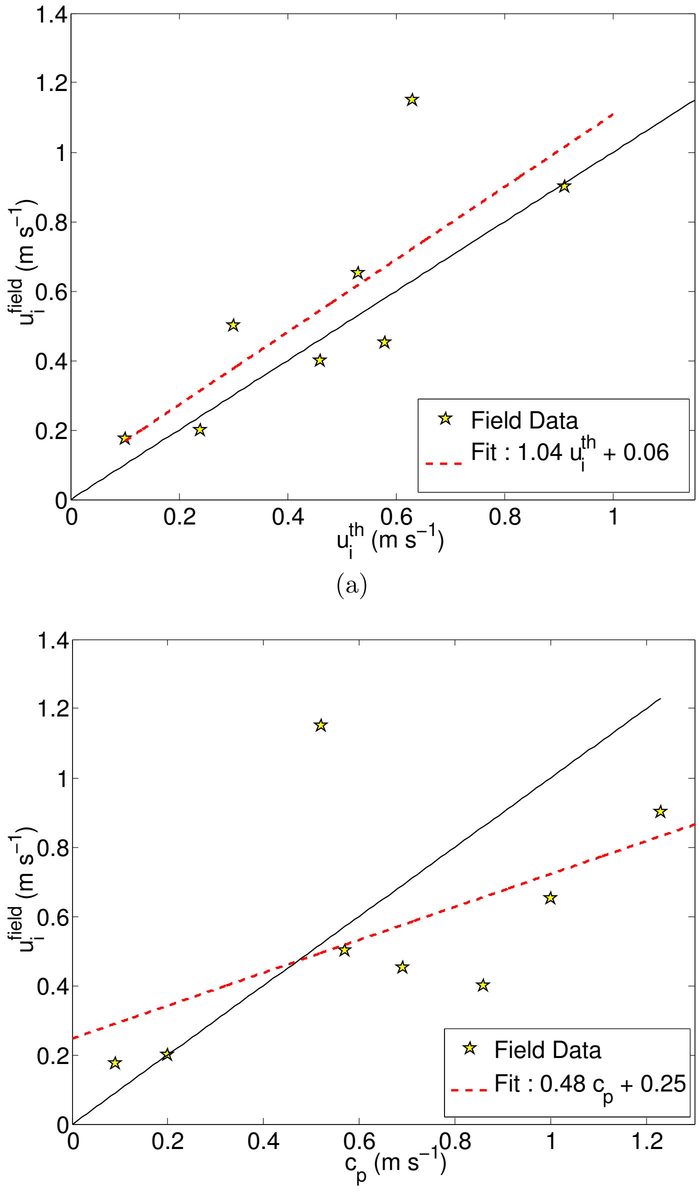

(a)

(b)

Figure 10.17: Observed alongshore speed, u_i^{field}, as a function of (a) the theoretical inclined-wall speed, u_i^{th}, defined in (4.42), and (b) the theoretical inclined-wall speed, c_p, of Lentz & Helfrich (2002), for the plumes tabulated in Table 10.1. The solid line in the figures identifies (a) $u_i^{field} = u_i^{th}$ and (b) $u_i^{field} = c_p$, while the dashed line identifies the best linear fit given by (a) 1.04 $u_i^{th} + 0.06$ with a correlation of 0.79 and (b)0.48 $c_p + 0.25$ with a correlation of 0.55.

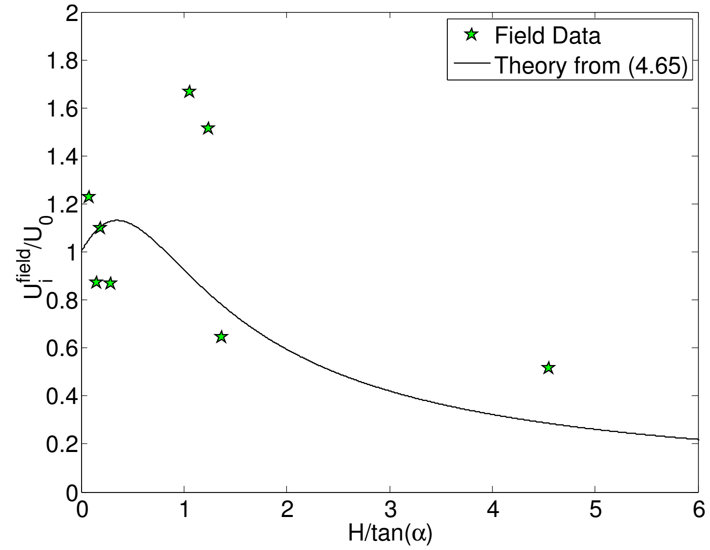

Figure 10.18: Ratio, U_i^{field}/U_0, of the non-dimensional observed alongshore velocity to the non-dimensional theoretical vertical-wall velocity, as a function of $H/\tan(\alpha)$, for the plumes tabulated in Table 10.1. The solid line represents the theoretical prediction according to (4.65).

6009, with a correlation of 0.67, and 0.54 w_p + 11690, with a correlation of 0.55, respectively. From Figure 10.19, despite the theory developed in Chapter 4 predicts the best the inclined-wall width of the plumes listed in Table 10.1, the agreement is not so good and plume width values are usually underestimated by the theory.

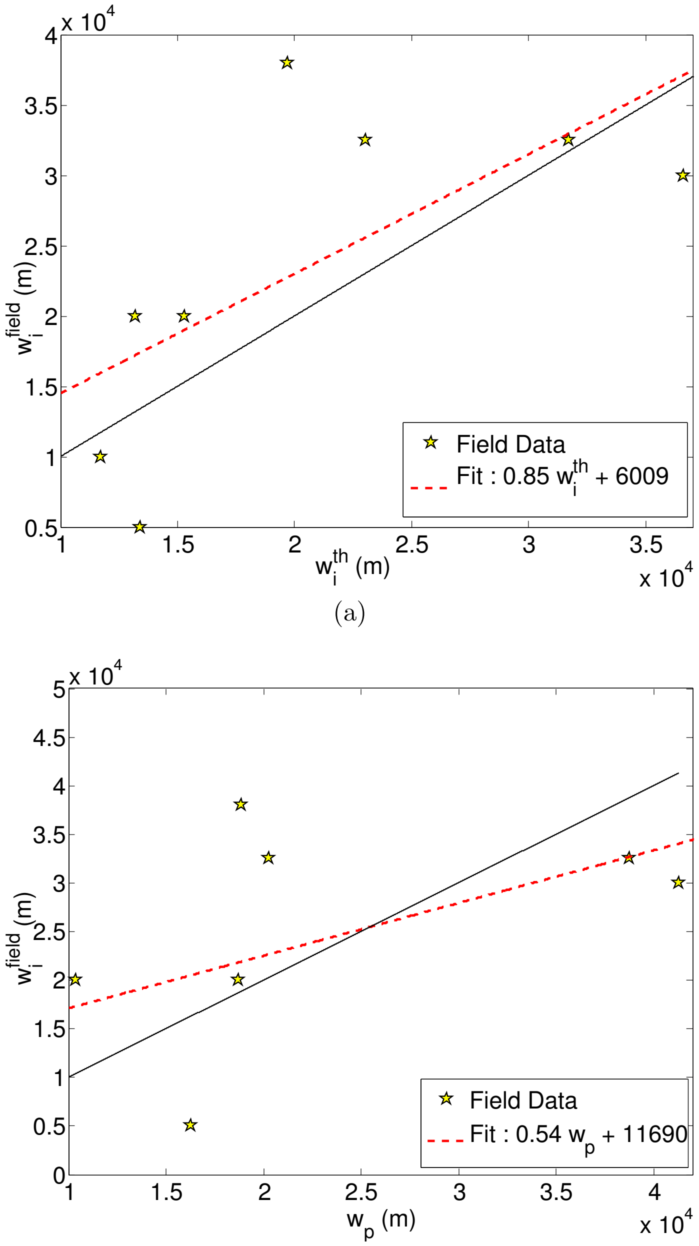

(a)

(b)

Figure 10.19: Observed width, w_i^{field}, as a function of (a) the theoretical inclined-wall width, w_i^{th}, defined in (4.36), and (b) the theoretical inclined-wall width, w_p, of Lentz & Helfrich (2002), for the plumes tabulated in Table 10.1. The solid line in the figures identifies (a) $w_i^{field} = w_i^{th}$ and (b) $w_i^{field} = w_p$, while the dashed line identifies the best linear fit given by (a) 0.85 $w_i^{th} + 6009$ with a correlation of 0.67 and (b)0.54 $w_p + 11690$ with a correlation of 0.55.

CHAPTER 11

The effect of the ambient ocean depth on vertical-wall coastal current evolution

This chapter attempts to address how the ambient ocean depth, H_D, affects the development of buoyant coastal currents flowing along a vertical coastline. Experimental results for coastal currents flowing along a vertical wall with varying the coastal wall depth, H_D (that is the height of the ambient salt water, H_{SW}, in the circular tank) are presented here.

11.1 Current length

Twenty five experiments investigating the effect of the ocean depth, H_D, on the nose propagation of a coastal current flowing along a vertical wall were carried out and are listed in Appendix B, Tables B.1, B.2 and B.3.

Vertical-wall experiments with deep coastal currents were repeated with varying the coastal wall depth, H_D. Results for the different currents were found to be identical. Figure 11.1 displays the non-dimensional current length, L, as a function of the dimensionless time, T, for three vertical-wall experiments with equal rotation rate, Ω, equal flow rate, q_0, equal reduced gravity, $g\prime$, but different ambient ocean depth, H_D. From Figure 11.1, decreasing the ambient ocean depth, H_D, does not affect the current nose propagation. Surprisingly, the current propagation velocity is identical for a coastal plume flowing above a deep abyss, *i.e* a surface-trapped plume, and a coastal plume in contact with the ocean bottom, *i.e* a bottom-trapped plume.

Avicola & Huq (2002) distinguish between surface-advected plumes, for which the value of the non-dimensional ambient depth parameter, h_0/H_D, is less than

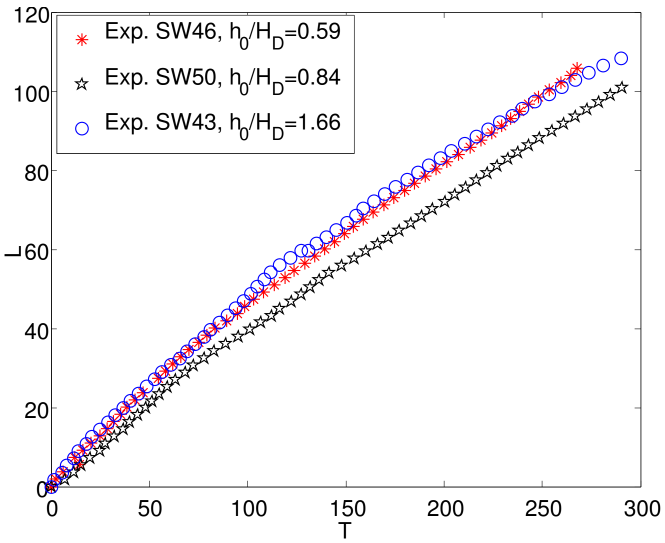

Figure 11.1: Non-dimensional current length, L, as a function of the dimensionless time, T,for three small-scale vertical-wall experiments with different ambient ocean depth, H_D.

0.2, and bottom-trapped plumes, for which the h_0/H_D value is greater than 0.8. From the discussion of their Figure 7, Avicola & Huq (2002) conclude that there is a significant difference in the propagation speed between surface-advected and bottom-trapped coastal currents, and that the current length data for the surface-advected plumes collapse onto another when non-dimensionalized while the current length data for the bottom-trapped plumes do not collapse. However, from the above discussion, no difference in the current propagation speed between surface-advected and bottom-trapped plumes flowing along a vertical-wall coastline was found and current length data were observed to collapse for both surface-advected and bottom-trapped plumes, contradicting the conclusion of Avicola & Huq (2002). Figure 11.2 displays the non-dimensional current length, L, as a function of the dimensionless time, T, for the surface-advected plumes of the small-scale experiments of Thomas & Linden (2007). The current length data for the surface-advected plumes from the small-scale experiments of Thomas & Linden (2007) do not collapse onto another as it is suggested by Avicola & Huq (2002). Furthermore, the non-dimensional current length, L, for the bottom-trapped plume, F, of Avicola & Huq (2002) is seen to collapse with the non-dimensional current length, L, of the surface-advected plumes from the small-scale inclined-wall experiments presented in this study (Figure 11.3), contradicting again the conclusion of Avicola & Huq (2002). Therefore, it seems that the reason for the experiment F of Avicola & Huq (2002) not to collapse with the other experiments does not result from the plume being bottom-trapped but instead comes from the fact that the plume has a large I and Ek_H values.

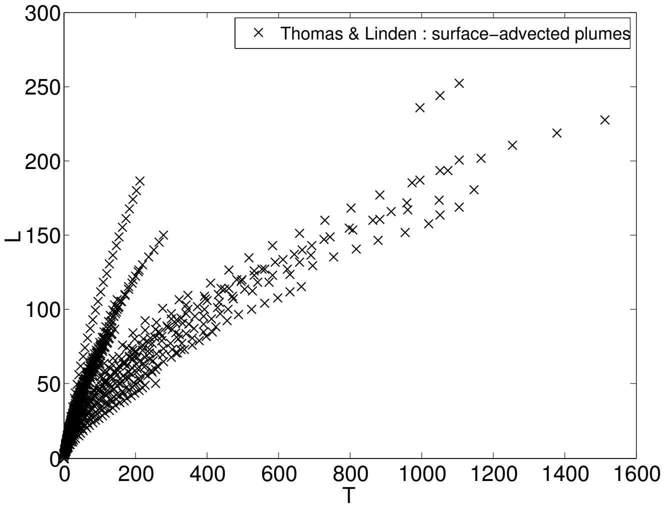

Figure 11.2: Non-dimensional current length, L, as a function of the dimensionless time, T, for the surface-advected plumes from the small-scale experiments of Thomas & Linden (2007).

11.2 Current surface velocity

PIV experiments were carried out for only two combinations of the experimental parameters Ω, $g\prime$ and q_0, to produce two deep currents. For these two deep cases, experiments were repeated with varying the ambient ocean depth, H_D. In all experiments, instabilities were observed along the coastal currents, making not possible the current width measurements. The details of these experiments are listed in the Tables D.1 and D.2 of Appendix D.

Figure 11.4 displays the alongshore velocity, u, as a function of the time, t, measured at the alongshore distance downstream from the source, $d_s = 112.43\ cm$, for two PIV vertical-wall experiments with equal rotation rate, Ω, equal flow rate, q_0, equal reduced gravity, $g\prime$, but different ambient ocean depth, H_D. Figure 11.4a shows a high degree of instabilities in the azimuthal component of the current velocity, which suggests that the current position is oscillating radially along its length. Figure 11.4b, on the other hand, shows a much smoother increase in the current velocity, as well as a more stable radial current position. This observation is consistent with the results of Whitehead & Chapman (1986) who found

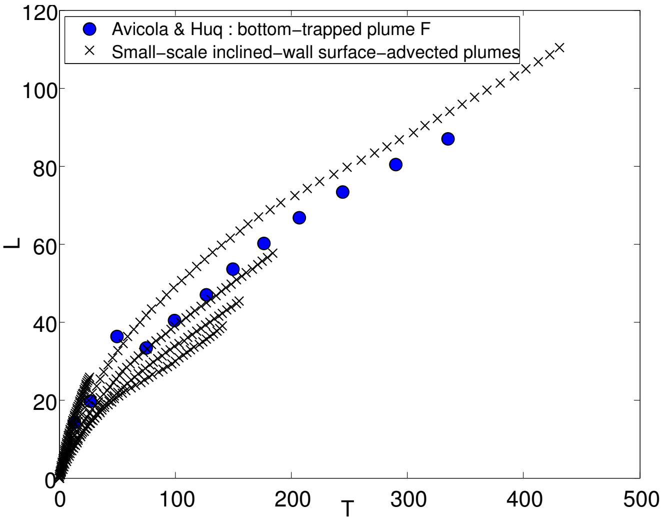

Figure 11.3: Non-dimensional current length, L, as a function of the dimensionless time, T, for the surface-advected plumes from the small-scale inclined-wall experiments presented in this study and for the bottom-trapped experiment, F, of Avicola & Huq (2002).

that in the presence of a sloping wall, the gravity current becomes more laminar. In these experiments, the coastal plumes are observed as well to become more laminar when they interact with the bottom of the tank.

Figure 11.5 displays the alongshore velocity, u, as a function of the radial position, measured at the alongshore distance downstream from the source, $d_s = 112.4\ cm$, and at the time $t = 124.48\ s$, for three PIV vertical-wall experiments with equal rotation rate, Ω, equal flow rate, q_0, equal reduced gravity, $g\prime$, but different ambient ocean depth, H_D. The value of the alongshore velocity is smaller in the experiment with the smallest value for the ambient ocean depth parameter but this is probably due to the presence of the strong instabilities in this experiment. The across-shore distance occupied by the coastal current/instability system is the same for the three experiments.

Therefore, the major difference observed on coastal plumes when decreasing the ambient ocean depth is that currents become more laminar when interacting with the tank bottom. Of course, this study is not complete and some more experiments have to be performed to get results, in particular, for the current width.

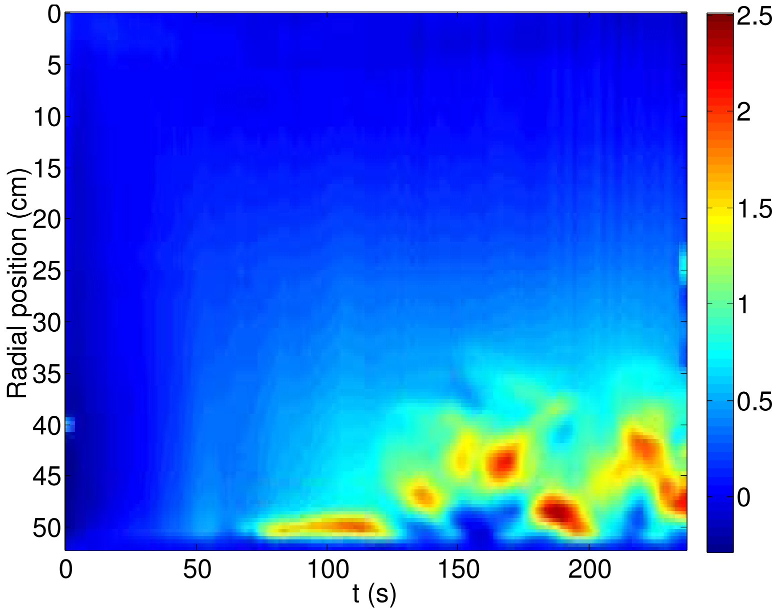

(a) Experiment $J02$, $h_0/H_D = 0.52$.

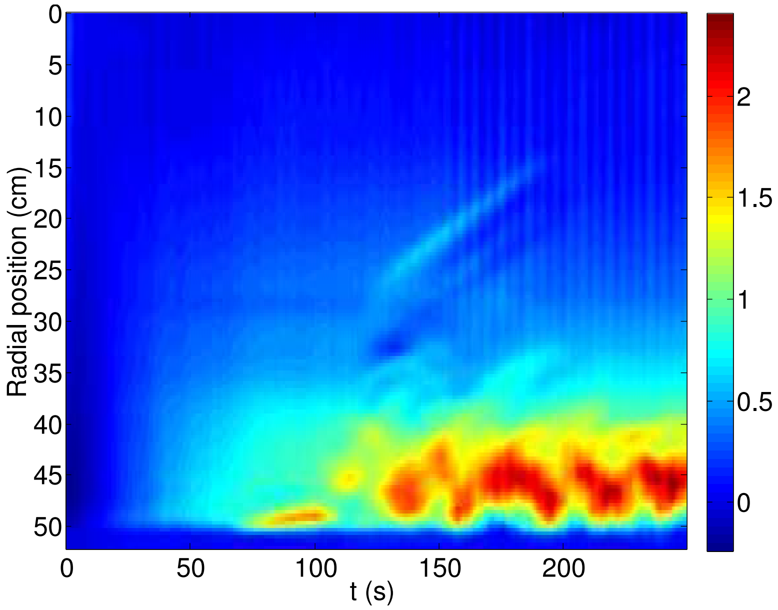

(b) Experiment $J11$, $h_0/H_D = 0.85$.

Figure 11.4: Alongshore velocity, u ($cm\ s^{-1}$), as a function of the time, t (s), measured at the alongshore distance downstream from the source, $d_s = 112.4\ cm$, for two PIV vertical-wall experiments with different ambient ocean depth, H_D. The color bar in each figure is for velocity (in $cm\ s^{-1}$).

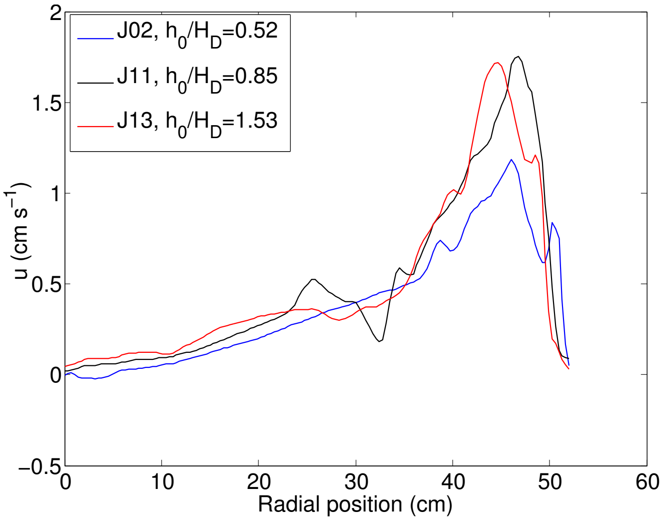

Figure 11.5: Alongshore velocity, u, as a function of the radial position for three PIV vertical-wall experiments with different ambient ocean depth, H_D, measured at the alongshore distance downstream from the source, $d_s = 112.4\ cm$, and at the time $t = 124.48\ s$.

Part V

Conclusion

CHAPTER 12

Conclusion

In the first part of this thesis, numerical simulations, conducted with the Regional Ocean Modeling System ($ROMS$), and investigating the dynamics of gravity-driven coastal currents flowing along a simple vertical-wall coastline, have been described. Two complementary studies have been performed: one without explicit lateral viscosity (inviscid) and another using the molecular value of viscosity. The purposes of the investigation are two-fold: first, to quantify departures from the geostrophic theory of Thomas & Linden (2007), and second, to investigate the internal dynamics of the developing plumes.

The model of Thomas & Linden (2007) assumes steady inviscid plumes propagating along a vertical wall, invariance in the along-shore direction, geostrophic equilibrium, and a dominant along-shore velocity which vanishes at the coast. To assess these assumptions, results from the numerical studies have been compared to the geostrophic model of Thomas & Linden (2007), to their small-scale laboratory vertical-wall experiments, and to a complementary set of laboratory vertical-wall experiments conducted at Warwick University (the latter using the PIV method to better identify plume widths and surface velocity fields). The kinematic properties (lengths, widths, velocities) of the experimental and numerical plumes have been determined and compared. Dependences on the primary non-dimensional parameters – the non-dimensional isopycnal slope, I, and the horizontal Ekman number, Ek_H – have also been determined.

Upon release of the buoyant water in the numerical and laboratory experiments, both an anti-cyclonic bulge growing in the vicinity of the estuary and a coastal current flowing downstream of the bulge in the direction of Kelvin wave propagation are found to develop. The rate of elongation of the plumes in the inviscid numerical simulations typically exceeds the estimate given by the geostrophic theory, and approaches the best the rate of elongation of the plumes produced in the laboratory experiments conducted at smallest horizontal Ekman number. In contrast, the rate of elongation of the plumes in the viscous numerical simulations duplicates quite well the rate of the elongation of the plumes in the laboratory experiments at comparable horizontal Ekman number. During the initial evolution of the plumes from the viscous numerical simulations, the plume propagation rate is larger than the geostrophic prediction, then the plumes decelerate to finally propagate at nearly constant speed. The magnitude of the plume deceleration is most important at the highest values of the horizontal Ekman number. The discrepancies between the viscous numerical simulations (and thus laboratory experiments) and the geostrophic model for the plume propagation rate are the most significant when the lateral viscous forces are the largest (that is, for high horizontal Ekman number). The dimensionless number, I (characterizing the isopycnal slope) is also noticed to have an impact on plume propagation speed: plumes with a large isopycnal slope (large I), that is plumes which are deep and narrow, are observed to be slower than the predicted geostrophic velocity.

The width of the plumes is observed to increase over the duration of each experiment, and to follow a simple curve growing as $t^{1/2}$. Agreement between numerical simulation and PIV experiments is found for the plumes with small horizontal Ekman number. The width of the plumes for the numerical simulations and laboratory experiments at large horizontal Ekman number can only be compared at early time as instabilities occur in these plumes and make the width measurement unreliable at later time. Good agreement between the numerical simulations and laboratory experiments is also found for the plume width at large horizontal Ekman number. When quantifying the plume width with the geostrophic width of Thomas & Linden (2007), best agreement is found at low horizontal Ekman number and low isopycnal slope, that is for wide and shallow plumes in a system in which lateral viscous forces are small. The plume depth profile in the numerical simulations is observed to decrease along the wall only in the final portion of the plume length, contradicting Thomas & Linden (2007) who suggest a linear decrease for the plume depth along the coastal wall.

Maximum surface velocities have been measured and compared for the numerical simulations and PIV experiments at a fixed distance downstream from the source as a function of time. At early times, the maximum surface velocity is extracted from the plume nose and at a later time, it is extracted from the coastal plume. In the nose region, the maximum surface velocities are the highest in the numerical simulations and exceed the theoretical prediction by a factor of about 2. By contrast, in the laboratory experiments, the maximum surface velocities are the lowest in the nose and are much slower than the geostrophic velocity. These differences are suggested to have arisen from differences in the buoyancy injection mechanisms employed in the laboratory experiments and numerical simulations. Maximum surface velocities of the numerical simulations compare quite well with the maximum surface velocities of the PIV experiments at small horizontal Ekman number inside the coastal plume (not at the nose). From examination of the maximum velocity in the numerical simulations at different vertical levels, the geostrophic velocity given by the theory is not reached at the surface but instead below the surface.

The internal dynamics of the plumes is examined by producing cross-plume and along-plume momentum balances. The numerical plumes are found to rapidly attain geostrophic balance with a maximum velocity in the plume greater than the theoretically expected geostrophic velocity. This is in agreement with the observed maximum surface velocities in the numerical and PIV experiments. In disagreement with the theoretical assumptions, the along-shore velocity in the numerical simulations does not vanish at the wall (especially in the inviscid numerical simulations in which the along-shore velocity reaches its maximum at the coastal wall). Instabilities are observed to develop along the plume edge for some experimental parameter combinations. The formation of the instabilities observed in the present experiments depends on the magnitude of the horizontal Ekman number and the dimensionless parameter, I, characterizing the isopycnal slope. Values of I greater than 0.3 generally produce instabilities in the buoyant outflow. The instabilities are expected to be predominantly baroclinic as plumes with large I values are deep and narrow, and then have enough potential energy (which is the energy source of baroclinic instabilities) available to be released into the instability process. Furthermore, to strengthen this result, it has been shown that the unstable experiments presented in this study satisfy the two criteria of Griffiths & Linden (1981b) to have baroclinic instabilities, that is unstable plumes have the square of the ratio of the internal Rossby radius of deformation to the horizontal length scale of the flow larger than 1, and the fraction of the total fluid depth occupied by the layer inside the front larger than 0.1.

The rate of mixing in the buoyant plumes, estimated from the rate of production of water of intermediate density, does not appear to depend importantly on whether the plumes were stable or unstable. However, the total amount of mixing undergone in a single experiment is much greater for the unstable experiments. The two results are reconciled by noting that the viscous unstable experiments occupy a longer elapsed time.

Overall, the theory of Thomas & Linden (2007) is found to best reproduce the coastal currents with the weakest viscous forces (small horizontal Ekman number in the small-scale study), but substantial departures from the theory occur as the viscous forces magnitude increases. When combining the results of the first part of this thesis, the coastal currents are found to be wider and slower than the theory when the viscous forces are the greatest in the fluid system, while the coastal plumes are faster than the theoretical prediction when the viscous forces are the most negligible (as it is the case in the inviscid numerical simulations).

The second part of this thesis is concerned with the dynamics of gravity-driven coastal currents propagating along a more realistic inclined-wall coastline. The geostrophic model of Thomas & Linden (2007) has been extended to inclined coastlines. Similarly toYankovsky & Chapman (1997) and Lentz & Helfrich (2002), the depth for a plume flowing along an inclined coastline has been assumed to be the same depth as the depth for a plume flowing along a vertical-wall coastline. The extended model for sloping walls predicts that plumes propagating along an inclined wall do not necessarily slow down compare to plumes flowing along a vertical wall, they can also be faster or propagate at same speed than vertical-wall plumes. The predictions of the generalized model have been compared to two complementary experimental data sets: one large-scale study conducted in the Trondheim Coriolis facility and one small-scale study performed at Warwick University (the latter using the PIV method to better identify plume widths and surface velocity fields). In addition, experimental data for the propagation velocity and the width of the plumes flowing along inclined coastlines from the studies of Avicola & Huq (2002), Whitehead & Chapman (1986) and Lentz & Helfrich (2002), and from oceanic observations, have also been compared to the extended geostrophic model and to the scaling of Lentz & Helfrich (2002). Dependences on the primary non-dimensional parameters – the non-dimensional isopycnal slope, I, the horizontal Ekman number, Ek_H, and the non-dimensional ambient depth parameter, h_0/H_D – have also been determined.

Similarly to plumes flowing along a vertical coastline, upon release of freshwater along an inclined coastline, both an anti-cyclonic bulge growing in the vicinity of the estuary and a coastal current flowing downstream of the bulge in the direction of Kelvin wave propagation are found to develop. Contrarily to vertical-wall plumes, there is a trend for the gyre position to slightly shift just upstream of the source. From experimental observations, plumes propagating along an inclined coastline can propagate slower than plumes flowing along a vertical coastline. However, in some laboratory experiments, no difference at all on the whole evolution of the coastal current can be observed when introducing an inclined coastline. Equally, during some experiments, coastal plumes are observed to propagate faster over an inclined wall rather than over a vertical wall. These two latter observations contradict the results of Whitehead & Chapman (1986) who find that a coastal current flowing over a sloping wall slows down during the experiment.

A comparison of the inclined-wall experiments from this study for the plume propagation velocity with the prediction of the extended model reveals a quite poor agreement. The discrepancy between the experimental and theoretical inclined-wall plume velocity is seen to depend on the horizontal Ekman number magnitude: for large values of the horizontal Ekman number (values obtained in the small-scale study), the plumes in the laboratory are slower than the theoretical prediction, while for very low values of the horizontal Ekman number – thus large values of the Reynolds number (values obtained in the large-scale study), the plumes in the laboratory are faster than the theoretical prediction. Generally, the plumes with very low horizontal Ekman number (thus with large Reynolds number) are observed to propagate at constant speed. As the horizontal Ekman number value increases, the plumes are seen to slow down, to finally propagate at a constant speed slower than the theoretical prediction, and the magnitude of the plume deceleration is found to be the most important at the highest values of the horizontal Ekman number (similar results have been obtained in the vertical-wall study). This result is strengthened by the very good agreement found for the plume propagation velocity between the extended model and the experiments of Avicola & Huq (2002), Whitehead & Chapman (1986) and Lentz & Helfrich (2002) which simulated inclined-wall plumes in the range of the horizontal Ekman number for which the agreement is found between the experiments from this study and the extended theoretical model. The agreement between experiments and theory seems also to depend on the non-dimensional ambient depth parameter: agreement is always found for the plumes with very large h_0/H_D values, thus for the plumes the most in contact with the sloping wall (bottom-trapped plumes). The extended model has also been compared to oceanic observations and it turns out to predict quite well the propagation speed of these oceanic plumes.

Data from the large-scale laboratory study at the Coriolis facility at Trondheim reveal that the plume depth at which the interface between the coastal plume and the ambient water intersects the inclined coastline is best predicted by the theoretical depth of a plume flowing along a vertical wall, predicted by the model of Thomas & Linden (2007). The data for the plume width from the small-scale inclined-wall experiments presented in this study follow a single curve growing as $t^{1/2}$ and collapse with the small-scale vertical-wall plume width data (except for the two inclined-wall experiments with the largest value for the non-dimensional ambient depth parameter which expand the furthest offshore). A good agreement is found between the small-scale experiments of this study, the experiments of Avicola & Huq (2002) and Lentz & Helfrich (2002), and the extended model for the plume width. The values of the width for the plumes flowing along an inclined coastline increase as the values of the non-dimensional ambient depth parameter increase. Thus the bottom-trapped plumes are the widest. Best agreement between the experiments and the theory for the plume width is found for the plumes with large non-dimensional ambient depth parameter and with small horizontal Ekman number, that is for strong bottom-trapped plumes (whatever is the value of the horizontal Ekman number), and for weak bottom-trapped and surface-advected plumes in a fluid system with weak lateral viscous forces. Weak bottom-trapped and surface-advected plumes (small h_0/H_D values) in a fluid system with large viscous forces (large Ek_H values) are wider than the theoretical prediction.

The scaling theory of Lentz & Helfrich (2002) for plumes flowing along an inclined coastline has also been compared to the extended theory, to the inclined-wall experiments presented in this study and to the experiments of Avicola & Huq (2002), Whitehead & Chapman (1986) and Lentz & Helfrich (2002). Similarly to the extended model, a poor agreement is found between the predicted propagation speed of Lentz & Helfrich (2002) and the measured plume propagation speed in the large-scale experiments, while a good agreement is found between the four small-scale studies and the scaling theory of Lentz & Helfrich (2002) for the plume propagation speed. The extended model presented in this study agrees the best with the four small-scale experimental studies for the plume propagation speed while the scaling theory of Lentz & Helfrich (2002) compares the best with the small-scale experimental studies for the plume width.

A last part briefly investigates the impact the bottom of the tank can have on the evolution of a coastal current flowing along a vertical wall. A set of experiments have shown that when the non-dimensional ambient depth parameter increases (therefore when the depth of the ambient water in the tank is reduced), the propagation speed for a coastal current flowing along a vertical coastline does not change. Furthermore, it has been seen that the rate of elongation for a bottom-trapped plume can collapse with the rate of elongation for a surface-advected plume, contradicting the conclusion of Avicola & Huq (2002). In agreement with Whitehead & Chapman (1986), coastal currents are observed to become more laminar when they interact with the ocean bottom. The plume width could not be studied in this last part as the presence of instabilities in the coastal currents made the width measurements unreliable.

The main unexpected result for the plumes flowing along an inclined coastline is that a coastal current flowing over an inclined wall can be slower than a plume flowing over a vertical wall, as concluded Whitehead & Chapman (1986), and can also be faster or propagate at same speed than a vertical-wall plume (result predicted by the extended model and confirmed by experimental observations). Another important result is that, whether the topography is a sloping wall or a vertical wall coastline, the lateral viscous forces play an important role in the coastal current evolution. Indeed, the geostrophic model of Thomas & Linden (2007) for a vertical coastline and the extended model presented in this study for a sloping wall predicts the best the experiments with low horizontal Ekman numbers (for the plume propagation speed and width). When the magnitude of the viscous forces increases (large Ek_H values), the plumes, in both studies (vertical and inclined walls), are seen to slow down to finally propagate at a constant speed smaller than the geostrophic velocity, and to be larger than the predicted width. The rate of deceleration of the plumes, in both studies, is observed to be the most important at largest horizontal Ekman numbers. On the other hand, the coastal currents with a very low horizontal Ekman number, therefore with a large Reynolds number, produced in the large-scale study only, propagate at a constant speed, faster than the geostrophic prediction. When the viscous forces become significant in the fluid system, that is in the small-scale study mainly, viscosity must provide a nearly constant decelerating force to make the flow propagates slower than the theory, while in the large-scale study, turbulence turns out to be important (large Reynolds number) and must play a role in the discrepancy between the measured velocity and the geostrophic prediction.

Grégorio *et al.* (2011) examined the potential role of the viscous forces by a slight modification of the theory proposed by Thomas & Linden (2007), retaining many of their original assumptions – i.e., x-invariant, rotationally dominated, steady flow – but introducing molecular viscous forces in the cross-plume direction. Grégorio *et al.* (2011) obtained that the velocity discrepancy is proportional to the square root of the horizontal Ekman number. However, Grégorio *et al.* (2011) did not consider the case of very low values for the horizontal Ekman number (thus plumes with large Reynolds number), obtained in larger-scale facilities. Hence the geostrophic theory needs some further considerations to predict better experiments with very low horizontal Ekman number (large Reynolds number). In addition, as it has been discussed, some experiments (usually with quite large horizontal Ekman number) have been seen to accelerate at the start of the experiments, then to slow down to finally propagate at constant velocity. Temporal variations seems also to be important during the first stage of the experiments, and thus, need to be considered in the theory.

In the theoretical chapter of this thesis, the depth for a coastal current flowing over an inclined wall has been found to be different from the depth of a coastal current flowing over a vertical wall. However, experimental observations have showed that the depth of a plume flowing over a sloping bottom is best predicted by the theoretical vertical-wall plume depth of Thomas & Linden (2007), it is why it has been assumed in the theory presented in this study that the depth for a coastal current flowing over an inclined wall is supposed to be equal to the depth of a coastal current flowing over a vertical wall. In the future, it would be interesting to compare the theory and the experimental results presented here with a theory considering that the depth for a plume flowing over an inclined wall would be defined as in (4.30). Lastly, and in order to approach a real world situation, it would be interesting to study the dynamics of a coastal plume when the freshwater discharge is varied during the experiments and when a rough topography is introduced to reproduce ocean coastline irregularities.

Bibliography

Avicola, G. & Huq, P. (2002). Scaling analysis for the interaction between a buoyant coastal current and the continental shelf : experiments and observations, *J. Phys. Oceanogr.* **32**(11): 3233–3248.

Avicola, G. & Huq, P. (2003a). The characteristics of the recirculating bulge region in coastal buoyant outflows, *J. Mar. Res.* **61**(4): 435–463.

Avicola, G. & Huq, P. (2003b). The role of outflow geometry in the formation of the recirculating bulge region in coastal buoyant outflow, *J. Mar. Res.* **61**(4): 411–434.

Brend, M. A. (2009). *Traversing SPIV for the measurement of vortex rings under background rotation*, PhD thesis, University of Warwick.

Chabert D'Hières, G., Didelle, H. & Obaton, D. (1991). A laboratory study of surface boundary currents : application to the algerian current, *J. Geophys. Res.* **96**(C7): 12,539–12,548.

Chant, R. J. (2011). Interactions between estuaries and coasts: river plumes - their formation, transport and dispersal, *in* E. Wolanski, D. S. McLusky, S. Monismith & R. Uncles (eds), *Treatise on Estuarine and Coastal Science*, Elsevier Press.

Chant, R. J., Glenn, S. M., Hunter, E., Kohut, J., Chen, R. F., Houghton, R. W., Bosch, J. & Schofield, O. (2008). Bulge formation of a buoyant river outflow, *J. Geophys. Res.* **113**(C01017).

Chao, S. Y. (1988). River-forced estuarine plumes, *J. Phys. Oceanogr.* **18**(1): 72–88.

Chao, S.-Y. & Boicourt, W. C. (1986). Onset of estuarine plumes, *J. Phys. Oceanogr.* **16**: 2137–2149.

Chapman, D. C. & Lentz, S. J. (1994). Trapping of a coastal density front by the bottom boundary layer, *J. Phys. Oceanogr.* **24**(7): 1464–1479.

Csanady, G. T. (1984). Circlation induced by river inflow in well mixed water over a sloping continental shelf, *J. Phys. Oceanogr.* **14**(11): 1703–1711.

Cushman-Roisin, B. (1994). *Introduction to geophysical fluid dynamics*, Prentice Hall.

Ellingsen, I. H. (2004). *Internal tides and the spread of river plumes in the Trondheim Fjord*, PhD thesis, Norwegian University of Science and Technology.

Fong, D. A. & Geyer, W. R. (2002). The alongshore transport of freshwater in a surface-trapped river plume, *J. Phys. Oceanogr.* **32**(3): 957–972.

Framinan, M. B., Valle-Levinson, A., Sepulveda, H. H. & Brown, O. B. (2008). Tidal variations of flow convergence, shear, and stratification, at the rio de la plata estuary turbidity front, *J. Geophys. Res.* **113**.

Garvine, R. W. (1977). Observations of the motion field of the connecticut river plume, *J. Geophys. Res.* **82**(3): 441454.

Garvine, R. W. (1995). A dynamical system for classifying buoyant coastal discharges, *Cont. Shelf Res.* **15**(13): 1585–1596.

Garvine, R. W. (2001). The impact of model configuration in studies of buoyant coastal discharge., *J. Mar. Res.* **59**(2): 193–225.

Grégorio, S. O., Haigvogel, D. B., Thomas, P. J., Taskinoglu, E. S. & Skeen, A. J. (2011). Laboratory and numerical simulations of gravity-driven coastal currents:departures from geostrophic theory, *Dyn. Atmos. Oceans.* **52**: 20–50.

Griffiths, R. W. (1986). Gravity currents in rotating systems, *Annu. Rev. Fluid Mech.* **18**: 59–89.

Griffiths, R. W. & Hopfinger, E. J. (1983). Gravity currents moving along a lateral boundary in a rotating fluid., *J. Fluid Mech.* **134**: 357–399.

Griffiths, R. W. & Linden, P. F. (1981a). The stability of buoyancy-driven coastal currents, *Dyn. Atmos. Oceans* **5**: 281–306.

Griffiths, R. W. & Linden, P. F. (1981b). The stability of vortices in a rotating, stratified fluid, *J. Fluid Mech.* **105**: 283–316.

Hacker, J. (1996). *Gravity currents in rotating channels*, PhD thesis, Universiy of Cambridge.

Haidvogel, D. B., Arango, H., Budgell, W. P., Cornuelle, B. D., Curchitser, E., Lorenzo, E. D., Fennel, K., Geyer, W. R., Hermann, A. J., Lanerolle, L., Levin, J., McWilliams, J. C., Miller, A. J., Moore, A. M., Powell, T. M., Shchepetkin, A. F., Sherwood, C. R., Signell, R. P., Warner, J. C. & Wilkin, J. (2007). Ocean forecasting in terrain-following coordinates: Formulation and skill assessment of the regional ocean modeling system, *J. Comput. Phys.* **227**: 3595–3624.

Hickey, B. M., Pietrafesa, L. J. & Boicourt, W. C. (1998). The colombia river plume study : subtidal variability in the velocity and salinity fields, *J. Geophys. Res.* **103**(C5): 10339–10368.

Horner-Devine, A. R., Fong, D. A., Monismith, S. G. & Maxworthy, T. (2006). Laboratory experiments simulating a coastal river inflow, *J. Fluid Mech.* **555**: 203–232.

Ito, T., Ohnishi, M., Isoda, Y., Nakayama, T., Shima, S., Kuroda, H., Iwahashi, M. & Sato, C. (2003). Variation of velocity and volume transport of the tsugaru warm current in the winter 1999-2000, *Geophys. Res. Lett.* **30**.

Lentz, S. J. & Helfrich, K. R. (2002). Buoyant gravity currents along a sloping bottom in a rotating fluid, *J. Fluid Mech.* **464**: 251–278.

Lentz, S. T., Elgar, S. & Guza, R. T. (2003). Observations of the flow field near the nose of a buoyant coastal current., *J. Phys. Oceanogr.* **33**(4): 933–943.

Liu, Y., MacCready, P., Hickey, B. M., Dever, E. P., Kosro, P. M. & Banas, N. S. (2009). Evaluation of a coastal ocean circulation model for the columbia river plume in summer 2004, *J. Geophys. Res.* **114**.

Matsuyama, M., Wadaka, M., Abe, T., Aota, M. & Koike, Y. (2006). Current structure and volume transport of the soya warm current in summer, *J. Oceanogr.* **62**: 197–205.

Mertz, G., El-Sabh, M. I., Proulx, D. & Condal, A. R. (1988). Instability of a buoyancy-driven coastal jet : the gaspé current and its st. lawrence precursor., *J. Geophys. Res.* **93**(C6): 6885–6893.

Millot, C. (1985). Some features of the algerian current., *J. Geophys. Res.* **90**(C4): 7169–7176.

Munchow, A. & Garvine, R. W. (1993a). Buoyancy and wind forcing of a coastal current, *J. Mar. Res.* **51**: 293–322.

Munchow, A. & Garvine, R. W. (1993b). Dynamical properties of a buoyancy-driven coastal current, *J. Geophys. Res.* **98**(C11): 20063–20077.

Nof, D. & Pichevin, T. (2001). The ballooning of outflows, *J. Phys. Oceanogr.* **31**(10): 3045–3058.

Obaton, D., Millot, C., Chabert D'Hières, G. & Taupier-Letage, I. (2000). The algerian current : comparison between in situ and laboratory data sets, *Deep-Sea Res. Part I* **47**: 2159–2190.

Rivas, D., Velasco Fuentes, O. U. & Ochoa, J. (2005). Topographic effects on the dynamics of gravity currents in a rotating system, *Dyn. Atmos. Oceans* **39**: 227–249.

Rossby, C. G. (1938). On the mutual adjustment of pressure and velocity distributions in certain simple current systems, *ii*, *J. Mar. Res.* **1**: 239–263.

Shchepetkin, A. F. & McWilliams, J. C. (2005). The regional ocean modeling system (roms): A split-explicit, free-surface, topography-following coordinates ocean model, *Ocean Model.* **9**: 347–404.

Simpson, J. E. (1987). *Gravity currents: in the environment and the laboratory.*

Simpson, J. E. & Britter, R. E. (1979). The dynamics of the head of a gravity current advancing over a horizontal surface, *J. Fluid Mech.* **94**: 477–495.

Simpson, J. H., Bos, W. G., Schirmer, F., Souza, A. J., Rippeth, T. P., Jones, S. E. & Hydes, D. (1993). Periodic stratification in the rhine rofi in the north sea, *Oceanol. Acta* **16**: 23–32.

Stern, M. E., Whitehead, J. A. & Hua, B.-L. (1982). The intrusion of a density current along the coast of a rotating fluid, *J. Fluid Mech.* **123**: 237–265.

Thomas, A. C. & Weatherbee, R. A. (2006). Satellite measured temporal variability of the columbia river plume, *Remote Sens. Environ.* **100**: 167–178.

Thomas, P. J. & Linden, P. F. (2007). Rotating gravity currents: small-scale and large-scale laboratory experiments and a geostrophic model, *J. Fluid Mech.* **578**: 35–65.

Vinger, A. & McClimans, T. A. (1980). Laboratory studies of baroclinic coastal currents along a straight, vertical coastline, *Technical Report STF60 A80081*, Norwegian Hydrodynamic Laboratories.

Whitehead, J. A. & Chapman, D. C. (1986). Laboratory observations of a gravity current on a sloping bottom : the generation of shelf waves, *J. Fluid Mech.* **172**: 373–399.

Wright, D. G. (1989). On the alongshelf evolution of an idealized density front, *J. Phys. Oceanogr.* **19**(4): 532–541.

Yankovsky, A. E. & Chapman, D. C. (1997). A simple theory for the fate of buoyant coastal discharges, *J. Phys. Oceanogr.* **27**(7): 1386–1401.

Zhang, W. G., Wilkin, J. L., Levin, J. C. & Arango, H. G. (2009). An adjoint sensitivity study of buoyancy- and wind-driven circulation on the new jersey inner shelf, *J. Phys. Oceanogr.* **39**(7): 16521668.

APPENDIX A

Appendix A

The values of the parameters from Tables A.1 - A.4, listed in order, are the bottom slope, α (°), the Coriolis parameter, f (s^{-1}), the reduced gravity anomaly, $g\prime$ ($cm\ s^{-2}$), the flow rate, q_0 ($cm^3\ s^{-1}$), the ambient ocean depth, H_D (cm), the theoretical current depth, h_0 (cm), the theoretical current width, w_0 (cm), the dimensionless parameter, I, the horizontal Ekman number, Ek_H, the vertical Ekman number, Ek_V, the Reynolds number, Re, and the non-dimensional ambient depth parameter, h_0/H_D.

Exp.	L1AT	L2AT	L3AT	L4T	L5T	L6T
α	90	90	90	90	90	90
f	2	2	2	2	3	3
g'	2.03	6.15	16.17	31.8	6.14	16.23
q_0	10	10	10	10	10	10
H_D	10.4	10.4	10.4	10.5	11.1	11.1
h_0	4.44	2.55	1.57	1.12	3.13	1.92
w_0	2.12	2.8	3.57	4.22	2.07	2.63
I	1.036	0.533	0.298	0.199	0.8	0.447
Ek_H	1.11×10^{-3}	6.38×10^{-4}	3.93×10^{-4}	2.8×10^{-4}	7.82×10^{-4}	4.81×10^{-4}
Ek_V	2.54×10^{-4}	7.69×10^{-4}	2.02×10^{-3}	3.98×10^{-3}	3.41×10^{-4}	9.02×10^{-4}
Re	338	588	954	1337	480	780
h_0/H_D	0.43	0.25	0.15	0.11	0.28	0.17
Exp.	L7T	L8T	L9T	L10T	L11T	L12T
α	90	90	90	90	90	90
f	3	3	5	5	5	5
g'	31.27	2	6.13	15.98	31.85	2
q_0	10	10	10	10	10	10
H_D	11.1	11.1	13.4	13.4	13.4	13.4
h_0	1.39	5.48	4.04	2.5	1.77	7.07
w_0	3.1	1.56	1.41	1.79	2.12	1.06
I	0.301	1.568	1.335	0.751	0.497	2.614
Ek_H	3.46×10^{-4}	1.37×10^{-3}	1.01×10^{-3}	6.25×10^{-4}	4.43×10^{-4}	1.77×10^{-3}
Ek_V	1.74×10^{-3}	1.11×10^{-4}	1.23×10^{-4}	3.2×10^{-4}	6.37×10^{-4}	4×10^{-5}
Re	1083	274	371	600	847	212
h_0/H_D	0.12	0.49	0.3	0.19	0.13	0.53
Exp.	L13T	L14T	L15T	L16T	L17T	L18T
α	90	90	90	90	90	90
f	1	1	1	1	1	1
g'	6.11	16.07	31.82	2.03	6.14	16.04
q_0	10	10	10	10	20	20
H_D	10.2	10.2	10.2	10.2	10.2	10.2
h_0	1.81	1.12	0.79	3.14	2.55	1.58
w_0	4.7	5.99	7.1	3.57	5.6	7.12
I	0.268	0.15	0.099	0.518	0.306	0.172
Ek_H	4.52×10^{-4}	2.79×10^{-4}	1.98×10^{-4}	7.85×10^{-4}	3.19×10^{-4}	1.97×10^{-4}
Ek_V	3.06×10^{-3}	8.04×10^{-3}	1.59×10^{-2}	1.02×10^{-3}	1.54×10^{-3}	4.01×10^{-3}
Re	829	1345	1892	478	1175	1900
h_0/H_D	0.18	0.11	0.08	0.31	0.25	0.15

Table A.1: Parameters of the small-scale experiments of Thomas & Linden (2007).

Exp.	L19T	L20T	L21T	L22T	L23T	L24T
α	90	90	90	90	90	90
f	1	1	2	2	2	2
g'	31.9	2.02	6.12	15.94	31.78	1.98
q_0	20	20	20	20	20	20
H_D	10.2	10.2	10.6	10.6	10.6	10.6
h_0	1.12	4.45	3.62	2.24	1.59	6.36
w_0	8.45	4.24	3.33	4.23	5.02	2.51
I	0.114	0.597	0.614	0.346	0.229	1.208
Ek_H	1.4×10^{-4}	5.56×10^{-4}	4.52×10^{-4}	2.8×10^{-4}	1.98×10^{-4}	7.95×10^{-4}
Ek_V	7.98×10^{-3}	5.05×10^{-4}	3.83×10^{-4}	9.96×10^{-4}	1.99×10^{-3}	1.24×10^{-4}
Re	2679	674	830	1339	1891	472
h_0/H_D	0.11	0.44	0.34	0.21	0.15	0.6
Exp.	L25T	L26T	L27T	L28T	L29T	L30T
α	90	90	90	90	90	90
f	3	3	3	3	5	5
g'	6.04	15.86	31.58	1.96	6.35	16.15
q_0	20	20	20	20	20	20
H_D	11.3	11.3	11.3	11.8	13.3	13.3
h_0	4.46	2.75	1.95	7.82	5.61	3.52
w_0	2.45	3.11	3.7	1.85	1.69	2.13
I	0.928	0.520	0.344	1.824	1.501	0.858
Ek_H	5.57×10^{-4}	3.44×10^{-4}	2.44×10^{-4}	9.78×10^{-4}	7.02×10^{-4}	4.4×10^{-4}
Ek_V	1.68×10^{-4}	4.41×10^{-4}	8.77×10^{-4}	5.44×10^{-5}	6.35×10^{-5}	1.62×10^{-4}
Re	673	1091	1539	383	535	852
h_0/H_D	0.39	0.24	0.17	0.66	0.42	0.26
Exp.	L31T	L32T	L33T	L34T	L35T	L36T
α	90	90	90	90	90	90
f	5	5	1	1	1	1
g'	31.74	2.28	6.19	16.04	31.74	2.26
q_0	20	20	28.12	28.12	28.12	28.12
H_D	13	13.3	10.2	10.2	10.2	10.2
h_0	2.51	9.37	3.01	1.87	1.33	4.99
w_0	2.52	1.31	6.11	7.75	9.19	4.75
I	0.572	2.776	0.326	0.184	0.122	0.597
Ek_H	3.14×10^{-4}	1.17×10^{-3}	2.68×10^{-4}	1.66×10^{-4}	1.18×10^{-4}	4.43×10^{-4}
Ek_V	3.17×10^{-4}	2.28×10^{-5}	1.1×10^{-3}	2.85×10^{-3}	5.64×10^{-3}	4.02×10^{-4}
Re	1195	320	1399	2253	3169	846
h_0/H_D	0.19	0.7	0.18	0.31	0.13	0.49

Table A.2: Parameters of the small-scale experiments of Thomas & Linden (2007).

Exp.	L37T	L38T	L39T	L40T	L41T	L42T
α	90	90	90	90	90	90
f	2	2	2	2	3	3
g'	6.23	16.04	31.5	2.23	6.22	16.13
q_0	28.12	28.12	28.12	28.12	28.12	28.12
H_D	10.6	10.6	10.6	10.6	11.3	11.3
h_0	4.25	2.65	1.89	7.1	5.21	3.23
w_0	3.64	4.61	5.46	2.81	2.68	3.4
I	0.65	0.369	0.246	1.205	0.976	0.551
Ek_H	3.78×10^{-4}	2.35×10^{-4}	1.68×10^{-4}	6.31×10^{-4}	4.63×10^{-4}	2.88×10^{-4}
Ek_V	2.77×10^{-4}	7.13×10^{-4}	1.4×10^{-3}	9.91×10^{-5}	1.23×10^{-4}	3.19×10^{-4}
Re	993	1593	2232	594	810	1304
h_0/H_D	0.4	0.25	0.18	0.67	0.46	0.29
Exp.	L43T	L44T	L45T	L46T	L47T	L48T
α	90	90	90	90	90	90
f	3	3	5	5	5	5
g'	31.66	2.28	6.32	16.14	31.38	2.39
q_0	28.12	28.12	28.12	28.12	28.12	28.12
H_D	11.3	11.3	13.2	13.3	13.3	13.3
h_0	2.31	8.6	6.67	4.17	2.99	10.85
w_0	4.03	2.09	1.84	2.32	2.74	1.44
I	0.368	1.783	1.612	0.918	0.616	2.889
Ek_H	2.05×10^{-4}	7.65×10^{-4}	5.93×10^{-4}	3.71×10^{-4}	2.66×10^{-4}	9.64×10^{-4}
Ek_V	6.25×10^{-4}	4.5×10^{-5}	4.5×10^{-5}	1.15×10^{-4}	2.23×10^{-4}	1.7×10^{-5}
Re	1827	490	632	1011	1409	389
h_0/H_D	0.2	0.76	0.51	0.31	0.23	0.82
Exp.	L49T	L50T	L51T	L52T	L53T	L54T
α	90	90	90	90	90	90
f	1	1	1	1	2	2
g'	6.25	16.07	31.48	2.27	6.27	16.12
q_0	3.18	3.18	3.18	3.18	3.18	3.18
H_D	10.3	10.3	10.4	10.3	10.6	10.7
h_0	1.01	0.63	0.45	1.67	1.42	0.89
w_0	3.55	4.5	5.32	2.76	2.11	2.68
I	0.21	0.119	0.08	0.385	0.419	0.238
Ek_H	7.93×10^{-4}	4.95×10^{-4}	3.53×10^{-4}	1.32×10^{-3}	1.12×10^{-3}	6.98×10^{-4}
Ek_V	9.83×10^{-3}	2.53×10^{-2}	4.95×10^{-2}	3.57×10^{-3}	2.46×10^{-3}	6.34×10^{-3}
Re	473	758	1061	285	335	537
h_0/H_D	0.1	0.06	0.04	0.16	0.13	0.08

Table A.3: Parameters of the small-scale experiments of Thomas & Linden (2007).

Exp.	L55T	L56T	L57T	L58T	L59T	L60T
α	90	90	90	90	90	90
f	2	2	3	3	3	3
g'	31.84	2.25	6.37	15.91	30.91	2.25
q_0	3.18	3.18	3.18	3.18	3.18	3.18
H_D	10.7	10.7	11.1	11.4	11.1	11.3
h_0	0.63	2.38	1.73	1.1	0.79	2.91
w_0	3.17	1.64	1.57	1.97	2.32	1.21
I	0.158	0.775	0.622	0.359	0.241	1.162
Ek_H	4.97×10^{-4}	1.87×10^{-3}	1.36×10^{-3}	8.61×10^{-4}	6.18×10^{-4}	2.29×10^{-3}
Ek_V	1.25×10^{-2}	8.84×10^{-4}	1.11×10^{-3}	2.78×10^{-3}	5.4×10^{-3}	3.93×10^{-4}
Re	755	201	276	436	607	164
h_0/H_D	0.06	0.22	0.16	0.1	0.07	0.26
Exp.	L61T	L62T	L63T	L64T	L65T	L66T
α	90	90	90	90	90	90
f	5	5	5	5	5	1
g'	6.29	15.85	31.45	2.22	86.45	86.25
q_0	3.18	3.18	3.18	3.18	20	20
H_D	13.4	13.4	13.4	13.3	13.3	10.2
h_0	2.25	1.42	1.01	3.78	1.52	0.68
w_0	1.06	1.34	1.59	0.82	3.24	10.84
I	1.045	0.6	0.398	1.953	0.313	0.063
Ek_H	1.77×10^{-3}	1.11×10^{-3}	7.91×10^{-4}	2.98×10^{-3}	1.9×10^{-4}	8.51×10^{-5}
Ek_V	3.96×10^{-4}	9.97×10^{-4}	1.98×10^{-3}	1.4×10^{-4}	8.65×10^{-4}	2.16×10^{-2}
Re	212	337	474	126	1972	4405
h_0/H_D	0.17	0.11	0.08	0.28	0.11	0.07

Table A.4: Parameters of the small-scale experiments of Thomas & Linden (2007).

APPENDIX B

Appendix B

The values of the parameters from Tables B.1 - B.4, listed in order, are the bottom slope, α (°), the Coriolis parameter, f (s^{-1}), the reduced gravity anomaly, $g\prime$ ($cm\ s^{-2}$), the flow rate, q_0 ($cm^3\ s^{-1}$), the ambient ocean depth, H_D (cm), the theoretical current depth, h_0 (cm), the theoretical current width, w_0 (cm), the dimensionless parameter, I, the horizontal Ekman number, Ek_H, the vertical Ekman number, Ek_V, the Reynolds number, Re, and the non-dimensional ambient depth parameter, h_0/H_D.

Exp.	SW25	SW26	SW27	SW28	SW29	SW30
α	90	90	90	90	90	90
f	3.05	3	2.99	3.01	0.98	3
g'	3	3.01	7.58	18.72	18.77	3.01
q_0	20.15	20.33	20.33	20.33	20.33	20.03
H_D	5.6	5.7	5.6	5.7	5.45	4.3
h_0	6.4	6.36	4	2.6	1.46	6.32
w_0	2.03	2.06	2.6	3.25	7.53	2.05
I	1.438	1.413	0.811	0.475	0.154	1.412
Ek_H	7.94×10^{-4}	7.83×10^{-4}	4.93×10^{-4}	3.15×10^{-4}	1.79×10^{-4}	7.89×10^{-4}
Ek_V	8×10^{-5}	8.24×10^{-5}	2.08×10^{-4}	5.07×10^{-4}	4.79×10^{-3}	8.33×10^{-5}
Re	472	479	761	1192	2091	475
h_0/H_D	1.14	1.12	0.72	0.45	0.27	0.47
Exp.	SW31	SW32	SW33	SW34	SW35	SW37
α	90	90	90	90	90	90
f	3	1	1	3	2.04	3
g'	7.62	3.01	2.92	3.01	3.02	3
q_0	20.03	20.03	20.19	28.11	28.11	28.11
H_D	4.4	4.4	2.3	12.4	6.9	5.9
h_0	3.97	3.65	3.71	7.48	6.16	7.5
w_0	2.59	4.69	4.67	2.24	2.99	2.24
I	0.807	0.47	0.478	1.508	1.023	1.512
Ek_H	4.96×10^{-4}	4.55×10^{-4}	4.6×10^{-4}	6.65×10^{-4}	5.48×10^{-4}	6.67×10^{-4}
Ek_V	2.12×10^{-4}	7.51×10^{-4}	7.29×10^{-4}	5.96×10^{-5}	1.29×10^{-4}	5.93×10^{-5}
Re	757	824	816	563	685	562
h_0/H_D	0.9	0.83	1.61	0.6	0.89	1.27
Exp.	SW38	SW39	SW40	SW41	SW42	SW43
α	90	90	90	90	90	90
f	2.03	2.03	3.01	1	2.01	2.03
g'	3	3	3	3.01	3	3.07
q_0	19.95	3.19	28.11	19.95	28.11	19.95
H_D	6.1	6.1	9	3.85	3	3.1
h_0	5.2	2.08	7.51	3.67	6.13	5.13
w_0	2.75	1.74	2.23	4.63	3.02	2.77
I	0.957	0.661	1.518	0.476	1.012	0.941
Ek_H	6.52×10^{-4}	1.63×10^{-3}	6.68×10^{-4}	4.59×10^{-4}	5.45×10^{-4}	6.43×10^{-4}
Ek_V	1.82×10^{-4}	1.14×10^{-3}	5.88×10^{-5}	7.34×10^{-4}	1.33×10^{-4}	1.87×10^{-4}
Re	575	230	561	816	688	583
h_0/H_D	0.85	0.34	0.83	0.95	2.04	1.66

Table B.1: Parameters of the small-scale experiments conducted at Warwick.

Exp.	SW44	SW45	SW46	SW47	SW48	SW49
α	90	90	90	90	90	90
f	1.01	3.01	2.04	0.99	2.03	3.02
g'	3.01	3	2.99	3	3	3.01
q_0	19.95	28.11	19.95	19.95	28.11	28.11
H_D	3.2	4.1	8.9	8.35	10.45	10.55
h_0	3.67	7.52	5.21	3.62	6.16	7.5
w_0	4.63	2.23	2.74	4.72	3	2.23
I	0.476	1.52	0.961	0.465	1.021	1.517
Ek_H	4.59×10^{-4}	6.69×10^{-4}	6.53×10^{-4}	4.54×10^{-4}	5.48×10^{-4}	6.67×10^{-4}
Ek_V	7.34×10^{-4}	5.87×10^{-5}	1.8×10^{-4}	7.72×10^{-4}	1.3×10^{-4}	5.89×10^{-5}
Re	816	561	574	826	684	562
h_0/H_D	1.15	1.83	0.59	0.43	0.59	0.71
Exp.	SW50	S4	S5	S6	S7	S8
α	90	59.2	59.2	59.2	59.2	59.2
f	2.02	1.01	3.03	3.02	0.98	0.99
g'	3.06	3	3	3.03	7.59	7.47
q_0	19.91	3.11	20.1	3.11	3.11	20.1
H_D	6.1	3.01	2.11	1.33	3.88	6.13
h_0	5.12	1.45	6.37	2.49	0.9	2.31
w_0	2.78	2.91	2.04	1.29	3.76	5.93
I	0.937	0.328	1.428	0.974	0.183	0.27
Ek_H	6.43×10^{-4}	1.16×10^{-3}	7.93×10^{-4}	2×10^{-3}	7.21×10^{-4}	2.87×10^{-4}
Ek_V	1.89×10^{-4}	4.71×10^{-3}	8.13×10^{-5}	5.35×10^{-4}	1.27×10^{-2}	1.9×10^{-3}
Re	583	322	473	187	520	1306
h_0/H_D	0.84	0.48	3.02	1.87	0.23	0.38
Exp.	S9	S10	S13	S14	SB1	SB11
α	59.2	59.2	59.2	59.2	59.2	59.2
f	3	3.01	0.99	3.01	2.98	1
g'	7.53	7.55	18.68	18.52	3.07	3.06
q_0	3.11	20.1	3.11	3.11	28.12	3.27
H_D	1.68	2.67	4.85	2.1	2.33	3.08
h_0	1.57	4	0.57	1.01	7.39	1.46
w_0	1.62	2.58	4.69	2.03	2.26	2.98
I	0.56	0.815	0.107	0.328	1.484	0.325
Ek_H	1.26×10^{-3}	4.98×10^{-4}	4.61×10^{-4}	8.08×10^{-4}	6.57×10^{-4}	1.12×10^{-3}
Ek_V	1.35×10^{-3}	2.08×10^{-4}	3.09×10^{-2}	3.29×10^{-3}	6.13×10^{-5}	4.65×10^{-3}
Re	297	753	814	464	570	335
h_0/H_D	0.94	1.5	0.12	0.48	3.17	0.47

Table B.2: Parameters of the small-scale experiments conducted at Warwick.

Exp.	SB15	SB21	SB23	SB27	SB28	SB30
α	59.2	59.2	59.2	59.2	59.2	59.2
f	1.11	2.01	2.98	0.99	1.02	2.05
g'	18.57	3.09	3.09	18.81	18.69	3.25
q_0	3.27	28.29	28.29	3.21	19.92	19.92
H_D	2.77	3.15	2.34	4.89	7.55	2.87
h_0	0.86	6.06	7.39	0.58	1.47	5.02
w_0	2.68	3.05	2.27	4.73	7.3	2.78
I	0.231	0.996	1.48	0.107	0.159	0.921
Ek_H	6.59×10^{-4}	5.36×10^{-4}	6.53×10^{-4}	4.42×10^{-4}	1.85×10^{-4}	6.3×10^{-4}
Ek_V	6.39×10^{-3}	1.35×10^{-4}	6.13×10^{-5}	3×10^{-2}	4.54×10^{-3}	1.93×10^{-4}
Re	569	700	574	829	2030	595
h_0/H_D	0.31	1.92	3.16	0.12	0.2	1.75
Exp.	SB31	SB34	SB35	SB36	SB41	SB42
α	59.2	59.2	59.2	59.2	59.2	59.2
f	0.98	2.06	0.98	2.04	2.03	3.02
g'	3	18.64	3.06	2.98	3.05	3.05
q_0	19.92	19.92	19.92	19.92	28.29	28.29
H_D	4.91	4.43	4.92	2.82	3.12	2.31
h_0	3.61	2.1	3.58	5.22	6.14	7.48
w_0	4.75	4.29	4.76	2.73	3.01	2.24
I	0.461	0.325	0.457	0.965	1.014	1.508
Ek_H	4.53×10^{-4}	2.64×10^{-4}	4.49×10^{-4}	6.56×10^{-4}	5.42×10^{-4}	6.61×10^{-4}
Ek_V	7.84×10^{-4}	1.1×10^{-3}	7.93×10^{-4}	1.79×10^{-4}	1.31×10^{-4}	5.92×10^{-5}
Re	828	1423	835	572	692	567
h_0/H_D	0.74	0.47	0.73	1.85	1.97	3.23

Table B.3: Parameters of the small-scale experiments conducted at Warwick.

Exp.	SB43	I1	I2	I4	I5	I6
α	59.2	18.5	18.5	18.5	18.5	18.5
f	2.03	0.99	2.04	0.99	2.06	1.01
g'	3.06	2.98	3	18.64	18.66	18.68
q_0	3.21	19.91	19.91	3.25	3.25	19.91
H_D	1.81	1.52	0.88	1.53	0.88	2.36
h_0	2.07	3.64	5.21	0.59	0.85	1.47
w_0	1.75	4.69	2.74	4.74	2.73	7.31
I	0.657	0.47	0.962	0.108	0.226	0.159
Ek_H	1.61×10^{-3}	4.58×10^{-4}	6.54×10^{-4}	4.51×10^{-4}	6.52×10^{-4}	1.85×10^{-4}
Ek_V	1.15×10^{-3}	7.57×10^{-4}	1.8×10^{-4}	2.95×10^{-2}	6.74×10^{-3}	4.56×10^{-3}
Re	233	819	573	831	575	2031
h_0/H_D	1.14	2.4	5.89	0.38	0.96	0.62
Exp.	I7	I9				
α	18.5	18.5				
f	2.04	2.11				
g'	18.65	3				
q_0	19.91	3.25				
H_D	1.4	0.55				
h_0	2.09	2.14				
w_0	4.33	1.7				
I	0.321	0.689				
Ek_H	2.62×10^{-4}	1.64×10^{-3}				
Ek_V	1.13×10^{-3}	1.04×10^{-3}				
Re	1431	228				
h_0/H_D	1.49	3.89				

Table B.4: Parameters of the small-scale experiments conducted at Warwick.

Appendix C

The values of the parameters from Tables C.1 - C.4, listed in order, are the bottom slope, α (°), the Coriolis parameter, f (s^{-1}), the reduced gravity anomaly, $g\prime$ ($cm\ s^{-2}$), the flow rate, q_0 ($cm^3\ s^{-1}$), the ambient ocean depth, H_D (cm), the theoretical current depth, h_0 (cm), the theoretical current width, w_0 (cm), the dimensionless parameter, I, the horizontal Ekman number, Ek_H, the vertical Ekman number, Ek_V, the Reynolds number, Re, and the non-dimensional ambient depth parameter, h_0/H_D.

Exp.	T1	T2	T4	T5	T6	T7
α	60	60	60	60	60	60
f	0.53	0.53	0.53	0.21	0.21	0.21
g'	6.42	6.27	6.2	6.06	5.91	5.91
q_0	500	250	845	500	230	920
H_D	21.28	17.79	24.05	42.42	34.72	49.1
h_0	9.1	6.51	12.04	5.86	4.02	8.05
w_0	20.32	16.99	22.97	40.51	33.16	46.89
I	0.302	0.267	0.343	0.122	0.106	0.14
Ek_H	4.55×10^{-5}	6.51×10^{-5}	3.56×10^{-5}	2.93×10^{-5}	4.37×10^{-5}	2.19×10^{-5}
Ek_V	2.27×10^{-4}	4.43×10^{-4}	1.3×10^{-4}	1.4×10^{-3}	2.97×10^{-3}	7.42×10^{-4}
Re	8239	5757	10526	12802	8574	17149
h_0/H_D	0.43	0.37	0.5	0.14	0.12	0.16
Exp.	T8	T9	T10	T11	T12	T13
α	60	60	60	60	40	40
f	0.21	0.87	0.87	0.87	0.87	0.86
g'	5.76	6.06	5.91	6.21	5.99	6.51
q_0	920	580	230	880	480	200
H_D	48.79	15.11	11.89	16.81	9.54	7.9
h_0	8.15	12.88	8.22	15.7	11.81	7.27
w_0	46.59	14.42	11.36	16.05	13.67	11.31
I	0.142	0.524	0.443	0.564	0.511	0.403
Ek_H	2.22×10^{-5}	5.55×10^{-5}	8.93×10^{-5}	4.46×10^{-5}	6.15×10^{-5}	9.09×10^{-5}
Ek_V	7.24×10^{-4}	6.97×10^{-5}	1.71×10^{-4}	4.66×10^{-5}	8.24×10^{-5}	2.2×10^{-4}
Re	16930	6757	4197	8406	6097	4127
h_0/H_D	0.17	0.85	0.69	0.93	1.24	0.92
Exp.	T14	T15	T16	T17	T18	T19
α	40	40	40	40	40	40
f	0.86	0.53	0.53	0.53	0.21	0.21
g'	6.43	6.5	6.5	6.43	6.58	6.43
q_0	880	500	210	900	500	190
H_D	11.4	14.31	11.49	16.49	28.87	22.54
h_0	15.34	9.01	5.85	12.18	5.62	3.51
w_0	16.33	20.5	16.46	23.61	41.35	32.28
I	0.546	0.298	0.251	0.338	116	0.097
Ek_H	4.36×10^{-5}	4.51×10^{-5}	6.97×10^{-5}	3.38×10^{-5}	2.81×10^{-5}	4.61×10^{-5}
Ek_V	4.94×10^{-5}	2.33×10^{-4}	5.51×10^{-4}	1.27×10^{-4}	1.52×10^{-3}	3.91×10^{-3}
Re	8603	8321	5383	11083	13340	8129
h_0/H_D	1.35	0.63	0.51	0.74	0.19	0.16

Table C.1: Parameters of the large-scale experiments conducted at Trondheim.

Exp.	T20	T21	T22	T23	T24	T25
α	40	40	40	25.9	25.9	25.9
f	0.21	0.53	0.53	0.86	0.86	0.87
g'	6.5	2.99	3.07	3.37	3.37	3.37
q_0	920	500	900	920	210	550
H_D	32.52	11.82	13.7	6.32	4.38	5.55
h_0	7.67	13.26	17.63	21.72	10.36	16.81
w_0	48.02	16.93	19.63	14	9.7	12.29
I	0.132	0.472	0.527	0.816	0.606	0.738
Ek_H	2.09×10^{-5}	6.63×10^{-5}	4.9×10^{-5}	5.9×10^{-5}	1.23×10^{-4}	7.64×10^{-5}
Ek_V	8.17×10^{-4}	1.08×10^{-4}	6.07×10^{-5}	2.45×10^{-5}	1.08×10^{-4}	4.09×10^{-5}
Re	17984	5655	7658	6354	3039	4907
h_0/H_D	0.23	1.12	1.29	3.44	2.37	3.03
Exp.	T28	T29	T31	T32	T33	T34
α	25.9	25.9	25.9	50	50	50
f	0.87	0.87	0.87	0.87	1.04	1.24
g'	4.64	4.64	4.34	4.03	4.04	4.04
q_0	500	230	100	110	100	130
H_D	5.87	4.82	3.85	7.49	6.37	5.99
h_0	13.66	9.29	6.33	6.88	7.19	8.92
w_0	13	10.67	8.52	8.58	7.3	6.87
I	0.598	0.514	0.453	0.481	0.567	0.708
Ek_H	6.83×10^{-5}	1.01×10^{-4}	1.58×10^{-4}	1.56×10^{-4}	1.8×10^{-4}	1.72×10^{-4}
Ek_V	6.19×10^{-5}	1.33×10^{-4}	2.87×10^{-4}	2.43×10^{-4}	1.85×10^{-4}	1.02×10^{-4}
Re	5490	3715	2369	2397	2086	2186
h_0/H_D	2.33	1.93	1.65	0.92	1.13	1.49
Exp.	T35	T36	T37	T38	T39	T40
α	50	50	50	50	50	50
f	0.53	0.21	0.86	1.06	0.21	1.23
g'	4.11	4.11	4.11	4.04	4.04	4.04
q_0	110	110	330	410	395	440
H_D	10.86	21.82	9.99	8.99	29.9	8.14
h_0	5.34	3.35	11.74	14.64	6.41	16.39
w_0	12.45	25	11.45	10.3	34.27	9.33
I	0.292	0.115	0.586	0.761	0.15	0.902
Ek_H	1.21×10^{-4}	7.62×10^{-5}	8.89×10^{-5}	8.93×10^{-5}	4.06×10^{-5}	9.32×10^{-5}
Ek_V	6.6×10^{-4}	4.24×10^{-3}	8.46×10^{-5}	4.42×10^{-5}	1.16×10^{-3}	3.01×10^{-5}
Re	3092	4921	4217	4201	9246	4026
h_0/H_D	0.49	0.15	1.17	1.63	0.21	2.01

Table C.2: Parameters of the large-scale experiments conducted at Trondheim.

Exp.	T41	T42	T44	T45	T46	T47
α	50	50	50	50	50	50
f	1.24	0.82	1.24	1.2	0.21	0.53
g'	4.04	21.12	21.11	21.12	21.19	21.35
q_0	800	870	880	110	100	100
H_D	9.41	19.79	14.56	8.89	32.1	16.06
h_0	22.18	8.23	10.18	3.54	1.41	2.23
w_0	10.78	22.68	16.69	10.18	36.78	18.4
I	1.023	0.255	0.387	0.246	0.042	0.106
Ek_H	6.93×10^{-5}	2.36×10^{-5}	2.89×10^{-5}	8.04×10^{-5}	3.52×10^{-5}	5.57×10^{-5}
Ek_V	1.64×10^{-5}	1.8×10^{-4}	7.78×10^{-5}	6.67×10^{-4}	2.4×10^{-2}	3.8×10^{-3}
Re	5411	15858	12972	4667	10654	6732
h_0/H_D	2.36	0.42	0.54	0.4	0.04	0.14
Exp.	T48	T49	T50	T51	T52	T53
α	50	40	40	40	40	40
f	0.53	0.53	0.82	1.02	1.22	1.24
g'	21.27	2.7	2.77	2.77	2.77	2.77
q_0	900	900	510	560	530	110
H_D	27.71	13.2	8.34	7.26	6.25	4.17
h_0	6.71	18.87	17.4	20.31	21.64	9.93
w_0	31.76	18.9	11.94	10.4	8.95	5.97
I	0.166	0.574	0.776	0.981	1.164	0.863
Ek_H	1.86×10^{-5}	5.24×10^{-5}	8.53×10^{-5}	9.07×10^{-5}	1.02×10^{-4}	2.26×10^{-4}
Ek_V	4.18×10^{-4}	5.26×10^{-5}	4.02×10^{-5}	2.38×10^{-5}	1.74×10^{-5}	8.16×10^{-5}
Re	20120	7155	4397	4136	3673	1661
h_0/H_D	0.24	1.43	2.09	2.8	3.47	2.38
Exp.	T54	T55	T56	T57	T58	T59
α	40	40	40	40	40	40
f	1.05	0.85	0.53	0.21	0.75	0.64
g'	2.84	2.84	2.84	2.85	2.85	2.85
q_0	130	110	110	110	110	110
H_D	4.95	5.6	7.95	15.93	6.13	6.89
h_0	9.82	8.1	6.41	4.03	7.61	7.04
w_0	7.09	8.02	11.38	22.81	8.78	9.87
I	0.746	0.579	0.363	0.143	0.512	0.438
Ek_H	1.89×10^{-4}	1.84×10^{-4}	1.46×10^{-4}	9.15×10^{-5}	1.73×10^{-4}	1.6×10^{-4}
Ek_V	9.83×10^{-5}	1.8×10^{-4}	4.6×10^{-4}	2.94×10^{-3}	2.3×10^{-4}	3.14×10^{-4}
Re	1985	2038	2575	4098	2169	2344
h_0/H_D	1.99	1.45	0.81	0.25	1.24	1.02

Table C.3: Parameters of the large-scale experiments conducted at Trondheim.

Exp.	T61	T62	T63	T64	T65	T66
α	40	40	90	90	90	90
f	1.02	1.23	0.82	1.01	0.21	0.82
g'	2.84	2.84	2.84	2.84	2.84	2.84
q_0	270	295	300	290	275	530
H_D	6.07	5.39	40	40	40	40
h_0	13.95	16.01	13.19	14.38	6.38	17.52
w_0	8.69	7.73	10.51	8.93	28.66	12.13
I	0.839	1.029	0.689	0.841	0.173	0.77
Ek_H	1.29×10^{-4}	1.36×10^{-4}	1.1×10^{-4}	1.24×10^{-4}	5.8×10^{-5}	8.26×10^{-5}
Ek_V	5.02×10^{-5}	3.16×10^{-5}	6.97×10^{-5}	4.78×10^{-5}	1.17×10^{-3}	3.97×10^{-5}
Re	2902	2764	3411	3026	6468	4539
h_0/H_D	2.3	2.97	0.33	0.36	0.16	0.44
Exp.	T67	T68	T69	T70	T71	T72
α	90	90	90	90	90	90
f	1.22	0.83	0.81	1.22	1.21	0.83
g'	2.84	6.49	6.49	6.49	6.49	21.39
q_0	610	550	110	300	910	570
H_D	40	40	40	40	40	40
h_0	22.86	11.83	5.25	10.6	18.45	6.63
w_0	9.37	15	10.16	9.65	12.75	20.4
I	1.172	0.475	0.338	0.619	0.772	0.234
Ek_H	9.37×10^{-5}	5.38×10^{-5}	1.19×10^{-4}	8.84×10^{-5}	5.07×10^{-5}	2.91×10^{-5}
Ek_V	1.57×10^{-5}	8.65×10^{-5}	4.47×10^{-4}	7.32×10^{-5}	2.42×10^{-5}	2.75×10^{-4}
Re	4003	6973	3145	4244	7398	12886
h_0/H_D	0.57	0.3	0.13	0.27	0.46	0.17
Exp.	T73	T74	T75			
α	90	90	90			
f	1.19	1.18	0.84			
g'	21.31	21.25	21.18			
q_0	580	920	120			
H_D	40	40	40			
h_0	8.06	10.09	3.09			
w_0	15.52	17.61	13.56			
I	0.34	0.368	0.176			
Ek_H	3.47×10^{-5}	2.74×10^{-5}	6.44×10^{-5}			
Ek_V	1.29×10^{-4}	8.35×10^{-5}	1.24×10^{-3}			
Re	10791	13676	5820			
h_0/H_D	0.2	0.25	0.08			

Table C.4: Parameters of the large-scale experiments conducted at Trondheim.

APPENDIX D

Appendix D

The values of the parameters from Tables D.1 - D.4, listed in order, are the bottom slope, α ($^\circ$), the Coriolis parameter, f (s^{-1}), the reduced gravity anomaly, $g\prime$ ($cm\ s^{-2}$), the flow rate, q_0 ($cm^3\ s^{-1}$), the ambient ocean depth, H_D (cm), the theoretical current depth, h_0 (cm), the theoretical current width, w_0 (cm), the dimensionless parameter, I, the horizontal Ekman number, Ek_H, the vertical Ekman number, Ek_V, the Reynolds number, Re, and the non-dimensional ambient depth parameter, h_0/H_D.

Exp.	D01	D02	D03	D04	D05	D06
α	90	90	90	90	90	90
f	2.99	2.04	2.08	0.99	2.1	1.01
g'	2.99	2.99	2.99	3.01	2.99	2.99
q_0	28.27	20.08	20.08	20.08	3.17	3.17
H_D	11.9	9	6	6	4.3	4
h_0	7.52	5.24	5.29	3.64	2.11	1.46
w_0	2.24	2.74	2.7	4.71	1.69	2.93
I	1.511	0.964	0.982	0.467	0.686	0.33
Ek_H	6.65×10^{-4}	6.52×10^{-4}	6.58×10^{-4}	4.53×10^{-4}	1.67×10^{-3}	1.15×10^{-3}
Ek_V	5.92×10^{-5}	1.79×10^{-4}	1.72×10^{-4}	7.59×10^{-4}	1.07×10^{-3}	4.62×10^{-3}
Re	472	479	761	1192	2091	475
h_0/H_D	0.63	0.58	0.88	0.61	0.49	0.37
Exp.	D07	D08	D09	D10	D11	D12
α	90	90	90	90	90	90
f	2.1	0.99	2.05	1.01	2.02	1.02
g'	18.65	18.72	18.74	18.72	3	18.68
q_0	20.08	20.08	3.17	3.17	20.08	28.27
H_D	4	3.6	4.1	3.9	3.75	3.6
h_0	2.13	1.46	0.83	0.58	5.2	1.75
w_0	4.23	7.47	2.72	4.63	2.76	7.97
I	0.331	0.155	0.223	0.11	0.953	0.171
Ek_H	2.65×10^{-4}	1.81×10^{-4}	6.57×10^{-4}	4.61×10^{-4}	6.48×10^{-4}	1.55×10^{-4}
Ek_V	1.05×10^{-3}	4.77×10^{-3}	7.02×10^{-3}	2.89×10^{-2}	1.83×10^{-4}	3.2×10^{-3}
Re	564	575	570	827	225	325
h_0/H_D	0.53	0.4	0.2	0.15	1.39	0.49
Exp.	J01	J02	J03	J04	J05	J06
α	90	90	90	90	90	90
f	2.05	2.09	2.13	1	1.01	2.04
g'	2.99	2.99	2.99	2.99	2.99	18.66
q_0	3.21	19.99	28.28	3.21	19.99	3.21
H_D	9.8	10.1	10.2	10.3	10.3	10.2
h_0	2.1	5.29	6.34	1.47	3.68	0.84
w_0	1.73	2.69	2.89	2.96	4.63	2.74
I	0.67	0.99	1.08	0.33	0.48	0.22
Ek_H	1.63×10^{-3}	6.62×10^{-4}	5.61×10^{-4}	1.14×10^{-3}	4.6×10^{-4}	6.52×10^{-4}
Ek_V	1.11×10^{-3}	1.71×10^{-4}	1.17×10^{-4}	4.64×10^{-3}	7.27×10^{-4}	7×10^{-3}
Re	230	567	669	328	814	575
h_0/H_D	0.21	0.52	0.62	0.14	0.36	0.08

Table D.1: Parameters of the PIV experiments conducted at Warwick.

Exp.	J07	J08	J09	J10	J11	J12
α	90	90	90	90	90	90
f	2.1	1	1	1.01	2.12	2.11
g'	18.65	18.63	18.62	18.61	2.98	2.98
q_0	19.99	3.21	19.99	28.28	19.99	28.28
H_D	10.2	10.1	10.2	10.3	6.3	6.3
h_0	2.12	0.59	1.47	1.75	5.33	5.33
w_0	4.23	4.67	7.39	7.98	2.66	2.91
I	0.331	0.109	0.157	0.171	1.002	1.071
Ek_H	2.65×10^{-4}	4.58×10^{-4}	1.83×10^{-4}	1.55×10^{-4}	6.67×10^{-4}	5.6×10^{-4}
Ek_V	1.06×10^{-3}	2.89×10^{-2}	4.66×10^{-3}	3.21×10^{-3}	1.66×10^{-4}	1.18×10^{-4}
Re	1413	819	2046	2419	562	670
h_0/H_D	0.21	0.06	0.14	0.17	0.85	1.01
Exp.	J13	J14	C01	C02	C03	C04
α	90	90	59.2	59.2	59.2	59.2
f	2.14	2.12	2.01	1.01	2.05	0.98
g'	2.98	2.98	3	3	18.77	18.85
q_0	19.99	28.28	3.17	3.17	20.08	20.08
H_D	3.5	3.5	1.86	3.02	4.46	7.76
h_0	5.36	5.34	2.06	1.46	2.1	1.45
w_0	2.64	2.9	1.75	2.92	4.32	7.51
I	1.011	1.074	0.656	0.33	0.322	0.154
Ek_H	6.7×10^{-4}	5.61×10^{-4}	1.63×10^{-3}	1.15×10^{-3}	2.61×10^{-4}	1.8×10^{-4}
Ek_V	1.63×10^{-4}	1.17×10^{-4}	1.17×10^{-3}	4.6×10^{-3}	1.11×10^{-3}	4.84×10^{-3}
Re	560	669	230	325	1436	2080
h_0/H_D	1.53	1.81	1.14	0.48	0.47	0.19
Exp.	C05	C06	H01	H02	H03	H04
α	59.2	59.2	59.2	59.2	59.2	59.2
f	2.03	0.98	2.08	2.08	2.11	1.01
g'	18.76	18.66	2.98	2.99	2.99	2.99
q_0	3.17	3.17	3.21	19.99	28.28	3.21
H_D	2.84	4.88	1.77	2.79	3.01	3.04
h_0	0.83	0.58	2.11	5.28	6.31	1.47
w_0	2.75	4.72	1.71	2.7	2.92	2.94
I	0.22	0.107	0.681	0.983	1.066	0.331
Ek_H	6.53×10^{-4}	4.56×10^{-4}	1.65×10^{-3}	6.6×10^{-4}	5.58×10^{-4}	1.15×10^{-3}
Ek_V	7.18×10^{-3}	3.04×10^{-2}	1.08×10^{-3}	1.72×10^{-4}	1.19×10^{-4}	4.57×10^{-3}
Re	574	822	228	568	672	327
h_0/H_D	0.29	0.12	1.2	1.89	2.1	0.48

Table D.2: Parameters of the *PIV* experiments conducted at Warwick.

Exp.	H05	H06	H07	H08	H09	H10
α	59.2	59.2	59.2	59.2	59.2	59.2
f	0.99	2.11	2.11	2.12	1	0.98
$g\prime$	2.99	2.99	18.58	18.57	18.57	18.56
q_0	19.99	19.99	3.21	19.99	3.21	19.99
H_D	4.86	2.76	2.76	4.34	4.84	7.72
h_0	3.64	5.31	0.85	2.14	0.59	1.46
w_0	4.70	2.67	2.67	4.20	4.69	7.47
I	0.468	0.994	0.231	0.335	0.109	0.155
Ek_H	4.55×10^{-4}	6.64×10^{-4}	6.66×10^{-4}	2.67×10^{-4}	4.57×10^{-4}	1.82×10^{-4}
Ek_V	7.6×10^{-4}	1.69×10^{-4}	6.48×10^{-3}	1.03×10^{-3}	2.92×10^{-2}	4.79×10^{-3}
Re	823	565	563	1402	821	2060
h_0/H_D	0.75	1.92	0.31	0.49	0.12	0.19
Exp.	H11	B01	B02	B03	B04	B05
α	59.2	18.5	18.5	18.5	18.5	18.5
f	0.98	1.01	2.04	2.01	2.07	0.98
$g\prime$	18.56	3	3	3.01	3.08	3
q_0	28.28	28.28	20.08	20.08	20.08	20.08
H_D	8.43	1.50	0.89	0.90	0.88	1.53
h_0	1.73	3.68	5.22	5.18	5.19	3.63
w_0	8.16	4.65	2.75	2.77	2.73	4.75
I	0.166	0.476	0.960	0.947	0.959	0.463
Ek_H	1.53×10^{-4}	4.58×10^{-4}	6.5×10^{-4}	6.46×10^{-4}	6.47×10^{-4}	4.52×10^{-4}
Ek_V	3.4×10^{-3}	7.32×10^{-4}	1.8×10^{-4}	1.85×10^{-4}	1.79×10^{-4}	7.73×10^{-4}
Re	2452	819	577	581	580	830
h_0/H_D	0.21	2.45	5.88	5.78	5.87	2.36
Exp.	B06	B07	B08	B09	B10	B11
α	18.5	18.5	18.5	18.5	18.5	18.5
f	2.08	1.01	0.98	2.05	2.05	0.98
$g\prime$	3	3	3	18.84	18.73	18.72
q_0	3.17	3.17	3.17	20.08	20.08	20.08
H_D	0.55	0.95	0.97	1.40	1.40	2.43
h_0	2.09	1.46	1.44	2.09	2.10	1.45
w_0	1.71	2.93	3.00	4.33	4.33	7.50
I	0.677	0.329	0.320	0.320	0.322	0.154
Ek_H	1.65×10^{-3}	1.15×10^{-3}	1.14×10^{-3}	2.6×10^{-4}	2.61×10^{-4}	1.81×10^{-4}
Ek_V	1.1×10^{-3}	4.63×10^{-3}	4.92×10^{-3}	1.12×10^{-3}	1.11×10^{-3}	4.82×10^{-3}
Re	227	325	330	1442	1437	2074
h_0/H_D	3.80	1.54	1.49	1.49	1.50	0.60

Table D.3: Parameters of the PIV experiments conducted at Warwick.

Exp.	B12	F01	F02	F03	F04	F05
α	18.5	18.5	18.5	18.5	18.5	18.5
f	2.1	2.06	2.11	2.12	1.01	0.99
$g\prime$	18.68	2.98	2.98	2.98	2.98	2.98
q_0	3.17	3.21	19.99	28.28	3.21	19.99
H_D	0.87	0.56	0.86	0.94	0.95	1.53
h_0	0.84	2.10	5.32	6.35	1.48	3.64
w_0	2.68	1.72	2.67	2.90	2.93	4.72
I	0.228	0.674	0.997	1.075	0.332	0.466
Ek_H	6.65×10^{-4}	1.64×10^{-3}	6.65×10^{-4}	5.61×10^{-4}	1.15×10^{-3}	4.55×10^{-4}
Ek_V	6.72×10^{-3}	1.1×10^{-3}	1.67×10^{-4}	1.17×10^{-4}	4.53×10^{-3}	7.67×10^{-4}
Re	564	229	564	668	326	824
h_0/H_D	0.97	3.78	6.16	6.77	1.56	2.38
Exp.	F06	F07	F08	F09	F10	
α	18.5	18.5	18.5	18.5	18.5	
f	2.08	2.09	1.02	1	1	
$g\prime$	18.55	18.54	18.54	18.54	18.54	
q_0	3.21	19.99	3.21	19.99	28.28	
H_D	0.87	1.37	1.49	2.38	2.60	
h_0	0.85	2.12	0.59	1.47	1.75	
w_0	2.69	4.25	4.61	7.37	8.04	
I	0.228	0.330	0.111	0.158	0.170	
Ek_H	6.61×10^{-4}	2.65×10^{-4}	4.62×10^{-4}	1.84×10^{-4}	1.55×10^{-4}	
Ek_V	6.65×10^{-3}	1.06×10^{-3}	2.79×10^{-2}	4.62×10^{-3}	3.27×10^{-3}	
Re	567	1413	811	2040	2426	
h_0/H_D	0.97	1.55	0.40	0.62	0.67	

Table D.4: Parameters of the PIV experiments conducted at Warwick.

APPENDIX E

Appendix E

The values of the parameters from Table E.1, listed in order, are the coastal wall depth, H_C (cm), the bottom slope, α ($^\circ$), the Coriolis parameter, f (s^{-1}), the reduced gravity anomaly, g' ($cm\ s^{-2}$), the flow rate, q_0 ($cm^3\ s^{-1}$), the ambient ocean depth, H_D (cm), the theoretical current depth, h_0 (cm), the theoretical current width, w_0 (cm), the dimensionless parameter, I, the horizontal Ekman number, Ek_H, the vertical Ekman number, Ek_V, the Reynolds number, Re, and the non-dimensional ambient depth parameter, h_0/H_D.

The values of the parameters from Tables E.2 - E.4, listed in order, are the bottom slope, α ($^\circ$), the Coriolis parameter, f (s^{-1}), the reduced gravity anomaly, g' ($cm\ s^{-2}$), the flow rate, q_0 ($cm^3\ s^{-1}$), the ambient ocean depth, H_D (cm), the theoretical current depth, h_0 (cm), the theoretical current width, w_0 (cm), the dimensionless parameter, I, the horizontal Ekman number, Ek_H, the vertical Ekman number, Ek_V, the Reynolds number, Re, and the non-dimensional ambient depth parameter, h_0/H_D.

Exp.	A	B	C	D	E	F
H_C	7	10.5	7	10	10	2.5
α	19.1	19.1	19.1	90	90	90
f	0.36	2.06	0.9	2.06	0.9	1.26
g'	2.45	11.21	24.68	10.24	4.89	2.94
q_0	1.33	5.84	10.01	6.67	6.67	6.67
H_D	8.6	11.42	9.38	10	10	2.5
h_0	0.63	1.47	0.85	1.64	1.57	2.39
w_0	4.86	2.78	7.22	2.81	4.35	2.98
I	0.111	0.344	0.104	0.373	0.254	0.482
Ek_H	1.18×10^{-3}	6.27×10^{-4}	2.13×10^{-4}	6.14×10^{-4}	5.87×10^{-4}	8.96×10^{-4}
Ek_V	7.11×10^{-2}	2.26×10^{-3}	1.52×10^{-2}	1.81×10^{-3}	4.53×10^{-3}	1.39×10^{-3}
Re	319	598	1757	611	639	418
h_0/H_D	0.07	0.13	0.09	0.16	0.16	0.96
Exp.	G	H				
H_C	1.25	0.5				
α	19.1	19.1				
f	2.06	0.84				
g'	10.24	22.76				
q_0	7	10.01				
H_D	2.19	2.96				
h_0	1.68	0.86				
w_0	2.85	7.45				
I	0.376	0.102				
Ek_H	5.99×10^{-4}	2.15×10^{-4}				
Ek_V	1.72×10^{-3}	1.61×10^{-2}				
Re	626	1747				
h_0/H_D	0.77	0.29				

Table E.1: Parameters of the experiments of Avicola & Huq (2002).

Exp.	1	2	3	4	5	6
α	11.5	11.5	11.5	11.5	11.5	11.5
f	0.48	1.14	2.32	1.68	1.32	0.86
g'	7.8	7.3	6.9	6.4	5.9	5.4
q_0	38	38	38	38	38	38
H_D	2.42	1.24	0.72	0.9	1.06	1.43
h_0	2.16	3.45	5.06	4.47	4.12	3.48
w_0	12.1	6.22	3.6	4.5	5.28	7.13
I	0.145	0.358	0.754	0.571	0.471	0.324
Ek_H	1.42×10^{-4}	2.27×10^{-4}	3.33×10^{-4}	2.94×10^{-4}	2.71×10^{-4}	2.29×10^{-4}
Ek_V	4.45×10^{-3}	7.39×10^{-4}	1.69×10^{-4}	2.98×10^{-4}	4.46×10^{-4}	9.61×10^{-4}
Re	2636	1655	1128	1276	1382	1638
h_0/H_D	0.89	2.77	7.02	4.96	3.9	2.44
Exp.	7	8	9	10	11	12
α	11.5	11.5	11.5	11.5	11.5	11.5
f	1.14	2.12	1.94	1.74	2.52	2.42
g'	4.9	7.8	7.5	7.2	6.9	6.7
q_0	38	38	38	38	38	38
H_D	1.13	0.79	0.84	0.9	0.68	0.69
h_0	4.2	4.54	4.43	4.29	5.27	5.24
w_0	5.63	3.97	4.2	4.51	3.38	3.46
I	0.455	0.64	0.599	0.551	0.818	0.8
Ek_H	2.77×10^{-4}	2.99×10^{-4}	2.92×10^{-4}	2.82×10^{-4}	3.47×10^{-4}	3.45×10^{-4}
Ek_V	4.96×10^{-4}	2.28×10^{-4}	2.62×10^{-4}	3.13×10^{-4}	1.43×10^{-4}	1.51×10^{-5}
Re	1356	1254	1286	1330	1082	1088
h_0/H_D	3.73	5.72	5.27	4.75	7.79	7.57

Table E.2: Parameters of the experiments of Whitehead & Chapman (1986).

Exp.	1	2	3	4	5	6
α	5.7	5.7	5.7	5.7	5.7	5.7
f	1	1	1	1	1	0.5
g'	7.53	21.75	21.65	2.32	14.68	22.12
q_0	18.3	18.3	18.3	18.3	18.3	18.3
H_D	0.58	0.75	0.75	0.43	0.68	1.27
h_0	2.2	1.3	1.3	3.97	1.58	0.91
w_0	5.76	7.51	7.5	4.29	6.81	12.69
I	0.266	0.141	0.141	0.540	0.178	0.070
Ek_H	3.01×10^{-4}	1.7×10^{-4}	1.78×10^{-4}	5.43×10^{-4}	2.16×10^{-4}	1.24×10^{-4}
Ek_V	2.06×10^{-3}	5.94×10^{-3}	5.92×10^{-3}	6.34×10^{-4}	4.01×10^{-3}	2.42×10^{-2}
Re	1245	2116	2111	691	1738	3018
h_0/H_D	3.83	1.73	1.73	9.25	2.32	0.72
Exp.	7	8	9	10	11	12
α	5.7	5.7	5.7	5.7	16.6	16.6
f	0.5	0.5	0.5	0.5	1	1
g'	3.79	13.97	8.7	2.11	22.96	3.1
q_0	18.3	18.3	18.3	18.3	18.3	18.3
H_D	0.82	1.13	1	0.71	2.21	1.34
h_0	2.2	1.14	1.45	2.94	1.26	3.44
w_0	8.16	11.31	10.05	7.05	7.61	4.62
I	0.201	0.092	0.122	0.286	0.136	0.454
Ek_H	3×10^{-4}	1.56×10^{-4}	1.98×10^{-4}	4.02×10^{-4}	1.72×10^{-4}	4.69×10^{-4}
Ek_V	4.14×10^{-3}	1.53×10^{-2}	9.51×10^{-3}	2.31×10^{-3}	6.27×10^{-3}	8.47×10^{-4}
Re	1249	2398	1893	932	2174	799
h_0/H_D	2.69	1.01	1.44	4.18	0.57	2.57
Exp.	13	14	15	16	17	18
α	16.6	16.6	16.6	16.6	16.6	16.6
f	0.4	0.2	0.5	0.2	0.2	1
g'	22.81	22.53	12.1	12.17	10.65	4.41
q_0	18.3	18.3	18.3	18.3	19.2	19.2
H_D	4.38	7.35	3.16	6.3	6.17	1.48
h_0	0.8	0.57	1.23	0.78	0.85	2.95
w_0	15.11	25.34	10.91	21.72	21.26	5.1
I	0.055	0.028	0.1	0.04	0.044	0.371
Ek_H	1.09×10^{-4}	7.79×10^{-5}	1.68×10^{-4}	1.06×10^{-4}	1.11×10^{-4}	3.84×10^{-4}
Ek_V	3.9×10^{-2}	1.54×10^{-1}	1.32×10^{-2}	8.31×10^{-2}	6.93×10^{-2}	1.15×10^{-3}
Re	3426	4816	2232	3539	3391	976
h_0/H_D	0.18	0.08	0.39	0.12	0.14	1.99

Table E.3: Parameters of the experiments of Lentz & Helfrich (2002).

Exp.	19	20	21	22	23	24
α	16.6	16.6	16.6	16.6	5.7	5.7
f	0.8	1	1	0.5	1	1
$g\prime$	10.93	22.35	3.55	11.13	2.51	2.41
q_0	19.2	19.2	19.2	19.2	19.2	19.2
H_D	2.19	2.22	1.4	3.14	0.44	0.44
h_0	1.68	1.31	3.29	1.31	3.91	3.99
w_0	7.57	7.65	4.83	10.81	4.43	4.39
I	0.172	0.14	0.422	0.106	0.520	0.533
Ek_H	2.18×10^{-4}	1.71×10^{-4}	4.28×10^{-4}	1.71×10^{-4}	5.09×10^{-4}	5.2×10^{-4}
Ek_V	4.45×10^{-3}	5.82×10^{-3}	9.24×10^{-4}	1.16×10^{-2}	6.54×10^{-4}	6.28×10^{-4}
Re	1718	2197	876	2193	736	721
h_0/H_D	0.76	0.59	2.35	0.42	8.83	9.1
Exp.	25	26	27	28		
α	5.7	5.7	5.7	5.7		
f	0.8	0.7	0.5	0.2		
$g\prime$	4.14	8.33	10.33	15.43		
q_0	19.2	19.2	19.2	19.2		
H_D	0.59	0.78	1.06	2.33		
h_0	2.72	1.8	1.36	0.71		
w_0	5.94	7.82	10.61	23.33		
I	0.308	0.177	0.111	0.035		
Ek_H	3.55×10^{-4}	2.34×10^{-4}	1.78×10^{-4}	9.19×10^{-5}		
Ek_V	1.68×10^{-3}	4.43×10^{-3}	1.08×10^{-2}	1×10^{-1}		
Re	1057	1603	2112	4082		
h_0/H_D	4.59	2.3	1.28	0.3		

Table E.4: Parameters of the experiments of Lentz & Helfrich (2002).